Absorption and oscillation tomography of the deep Earth with KM3NeT and future atmospheric neutrino detectors

Lukas Maderer

Université Paris Cité

Université Paris Cité
École doctorale STEP'UP - ED N°560
Laboratoire AstroParticule et Cosmologie

Absorption and oscillation tomography of the deep Earth with KM3NeT and future atmospheric neutrino detectors

Par Lukas Maderer

Thèse de doctorat de Physique de l'Univers

dirigée par Edouard Kaminski
et co-encadrée par Véronique van Elewyck

Présentée et soutenue publiquement le 21 octobre 2022

Devant un jury composé de:

Pr. Edouard KAMINSKI, *Institut de Physique du Globe de Paris*	Directeur de thèse
Dr. Jacques MARTEAU, *Université Claude Bernard Lyon-I*	Rapporteur
Pr. Livia LUDHOVA, *RWTH Aachen University*	Rapportrice
Pr. Arwen DEUSS, *University of Utrecht*	Examinatrice
Dr. Thomas EBERL, *University of Erlangen-Nürnberg*	Examinateur
Pr. Thomas PATZAK, *Université Paris Cité*	Président
Dr. Véronique VAN ELEWYCK, *Université Paris Cité*	Membre invité

Titre: Tomographie par absorption et par oscillation de la terre profonde avec KM3NeT et les futurs détecteurs de neutrinos atmosphériques

Résumé en français: La structure et la composition de la Terre profonde sont déterminées par des méthodes sismiques, et des modèles géochimiques basés sur des météorites primitives. Les contraintes apportées par ces techniques laissent cependant des questions sans réponse, comme la composition exacte du noyau externe ou la nature des zones présentant des anomalies sismiques à la limite noyau/manteau (LLSVP). Les neutrinos sont des particules élémentaires neutres qui n'interagissent avec la matière que par la force faible et sont donc capables de couvrir de grandes distances, même à travers des milieux denses comme la Terre. Ils ouvrent ainsi une nouvelle voie pour étudier la Terre profonde. En étudiant l'absorption des neutrinos atmosphériques $\gtrsim$30 TeV, la *tomographie d'absorption* permet de tirer des conclusions sur la densité moyenne de matière le long du trajet des neutrinos. De plus, à des énergies de quelques GeV, la *tomographie d'oscillation* exploite le fait que les oscillations de saveur des neutrinos sont affectées par la densité d'électrons le long de la trajectoire du neutrino, une observable liée à la fois à la densité de matière et à la composition chimique des milieux traversés.

Les premières études de cette thèse sont réalisées pour les deux détecteurs de Cherenkov à eau ARCA et ORCA, actuellement en cours de construction dans la mer Méditerranée dans le cadre de l'infrastructure KM3NeT. La réponse du détecteur est modélisée à l'aide de simulations Monte Carlo développées au sein de la collaboration KM3NeT. La tomographie par absorption avec ARCA peut résoudre le profil de densité radiale moyen de la Terre avec une séparation claire du noyau et du manteau. La précision de la mesure avec les neutrinos atmosphériques est insuffisante pour étudier des structures plus fines, mais de meilleurs résultats pourraient être obtenus en exploitant le flux de neutrinos astrophysiques de haute énergie tel qu'observé par IceCube. Pour ORCA, les variations de densité par rapport au PREM peuvent être contraintes avec une précision respective de $+24\,\%/-32\,\%$ pour le noyau interne et de $\pm5\,\%$ pour le manteau inférieur, avec 10 années de données. Sur la même échelle de temps, ORCA pourrait contraindre les variations de densité des grandes anomalies sismiques dans le manteau profond à $+24\,\%/-21\,\%$. La sensibilité au rapport proton/nucléon (Z/A) dans le noyau externe est quant à elle de $\pm5\,\%$.

La deuxième partie de cette thèse utilise une approche plus générique basée sur des fonctions de réponse paramétrées, permettant de comparer les capacités d'ORCA avec d'autres détecteurs de neutrinos actuellement en construction, tels que le détecteur HyperKamiokande à eau-Cherenkov et l'expérience DUNE à argon liquide. HyperKamiokande offre la plus grande sensibilité à la composition du noyau externe (Z/A), avec une précision de $\sim$2.5 %. Cependant, une précision inférieure à un pour cent reste nécessaire pour distinguer les modèles concurrents de composition du noyau. Un détecteur hypothétique de "nouvelle génération", de taille et de capacité de détection accrues, est proposé à cet effet. Bien que la réalisation d'un tel détecteur soit difficile avec les budgets et technologies actuels, il apporterait une contribution significative à la connaissance de la composition du noyau externe et de la nature des anomalies sismiques, donc à la compréhension de l'origine et de la dynamique de la Terre profonde.

Mots-clés: neutrino, oscillation, absorption, Terre, matière, LLSVP.

Résume Dans l'espoir d'avoir un aperçu de ce qui se passe au-delà du modèle standard, plusieurs expériences sur les neutrinos sont en cours de construction dans le monde entier, dépassant la dernière génération de détecteurs génération en termes de taille et de performances. Cela n'ouvre pas seulement des perspectives fascinantes sur physique des particules, mais peut également ouvrir une nouvelle fenêtre pour étudier l'intérieur de la Terre. La possibilité de le faire en étudiant l'oscillation et l'absorption des neutrinos en fonction de la matière a été étudiée dans cette thèse.

Une partie de cette thèse s'est concentrée sur l'expérience KM3NeT, qui construit actuellement un réseau de détecteurs Water-Cherenkov dans la mer Méditerranée. KM3NeT/ORCA est conçue pour la détection des neutrinos GeV produits dans l'atmosphère, tandis que l'expérience KM3NeT/ARCA est optimisé pour la mesure des neutrinos de l'ordre du TeV et plus, y compris les neutrinos atmosphériques et astrophysiques. KM3NeT est donc un parfait candidat pour réaliser la tomographie d'oscillation et d'absorption. Comme les détecteurs sont encore en construction, leurs performances sont simulées à l'aide d'un cadre d'analyse spécialement développé qui utilise des simulations de Monte Carlo de la collaboration. Le logiciel – initialement conçu pour des études de sensibilité sur les paramètres d'oscillation – a été adapté par mes soins pour être utilisé avec ARCA et pour calculer les effets d'oscillation et d'absorption sur la base de différents modèles de Terre modiables en 1D et 3D. Cette nouvelle fonctionnalité a permis de réaliser multiples études pionnières avec KM3NeT.

La tomographie par absorption, étant sensible à la densité de la matière le long d'une trajectoire de neutrino, peut être utilisée pour balayer le de densité de la Terre dans un modèle approximatif composé de 5 couches, chacune avec une densité constante calculée selon le modèle de référence préliminaire de la Terre (PREM). Le concept d'analyse principale a pu être démontré, montrant le potentiel de l'ARCA pour détecter le noyau de la Terre, avec des performances globalement comparables à une étude similaire d'IceCube sur une prévision de 10 ans d'acquisition de données. Une amélioration possible des sensibilités en exploitant le flux de neutrinos astrophysiques a été étudiée, mais elle ne montre qu'un faible effet car la Terre devient opaque pour les neutrinos dans cette gamme de haute énergie. L'étude des petites hétérogénéités de densité dans le manteau inférieur de la Terre, appelées *large low shear velocity provinces* (LLSVP), semble hors de portée de la tomographie par absorption dans le contexte des détecteurs de neutrinos atmosphériques à haute énergie existants comme ARCA.

La tomographie par oscillation est sensible à la densité électronique n_e dans le milieu de propagation d'un neutrino, qui est proportionnelle au produit de la densité de matière ρ et du rapport proton/nucléon Z/A. En supposant que l'une de ces quantités est connue des sciences de la Terre, on peut mesurer l'autre.

En répétant l'analyse du profil de densité de la Terre avec ORCA, on obtient un pouvoir de résolution nettement supérieur, jusqu'à une précision de $+24\,\%/-32\,\%$ pour le noyau interne et de $\pm 5\,\%$ pour le manteau inférieur avec 10 ans de données ORCA. L'amélioration est due au flux plus élevé de neutrinos dans la gamme d'énergie oscillante. L'utilisation de contraintes gravitationnelles sur la masse et l'inertie de la Terre améliore encore le résultat, car les effets de corrélation entre les couches sont supprimés. Cependant, l'approximation d'un modèle à 5 couches semble être trop simplifiée en ce qui concerne les résolutions obtenues, en particulier dans la région du manteau externe avec diverses petites zones de transition de densité différente. Dans

une étape suivante, au lieu d'ajuster des densités constantes, ρ a été mesuré par rapport au PREM. Cette approche est également couramment utilisée en géophysique et ouvre la porte à une utilisation combinée du neutrino avec les données sismiques *e.g.* l'étude de l'oscillation et de la tomographie d'absorption fait l'objet de mon exposé au CICR.

L'étude des LLSVP semble plus réalisable avec la tomographie d'oscillation. Une évaluation du signal des LLSVP à différents endroits de la Terre par rapport à la position du détecteur a révélé que les longues sections transversales de neutrinos à travers un LLSVP dans une fenêtre angulaire étroite sont favorisées par rapport aux courtes sections transversales dans une fenêtre angulaire large. Dans le cas concret d'ORCA, cette condition sur la position du LLSVP est remplie presque parfaitement pour le LLSVP africain. Cependant, seuls les LLSVP avec des densités relatives $+24\,\%/-21\,\%$ par rapport au manteau environnant peuvent être détectés, ce qui correspond à environ 10 fois les estimations d'anomalies de densité basées sur les mesures sismiques. Il est intéressant de noter que les contributions des deux canaux PID, à savoir les événements de type piste et douche, diffèrent fortement entre l'étude des hétérogénéités du noyau externe et du manteau, ce qui indique que les détecteurs de neutrinos peuvent en fait être optimisés pour des questions géophysiques spécifiques. La dernière analyse présentée de KM3NeT s'est concentrée sur le Z/A du noyau externe, en supposant que sa densité était connue grâce au PREM. La sensibilité au Z/A dans le noyau externe s'est avérée être de $\pm 5\,\%$. Ce résultat est obtenu de la même manière que dans une thèse antérieure sur la tomographie des oscillations avec ORCA. Les améliorations apportées à la simulation de Monte Carlo et les nouvelles hypothèses sur les paramètres d'oscillation basées sur les résultats globaux actualisés montrent un net gain de sensibilité par rapport à l'ancienne analyse, ce qui montre que le potentiel de la tomographie des oscillations de neutrinos peut encore bénéficier d'une meilleure connaissance du détecteur.

Afin de distinguer les modèles réalistes de la composition du noyau externe et d'identifier les éléments légers qu'il contient, une précision inférieure à un pour cent est nécessaire en raison de la similitude des valeurs Z/A du fer, du silicium ou de l'oxygène. Dans la deuxième partie de cette thèse, des détecteurs de différentes conceptions et techniques de détection sont évalués quant à leur pouvoir de performance sur la contrainte de la composition du noyau externe, dans le but de définir les exigences pour un potentiel détecteur de prochaine génération (NextGen) qui serait capable d'exclure réellement des compositions de modèles réalistes. Chronologiquement, la plupart des travaux présentés dans ce chapitre ont été réalisés pendant la première année de mon doctorat et ont conduit à plusieurs contributions dans des conférences et des ateliers, à une publication dans Europhysics News [1] et à un article soumis à Frontier Geoscience [2], tous axés sur la composition chimique du noyau externe. Au lieu d'utiliser une simulation MC spécifique pour simuler un détecteur, des réponses paramétrées sont utilisées pour un réglage flexible des propriétés de base du détecteur, comme la taille et la résolution. Les types de détecteurs étudiés comprennent un détecteur de Cherenkov à eau de grand volume de type ORCA, une conception de réservoir d'eau avec une résolution améliorée au prix du volume instrumenté à la HyperKamiokande et une expérience de type DUNE utilisant un TPC rempli d'argon liquide. Les configurations de détecteur de type DUNE et ORCA donnent des résultats similaires, tandis que HyperKamiokande atteint une précision de $\sim$2.5 % après 20 ans de fonctionnement.

L'effet de compromis entre la taille et les performances du détecteur est l'une de nos conclusions les plus solides.
Sur la base de ces résultats, une configuration NextGen a été définie avec un pouvoir de résolution similaire à celui d'HyperKamiokande mais avec un volume instrumenté environ 30 fois plus grand. Un tel détecteur serait capable d'exclure un modèle de noyau externe riche en hydrogène d'ici 15 ans. Bien qu'un tel détecteur puisse sembler irréalisable à l'heure actuelle, il faut savoir que la technologie existe déjà et est utilisée dès à présent. Avec un budget et une main-d'œuvre appropriés, un détecteur de tomographie par neutrinos aussi puissant pourrait être construit, alors que la limitation théorique de la sismologie pour contraindre directement les compositions chimiques ne sera jamais surmontée.

Perspectives La tomographie des neutrinos présente le potentiel général de contribuer à une meilleure connaissance de l'intérieur de la Terre. Cependant, la génération actuelle de détecteurs n'atteint pas encore la précision nécessaire pour s'attaquer seule aux questions ouvertes des géosciences. Le début de la collaboration avec les sismologues de l'université d'Utrecht, le professeur Arwen Deuss et sa doctorante Rûna van Tent, offre un grand potentiel en ce qui concerne la combinaison des données neutrinos et sismiques.
Les outils développés au cours de mon doctorat peuvent être considérés comme une base solide pour les futurs physiciens neutrinos dans le but de réaliser des tomographies neutrinos. En particulier, la mise en œuvre d'un modèle de Terre en 3D ouvre de nouvelles possibilités intéressantes, telles que la modélisation d'hétérogénéités 3D plus complexes dans le manteau, et plus généralement la tomographie 3D de la Terre à l'aide de détecteurs de neutrinos multiples.

`EarthProbe` et `SWIM`, les deux frameworks utilisés durant cette thèse, ont été créés à l'origine par un ancien doctorant d'APC, Simon Bourret. En fait, ils partagent de nombreuses classes et la conception générale est similaire. Il serait intéressant d'implémenter la réponse paramétrée du détecteur de `EarthProbe` dans `SWIM`, afin de faciliter le développement et d'éviter les décalages potentiels dus à de légères divergences dans le code, en se concentrant sur un seul environnement logiciel.

Travaux supplémentaires Parallèlement à l'analyse proprement dite, le cadre paramétrique `EarthProbe` et le cadre MC `SWIM` ont été étendus par de multiples fonctionnalités concernant la tomographie par neutrinos, mais ont également été maintenus et améliorés à tous les niveaux du développement logiciel. Cela est particulièrement vrai pour `SWIM` qui est devenu l'un des principaux cadres d'analyse du groupe de travail sur l'oscillation de KM3NeT. L'implémentation des effets d'absorption et des modèles d'entrée à des énergies plus élevées, ainsi qu'un fichier d'entrée approprié construit à partir du MC ARCA, ouvre également la possibilité d'utiliser `SWIM` pour ARCA et démontre en outre comment, en principe, tout MC peut être utilisé pour simuler le détecteur respectif – l'une des motivations pour développer `SWIM` en premier lieu. `EarthProbe` a été utilisé par l'étudiant M1 Romain van den Broucke pour une étude sur la sensibilité d'ARCA à la section transversale des neutrinos de haute énergie, en utilisant les nouveaux outils que j'ai développés.

`ParamPID`, le paquet d'apprentissage automatique basé sur python pour la clas-

sification des événements, est devenu un pilier important de l'analyse des oscillations et sera maintenu et amélioré par d'autres collaborateurs. Avec mon cadre pour la création de caractéristiques d'entraînement (tous deux décrits dans la note technique B), il fournit un outil puissant pour améliorer le PID de KM3NeT en ajoutant et en évaluant davantage de caractéristiques. Ses performances ont été présentées sous forme de poster lors de la conférence Neutrino2022 [3].
J'ai utilisé `ParamPID` pour entraîner le premier PID de ARCA pour la classification voie/douche et neutrino/muon. Un article comparant différentes techniques d'apprentissage automatique (apprentissage profond, réseaux de neurones à graphe/convolutionnels) pour la classification des événements dans ARCA est en préparation. Des efforts sont faits pour distinguer les neutrinos atmosphériques et astrophysiques.
De plus, dans une mini production d'ORCA4 avec des efficacités PMT alternées, grâce à mon cadre adapté, le PID a été pour la première fois créé automatiquement comme une partie de la chaîne MC.

Title: Absorption and oscillation tomography of the deep Earth with KM3NeT and future atmospheric neutrino detectors

Abstract: Structure and composition of the deep Earth are constrained by seismic methods and geochemical models based on primitive meteorites. These leave some questions unsolved, such as the exact composition of the outer core or the nature of seismic anomalies at the core/mantle boundary (LLSVP). Neutrinos are neutral elementary particles that only interact with matter by the weak force and are thus able to cover large distances even through dense media such as the Earth, opening a new window to study our planet's interior. By studying absorption of atmospheric neutrinos $\gtrsim$30 TeV, *absorption tomography* allows to draw conclusions about the average matter density along the neutrino path. Furthermore, at energies of a few GeV, *oscillation tomography* exploits the fact that neutrino flavour oscillations are affected by the electron density along the neutrino path, an observable connected to both the matter density and chemical composition of the traversed media.

The first studies in this thesis are performed for the two water-Cherenkov detectors ARCA and ORCA, currently being built in the Mediterranean Sea as part of the KM3NeT infrastructure. The detector response is modelled using Monte Carlo simulations developed within the KM3NeT Collaboration. Absorption tomography with ARCA can resolve the average radial density profile of the Earth with a clear separation of core and mantle. The precision from studying atmospheric neutrinos alone appears insufficient to study finer structures. Improvements could come by exploiting the high energy astrophysical neutrino flux, as detected by IceCube. From oscillation tomography with ORCA, density variations compared to PREM can be constrained with a respective precision of $+24\,\%/-32\,\%$ for the inner core and $\pm5\,\%$ for the lower mantle, with 10 yr of ORCA data. In the same timescale, ORCA could constrain the density variations of large seismic anomalies in the deep mantle to $+24\,\%/-21\,\%$. The sensitivity to the proton-to-nucleon ratio (Z/A) in the outer core was found to be $\pm5\,\%$.

The second part of this thesis uses a more generic approach based on parameterised response functions, allowing to compare the capabilities of ORCA with other neutrino detectors currently under construction, such as the water-Cherenkov detector Hyper-Kamiokande and the Liquid Argon experiment DUNE. HyperKamiokande is found to provide the highest sensitivity to the outer core composition (Z/A), with a precision of $\sim$2.5 %. However, a sub-percent precision is needed to distinguish concurrent models of core composition. A hypothetical 'Next-Generation' detector with enhanced size and detection capabilities is proposed for that purpose. Albeit the realisation of such a detector seems challenging with current budgets and technologies, it could make a significant contribution to the knowledge of the outer core composition, as well as the nature of LLSVPs, hence the understanding of deep Earth dynamics.

Keywords: neutrino, oscillation, absorption, Earth, matter, LLSVP.

Acknowledgements

This thesis marks the end of multiple journeys in my life. Journeys that would not have been possible without the help of many special people.
The journey to Paris was not an easy one. Setting foot in France would have been not half as easy and joyful without the help of Gisela, who let me, a stranger, live in her house and guide me through the jungle of french administration, until I found a place on my own. I am grateful for the warm welcome I received from all the people at APC and the support I received not only at work but also in my daily life in Paris. My colleagues from all around the world and all the other fascinating people I met here made the last three years an indescribable valuable experience, that I wouldn't want to miss.
The journey of becoming a doctor was only possible because of my supervisors Véronique and Edouard, who offered me this great opportunity to work on such an interesting subject and guiding me through all the difficult phases of the doctorate. I can't name all the people at APC, KM3NeT or anywhere else who helped me in so many ways to finish this thesis and taught so many things, but be assured that I truly appreciate all your inputs. My special thanks go to João, who always had an open ear for me and shared his enriching thoughts with me.
The journey of becoming a physicist reaches back a long way. My very first teacher, Mrs. Zenk, taught me the joy of learning, and my first teachers in mathematics and physics, Mr. Pfeiffer and Mr. Utz, awakened in me an enthusiasm for their subject and thus showed how important role models are for young students. In the end, I owe it to Mr. Eberl's lecture that I dedicated myself to the study of neutrinos and set foot into the KM3NeT collaboration.
The journey of growing up will probably never really end, but at least at this point I want to express how proud I am of having such amazing friends who supported me all the way from Germany, believed in me and pushed to where I am now. And finally, I thank my parents, my brother and my grandparents, for encouraging my passion for science and supporting me in every possible way. Without you I could not have achieved this.

Contents

List of Figures

List of Tables

Introduction

Studying the Earth's interior has always been of great interest for scientists and philosophers throughout mankind. The underworld was origin of uncountable numbers of myths and legends, one of the most famous being its interpretation as hell consistent of 9 concentric layers by Dante's *Inferno*. Until the 17th century, theories of a hollow Earth enclosing a sun or even other planets existed, trying to explain the Earth's internal temperature gradient and its varying magnetic field. It was not until the 20th century that the model of an Earth's core prevailed - and with it a shell-shaped Earth structure that ironically comes close to Dante's poem from half a millennium ago. But even with today's technology, many questions about the inner structure and dynamics of our planet remain unanswered, which is no wonder if we compare the scales: the deepest man-made drill hole is only 12 262 m - the Earth's core boundary at 2900 km! And other than in Jules Verne's *Voyage au centre de la terre* it is unlikely for humans to go much deeper in the near future.

This thesis is motivated by the need for new techniques for geophysical measurements. As we will learn, the neutrino is a weakly interacting particle which nevertheless 'feels' the presence of matter and is thus at least in theory a perfect candidate for the tomography of the Earth.

The elusive nature of the neutrino is at the same time the biggest obstacle, as their detection becomes very challenging. Luckily, despite the little chance of success, particle physicists made huge efforts to make neutrino detectors possible. Today one can look back on almost a century of remarkable history in neutrino physics, awarded with multiple Nobel prizes. Now that the concepts and reliability of the first generations of neutrino detectors have proven their worth, a new era of detectors lies in front of us. The sheer numbers of neutrino experiments, their advanced technologies and scales that go up to cubic-kilometres open up unprecedented possibilities for neutrino physicists.

The structure of this thesis is separated into three parts.

Part I serves as an introduction about the scientific background and the experimental state of the art. Chapter 1 is dedicated to neutrino physics, covering its general properties and sources of neutrinos. Strong emphasis is laid on neutrino oscillations and neutrino interactions with matter, as the first is the basis for the concept of *oscillation tomography* and the latter of *absorption tomography*, the two core principles of neutrino tomography. The theory of neutrino interactions are further crucial to grasp the methodology of neutrino detectors, which is discussed in chapter 2 together with the introduction of a few existing experiments. Chapter 3 starts with an introduction into Earth sciences (from the humble perspective of a particle physicist). Open questions of geoscience are introduced and how neutrinos could at least help to find answers to them. The last section of Part I highlights previous work on neutrino tomography.

Part II covers the technical and analytical methods of the presented work. Although not exclusively discussed, an emphasis of this thesis is laid on the cubic-kilo metre neutrino telescope KM3NeT that builds two water Cherenkov neutrino detectors in the Mediterranean Sea. Its experimental setup is in described in detail in Chapter 4. The Monte Carlo simulation chain of KM3NeT, which is used for its specific analysis, is described in Chapter 5. A crucial part of any analysis in KM3NeT is the event classification into signal and background and further into physical interaction channels. As personal contribution to the KM3NeT collaboration, I developed a machine-learning framework for this task, to which Chapter 6 is devoted. Chapter 7 describes in detail the frameworks that were used for the present analyses. In a first step the physical models from Part I are included. Next, as the detectors under investigation are not fully constructed yet, their response has to be simulated, where two different approaches are worked out. Finally the statistical methods that are used to draw robust conclusions are explained.

Part III presents the results of my three years work on neutrino tomography. It is ordered from least to most promising rather than chronologically. Chapter 8 shows the first perspectives of performing absorption tomography KM3NeT/ARCA, *i.e.* constraining the radial density profile of the Earth and the sensitivity to supposed inhomogeneous regions at the base of the Earth's mantle. Thanks to the design of the analysis framework, the here presented methods can also be used for KM3NeT/ORCA on oscillation tomography, shown in chapter 9. As I found higher sensitivities on Earth parameters from ORCA than for ARCA, the analysis is here continued to a deeper level and includes also a systematic study of the outer core composition. The final chapter 10 covers a wider picture of neutrino neutrino tomography by studying other experiments than KM3NeT and further investigates the capabilities of a theoretical neutrino detector of the next generation.

Part I

Scientific and experimental state of the art

Chapter 1

Neutrino physics

Contents

This chapter starts with an general overview of the fundamental properties of the neutrino. Sources of neutrinos are discussed, with a dedicated section to atmospheric neutrinos, which are the most relevant for this work. Neutrino oscillations in vacuum and matter are explained first in general and eventually for atmospheric neutrinos that traverse the Earth. The link between resonance effects in the oscillations and Earth properties is pointed out here. The final section on neutrino interactions with matter builds not only the backbone for absorption tomography but also for the detection of neutrinos. Focus is again set on neutrino energies of relevance for the atmospheric neutrino spectrum.

1.1 The neutrino in a nutshell

Postulated already in 1930 by Pauli[4], the neutrino is one of the oldest elementary particles of the modern standard model (SM) of particle physics. It carries no electrical charge and has a spin of $\frac{1}{2}$, thus belonging to the fermion family. It can only interact with matter via the weak force by the exchange of $W^{\pm}$ (charged current (CC)) and Z^0 (neutral current (NC)) bosons, leading to a very small interaction cross section of $\sigma/E \approx 10^{-38}\,\mathrm{cm}^2/\mathrm{GeV}$, many orders of magnitude lower than for other fermions. This makes the study of neutrinos challenging; after being labeled as 'undetectable particle' for more than two decades, the first experimental evidence for the existence of neutrinos was only found in 1956 via the observation of the electron antineutrino capture

$$\bar{\nu}_e + p \rightarrow e^+ + n \tag{1.1}$$

in the reactor experiment of Reines and Cowan[5]. On the other hand, the low interaction probability opens many unique possibilities, mainly in the field of astrophysics where neutrinos could serve as a new type of messenger particles (nearly) unaffected by matter along their long journey to the Earth. Another application that is only possible because of the neutrino's small cross section, is the tomography of the Earth's interior - the topic of this thesis.

Neutrinos appear in three types, so called flavours, corresponding to the type of their charged leptonic counterparts: ν_e, ν_μ, ν_τ and their anti-particles $\bar{\nu}_e$, $\bar{\nu}_\mu$, $\bar{\nu}_\tau$. Measurements of the Z resonance with LEP at CERN confirmed the existence of three different active neutrino species in agreement with the SM[6].

While the neutrino is assumed to be massless in the SM, the discovery of neutrino oscillations (to be discussed in sec. 1.3) revealed that neutrinos actually have mass. From experiments with tritium decay (KATRIN[7]) the mass of the electron neutrino can be constrained to $<0.9\,\mathrm{eV}$[8]. Cosmological observations on the other hand can probe the combined mass of all active neutrino flavours . An overview about different probing methods and results is given in [9], that all hint to a total neutrino mass of $\sum m_\nu \approx \mathcal{O}(10^{-1}\,\mathrm{eV})$. A recent constrain from the combination of cosmological and terrestrial constraints sets an upper bound on the neurino masses at $\sum m_\nu < 0.12 - 0.69\mathrm{eV}$ at 2σ[10] and thus many orders of magnitudes lower than for all other particles of the SM. It is therefore commonly believed that a more sophisticated mechanism than the simple SM Higgs is responsible for the generation of the neutrino mass (see *e.g.* [11]).

Further it is still unknown whether the neutrino is a Dirac or a Majorana particle, *i.e.* if the neutrino is its own anti-particle[12]. As a consequence, the lepton number conservation would be broken, *e.g.* in the neutrinoless double beta ($0\nu\beta\beta$) decay, which is studied by several experiments (*e.g.* [13, 14]) to find the neutrino nature and set limits on a potential Majorana neutrino mass.

Neutrino physicists are eagerly looking for more phenomena of physics beyond the SM *e.g.* non-standard interactions of heavy sterile neutrinos, or violations of the charge-parity (CP) symmetry conservation. Although these topics will not be discussed in this thesis, they should illustrate the fascination that emanates from this special particle and why an evergrowing community of researches make such huge efforts to study it.

Neutrinos are generated in many processes driven by the weak interaction and thus

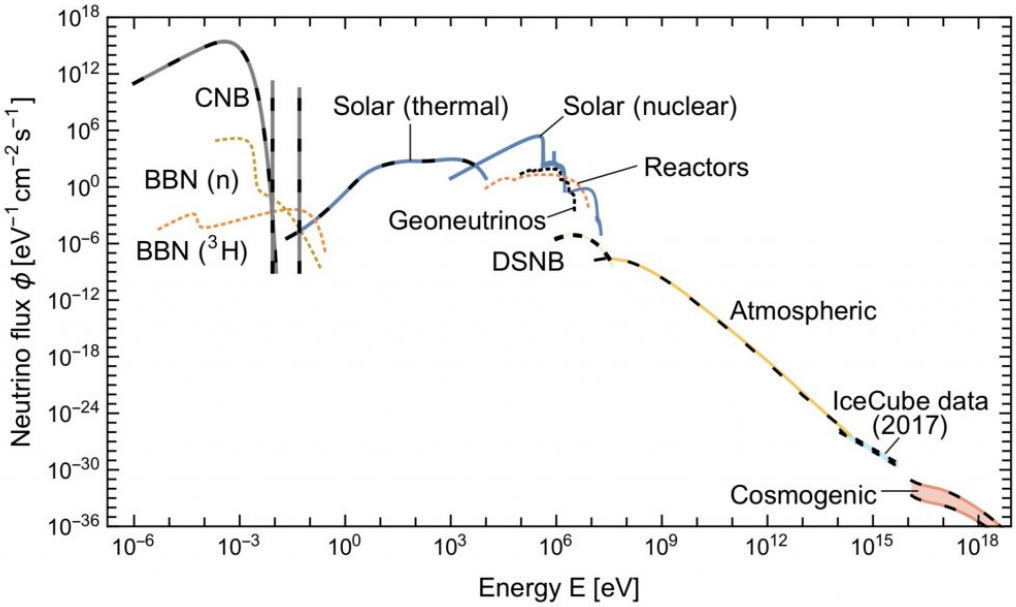

Figure 1.1: Neutrino fluxes from different sources, plotted over the neutrino energy (Figure taken from [15]). In this thesis, the focus lies on atmospheric neutrinos (yellow).

origin from numerous sources. The neutrino energy depends hereby on the underlying process and covers many orders of magnitudes, from MeV (radioactive decays) to EeV (astrophysical sources). The fluxes and energies of the most important neutrino sources are shown in Fig. 1.1.

Cosmological neutrinos are remnants from the Big Bang and an omnipresent neutrino analogue to the cosmic microwave background. Since these neutrinos were able to escape the early dense universe much earlier than photons, they would potentially allow us to gain information about the early history of the universe, such as the Big Bang nucleosynthesis (BBN)[16] epoch.

In fusion reactions in the sun, solar electron neutrinos are produced at MeV energies. A rule of thumb (which is often used to attract young physicists to the neutrino community) is that approximately 60 billion solar neutrinos pass the area of a fingernail per second. Their detection in the seventies with Homestake[17] led to the famous solar neutrino problem, that occupied physicists for many years: Their measured solar neutrino flux was about a factor 3 smaller than predicted by the standard solar model (SSM)[18]. Since both model and experiment seemed to be correct, the problem persisted up until the 1990's when new detectors and detection techniques came up: The first water-Cherenkov detector Kamiokande made the first directional counting observation of solar neutrinos. SAGE and GALLEX, two radiochemical experiments, lowered the energy detection threshold by using gallium as detection medium. The result of all experiments indicated a significant deficit in the solar neutrino flux with respect to the SSM prediction. A breakthrough in this long lasting mystery was achieved by the Sudbury Neutrino Observatory (SNO) in 2002 that had the capability to distinguish between charged-current interactions from electron neutrinos only and neutral-current interactions from all neutrino flavours, and thus quantify the overall solar neutrino flux. As it was in agreement with the SSM, this was the evidence that the observed

deficit in the solar electron neutrino flux was due to neutrino flavour transformation – neutrino oscillations – which were already detected in measurements of atmospheric neutrinos with SuperKamiokande[19].

An exceptional neutrino source is the explosive death of a star - a supernova (SN). During the collapse of a star an enormous amount of neutrinos is emitted within a few seconds. The first and only SN observed so far in neutrinos happened in 1987 and brought important insights into the processes involved in the last moments of a star[20]. Today, thanks to multiple of neutrino detectors deployed around the globe, astrophysicists wait in suspense for the next SN - an event predicted to occur about three times per century in our galaxy.

The neutrino flux in the MeV region is also occupied with reactor- and terrestrial electron antineutrinos from beta-decays. The reader with a geophysical background may be familiar with the latter under the name geoneutrinos, that are produced in radioactive decays in the Earth. Their detection is challenging due to the high background of reactor neutrinos, but was firstly reported in 2005 by KamLAND[21] and Borexino in 2010[22] and becomes even more feasible with upcoming experiments like SNO+[23] and JUNO[24]. As neutrino tomography, geoneutrino analyses combine interests of particle- and geophysicists and could *e.g.* help investigate the abundances of radioactive material like Uranium and Thorium in the Earth. An interesting summary on the detection of geoneutrinos is given in [25].

In the upper end of the spectrum, we expect neutrinos from violent astrophysical events within and beyond our galaxy. Among those sources, Active Galactic Nucleis (AGNs) appear as a prime candidate since the observation by IceCube of neutrinos correlated to the blazar TXS 0506+056[26], and cosmogenic neutrinos produced by interactions of ultra-high-energy cosmic rays with photons of the cosmic microwave background[27]. For neutrinos at 1 TeV with an approximate flux of $\sim 1\,\mathrm{km}^{-2}\,\mathrm{yr}^{-1}$ (Fig. 1.1) huge detectors are needed to detect even a single neutrino during the lifetime of the experiment. Such high energetic neutrinos can be detected with a high (sub-degree) angular resolution, opening the possibility to correlate them with their astrophysical sources. However in this work, almost exclusively atmospheric neutrinos are considered.

1.2 Atmospheric neutrinos

Within the wide energy range from GeV to tens of TeV the total neutrino flux is dominated by atmospheric neutrinos. We will see in sec. 3.2, that the energy ranges of interest for both oscillation and absorption tomography are perfectly covered by the atmospheric neutrino spectrum, which is thus discussed in detail now.

As indicated in the name, atmospheric neutrinos are produced in particle air showers in the upper Earth's atmosphere ($\sim$20 km), triggered by heavy, high energetic cosmic particles, mostly protons or heavier nuclei. The atmospheric neutrino flux ϕ can be modeled by solving the cascade equations for hadrons of species j that have traversed the atmosphere up to a slant depth X

$$\frac{\mathrm{d}\phi_j}{\mathrm{d}X} = -\frac{\phi_j}{\lambda_j} - \frac{\phi_j}{\lambda_j^{\mathrm{dec}}} + \sum_k S_{kj}(E_j, X), \tag{1.2}$$

where λ_j is the interaction length and λ_j^{dec} the decay length[28, 29]. The (re)generation functions S_{kj} describe the production of particles k from the initial hadron j. The atmospheric neutrino flux is typically described by two components. Pions and kaons are the most abundant hadrons in the air showers and make up the *conventional* flux, with the most dominant decay channels

$$\begin{aligned} K^- &\to \mu^- \bar{\nu}_\mu \to e^- \bar{\nu}_e \nu_\mu \bar{\nu}_\mu \\ K^- &\to \pi^- \pi^0 \end{aligned} \tag{1.3}$$

and

$$\pi^- \to \mu^- \bar{\nu}_\mu \to e^- \bar{\nu}_e \nu_\mu \bar{\nu}_\mu \tag{1.4}$$

(K^+ and π^+ decay analogue). Including the subsequent muon decay, the flavour ratio of the conventional flux is thus approximately

$$\overset{(-)}{\nu}_e : \overset{(-)}{\nu}_\mu : \overset{(-)}{\nu}_\tau = 1 : 2 : 0 \ . \tag{1.5}$$

The *prompt* flux is due to decays of heavy charmed mesons, mainly D's with a small contribution of B's. The competition between decay and interaction length in eq. 1.2 defines the dominant energy range for each component of the atmospheric flux. The decay length of a particle j can be expressed as

$$\lambda_j^{\text{dec}}(X) = \rho(X) \gamma c \tau_i \tag{1.6}$$

with the rest lifetime τ_i that is relativistically enhanced by the Lorentz factor γ. From that one can derive a *critical energy*, above which the decay length becomes larger than the interaction length, *i.e.* the probability to decay (and produce neutrinos) is higher than to lose energy by interactions with molecules in the atmosphere. Pions and kaons have a critical energy of $\mathcal{O}(10^2)$GeV, while the heavy B and D mesons have much larger critical energies of $\mathcal{O}(10^7)$GeV. Thus, the prompt neutrino flux is expected to dominate over the conventional flux at higher energies. Charmed mesons decay equally into all lepton flavours and yield thus a flavour ratio of $\overset{(-)}{\nu}_e : \overset{(-)}{\nu}_\mu : \overset{(-)}{\nu}_\tau = 1 : 1 : 1$.
The conventional atmospheric neutrino spectrum follows a power-law distribution

$$\phi_\nu(E) \sim E^{-\gamma} \tag{1.7}$$

with a spectral index $\gamma \approx 3.7$. The prompt flux follows closely the softer primary cosmic ray spectrum with $\gamma \approx 2.7$[28, 30].

As the flux of cosmic particles is approximately isotropic, also the production of atmospheric neutrinos is homogeneous over the globe. This isotropy is in fact broken: First, due to the geomagnetic field, charged cosmic particles get deflected differently, causing an azimuth dependence of the atmospheric neutrino flux. This 'east-west' asymmetry is of the order of $\sim$10 % for GeV neutrinos and decreases at higher energies[31]. Second, the zenith angle of the muons created in the meson decays of 1.3 affects its decay probability. In the lower and thus denser part of the atmosphere, the muon could interact with particles on its way rather than decaying. Muons coming

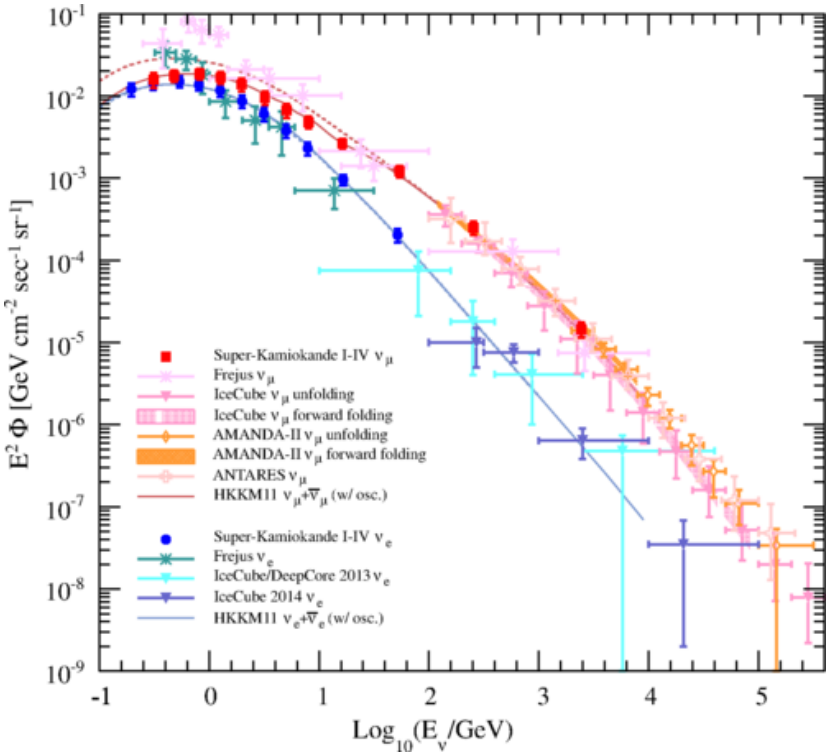

Figure 1.2: Measurements of the atmospheric neutrino flux by ANTARES[33], AMANDA[34], IceCube[35] and Frejus[36] (Taken from [39]).

from the horizon will traverse the thin atmosphere longer than straight up- or down-going muons and are thus more likely to decay and produce a neutrino. The expected flavour ratio $\nu_\mu/\nu_e \approx 2$ is thus only justified near the horizon, but increases towards the nadir/zenith, and further at higher energies, where the muon decay is suppressed due to its relativistically enhanced lifetime. The effect of the atmosphere density also leads to a seasonal variation in the neutrino flux due to changes of temperature[32]. The flux of atmospheric neutrinos has been measured by many experiments, like ANTARES[33], AMANDA[34], IceCube[35] and Frejus[36], with excellent agreement among each other (Fig. 1.2). Also shown in the plot are the flux predictions by MC simulations of the HKKM group[1]. Their work includes predictions of cosmic ray fluxes, their interaction in the atmosphere and the production of air showers. In the most recent publication [37] also the effects described above are included. Their results are publicly available at [38] and are used for the simulations in this work (discussed in sec. 7.2.1).

Fig. 1.3 shows the Honda flux for the Gran Sasso laboratory in Italy (at sea level), which is the closest simulated location to the ORCA site.

Honda tables are calculated for energies up to 10^4 GeV (Fig. 1.4). Figure 1.5 shows an extrapolation of the Honda flux up to 10^8 GeV together with the prompt component after models from Enberg et al.[40]. A newer calculation by Gauld et al.[29] that takes into account in particular different parton distribution functions based on LHCb measurements, is shown as reference. The prompt flux gets dominant over the conventional flux at $\sim 10^6$ GeV in the ν_μ-channel and $\sim 3 \times 10^4$ GeV in the ν_e-channel. Uncertain-

[1] also referred to as Honda flux.

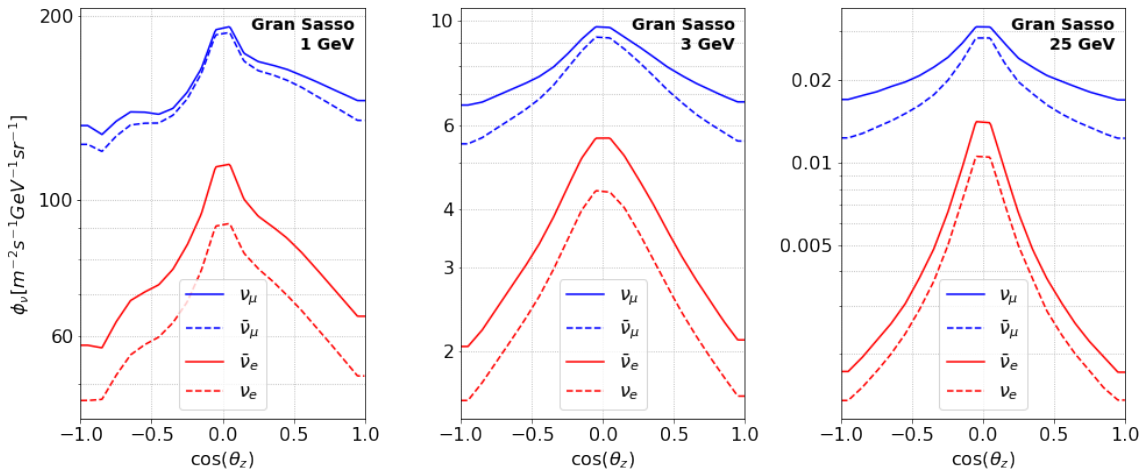

Figure 1.3: Atmospheric neutrino flux vs. $\cos(\theta_z)$ at the Gran Sasso laboratory, calculated by [37] for minimum solar activity, averaged over the azimuth angle. (Data taken from [38].)

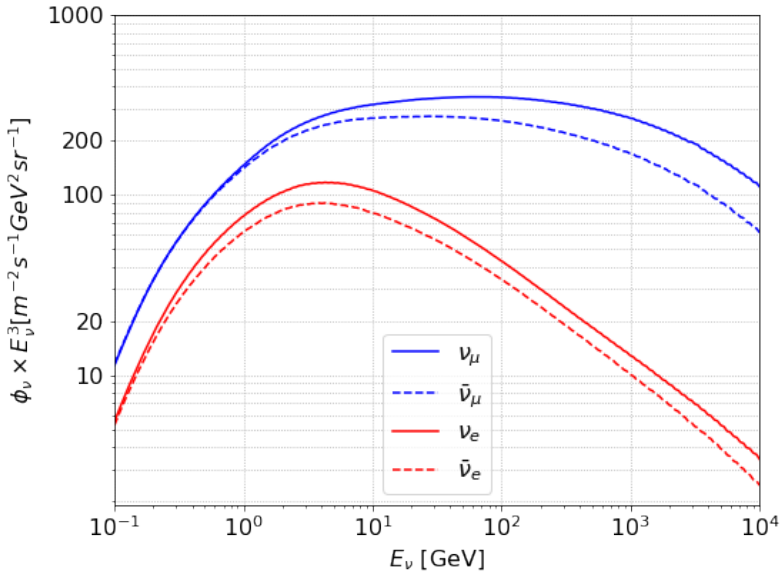

Figure 1.4: Honda flux as a function of energy for upgoing neutrinos predicted for Gran Sasso (Data taken from [38].)

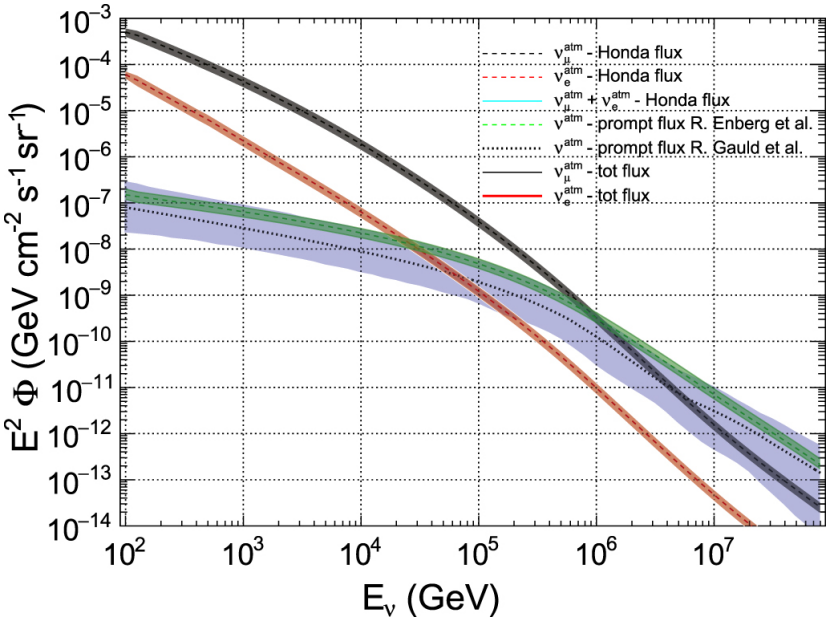

Figure 1.5: Atmospheric neutrino fluxes as a function of energy, for conventional[37] and prompt[42] component. The bands indicate the uncertainties. (Figure taken from [43].)

ties of each model are given in the respective reference and indicated here with error bands. For the conventional Honda flux, an uncertainty of $\pm 25\,\%$ was assumed. All models include a correction for the *knee* of the cosmic ray spectrum according to the prescription in [41].

1.3 Neutrino oscillation

As already mentioned in the introductory section, neutrino flavour oscillations are a phenomenon which is in conflict with the standard model, and is thus aim of many experimental and theoretical research.

The first part of this section gives the theoretical description of neutrino oscillations in vacuum, while the second part is focused on the effects of matter, which introduces a key formalism for studying the Earth with neutrinos.

1.3.1 Vacuum oscillations

From the construction of the SM it is convenient to describe neutrinos in two different bases. The flavour states of the neutrino ν_α, $\alpha \in \{e, \mu, \tau\}$ take part in the weak interaction, while the mass eigenstates ν_i, $i \in \{1, 2, 3\}$ describe the propagation of the neutrino. Each flavour eigenstate is a mixture of the three mass eigentstates (and vice versa)

$$\begin{pmatrix} \nu_e \\ \nu_\mu \\ \nu_\tau \end{pmatrix} = \mathcal{U} \times \begin{pmatrix} \nu_1 \\ \nu_2 \\ \nu_3 \end{pmatrix} = \begin{pmatrix} \mathcal{U}_{e1} & \mathcal{U}_{e2} & \mathcal{U}_{e3} \\ \mathcal{U}_{\mu 1} & \mathcal{U}_{\mu 2} & \mathcal{U}_{\mu 3} \\ \mathcal{U}_{\tau 1} & \mathcal{U}_{\tau 2} & \mathcal{U}_{\tau 3} \end{pmatrix} \times \begin{pmatrix} \nu_1 \\ \nu_2 \\ \nu_3 \end{pmatrix} \tag{1.8}$$

where $\mathcal{U}$ is a unitary mixing matrix ($\mathcal{U}\mathcal{U}^\dagger = \mathbb{1}$), named PMNS-matrix after the initials of its creators[44, 45]. The amplitude of the neutrino mass mixing is given by three mixing angles $\theta_{ij}, i \neq j$, and thus $\mathcal{U}$ can be parameterised by the rotations around the three vectors $|i\rangle$.

$$\mathcal{U} = \begin{pmatrix} 1 & 0 & 0 \\ 0 & c_{23} & s_{23} \\ 0 & -s_{23} & c_{23} \end{pmatrix} \begin{pmatrix} c_{13} & 0 & -s_{13}e^{i\delta} \\ 0 & 1 & 0 \\ -s_{13}e^{i\delta} & 0 & c_{13} \end{pmatrix} \begin{pmatrix} c_{12} & s_{12} & 0 \\ -s_{12} & c_{12} & 0 \\ 0 & 0 & 1 \end{pmatrix} \tag{1.9}$$

with the notation $c_{ij} = \cos(\theta_{ij})$ and $s_{ij} = \sin(\theta_{ij})$. Further, the CP phase δ is added, which for values $\neq 0$ or π would mean that $\mathcal{U}$ is not real, and thus breaks the CP invariance. This could have an impact on the models of leptogenesis during the Big Bang and may be an explanation for the matter-antimatter asymmetry in our observable universe[46]. In case of the neutrino being its own antiparticle, two additional majorana phases would appear. Since they would not affect oscillations, they are not included here.

From the mass mixing of neutrinos (eq. 1.8) one can derive neutrino flavour oscillations as follows. Assume a neutrino of flavour α is produced at time $t = 0$ with an initial state $|\nu_\alpha\rangle$. The evolution of a particle is given by the Schrödinger equation

$$i\frac{\partial|\psi(t)\rangle}{\partial t} = H|\psi(t)\rangle \tag{1.10}$$

with the (diagonal) Hamiltonian H in vacuum

$$H|\nu_i\rangle = E_i|\nu_i\rangle; \quad E_i = \sqrt{p_i^2 - m_i^2} \tag{1.11}$$

p_i being the momentum and m_i the mass of $|\nu_i\rangle$. The general solution of eq. 1.10 is

$$|\nu_\alpha\rangle_t = e^{-iHt}|\nu_\alpha\rangle = \sum_{i=1}^{3} e^{-iE_it}U_{\alpha i}^*|\nu_i\rangle \ . \tag{1.12}$$

The probability of a flavour transition $\alpha \to \beta$ is then given by

$$P(\alpha \to \beta)(t) = |\langle\nu_\beta|\nu_\alpha(t)\rangle|^2 = \sum_{i=1}^{3} U_{\beta i}e^{-i(E_i-E_j)t}U_{\alpha i}^*|\nu_i\rangle. \tag{1.13}$$

Note that eq. 1.13 is valid for all possible dimensions of $\mathcal{U}$, such as *e.g.* a 4-dimensional mixing matrix that would include one sterile neutrino type. Using the assumption of an ultra-relativistic particle with $m_i \ll E_i$, we can use the substitutes

$$E_i \simeq E_\nu + \frac{m_i^2}{2E_\nu}, \text{ and } t \simeq L \tag{1.14}$$

and find

$$(E_i - E_j)t \simeq \frac{\Delta m_{ij}^2}{2E_\nu}L \ . \tag{1.15}$$

Finally, the full equation for the probability of flavour transition writes as

$$\begin{aligned} P(\alpha \to \beta) = \delta_{\alpha\beta} - 4 \sum_{i>k} Re(\mathcal{U}_{\beta i}\mathcal{U}^*_{\beta k}\mathcal{U}^*_{\alpha i}\mathcal{U}_{\alpha k}) \sin^2\left(\frac{\Delta m^2_{ij}}{4E_\nu}L\right) \\ + 2\sum_{i>k} Im(\mathcal{U}_{\beta i}\mathcal{U}^*_{\beta k}\mathcal{U}^*_{\alpha i}\mathcal{U}_{\alpha k}) \sin\left(\frac{\Delta m^2_{ij}}{2E_\nu}L\right) \quad . \end{aligned} \tag{1.16}$$

From this expression we see, that the oscillation probability depends on the 4 parameters of the PMNS matrix, the squared mass differences Δm^2_{ij} and the ratio $\frac{L}{E}$. The latter depends on the type of experiment, *i.e.* the neutrino source, while the other parameters are given by nature.

Let us now discuss the simplified case of two-flavour oscillations, *i.e.* $\mathcal{U}$ being of shape 2×2 with only one mixing angle θ:

$$\begin{pmatrix} |\nu_\alpha\rangle \\ |\nu_\beta\rangle \end{pmatrix} = \begin{pmatrix} \cos\theta & \sin\theta \\ -\sin\theta & \cos\theta \end{pmatrix} \begin{pmatrix} |\nu_1\rangle \\ |\nu_2\rangle \end{pmatrix}. \tag{1.17}$$

Eq. 1.16 reduces then to

$$\begin{aligned} P(\alpha \to \beta) &= \sin^2 2\theta \sin^2\left(\frac{\Delta m^2}{4E}L\right) \\ &= 1 - P(\alpha \to \alpha). \end{aligned} \tag{1.18}$$

The oscillation amplitude is determined by the factor $\sin^2(2\theta)$, *i.e.* the mixing angle, while the oscillation phase in usual units is given by

$$\phi = \frac{\Delta m^2 L}{2E} \approx 1.27 \frac{(\Delta m^2[\mathrm{eV}^2]) \times (L[\mathrm{km}])}{(E[\mathrm{GeV}])}. \tag{1.19}$$

The *oscillation length* L_{osc} for a fixed neutrino energy E is defined as

$$\phi = 2\pi \frac{L}{L_{\mathrm{osc}}}. \tag{1.20}$$

One finds

$$\begin{aligned} L_{\mathrm{osc}} &= \frac{4\pi E[\mathrm{GeV}]}{\Delta m^2[\mathrm{eV}^2]} \\ &\simeq 2.47 \frac{E}{\Delta m^2}[\mathrm{km}] \end{aligned} \tag{1.21}$$

where for the last equation we switch from natural units ($\hbar = c = 1$) to SI units. Because of the tiny neutrino masses, the inverse proportionality to Δm^2 leads to macroscopic oscillation wave-lengths.

It is now obvious that the observation of neutrino oscillation is an evidence for the non-zero mass of neutrinos.

Fig. 1.6 shows the evolution of the survival probability $\alpha \to \alpha$ in vacuum in dependency of L/E. Obviously, at very small propagation lengths $L \ll L_{\mathrm{osc}}$ no oscillations occur. In the regime $L \gg L_{\mathrm{osc}}$ the oscillations average out in an experiment with limited resolution and the phase information is lost.

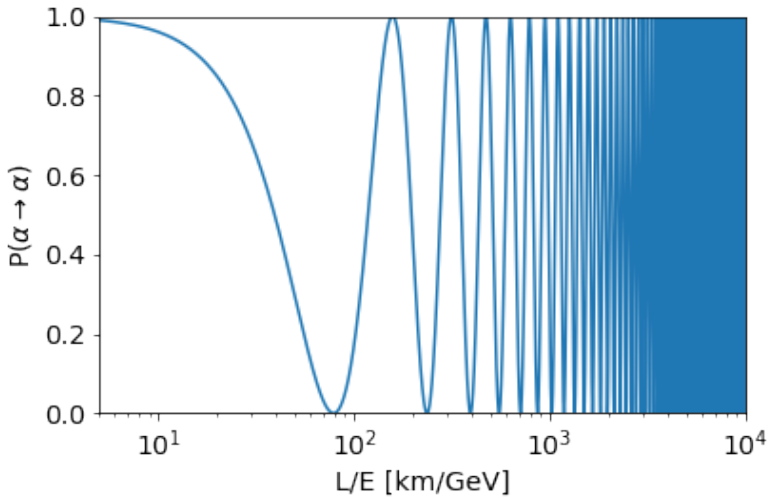

Figure 1.6: Survival probability $P(\alpha \to \alpha)$ in the 2-flavour case vs. L/E in vacuum.

Measurement of oscillation parameters In order to probe the oscillation parameters θ and Δm^2 one has to choose the observed energy range and the distance to the neutrino source accordingly. Thus, different experiments (solar, reactor, atmospheric) are able to test different regions of the $(\Delta m^2, \theta)$ parameter space.

The first evidence for neutrino oscillations was found by SuperKamiokande for atmospheric neutrinos in 1998[47] and SNO for solar neutrinos in 2002[48]. This groundbreaking result was awarded with the Nobel Prize in physics in the year 2015 "for the discovery of neutrino oscillations, which shows that neutrinos have mass".

In first approximation, the SuperKamiokande data can be suitably well described by a two-flavour mixing, as the dominant oscillation was $\nu_\mu \to \nu_\tau$. The estimated mixing parameters for the atmospheric oscillations were

$$|\Delta m^2|_{\text{atm}} \simeq 2.3 \times 10^{-3}\,\text{eV}^2, \quad \sin(2\theta_{\text{atm}})^2 \simeq 1.0 \tag{1.22}$$

which results in an oscillation length of the order of magnitude of the Earth's diameter

$$\left(\frac{L}{E}\right)_{\text{atm}} \sim 10^3\,\text{km}\,\text{GeV}^{-1}. \tag{1.23}$$

In order to precisely describe the oscillation of solar neutrinos - the answer to the solar neutrino problem mentioned earlier - matter effects have to be taken into account, that will be discussed in sec. 1.3.2. As these are strongly related to the mixing of flavour- and mass-eigenstates, again the two-flavour oscillation paradigm delivers a sufficient approximation of the observed disappearance of ν_e, *i.e.* $P(\nu_e \to \nu_e) < 1$, as was confirmed by SNO.
In addition, an independent measurement of reactor antineutrinos was run with the KamLAND detector in Japan, that also observed the $\bar{\nu}_e$ disappearance over the $\mathcal{O}(100\,\text{km})$ propagation from surrounding nuclear reactors[49] . The combination of solar and reactor data[50] yielded

$$\Delta m^2_{\text{sol}} \simeq 7.92 \times 10^{-5}\,\text{eV}^2, \quad \sin(2\theta_{\text{sol}})^2 \simeq 0.314\,. \tag{1.24}$$

Parameter	Normal Ordering	Inverted Ordering
$\sin^2\theta_{23}$	$0.573^{+0.016}_{-0.020}$	$0.553^{+0.016}_{-0.019}$
$\sin^2\theta_{13}$	$0.02219^{+0.00062}_{-0.00063}$	$0.02238^{+0.00063}_{-0.00062}$
$\frac{\Delta m^2_{31}}{10^{-3}\,\mathrm{eV}^2}$	$+2.517^{+0.026}_{-0.028}$	$+2.498^{+0.028}_{-0.028}$
$\delta_{CP}/^\circ$	97^{+27}_{-24}	282^{+26}_{-30}
$\sin^2\theta_{12}$	$0.304^{+0.012}_{-0.012}$	$0.304^{+0.013}_{-0.012}$
$\frac{\Delta m^2_{21}}{10^{-5}\,\mathrm{eV}^2}$	$7.42^{+0.021}_{-0.020}$	

Table 1.1: Best global fit of oscillation parameters from NuFit5.0[55], that are used as 'true' values during the analysis.

The resulting oscillation length

$$\left(\frac{L}{E}\right)_{\mathrm{atm}} \sim 10^4\,\mathrm{km\,GeV}^{-1} \tag{1.25}$$

is indeed of $\mathcal{O}(10\,\mathrm{km})$ for MeV reactor antineutrinos.

With two mixing angles and two independent squared mass differences found, one more mixing angle is needed to describe the flavour mixing in the 3D paradigm. The solar oscillation sector is associated with the 1-2 mixing and the atmospheric sector with the 2-3 mixing. Hints on the last missing mixing angle θ_{13} to be slightly greater than zero came from measurement of the ν_e-appearance channel $\nu_\mu \to \nu_e$ in accelerator experiments T2K[51] and MINOS[52]. Finally in 2012 the reactor experiments Double Chooz, Daya Bay and RENO found evidence for $\theta_{13} > 0$ in the $\bar{\nu}_e$-disappearance channel. The combined analysis of their data in[53] yields

$$\sin^2(2\theta_{13}) \simeq 0.1\ . \tag{1.26}$$

Combining available data of reactor, solar, accelerator and atmospheric neutrino experiments allows to generate a global best-fit value to all oscillations parameters[54]. Throughout this thesis they are taken from NuFit5.0[55] and are listed in Tab. 1.1.

One remaining questions is the ordering of the neutrino masses. The neutrino oscillation described by eq. 1.16 depends only on the squared difference between two mass eigenstates, but because $\sin^2(x) = \sin^2(-x)$ the sign of Δm^2 can not be resolved by measuring neutrino oscillations in vacuum. As we will see in the next section, this problem can be solved by studying neutrino oscillations in matter. While solar and reactor experiments revealed that $\Delta m_{\mathrm{sol}} = \Delta m^2_{12} > 0$, the sign of $\Delta m_{\mathrm{atm}} = \Delta m^2_{23}$ is still unknown and leads to the question of the neutrino mass ordering (NMO) (Fig. 1.7). The current global data favours the NO with $1.6(2.7)\sigma$ without(with) including data from SuperKamiokande. Throughout this thesis the normal mass ordering is assumed to be true. The analytical methods are not affected by that choice.

Finally, the value of δ_{CP} is yet to be determined. As the expected signal from a CP violating phase is small, large statistics are necessary to reach reasonable precision towards δ_{CP}. Combined data from long-baseline and reactor oscillation experiments hint towards a leptonic CP phase between π and 2π[56]. The latest results published by T2K[57] and NOνA[58] show a tension in the observed δ_{CP} for NO, which slightly releases for IO, thus hint to the latter case[55].

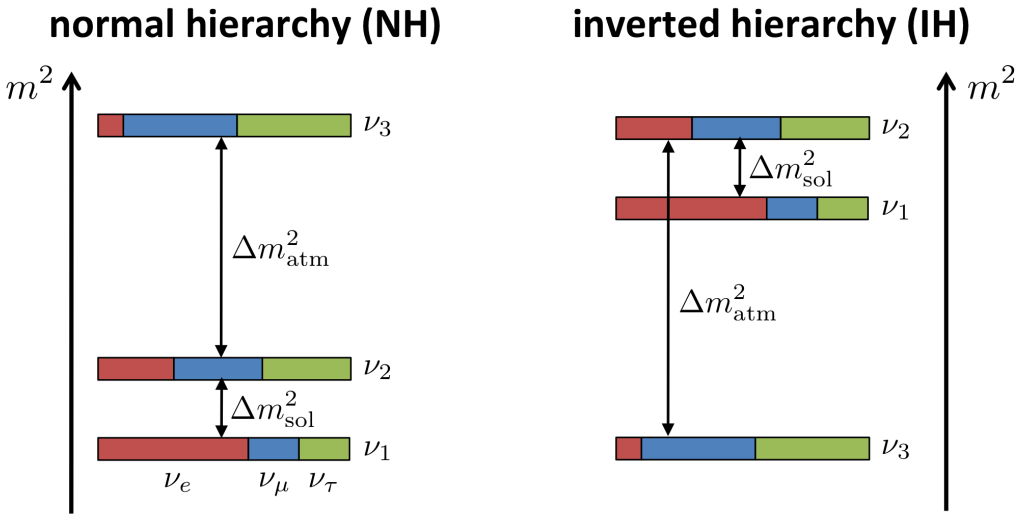

Figure 1.7: Sketch of the two possible neutrino mass orderings. Normal hierarchy: $m_1 < m_2 < m_3$; Inverted hierarchy: $m_3 < m_1 < m_2$. The colors illustrate the composition of the mass eigenstates by the flavour eigenstates. (Figure taken from [24].)

The latest update of the global best fit NuFit5.1[59] finds mainly a different octant for $\theta_{23} = 49.2° \rightarrow 42.1°$, which would in fact have a non-negligible impact on the oscillations of atmospheric neutrinos as measured with ORCA. This is mentioned to illustrate that the study of neutrino oscillation is ongoing and quantitative statements can change in the light of new findings.

1.3.2 Matter oscillations

In the previous section the neutrinos were assumed to propagate in vacuum. In the presence of ordinary matter, $\overset{(-)}{\nu}_e$ can undergo coherent elastic scattering via CC interaction with electrons, which leads to an effective phase shift of the mass eigenstates. Mathematically this extra potential is given by

$$V_{CC} = \pm\sqrt{2} G_F n_e \tag{1.27}$$

with the Fermi coupling constant G_F and the electron density n_e of the traversed medium. The extra potential due to NC interactions is identical for all neutrino flavours and does not affect the relative phases and oscillation probabilities. The sign of V_{CC} is positive for neutrinos and negative for anti-neutrinos. Wolfenstein predicted in 1978[60] that the extra potential will modify the flavour mixing of neutrinos, as the the Hamiltonian is no longer diagonal in the mass basis:

$$H_{\text{M, mass}} = H_{\text{Vac}} + \mathcal{U}^\dagger \begin{pmatrix} V_{CC} & 0 & 0 \\ 0 & 0 & 0 \\ 0 & 0 & 0 \end{pmatrix} \mathcal{U} \tag{1.28}$$

with H_{Vac} as defined in eq. 1.11. The predicted matter effect can be well understood in the 2-flavour case (eq. 1.17), where the Hamiltonian in the flavor eigenbase becomes

$$H_{\text{M,flv}} = \frac{1}{4E}\begin{pmatrix} \Delta m^2 \cos^2\theta + A_{CC} & \Delta m^2 \sin^2\theta \\ \Delta m^2 \sin^2\theta & \Delta m^2 \cos^2\theta - A_{CC} \end{pmatrix} \tag{1.29}$$

with

$$A_{CC} \equiv 2EV_{CC} = \pm 2\sqrt{2} G_F E n_e. \tag{1.30}$$

Diagonalizing $H_{\text{M, flv}}$ gives

$$U_M^\dagger H_{\text{M,flv}} U_M = \begin{pmatrix} \Delta^M m^2 & 0 \\ 0 & \Delta^M m^2 \end{pmatrix} \tag{1.31}$$

using the mixing matrix in matter

$$U_M = \begin{pmatrix} \cos\theta^M & \sin\theta^M \\ -\sin\theta^M & \cos\theta^M \end{pmatrix}. \tag{1.32}$$

The matter parameters θ^M and $\Delta^M m^2$ are linked with the vacuum parameters

$$\Delta^M m^2 = \xi \cdot \Delta m^2 \; ; \;\; \sin^2 2\theta^M = \frac{\sin^2 2\theta}{\xi^2} \tag{1.33}$$

through the mapping parameter

$$\xi = \sqrt{\sin^2 2\theta + \left(\cos 2\theta \mp \frac{2\sqrt{2} E G_F n_e}{\Delta m^2}\right)^2}. \tag{1.34}$$

We see that $\sin^2 2\theta^M$ gets maximal when the resonance condition

$$\mp \frac{2\sqrt{2} E G_F n_e}{\Delta m^2} = \cos 2\theta \tag{1.35}$$

is fulfilled, even for small vacuum mixing angles θ. The resonant enhancement of the oscillation probability (MSW-resonance [60, 61]) can only happen for neutrinos if $\Delta m^2 > 0$ or for anti-neutrinos if $\Delta m^2 < 0$, which is the key to determine the NMO. The neutrino energy range where the resonance appears depends on the the average electron density n_e of the traversed media:

$$E_{\text{res}} = \frac{\Delta m^2 \cos 2\theta}{2\sqrt{2} G_F n_e}. \tag{1.36}$$

The resonance enhancement of the mixing angle in matter delivers also the solution to the solar neutrino problem. At the core of the sun, where $V_{CC} \gg \frac{\Delta m^2}{2E} \rightarrow \theta_m \approx \frac{\pi}{2}$, a ν_e corresponds to a pure ν_2 eigenstate, according to the two flavour mixing of eq. 1.17 in matter using U_M. For an adiabatic evolution of the neutrino, *i.e.* density variations on larger scales than the oscillation length, the mass eigenstate of the neutrino does not change during the propagation. After leaving the sun no more electrons are present and consequently $V_{CC} \approx 0 \rightarrow \theta_m \approx \theta$. As sketched in Fig. 1.7, ν_2 is composed of approximately equal parts of each flavour eigenstate, which explains why the measured solar electron neutrino flux by the Homestake experiment was only about one-third of its expectation. This resonant flavour conversion is referred to as MSW-effect and occurs either for neutrinos or anti-neutrinos. Consequently, detecting this effect for solar ν_e revealed the sign of Δm^2_{sol}.

1.3.3 Oscillations of atmospheric neutrinos in the Earth

We now focus on the oscillations of atmospheric neutrinos during their passage through the Earth. The 3-flavour matter oscillation can be derived as shown in the previous section, like done in *e.g.* [62], assuming $\frac{\Delta m^2_{21}}{\Delta m^2_{31}} \ll 1$ and $\sin^2\theta_{13} \ll 1$:

$$P(\nu_\mu \to \nu_e) \simeq \sin^2\theta_{23}\sin^2 2\theta^M_{13}\sin^2\left(\frac{\Delta^M m^2_{31} L}{4E_\nu}\right) \tag{1.37}$$

$$\begin{aligned} P(\nu_\mu \to \nu_\mu) \simeq 1 &- \sin^2 2\theta_{23}\cos^2\theta^M_{13}\sin^2\left(\frac{(\Delta m^2_{31} + \Delta^M m^2_{31})L}{8E_\nu} + \frac{V_{CC}L}{4}\right) \\ &- \sin^2 2\theta_{23}\sin^2\theta^M_{13}\sin^2\left(\frac{(\Delta m^2_{31} - \Delta^M m^2_{31})L}{8E_\nu} + \frac{V_{CC}L}{4}\right) \\ &- \sin^4\theta_{23}\sin^2 2\theta^M_{13}\sin^2\left(\frac{\Delta^M m^2_{31} L}{4E_\nu}\right). \end{aligned} \tag{1.38}$$

The oscillation amplitudes are determined by the value of θ_{23}, which is close to the maximum of $\frac{\pi}{4}$. While factors of $\sin^2 2\theta_{23}$ are not sensitive to the octant of θ_{23}, *i.e.* $> \frac{\pi}{4}$ or $< \frac{\pi}{4}$ (octant degeneracy), terms of $\sin^2\theta_{23}$ lead to stronger amplitudes for values in the second octant.

The resonance energies can be computed for a default model of the Earth's core and mantle (see sec. 3.2) according to eq. 1.36:

$$E_{\text{res}} = \begin{cases} \sim 3\,\text{GeV} & \text{core} \\ \sim 7\,\text{GeV} & \text{mantle} \end{cases} \tag{1.39}$$

They are close to the peak region of the atmospheric neutrino flux. The effect of the MSW-resonance is well visible in the $P(\nu_\mu \to \nu_x)$ channel (Fig. 1.8) for neutrinos traversing the core.

The most important factor of eq. 1.36 is for us the electron density n_e, which is the basis for oscillation tomography, which theory will be further discussed in sec. 3.2.2.

Yet a different effect that affects Earth traversing neutrinos is called *parametric resonance*, that occurs for steps in the traversed density profile ('castle-wall' profile) with a periodicity that is synchronized with the change of oscillation phase[63, 64]. For multiple density modulations the oscillation probability builds up and can get large even for small mixing angles in vacuum and in matter. Neutrinos that cross the Earth core undergo such density modulations twice, which has in fact a strong effect on the oscillations.

1.4 Neutrino interaction with matter

Neutrinos can only interact with matter via the weak force[2] by the exchange of either a $W^\pm$ boson (CC) or a neutral Z boson (NC). The formalism is here introduced using the simplest case of a neutrino-fermion interaction, *i.e.* the scattering off an electron. The according Feynam diagrams are shown in Fig. 1.9. In a CC-interaction, the neutrino

[2] Gravity can be safely ignored.

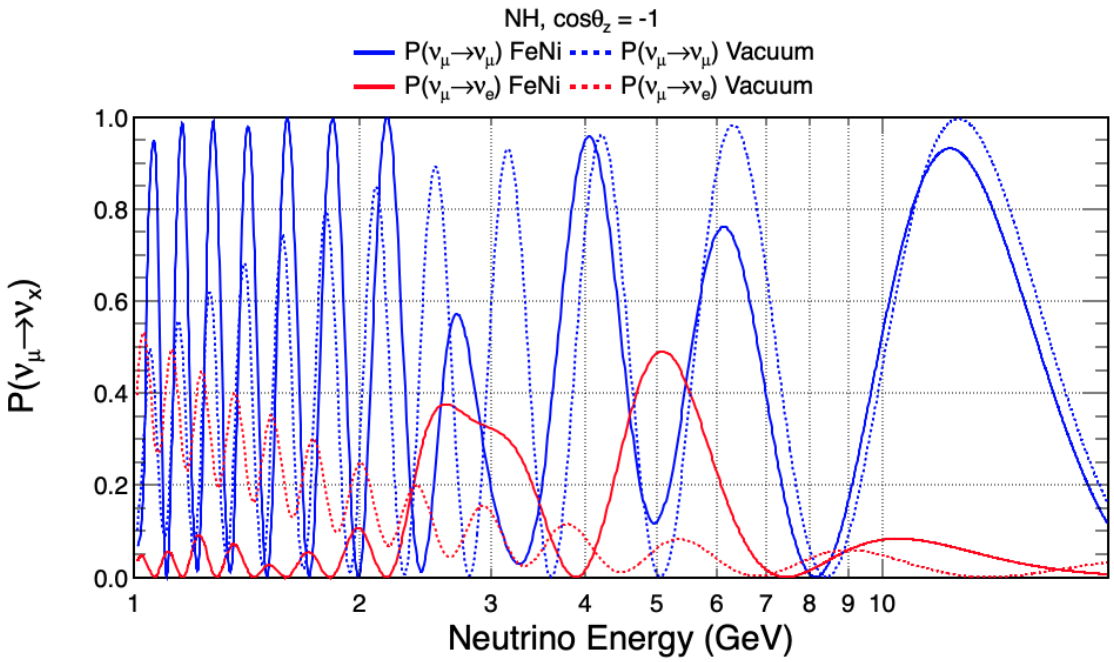

Figure 1.8: Vacuum vs. matter oscillations in the $\nu_\mu \to \nu_\mu/\nu_e$ channel for straight-upgoing neutrinos traversing the Earth's core. The MSW-resonance is best visible as two peaks in $P(\nu_\mu \to \nu_e)$, corresponding to the resonance energies expected for the electron densities in the core and the mantle.

turns into its charged leptonic counterpart. In the case of NC-interaction, the neutrino survives but loses some energy and is scattered.

In the standard model formalism of the electroweak force, the interaction amplitude is linked to the Fermi constant G_F. If the four-momentum transfer q is much smaller than the mass of the exchange boson (*i.e.* $|q^2| \ll m^2_{W,Z}$) it applies

$$G_F = \frac{g^2}{4\sqrt{2}m_W^2} = 1.1663788(7) \times 10^{-5}\text{GeV}^{-2} \tag{1.40}$$

with g being the fermion coupling.

A key parameter which is commonly used when speaking about neutrino interactions is the cross section σ, which can be thought of as the effective area of interaction of a particle. For a pure CC interaction where a neutrino scatters off a fermion (similar for antineutrino scattering off antifermion)

$$\nu_l + f \to l + f' \quad (l \neq f) \tag{1.41}$$

the total cross section is given by the expression

$$\sigma^{\text{CC}}(\nu f) \simeq \frac{G_F^2 s}{\pi} \tag{1.42}$$

From that, one can make two observations: first, the heavy W-boson ($m_W \approx 80.4\,\text{GeV}$) leads to a generally small coupling and thus small interaction cross sections. Second, as the center-of-mass energy s for the fermion in rest is $s = 2m_f(m_f + E_\nu)$, the cross

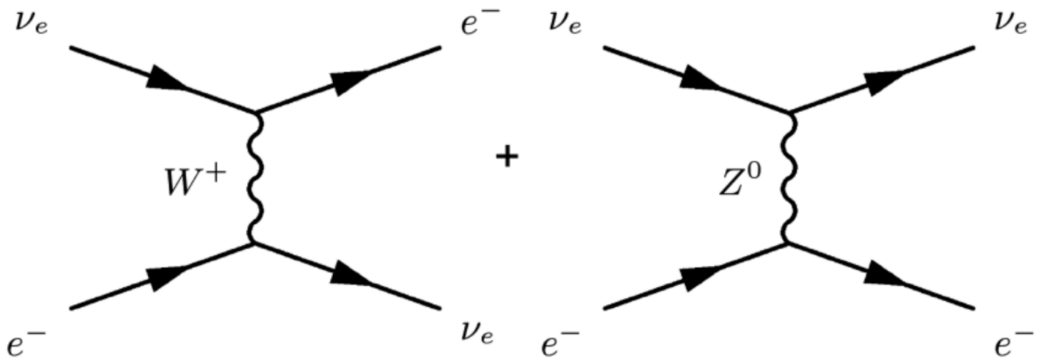

Figure 1.9: Feynman diagram of charged- and neutral current component of ν_e-e scattering. Figure taken from [65].

section consequently increases linearly with neutrino energy (since $E_\nu \gg m_f$), as well as with the mass of the target particle.

For antineutrino-fermion (or similar neutrino-antifermion) scattering, the conservation of angular momentum restrains the amount of possible final states, leading to a dependence on the scattering angle $\theta_{\nu l}$, that again is linked to the inelasticity y (Bjorken-y):

$$\begin{aligned} y &= 1 - \frac{E_f}{E_\nu} \\ &\equiv (1 - \cos(\theta_{\nu f}))/2 \end{aligned} \tag{1.43}$$

in the rest frame of the target fermion. We write then the differential cross section

$$\frac{d\sigma^{\mathrm{CC}}(\bar{\nu} f)}{dy} \simeq \frac{G_F^2 s}{\pi} \times (1-y)^2 \, . \tag{1.44}$$

A measurement of the differential (anti-)neutrino cross section at the CDHS experiment[66] is shown in Fig. 1.10. Integrating over y gives the ratio of $\sigma^{\mathrm{CC}}(\nu f)/\sigma^{\mathrm{CC}}(\bar{\nu} f) \simeq 3$[65].

In CC interactions, left-handed neutrinos couple only with left-handed fermions and right-handed antifermions, meaning they are maximally parity-violating. This is not the case for NC interactions, where a neutrino can couple to both the left- and the right-handed component of the fermion that the neutrino is interacting with. The differential cross section scales then with the right- and left-handed coupling constants (g_R, g_L) of the fermion, that are given by the weak mixing angle θ_W[68]:

$$\frac{d\sigma^{\mathrm{NC}}(\nu f)}{dy} \simeq \frac{G_F^2 s}{\pi}[g_L^2 + (1-y)^2 g_R^2], \quad \frac{d\sigma^{\mathrm{NC}}(\bar{\nu} f)}{dy} \simeq \frac{G_F^2 s}{\pi}[g_L^2 (1-y)^2 + g_R^2] \, . \tag{1.45}$$

At energies $E_\nu \gtrsim 1\,\mathrm{GeV}$, neutrinos are more likely to penetrate the atomic nuclei. The main scattering mechanisms (ordered by increasing energy range) are:

Elastic and quasielastic scattering The neutrino scatters off the entire nucleon, liberating it from the target. In case of a CC interaction, this process is referred to as *quasielastic scattering*, while for NC scattering it is called *elastic scattering*.

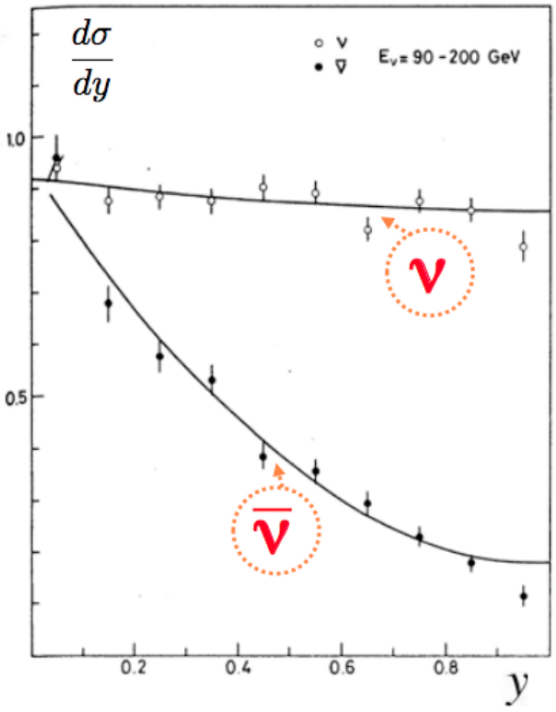

Figure 1.10: Differential cross section measurement in ν_μ-iron DIS at the CDHS experiment from 90 GeV to 200 GeV. Figure taken from [67].

Resonance production The target nucleon is excited to a resonant state. The resonance baryon decays to a variety of possible mesonic final states.

Deep inelastic scattering At high enough energies, neutrinos can directly resolve the quark constituents of the nucleon, breaking the nucleon apart. This interaction mode is discussed in more detail below.

Fig. 1.11 shows the contribution of each mechanism to the total $\nu_\mu/\bar{\nu}_\mu$ cross section with an isoscalar target (equal number of protons and neutrons in the nucleus), as measured in several experiments[69, 70, 71, 72]. The order of magnitude of σ at 1 GeV is about $10^{-38}\,\mathrm{cm}^2$. The total CC anti-neutrino cross section is approximately half of the neutrino cross section[73]. Artificial neutrino sources on Earth reach energies up to ~300 GeV - many orders of magnitude below the observed energies in the atmospheric and cosmic neutrino flux. Here, estimations of neutrino cross sections come from theoretical descriptions of scattering processes that are simulated in frameworks like `GENIE`[74].

Above ~10 GeV deep inelastic scattering (DIS) is the dominant interaction mechanism:

$$\nu_l N \to \nu_l X \text{ (NC)}; \quad \nu_l N \to l X \text{ (CC)} \tag{1.46}$$

with N the target nucleon and X an unspecified set of outgoing hadrons. The Feynman diagram is shown in Fig. 1.12. While the scattering off a single quark can be described as shown above, for DIS one has to take into account the parton distribution function of all constituent (anti)quarks[3]. Further, the $q\bar{q}$ sea quark content attenuates the strict

[3]For further details, see *e.g.* [65, 75].

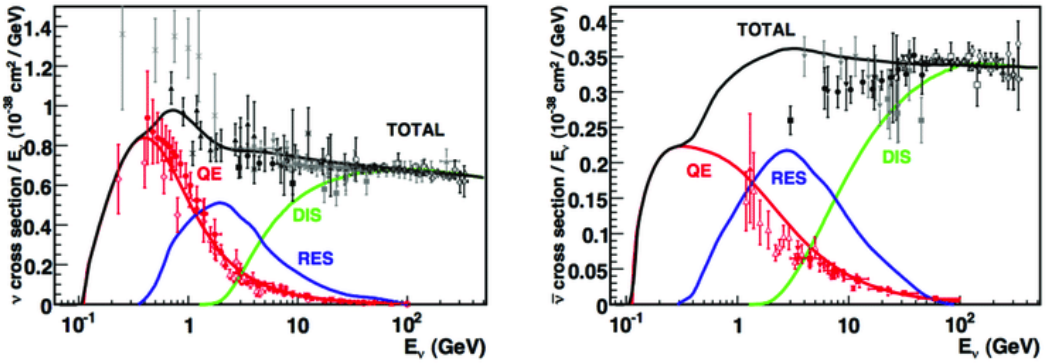

Figure 1.11: Total ν_μ and $\bar{\nu}_\mu$ per nucleon CC cross sections for an isoscalar target, divided by neutrino energy. (Figure taken from [65].)

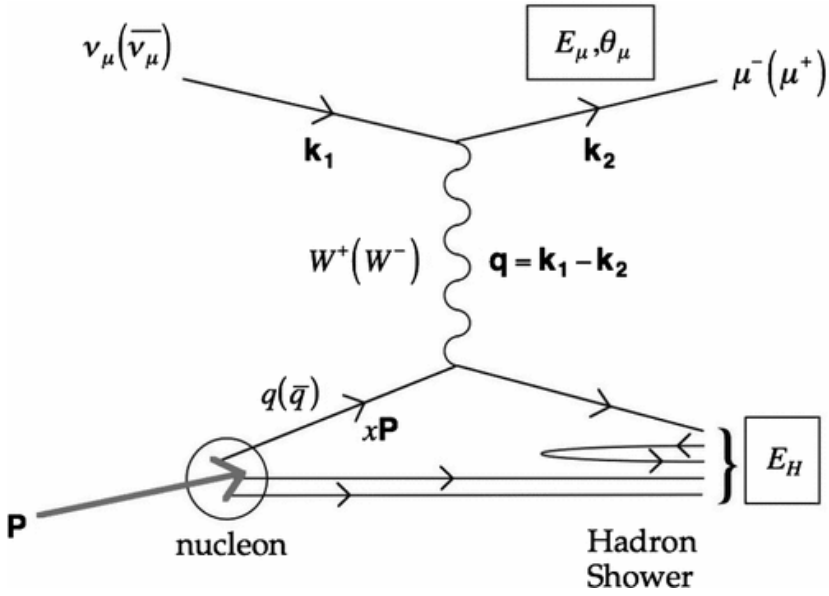

Figure 1.12: Feynman diagram of a DIS (anti)neutrino interaction with a nucleon (Figure taken from [65]). The four-momenta is denoted as k.

dependence on $(1-y)^2$ of the antineutrino CC cross sections, leading to roughly

$$\frac{\sigma_{CC}(\nu N)}{\sigma_{CC}(\bar{\nu} N)} \simeq 2; \quad \frac{\sigma_{NC}(\nu N)}{\sigma_{NC}(\bar{\nu} N)} \simeq 3 \tag{1.47}$$

for isoscalar targets. The DIS cross section increases linear with its energy, up to energies of about 1 PeV. In the high-energy regime, the contribution of q is not longer negligible and the cross section is suppressed by the propagator term $(m_W^2/(q^2+m_W^2))^2$, leading to an evolution $\sigma \sim E^{0.4}$[76]. The ultrarelativistic neutrino deposits a fraction y of its energy to the nucleon, ripping it apart and triggering chain processes of creation and decaying of short-lived hadrons (*hadronisation*).

One special effect of neutrino-matter interactions is the scattering of neutrinos with shell electrons of an atom. This resonant effect known as *Glashow resonance*[77] appears only for $\bar{\nu}_e$ at $E_\nu \simeq 6.3\,\text{PeV}$ and leads to an amplification of the cross section.

Chapter 2

Atmospheric neutrino detectors

Contents

Neutrinos can only be detected indirectly, *e.g.* by observing secondary particles of neutrino interactions with matter. Huge efforts are made to collect more atmospheric neutrino data, with detectors growing in size, costs and complexity. Some examples of prominent atmospheric neutrino detectors are: IceCube in the Antarctic ice, ANTARES in the Mediterranean Sea, Baikal-GDV in the eponymous lake in Russia and finally SuperKamiokande, a manmade watertank in Japan. All are taking data for many years now and were able to deliver groundbreaking insights into the world of neutrino-, astro- and particle-physics. It is thus no wonder, that each of these experiments have follow-up projects in planning: PINGU, KM3NeT/ORCA and ARCA and HyperKamiokande. In this chapter, the general detection principle of all the mentioned so called water-Cherenkov detectors is explained, with follow-up summary of the specific detector layouts. Thereafter we will learn about a different approach of neutrino detection with the liquid Argon detector DUNE, which aims for unprecedented reconstruction capabilities - at the cost of detector size.

2.1 Cherenkov detectors

Cherenkov detectors aim to detect the so called Cherenkov light which is produced when charged particles - in this case secondary particles produced by neutrino interactions - propagate faster than the light in this medium[78]. By reconstructing these secondary particles from the distribution of the Cherenkov radiation in the detector, one can infer the properties of the interacting neutrinos, namely its energy, direction and flavour.

2.1.1 Cherenkov radiation

A charged particle that propagates through a dielectric medium will polarize the atoms in its vicinity. If the velocity v of the charged particle exceeds that of the speed of light in the medium c_m, the polarization field along its trajectory is asymmetric. The following relaxation of the induced dipoles back to their ground state emits then a coherent wavefront, according to Huygens principle. The polarization of a medium (refraction index n) by a charged particle propagating at a velocity above the Cherenkov threshold

$$\beta = \frac{v}{c_m} \geq \frac{1}{n} \tag{2.1}$$

and the subsequent emission of photons is shown in Fig. 2.1a. The emitted photons create a forward propagating wavefront at the Cherenkov angle θ_C, given by [79][1]

$$\cos\theta_C = \frac{1}{\beta n}. \tag{2.2}$$

Figure 2.1b shows the origin of the characteristic Cherenkov cone, created by interference of the overlapping wavefronts.

The number of photons produced by the Cherenkov effect along the charged particle track per unit length is given by the Frank-Tamm equation [81]

$$\frac{\mathrm{d}N}{\mathrm{d}x} = 2\pi\alpha\left(1 - \frac{1}{\beta^2 n^2}\right)\int_{\lambda_1}^{\lambda^2} \frac{1}{\lambda^2}\mathrm{d}\lambda \tag{2.3}$$

for a range of wavelengths $[\lambda_1, \lambda_2]$, with the fine structure constant $\alpha = \frac{1}{137}$. For ultra-relativistic particles ($\beta = 1$) propagating in sea water ($n \approx 1.35$, transparent for $\lambda \in [300\,\mathrm{nm}, 600\,\mathrm{nm}]$), eq. 2.3 predicts $\approx 340\,\mathrm{cm}^{-1}$ photons. The number of total Cherenkov photons produced increases consequently (i) with the number of secondary particles produced in the neutrino interaction and (ii) with the propagation length of these particles. Both increase with the energy of the incident neutrino, meaning that high-energy neutrino events produce more light than low-energy events.

2.1.2 Event signature

In sec. 1.4 and in particular Fig. 1.12 we discussed the interaction of neutrinos with matter. Depending on the lepton flavour and the exchange boson, different particles are created in the interaction, and consequently different event signatures (or topologies) emerge.

[1] Original paper [78].

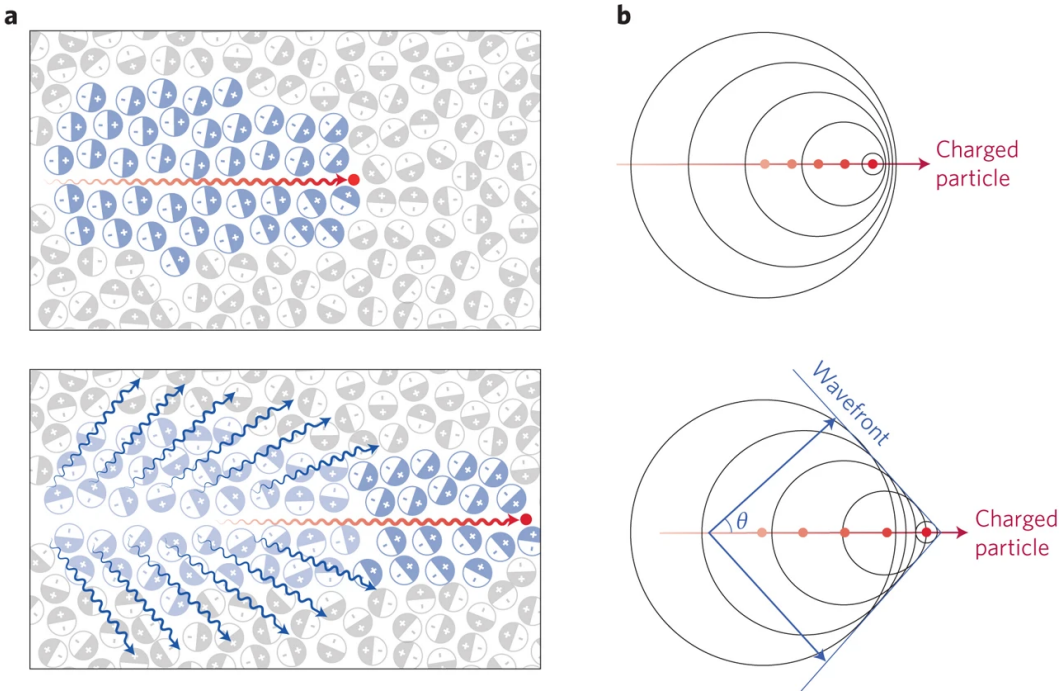

Figure 2.1: **a** Top: A charged particle (red dot) polarizes the atoms in the medium. Bottom: The relaxation of the dipole state results in emission of photons in the Cherenkov angle θ_C. **b** For particles with velocities $v > c_m$ the coherent wavefronts form the characteristic Cherenkov cone. (Figure taken from [80].)

- In every neutrino interaction, a hadron shower is produced when the target nucleus is ripped apart. All the hadrons have very short lifetimes and decay or interact almost instantly, *i.e.* close to the neutrino-nucleon interaction (*interaction vertex*), eventually reaching a low energetic state below the Cherenkov threshold. The term *shower-like* is used in this context as a centralized source of light within a short distance close to the neutrino interaction point.

- $\overset{(-)}{\nu}{}^{\mathrm{NC}}$: After a NC interaction, the neutrino leaves the detector with reduced energy at a (typically small) scattering angle. Only a hadronic shower is triggered, the neutrino does not leave any other trace.

- $\overset{(-)}{\nu}{}_{e}^{\mathrm{CC}}$: The produced $e^{\pm}$ initiates an electromagnetic shower of $e^{\pm}$ and γ with a similar extension as the hadronic shower. Due to the small radiation length of the initial $e^{\pm}$ (36 cm in water[68]), both the electromagnetic and hadronic showers are located close to the interaction vertex and are usually indistinguishable in large volume neutrino detectors.

- $\overset{(-)}{\nu}{}_{\mu}^{\mathrm{CC}}$: Muons can travel long distances in water before losing all their energy, approximately $4\,\mathrm{m\,GeV}^{-1}$[68]. Cherenkov light is emitted along the whole muon trajectory, leaving a *track-like* event signature. Note that aside from the hadronic shower, the exact same topology is produced by atmospheric muons that reach the detector (discussed also in sec. 4.2).

- $\overset{(-)}{\nu}{}_{\tau}^{\mathrm{CC}}$: Tau leptons produced in $\overset{(-)}{\nu}{}_{\tau}^{\mathrm{CC}}$-events poses a special case. The τ will not interact itself with matter, but it will decay almost instantaneous due to its short lifetime of $\sim 2.9 \times 10^{-13}$ s. Depending on its decay branch, it will produce an hadronic (branching ratio of 65 %) or electromagnetic (17 %) shower. A track-like event signature is only obtained from a decay into a muon(17 %)[68]. $\overset{(-)}{\nu}{}_{\tau}^{\mathrm{CC}}$-events can thus not be generally classified as track- or shower-like event. At very high energies (∼PeV) the τ can travel several meters due to the relativistic prolongation of its lifetime and thus producing a second particle shower spatially different from the hadronic shower, a so called double-bang event[82].

Figure 2.2 shows a schematic illustration of all the cases discussed above, including different scenarios of the tau-decay in $\overset{(-)}{\nu}{}_{\tau}^{\mathrm{CC}}$-events, labeled respectively as shower- and track-like. The common ground of the water-Cherenkov detectors introduced hereafter is thus the detection of Cherenkov photons induced by secondary particles from neutrino interactions. Because of its transparency and availability, the obvious choice of detector medium is water - either in fluid or solid form.

2.2 IceCube

The IceCube Neutrino Observatory is a high-energy neutrino detector deployed at the South Pole. It consists of 86 strings that are embedded between 1450 m and 2450 m below the surface of the ice with a horizontal spacing of 125 m and a vertical spacing between digital optical modules (DOMs) for the photon detection of 17 m, forming a 3D-array with a cubic-kilometre volume[84]. One advantage of building the detector

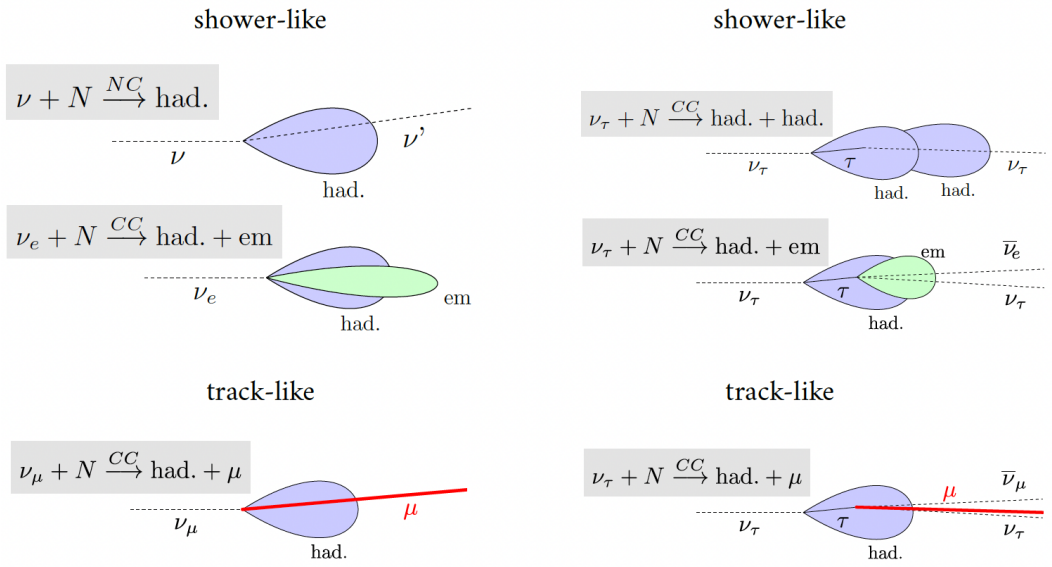

Figure 2.2: Schematic illustration of the possible event topologies, seperated to track- and shower-like. Left: ν_e and ν_μ CC+NC. Right: ν_τ CC for different decay channels, NC.(Figure taken from [83]).

in ice is that after the deployment of the strings the drill holes froze again, fixing the position of the DOMs. A downsize of the ice is that air pockets and dust lead to rather short scattering lengths of the Cherenkov light to be observed (see Tab. 2.1), which in particular complicates the reconstruction of the neutrino direction. A subset of 8 strings, called DeepCore[85], is deployed in its center below 1750 m, with a smaller horizontal (avg. 72 m) and vertical spacing (7 & 10 m). The higher density of the DeepCore DOMs compared to the rest of IceCube lowers the energy detection threshold to $\gtrsim$10 GeV, because even light from less luminous events can be collected, which allows for the observation of neutrino oscillations in that energy range. Another advantage of the self-contained sub-detector is, that the surrounding strings can be used as an efficient veto for atmospheric muons. The detector construction was completed in 2011 and data-taking is going on ever since. The official detector layout is shown in Fig. 2.3.

IceCube has made many important contributions to several fields of physics, from which two are especially relevant for this thesis.

One is the first observation of a high-energy cosmic neutrino flux extending up to the PeV range, opening a new window to multi-messenger astronomy[86]. Figure 2.4 shows their most resent flux measurement, as well as a review on analyses of the flux spectra in 10 yr of IceCube data[87]. Further, DeepCore was able to detect neutrino oscillations of GeV atmospheric neutrinos and added new constraints to the global picture of the atmospheric oscillation parameters (Fig. 2.5).

Two major upgrades are already planned for IceCube: First, IceCube Gen2 will extend its target volume by a factor of 10, by deploying additional strings with large spacing around the existing detector. Second, the PINGU[90] sub-array will be an even denser version of DeepCore, placed at its center with an instrumented volume of 6 Mt for precise measurements of neutrino oscillations in the GeV range.

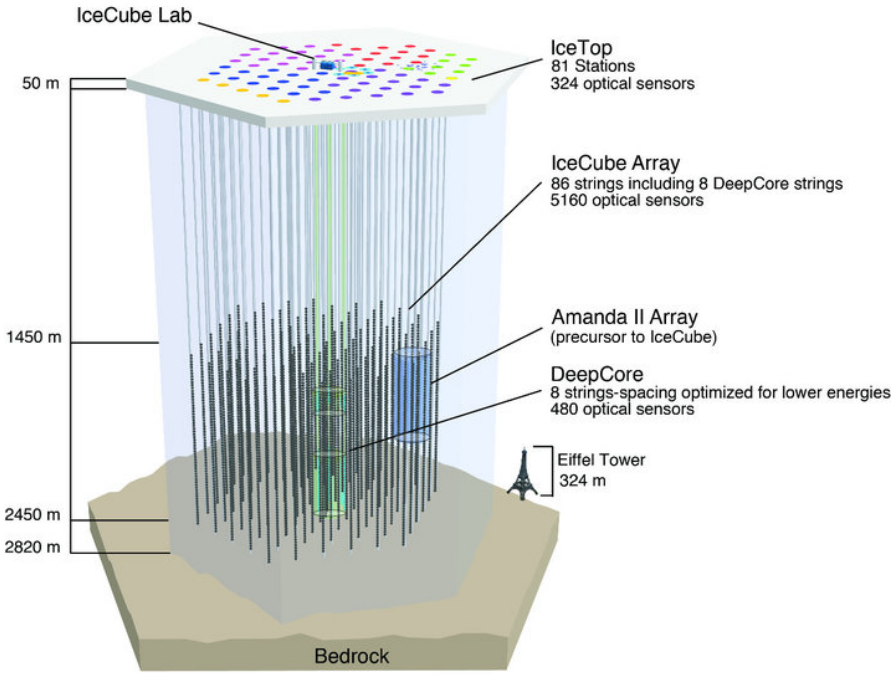

Figure 2.3: IceCube & DeepCore detector layout from [84].

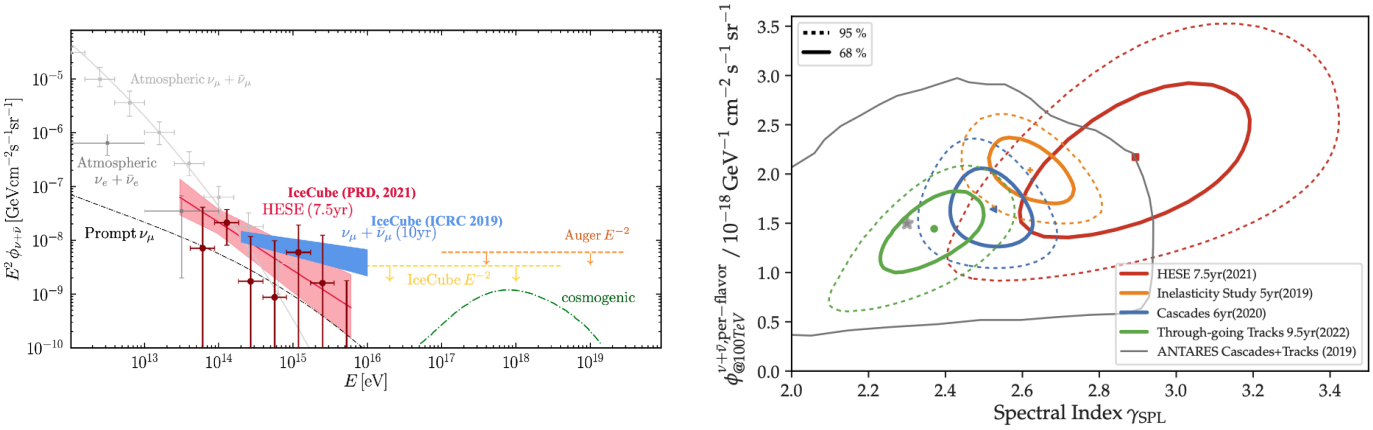

Figure 2.4: Left: Measurement of high-energy cosmic neutrinos [88]. **Right:** Best fit values of the cosmic flux spectra from different IceCube analyses[87].

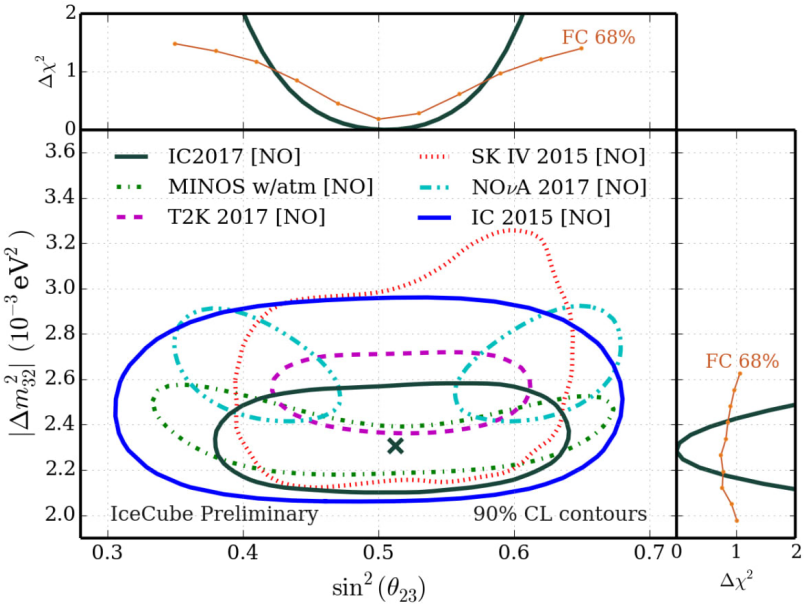

Figure 2.5: Measurement of oscillation parameters with DeepCore[89].

2.3 KM3NeT

The KM3NeT (KM^3 Neutrino Telescope) collaboration[43] is currently building two water-Cherenkov detectors in the Mediterranean sea. It is the successor of the ANTARES experiment[91] that was operating in the Mediterranean between 2007 and spring 2022 and is still source of important results to astrophysics. The KM3NeT detectors consist of 3D arrays of optical modules with updated technology and bigger instrumented volumes compared to ANTARES. A collection of 18 DOMs connected to a single backbone electro-optical cable is called a detection unit (DU, or string). The DOMs are attached to two Dyneema® fibre ropes with an average spacing of 9.3 m(ORCA) and 36 m(ARCA). The DUs are anchored on the seafloor by anchors and align vertically by the buoyancy. An extra buoy is also attached on top of the string, to stabilise the vertical alignment even at higher sea currents. One KM3NeT building block consists of 115 strings.

ORCA(Oscillation Research with Cosmics in the Abyss) is designed to measure the oscillations of atmospheric neutrinos in the energy range of 1 GeV to 500 GeV, with the dedicated goal to determine the neutrino mass ordering[92]. It is located ∼40 km south of Toulon at a depth of ∼2450 m. The strings are deployed with an horizontal spacing of ∼20 m as shown in the preliminary detector layout is shown in Fig. 2.6, reaching an instrumented volume of about 6 Mt.

ARCA(Astrophysical Research with Cosmics in the Abyss) on the other hand is designed for the observation of high-energy neutrinos from TeV up to hundreds of PeV. Although primarily designed to detect cosmic neutrino sources, it will also collect a lot of atmospheric neutrino data, which can be used for the purpose of absorption tomography. The ARCA detector consists of two identical building blocks, both located ∼ 100 km off-shore Sicily, Italy in ∼ 3500 m depth. The layout of a single building block is shown in Fig. 2.6, with an average horizontal spacing of 95 m, reaching the

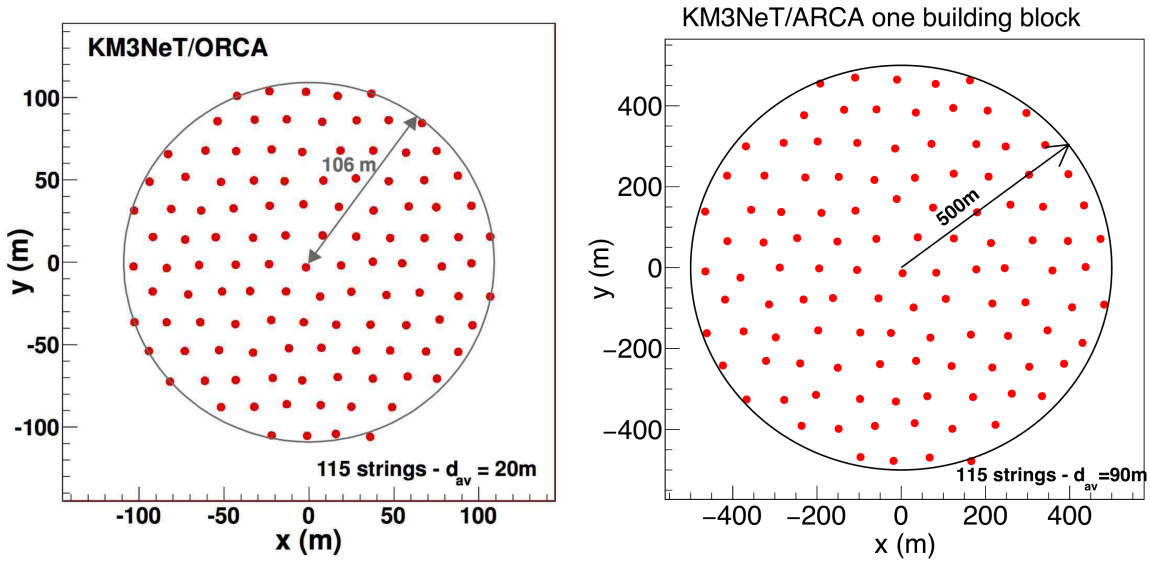

Figure 2.6: KM3NeT detector footprint. Left: ORCA, Right: One of the two identical building blocks of ARCA. Taken from [43].

name-giving cubic-kilometre volume.

Both detector sites use identical technical components, only their layout is optimised for neutrino detection in the energy region of interest.

The main difference to IceCube is obviously the properties of the surrounding medium. Compared to ice, seawater brings the disadvantage of a salt component (a source of background light due to radioactive decays of ^{40}K), bioluminescence and a continuous movement of the optical modules that has to be monitored and accounted for. Promising on the other hand is the purity of the deep seawater, reducing the scattering of photons and thus allowing a better intrinsic angular resolution.

With its two detectors, KM3NeT is a promising candidate for geoscientific research with neutrinos, as it allows for both oscillation and absorption tomography. One major part of this work thus focuses explicitly on neutrino tomography with KM3NeT. The full experiment is described in more detail in chapter 4.

2.4 Baikal-GVD

The Baikal-GVD (Baikal Gigaton Volume Detector) is currently the largest neutrino telescope operating in the northern hemisphere. The modular water-Cherenkov detector consists as of today of 7 clusters of 8 strings, with an instrumented volume of 0.35 km^3, as shown in Fig. 2.7[93] and is planned to be extended to 0.75 km^3(15 strings) by 2024 and even 1.5 km^3 in the following years. Strings within each cluster are separated by ∼60 m, neighbouring clusters by ∼300 m. Each string contains 12 optical modules with one PMT, spaced by 15 m .

On the one hand the Baikal lake provides excellent experimental conditions for the detector deployment, as in the winter period between January and March, the lake is covered by ice thick enough to support all machinery. Additionally, the lake ground is flat over a large area, which simplifies the accurate and stable positioning of the

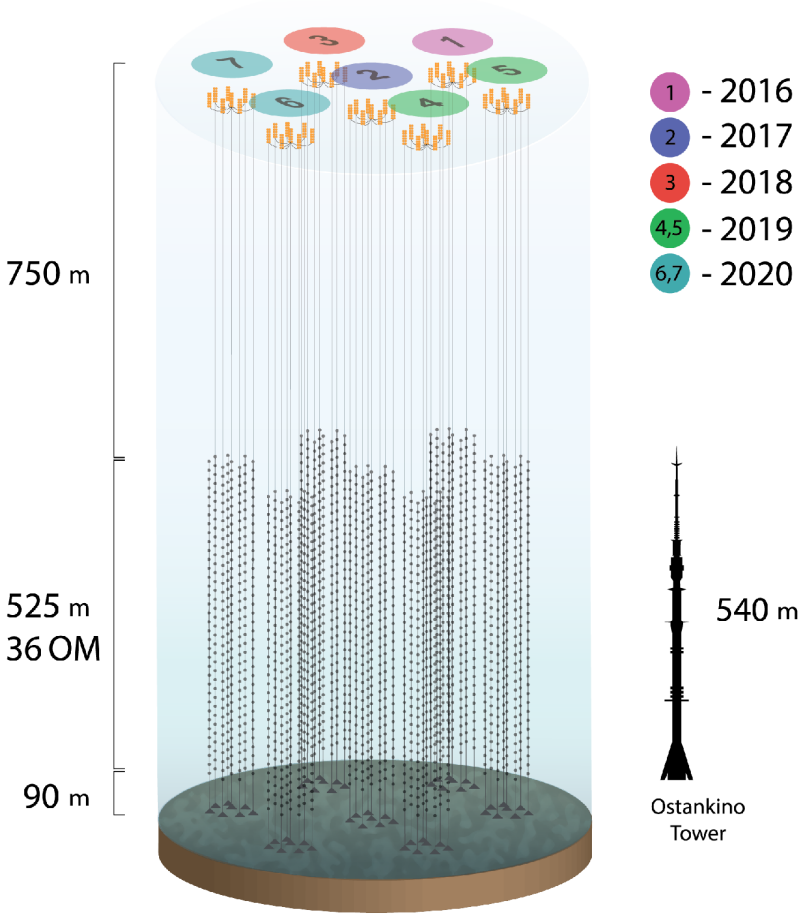

Figure 2.7: Baikal-GDV modular detector layout with deployment dates.

strings. On the other hand, the relatively thin layer of water does not provide an effective shielding from background sources. Also poor purity of the lake water results in only small scattering lengths. With an energy threshold of $\gtrsim$100 GeV Baikal-GVD will mostly detect TeV to PeV neutrinos and is thus also a good candidate detector for absorption tomography.

2.5 Hyper-Kamiokande

A water Cherenkov detector in form of a man-made water tank holding 3000 t of water with PMTs attached to the inner surface was build in 1982/1983 in the Mozumi mine in Japan, owned by the Kamioka mining cooperation, as a Nucleon Decay Experiment: KamiokaNDE. Soon it turned out that its setup was much better suited to detect neutrinos, leading to the construction of SuperKamiokande[19], a ten times bigger version ($\sim$50 kt) with more PMTs than its predecessor. Until today, SuperKamiokande is probably the most prominent experiment to study neutrino oscillations, crowned by the receipt of the Nobel Prize. After 25 years of operation, the third detector generation is planned: Hyper-Kamiokande[94]. Two tanks with 258 kt of water and a photocoverage of 40% of the surface area are foreseen to be build (Fig. 2.8). Next to

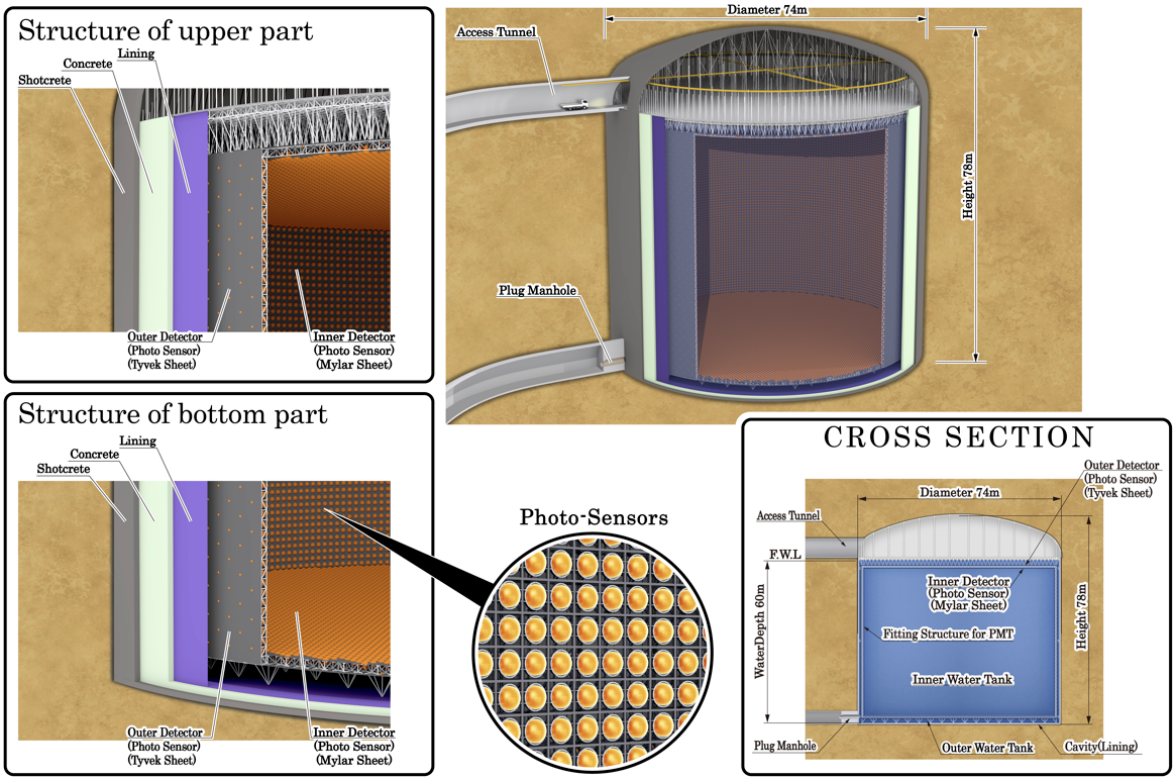

Figure 2.8: Detector design of Hyper-Kamiokande. The cylindrical structure is filled with purified water and its walls are covered with PMTs. (Taken from [94].)

Medium	Absorption length	Scattering length
Antarctic Ice[95]	40 m to 150 m	0.4 m to 2.4 m
Mediterranean deep water[96]	50 m to 70 m	30 m to 60 m
Lake Baikal water[97]	22 m to 25 m	30 m to 50 m
Purified water (Kamiokande)[19]	100 m	50 m

Table 2.1: Optical properties for water Cherenkov detectors at 400 nm wavelength. Values taken from [93] with respective references therein.

its size, the main improvement w.r.t to its predecessor SuperKamiokande are the faster PMTs with higher quantum efficiency (QE).

Due to the smaller size and the dense layout of photosensor, most of the produced Cherenkov light is detected by the PMTs in form of ring-like structures. This allows for a better reconstruction of angle, energy and flavour of neutrinos w.r.t. to neutrino telescopes - at the cost of the total event statistic. The detectors energy threshold is at several MeV, enabling it to perform oscillation tomography studies.

The tank is filled with purified water, showing excellent properties for the light propagation, as listed in Tab. 2.1, in comparison with the detector medium of the other water Cherenkov experiments discussed.

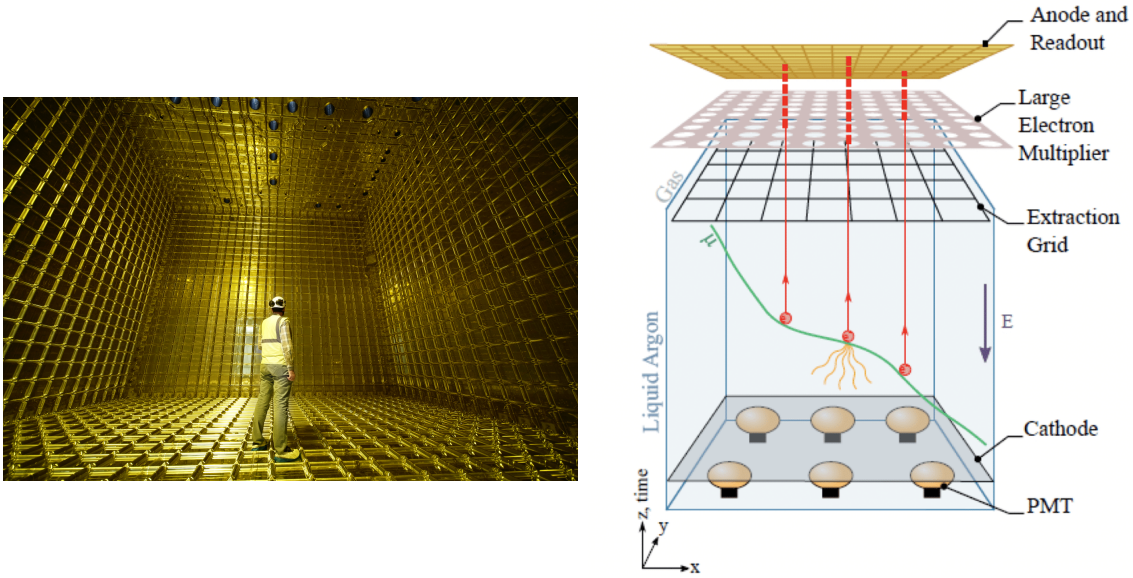

Figure 2.9: Left: Prototype of a DUNE TPC. (Image: Max Brice/Cern); Right: DUNE dual-phase detector principle[99].

2.6 The liquid Argon detector DUNE

A different approach for neutrino measurements is used by the Deep Underground Neutrino experiment DUNE[98], that is planning to build to detectors within into a high-density neutrino beam produced in a proton accelerator at Fermilab. One detector is located just downstream the neutrino source (near-detector) and a second one 1300 km further (far-detector) at the Sanford Underground Research Facility. One goal of DUNE is the testing of charge-parity symmetry violation by high-resolution measurements of neutrino flavour mixing in the far-detector, which is the one described in this section. Although DUNE is designed as a long-baseline experiment by measuring the oscillation properties of the neutrino beam, it is also able to study atmospheric neutrinos.

The DUNE far detector will consist of 4 modular time projection chamber (TPC) filled with liquid Argon (LArTPC). Electrons released during ionization of the Argon by secondary particles from neutrino interactions are driven to the walls of the TPC by a strong electric potential and induce a signal at the electronic wires that are mounted in a dense grid of three layers. The position of the signal together with the drift time of the electron allows for a very precise 3D reconstruction of the ionizing particles, and from that the attributes of the neutrino[99, 100].
Additional information comes from fast scintillation light that is collected by PMTs with the help of wavelength shifters and provides information about when the ionization electrons begin to drift. The drift time between ionization and collection of the electron further improves the event reconstruction. The operation principle as well as a picture of a DUNE prototype are shown in Fig. 2.9. At least one of the modules will be a two-phase detector that includes an additional argon gas layer above the liquid, increasing the electron gain under engineering barriers.

Resulting from the different detection principle, DUNEs event signature looks very

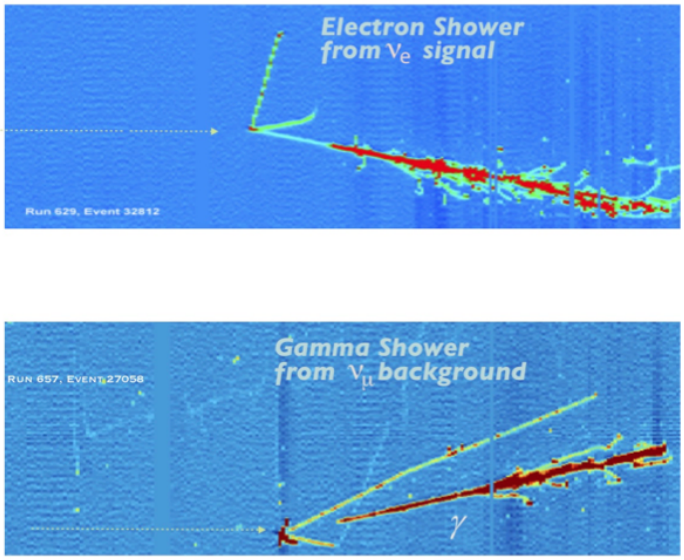

Figure 2.10: ν_e and ν_μ event as seen by the ArgoNeuT LArTPC. Figure taken from [102].

different from those seen by the large volume Cherenkov detectors discussed above. DUNE will not only be able to distinguish between track- and shower-like event topologies, but will actually measure the tracks of secondary particles, *e.g.* as in the ArgoNeuT LArTPC, shown in Fig. 2.10. Moreover, the magnetic field applied to the TPC also allows for the distinction between the charge of ionizing particles from the curvature of their trajectory and thus the polarization of the neutrino (ν or $\bar{\nu}$). Such capabilities thus bear great potential for accurate event reconstruction and classification [101].

Rising costs are delaying the projected launch of DUNE, a first phase is expected to operate together with the beam by 2029.

Chapter 3

Probing the Earth's interior with neutrinos

Contents

"What is inside?" A simple question that particle- and geophysicists have in common. The approach of particle science is quite brutal: collide your target particles at the speed of light and observe the remnants. Doing so with our planet would make many people very angry and be widely considered as a bad move[103].
Instead, in order to study the Earth's interior, geophysicists use seismic methods. The radial structure of the Earth is obtained from the velocity of body waves, establishing the picture of an inner solid core surrounded by a liquid outer core, a solid mantle and a thin crust. The chemical composition of the deep Earth cannot actually be directly derived from seismic data. However, complex interactions between thermal convection and chemical heterogeneities control the dynamics and thermal evolution of the deep Earth. In order to better understand these phenomena, new scientific approaches are necessary to gain additional information.
Due to their elusive nature, neutrinos can be used as messenger particles either by absorption or oscillation tomography. The physics potential of both methods contributing to Earth sciences is discussed here. Further, an overview is given about the current status of the field of neutrino tomography.

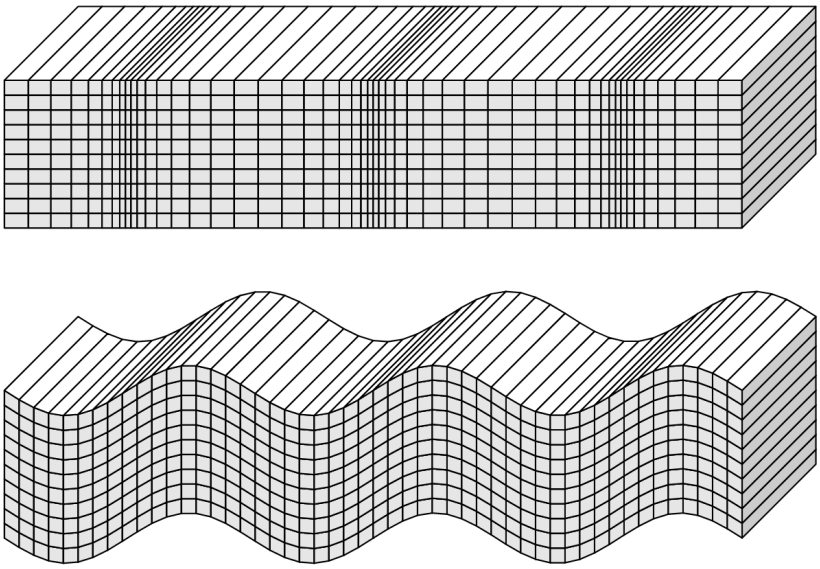

Figure 3.1: Sketch of matter displacements in P waves (top) and S waves (bottom). (Taken from [104].)

3.1 Introduction to the geophysics of the deep Earth

3.1.1 Seismic exploration of the Earth's interior

The most common method to study the Earth's interior are seismic measurements. Although barely moving during the lifetime of a human being, continental plate drifts cause earthquakes that are the origin of large vibrations all around the globe. These earthquakes can have dramatic consequences in the affected regions, but are a fundamental corner stone of Earth sciences and their study even forms a subfield by itself – seismology. This section is meant to give a brief overview of methods used in seismology.

Seismic data has in most cases the form of a seismogram, a record of the Earth surface motion at a specific location as a function of time. Such data is obtained with seismometers, which was in its most elementary form a loosely hung pen over a moving stripe of paper. When the Earth vibrates, the pen starts swinging and thus records data. Today 3-component broad-band electronic instruments are used.
Two types of body waves are recorded: P waves (compressional) and S waves (shear) that differ in the particles movement relative to the direction of propagation of the wave. Within P waves the matter moves parallel to the wave propagation, in S waves perpendicular to it (Fig. 3.1). Shear waves can not travel in fluids, a property that was used to show that the outer core is molten.

A special type of seismic vibrations affect the whole Earth and are called normal modes. They result only from the strongest Earthquakes (magnitude $M > 7$), when seismic waves propagate around the whole globe until at some frequencies, the eigenfrequencies of the Earth, standing waves form at the surface, that can be described by spherical nodes (3D model in Fig. 3.2). As for common seismic waves, normal mode data can be used to draw conclusions about the Earths interior. An introduction can

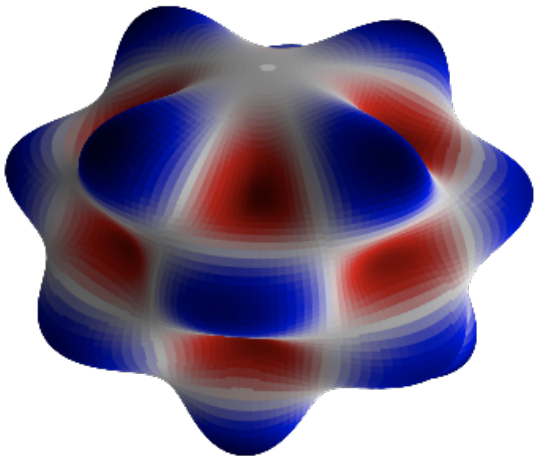

Figure 3.2: Exaggerated sketch of a whole Earth oscillation, corresponding to a ${}_0S_7$ spherical harmonic. Credits: Rûna van Tent.

be found *e.g.* in section 4.4 of [105].

A core formula for the description of seismic waves is the equation of motion

$$\rho \frac{\mathrm{d}^2 u_i}{\mathrm{d}t^2} = \mathrm{d}_j \tau_{ij} + f_i \ , \tag{3.1}$$

where ρ is the matter density, $\mathbf{u}$ the displacement vector and $\boldsymbol{\tau}$ the stress tensor $(i, j \in (x, y, z))$, summed over according to the summation convention. The body force term $\mathbf{f}$ generally contains a gravity term, that is important at very low frequencies, *i.e.* for normal mode seismology. For common travel time seismology it can be usually neglected. With that simplification, one can derive two solutions for eq. 3.1 (*e.g.* as in [104]). For P waves one finds

$$\nabla^2(\nabla \cdot \mathbf{u}) - \frac{1}{\alpha^2} \frac{\mathrm{d}^2(\nabla \cdot \mathbf{u})}{\mathrm{d}t^2} = 0, \tag{3.2}$$

with the P wave velocity

$$\alpha = \sqrt{\frac{\lambda + 2\mu}{\rho}}. \tag{3.3}$$

The *Lamé parameters* λ and ρ describe strain-stress relationship of the medium that were here used to find a substitution for $\boldsymbol{\tau}$. The corresponding S wave equation is

$$\nabla^2(\nabla \times \mathbf{u}) - \frac{1}{\beta^2} \frac{\mathrm{d}^2(\nabla \times \mathbf{u})}{\mathrm{d}t^2} = 0, \tag{3.4}$$

with the S wave velocity

$$\beta = \sqrt{\frac{\mu}{\rho}}. \tag{3.5}$$

The work of seismologists is now to use their data to reconstruct the S and P wave velocities during their propagation, which can be modeled in analogy to optic ray

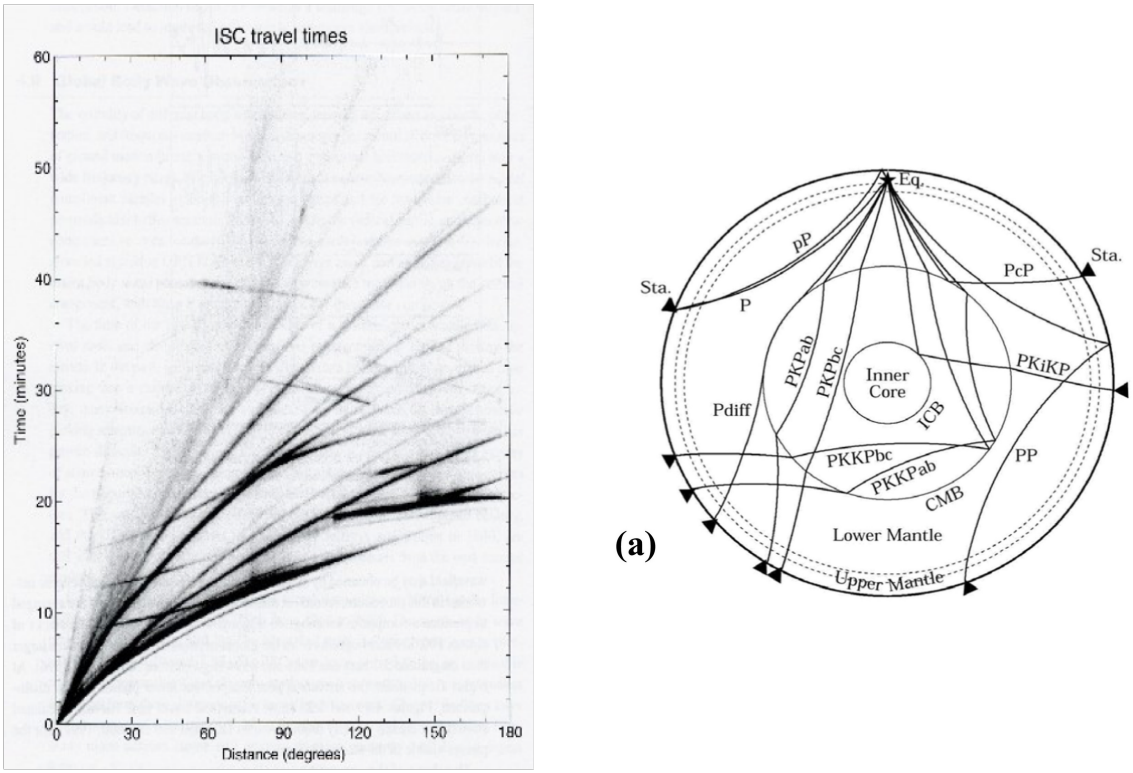

Figure 3.3: **(a)** Illustration of P wave propagation in the Earth.**(b)** Observed time-distance curves. The derivative at a given distance corresponds to the wave velocity. (Figure taken from [106].)

theory, *i.e.* taking into account to refraction and reflection at density transitions. This is done by combining seismic data recorded all around the globe into time-distance curves (*hodochrones*), where the derivative at a given distance corresponds to the wave velocity (Fig. 3.3).

The P and S wave velocities, and further the density profile can be then inversely reconstructed from eq. 3.2 and 3.4 as proposed for example by [107].

3.1.2 The preliminary reference Earth model

The few notions introduced in the previous section give a first hint about analysis methods of seismic data. Beyond the technical principles the real deal comes when data of many different seismic records around the Earth are combined. With technological progress, the number and the quality of seismic stations have multiplied manifold around the globe within the last century, as have the quantity and quality of data. To make the most of it, seismologists established the tradition of data-sharing very early. Huge data sets are freely available and can be used by anybody interested in seismology, a tactic that continuously leads to new findings.

The most prominent example of result from the analysis of combined geophysical data is the preliminary reference Earth model (PREM)[108]. The data set consists of over 1000 normal mode measurements and approximately 26000 body wave events (S and P waves). The three main results are parameterisations of the S and P wave

Layer	Radius r[km]	a [kg m^{-5}]	b [kg m^{-4}]	c [kg m^{-3}]
Inner core	1221.5	-2.177E-10	1.911E-08	1.309E+04
Outer core	3480	-2.412E-10	1.398E-04	1.235E+04
D" layer	3630	0	-5.001E-04	7.307E+03
Lower Mantle	5701	-3.092E-11	-2.444E-04	6.782E+03
Inner transition zone 1	5771	0	-2.329E-04	5.320E+03
Inner transition zone 2	5971	0	-1.260E-03	1.125E+04
Outer transition zone	6151	0	-5.971E-04	7.108E+03
Low velocity zone & lid	6347	0	1.087E-04	2.691E+03
Inner crust	6356	0	0	2.900E+03
Outer crust	6368	0	0	2.600E+03
Ocean	6371	0	0	1.020E+03

Table 3.1: Density parameterisation similar to PREM from http://www.typnet.net/Essays/EarthGrav.htm, used in eq. 3.6.

velocities as a function of depth (Fig. A.1) and a radial 1D density profile, where in each layer the density follows a polynomial form

$$\rho(h) = h \times a^2 + h \times b + c \,. \tag{3.6}$$

The parameters a, b and c are listed in table 3.1, where h denotes the radius starting from the Earth center.

The function is shown in Fig. 3.4, together with a 2D visualisation. As seismology constrains density variations, the absolute values for the density are obtained by using gravitational reference data, *i.e.* mass $M_\oplus = 5.9722(6) \times 10^{24}\,\mathrm{kg}$[109] and inertia $I_\oplus = 8.017\,36(97) \times 10^{31}\,\mathrm{kg\,km^2}$[110].

The main conclusions that can be drawn from PREM (but not exclusively) are

- Earth can be divided in three main layers: inner and outer core and mantle.
- The core-mantle boundary (CMB) represents a seismic and density jump between core and mantle.
- The outer core is liquid, as no S waves can travel through it.
- The outer core is less dense than the inner core.
- Strong anisotropies are found in the uppermost mantle region (depth<200 km). [1]

Due to the highly non-linear inversion of seismic data to wave velocities and in a second step to matter density, the precision of density models like PREM is complex to evaluate, but density uncertainties are usually considered as being at a sub-percent level, with a few percent uncertainties in very specific layers such as the D" layer at the base of the mantle. This statement is supported by most other models like *AK135*[111], that are usually published as variations to PREM, with only small relative differences.

[1] In fact, up to a depth of 670 km the mantle layering can vary for different models. In this work the term mantle refers generally to the whole mantle without any subdivisons.

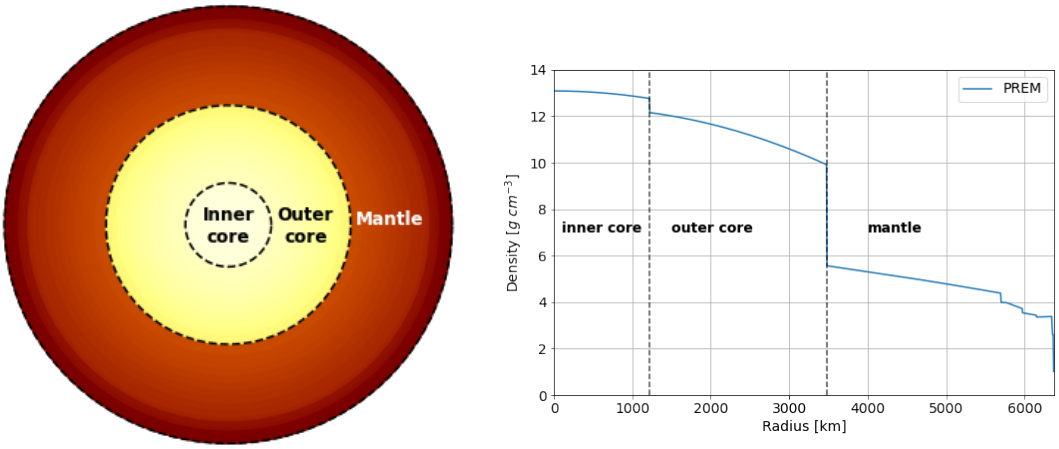

Figure 3.4: Earths density layers according to PREM[108]. The solid FeNi core is surrounded by a molten layer whose lower density than pure iron is due to the presence of lighter elements. The Earth's mantle is at first order a homogeneous pyrolite (with local 3D variations not accounted for in radial models). Finally, the surface of the Earth is covered by a thin crust.

3.1.3 The outer core

The density jump of ∼10 % between the Earth's inner and outer core can not only be explained by its liquid state, but requires the presence of lighter elements in the liquid FeNi alloy. Popular candidates are among others Silicon, Oxygen, Sulfur, Carbon and Hydrogen, and possibly any combination of all of them. With respect to the presence of these elements in the pre-planetary material, revealing the abundances of light elements in the core can help to better understand both its dynamics and the formation of the planet (as the core composition is a function of the pressure and temperature regime at which the core was formed) and has been discussed broadly in the field [112, 113, 114, 115]. As described earlier in this section, seismic measurements cannot directly constrain chemical compositions. Based on information from meteorites, on the density profiles inverted from seismic data, and on ab initio calculation and experimental petrology[2], it can be established that at first order the composition of the core is close to a FeNi alloy with a few percent of light elements, (*i.e.* elements lighter than Fe). Due to the low viscosity of the outer core (close to water), intense thermo-chemical convection is at play, which plays a key role in the generation of the magnetic field. It further justifies the assumption of the outer core being homogeneous (except perhaps for a very thin top layer enriched in light elements).
Table 3.2 shows a selection of models of the outer core composition, listing the amount of lighter elements in the unit of 'weight percent' (wt%), *i.e.* their contribution to the overall mass of the outer core. Throughout the rest of the thesis, I will frequently refer to the proton-to-nucleon ratio (Z/A) of the respective models, since this is the quantity that can be measured with neutrinos (see sec. 3.2.2). A pure iron-nickel alloy is given as reference, which corresponds to the (already excluded) hypothesis of an identical composition of inner and outer core.

[2]For neutrino physicists: Petrology = The study of rocks.

Model Label	FeNi -	$FeNiSi_2O_4$ Badro et al. [116]	$FeNiSi_7O_2$ Kaminski & Javoy [117]	FeNiSiH Tagawa et al. [118]	FeNiH Sakamaki et al. [119]
Composition	95 wt% Fe 5 wt% Ni - -	89 wt% Fe 5 wt% Ni 2 wt% Si 4 wt% O	86 wt% Fe 5 wt% Ni 7 wt% Si 2 wt% O	88.2 wt% Fe 5 wt% Ni 6.5 wt% Si 0.3 wt% H	94 wt% Fe 5 wt% Ni 1 wt% H -
Z/A	0.4661	0.4682	0.4691	0.4699	0.4714

Table 3.2: Models of Earth's outer core composition. For each model, the weight fraction of the different elements is shown as well as the corresponding average Z/A. In all models the Ni content is set to 5 wt% and Fe is the complement to 100 % once light elements have been taken into account. All elements considered in the different compositions have a Z/A between 0.46 and 0.50, except Hydrogen whose Z/A = 1 and increases the bulk Z/A of the alloy. All these models fit equally well the seismic constraints.

3.1.4 3D mantle heterogeneities and LLSVPs

While PREM gives an average density profile of the Earth, 3D variations relative to PREM must be studied to understand the dynamics of the deep Earth. Controversial discussions are held about known discontinuous regions, like the fine structure of the transition zone in the upper mantle, or of its lowermost parts a few hundred km above the CMB, the so called D" layer, where even chemical exchanges between core and mantle can occur. The largest 3D seismic anomalies in the deep mantle appear *e.g.* in maps of S wave velocities below Africa and the Pacific ocean, as in Fig. 3.5. These two regions are called large low shear velocity provinces (LLSVPs) and are usually interpreted as convective structures, or superplumes[3], either of pure thermal or of thermo-chemical nature. The height of the African LLSVP is estimated to about 1000 km, the Pacific anomaly about half of that. Both extend about 15 000 km across the CMB. Their densities differ only by a few percent relative to the surrounding mantle, although it is not clear whether they are lighter or denser[120]. The origin of these LLSVPs is yet unclear[121]. A first theory is that LLSVPs are related to the recycling of dense material brought at the CMB by subduction, whereas a second theory considers that LLSVPs contain pristine material remnant of the primitive Earth. So called ultra light velocity zones (ULVZs) reach density variations up to 10 percent, but are much smaller and are thus not explicitly studied here.

One part of this thesis is dedicated to the question whether the existence of such LLSVPs can be confirmed with neutrino tomography *e.g.* with ORCA, which could help to better understand the dynamic processes in the mantle.

3.2 Neutrino tomography

3.2.1 Absorption tomography

Neutrinos are such elusive particles, that absorption effects are usually negligible. Yet, as we saw that the DIS neutrino cross section increases linearly with its energy, given

[3] When speaking of convection in the (solid) mantle, it should be kept in mind that they happen in timescales of $\mathcal{O}(100\,\mathrm{Myr})$.

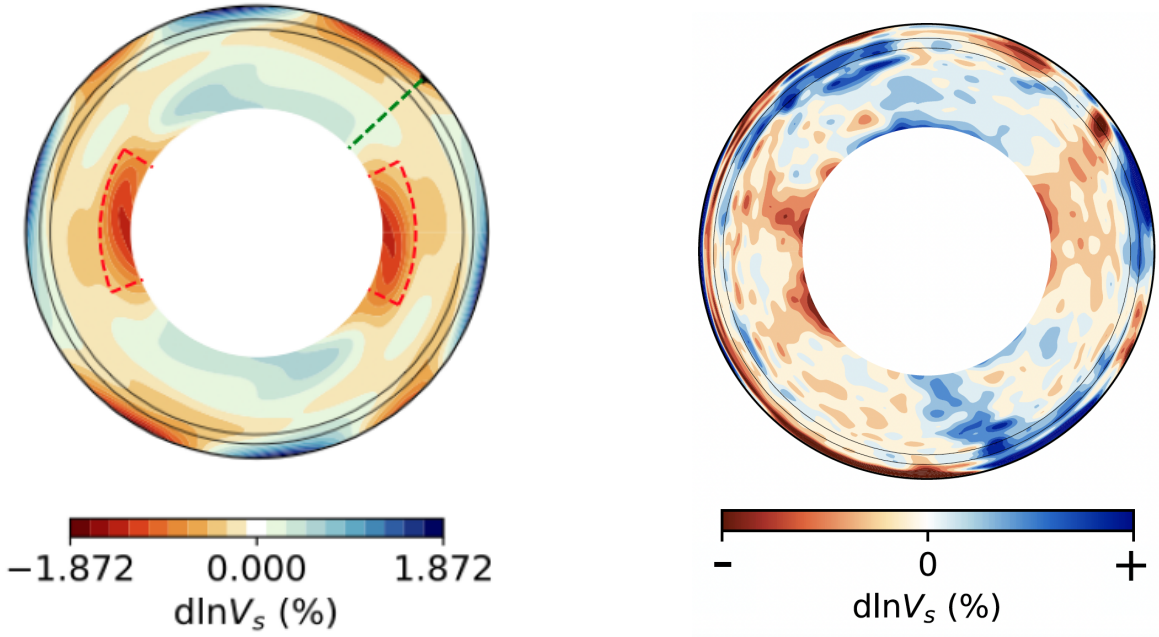

Figure 3.5: Left: Cross section of the $\mathrm{d}\ln V_s$ map from normal-mode tomography through the ORCA site (green line) and the African (right) and Pacific (left) LLSVPs (Credits: Rûna van Tent). The overlying red lines are estimates of the LLSVP shape, that are used in the analysis presented in Part III of this thesis. **Right:** Reference measurement from [122] using body waves, yielding higher resolution.

the matter density of the Earth, above $\sim 30\,\mathrm{TeV}$, the attenuation length of neutrinos

$$\lambda = n\sigma^{-1} \tag{3.7}$$

gets smaller than the diameter of the Earth ($2R_E = 12\,736\,\mathrm{km}$) and absorption has to be taken into account. The absorption probability is connected to the particles density n along the neutrino path and is thus the key parameter to measure in order to constrain the density profile of the Earth. A rather intuitive approach to density measurements of the Earth is thus to use high energetic neutrinos as a kind of X-ray for our planet. It is noteworthy, that the approach of the absorption tomography of the Earth can be inverted in order to measure the neutrino cross section given a fixed Earth density model, as done in *e.g.* [123][4].
Figure 3.6 shows the transmission probability of ν_μ as a function of its zenith angle (and thus propagation length through the Earth) and energy. Regarding the zenith angle, the large density jump at the CMB (dashed line at $\theta_z \approx 147°$) is nicely visible as a decrease of the absorption probability. In terms of energy one can already estimate where one can expect the main sensitivity towards the matter density: Below $\mathcal{O}(10^4)$ GeV neutrinos are barely absorbed, while almost no neutrinos above $\mathcal{O}(10^5)$ GeV make it through the core. The main focus of absorption tomography will lay therefore between these to energy ranges of zero- and complete absorption.

The base concept of absorption tomography is to reconstruct the absorption rates from the data. The main systematics that have to be taken into account are the

[4] A sensitivity study of the high-energy neutrino cross section was executed by a M1 student at APC, using the analysis tools developed during this thesis.

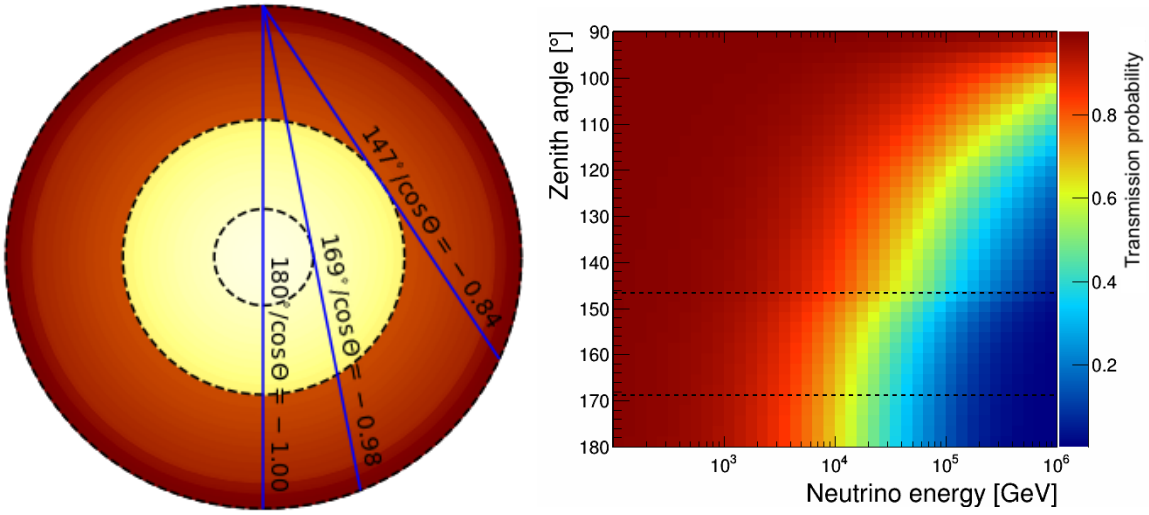

Figure 3.6: Concept of absorption tomography. The transmission probability of neutrinos (here ν_μ) decreases with its energy and the amount of matter along its propagation through Earth.

overall (atmospheric + astrophysical) neutrino flux and the neutrino cross sections. Additionally one has to be aware of the fact, that the absorption probability of a given baseline gives only information about the integrated density along the neutrino path. The sensitivity to the different layers of the Earth comes from the angular resolution of the detector. Neutrinos coming from between 169° & 147° are absorbed in both the mantle and the core. Since between 147° & 90° only the mantle density is probed it is still possible to trace back the absorption probability in the core only.

So far we have assumed a radial symmetric Earth and thus an absorption probability independent on the azimuth angle ϕ. For the study of local density anomalies as LLSVPs, an extra dimension in the histogram of the absorption probability has to be considered.

3.2.2 Oscillation tomography

In sec. 1.3 we heard about neutrino oscillations, the MSW-resonance and in particular its link to the electron density of the matter traversed by the neutrino. We will see now how this can be used to answer some of the questions discussed in the sec. 3.1. First, we agree that the electron density n_e is a product of the matter density ρ and the Z/A

$$n_e = \frac{N_A}{m_n} \cdot \rho \cdot \frac{Z}{A} \tag{3.8}$$

with the Avogadro number N_A and the neutron mass m_n. By constraining n_e with oscillation tomography, one can consequently draw conclusions on either the matter density or the Z/A of the Earth.

The Z/A is the key parameter to learn about the chemical composition of the Earth's matter. Hydrogen with only one proton in the nucleus has the maximum Z/A of 1, while *e.g.* iron has a Z/A$\simeq$ 0.4656. The inner core with an assumed share of 5 wt% nickel has a Z/A of 0.4661, a potential presence of oxygen, silicon or other

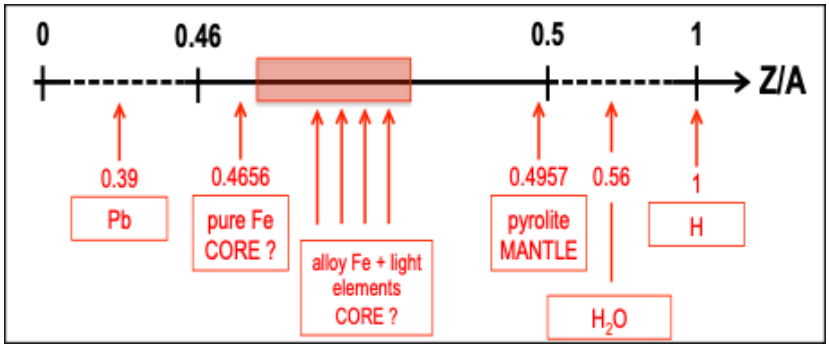

Figure 3.7: Examples values of Z/A.

light elements in the outer core would raise this value. A hydrogen loaded outer core would yield the most significant deviation in terms of Z/A. Fig. 3.7 shows the range for typical values of Z/A for common materials present in the Earth, like Iron and pyrolite, a "model" rock that shall produce oceanic basalts by partial melting but that remains unsampled. Realistic compositions tend to have very similar proton-to-nucleon ratios, as listed in Tab. 3.2 for a selection of Earth models. One further has to keep in mind that the Z/A is degenerated, *i.e.* different chemical composition can yield identical Z/A.

The concept of oscillation tomography is illustrated in Fig. 3.8. Neutrinos that traverse the Earth enter different layers, depending on their direction, *i.e.* the zenith angle θ (as in Fig. 3.6). For each possible trajectory one can calculate the oscillation probabilities of the respective neutrino flavour after as shown in section 1.3. The top panel in Fig. 3.8 shows the ν_μ survival $P(\nu_\mu \rightarrow \nu_\mu)$ and ν_e appearance $P(\nu_\mu \rightarrow \nu_e)$ probability of a straight up-going ν_μ over the whole propagation length, for the case of a FeNi alloy as present in the inner core and pyrolite as in the mantle (for better visualisation of the effect). The bottom panel Fig. 3.8 illustrates the oscillation dependency on the neutrino energy, again for a FeNi alloy and pyrolite in the outer core region.

The above explanation showed the effects of different outer core composition on neutrino oscillations, the same effect appears for variations of the matter density. In reality, the measurements of the neutrino oscillations alone has to be interpreted in the light of geophysics in order to draw conclusions about either the Z/A or the matter density.

3.3 Status of neutrino tomography

The idea of using neutrinos to study the Earth's interior is not new. Already in the 70s it was suggested to determine the Earth's density by measuring the absorption of neutrinos[124, 125, 126]. And with the discovery of neutrino oscillations, the possibility of probing the Earth's structure with oscillation tomography, *i.e.* by measuring matter enhanced oscillations, came up[127, 128]. Since both underlying phenomena – absorption and oscillation – are statistical processes, large data sets are necessary to draw conclusions about the Earth, which is a huge challenge regarding the small neutrino cross sections. With the current generation of neutrino detectors reaching the

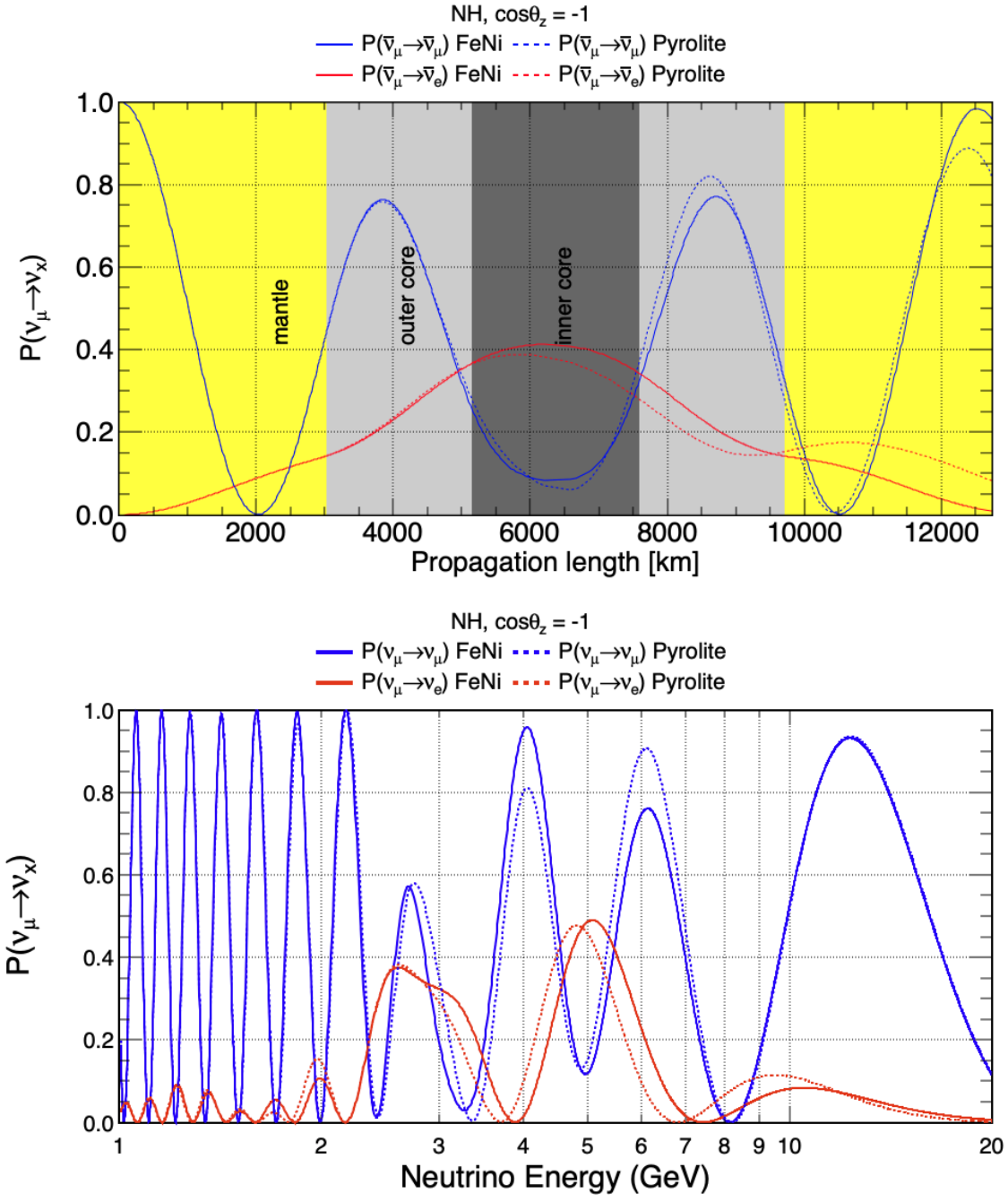

Figure 3.8: **Top** The probability for a 4 GeV ν_μ to survive or oscillate into a ν_e varies with the propagation length and the traversed matter. **Bottom** The effect of the chemical composition of the outer core towards the neutrino oscillations depend on the neutrino energy. For better visualisation of the effect, the comparison is made between a FeNi alloy and pyrolite.

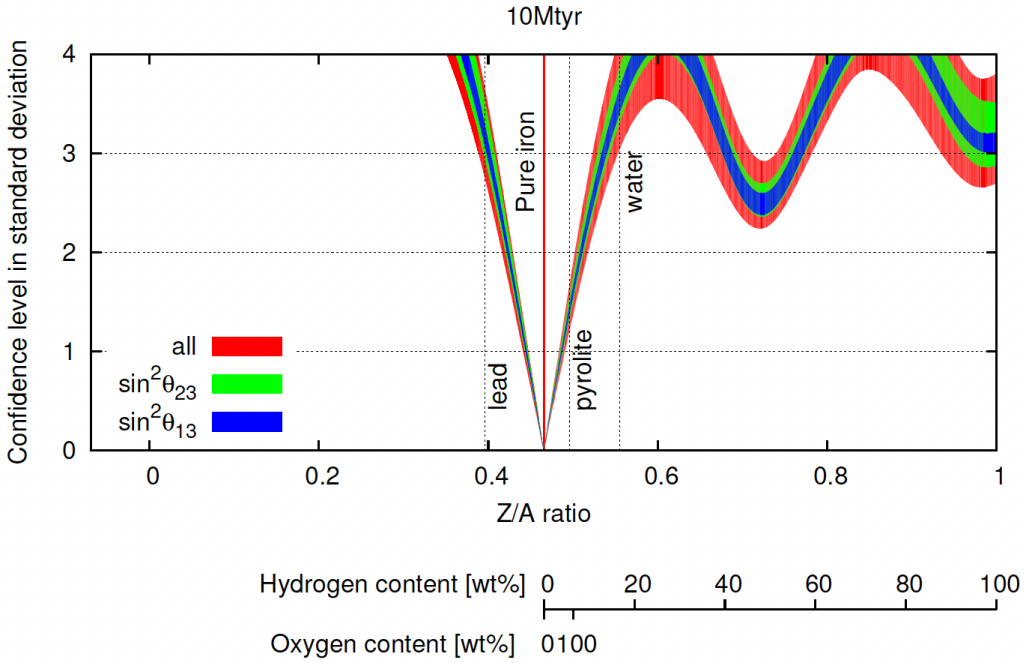

Figure 3.9: Sensitivity to the outer core Z/A for a 10 Mt yr exposure of HyperK[94]. The colored bands indicate uncertainties based on the respective mixing parameter. The Z/A is set to perspective given certain wt% of Hydrogen or Oxygen.

kilo- and even mega-tonne scales of instrumented detector mass, neutrino tomography comes within reach. During the last years, numerous studies about the feasibility of neutrino tomography were published. In this section, a small selection of studies with similar methods and research focus as used in this work are introduced[5].

Sensitivity studies on oscillation tomography with atmospheric neutrinos have been reported by the groups of Hyper-Kamiokande[94], DUNE[129, 130] and ORCA[131, 132], using Monte Carlo simulations of the respective detector and overall similar analysis methods. As we saw in sec. 1.3, neutrino oscillations are sensitive to both the matter- and the electron-density and publications usually focus on one quantity, while assuming the other as known (*e.g.* Z/A analysis of Hyper-Kamiokande, Fig. 3.9). Also, the set of underlying oscillation parameters may vary for different authors. The biggest impact concerning neutrino tomography origins from the treatment of known[6] Earth properties, *i.e.* its mass and inertia. Fixing these parameters usually decreases the uncertainties of neutrino tomography significantly, because deviations from underlying Earth models (*e.g.* PREM) strongly restrict the allowed range of the parameters of interest. Nevertheless, these studies by the respective working groups are of great interest. All of the detectors mentioned above are designed for the interest of particle physicist, the possibility of geoscience research is only an "extra gimmick". It is thus not well studied, which of the different detector types discussed in chapter 2 is the most suitable for neutrino tomography.

[5] A great overview of the field was given at the workshop Multi-messenger Tomography of Earth (MMTE 2022), where most of the publications listed here were presented.

[6] *i.e.* negligible uncertainties compared to the sensitivity of neutrino tomography.

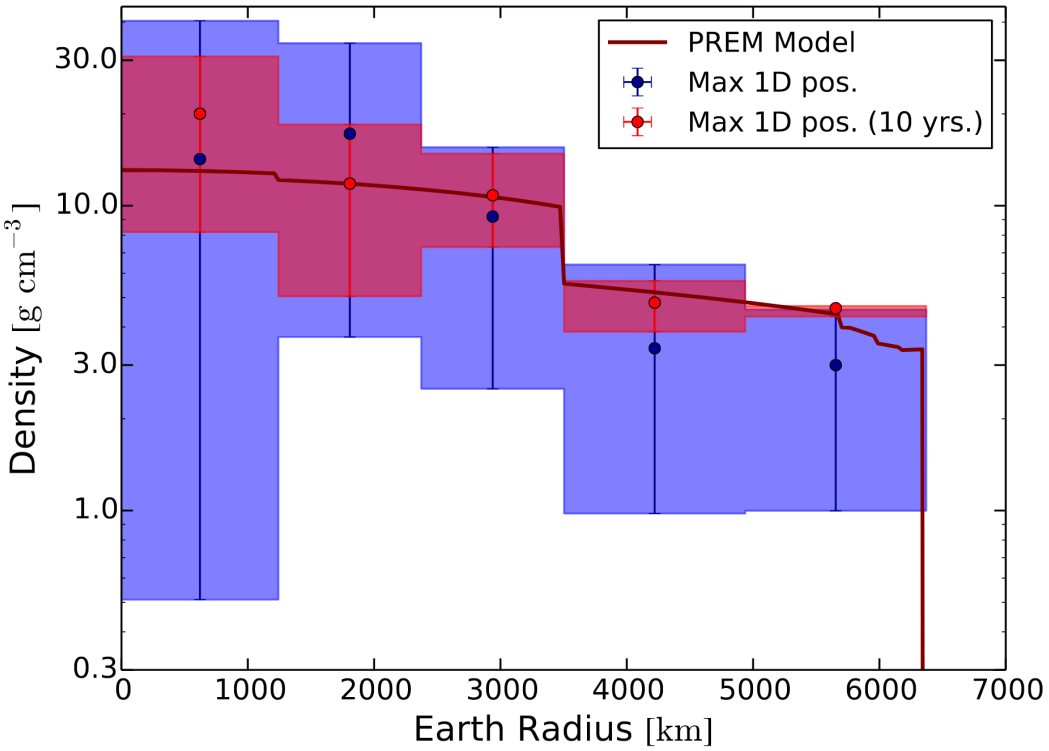

Figure 3.10: Fit of a 5-layer Earth model to one year of IceCube data[136] and a 10 yr forecast, with respect to PREM. Error bars represent 68% posterior intervals.

One big part of this work was therefore to investigate the performances of neutrino detectors in planning, which was already extensively discussed in [133] for Z/A measurements of the outer core. I extend their analysis by including also the shower channel into the analysis and further by performing benchmark tests for possible next-generation (NextGen) detectors with the aim to determine the requirements in order to deliver competitive results to geophysical measurements, focusing on actual models on the outer core.

Absorption tomography requires the detection of high energetic neutrinos in the TeV to PeV range, where the small neutrino flux makes huge detector volumes necessary. The worlds biggest neutrino telescope IceCube is currently the only detector that may collect enough statistics for systematic studies of the Earth density by measuring the absorption of neutrinos. A first analysis on this topic investigates the very fundamental task of confirming the existence and size of a dense Earth core with absorption tomography back in 2008[134] (and recently with oscillation tomography by ICAL[135]). A decade later, the first neutrino tomography study was performed with real data by [136]. With one year of IceCube data, the density profile of the Earth was profiled with neutrinos (Fig. 3.10) and – although being subject to large uncertainties – the resulting Earth mass and inertia fit to gravitational results.

In the light of the uprising interest in neutrino tomography and the manifold work done by the community it is important to define well the goal of this thesis and its unique contribution to geoscience. Funded by the interdisciplinary *80PRIME* project, special focus of the whole doctorate is to build a bridge between particle- and geophysi-

cists. While recent studies all show a proof of concept of the feasibility of neutrino tomography, publications are often tailored to neutrino physicist well familiar with the theory and the analysis methods. Since the results are however mostly interesting for geophysicists, the challenge lies within the presentation of new findings in order to be perceived.

KM3NeT with its two detectors ORCA and ARCA will be the first experiment to perform both oscillation and absorption tomography. By using a Monte Carlo based detector response for simulations of the experiment, sensitivities to the Earth's chemical composition and density profile (including anomalies) can be studied with the best possible accuracy (chapters 8 & 9). The analysis is further used as starting point for parameterised simulation frameworks, in order to find requirements for a theoretical future neutrino detector, designed specifically for neutrino tomography (chapter 10).

Part II

Technical and analytical methods

Chapter 4

KM3NeT

Contents

A general overview about the KM3NeT experiment was given in chapter 2. With its two detectors ORCA and ARCA, designed for the study of neutrinos at GeV energies and in between TeV to PeV, respectively, it is ideal for the case study of both oscillation and absorption tomography. In this chapter, the technical aspects of the experiment are described both on the hardware and software site. The innovative multi-PMT design is presented, which is one of the main differences from other 3D water Cherenkov telescopes. Being deployed in the Mediterranean Sea brings several difficulties with it. First, the varying detector environment requires for excellent detector calibration techniques. Second, salt and living organisms in the sea water are sources of optical background multiple orders of magnitude stronger than from the actual neutrino signal. Complex trigger algorithms are applied to select the relevant information.

4.1 Research infrastructure

4.1.1 Detector design

The KM3NeT experiment[1] uses DOMs that contain 31 photomultiplier tubes (PMTs) for the detection of the Cherenkov light. When a photon enters a PMT, it will free an electron of the cathode material which is accelerated to the anode by an applied voltage of ∼1000 V and triggers an electron avalanche that gives the electronic signal. A PMT signal that exceeds a certain threshold value is referenced to as a hit. The PMTs are - together with electronics and control elements - embedded in a transparent optical gel and enclosed in a thick glass sphere to withstand the water pressure (Fig. 4.1).
The usage of multiple PMTs per DOM is one of the major improvements compared to other water Cherenkov detectors with only single-PMT DOMs for multiple reasons:

- The overall photocathode area is increased, thus more photons are collected
- More directional information of the photons is collected
- The number of photons can be better counted
- The angular coverage is increased with respect to a single down-facing PMT

Further, the failure of a single PMT is not that significant anymore. More PMTs per DOM allow also more precise trigger conditions, *e.g.* the requirement for multiple hits per DOM per event. Additionally, due to the increased sensitivity on the direction of the detected photon, random coincident hits can be more easily identified as such, *e.g.* when they appear in two PMTs facing opposite direction, which helps to reduce the background rate.

A set of DUs is connected to a junction box (JB) for the power supply and digital connection. All JBs are again connected to one long undersea cable that leads to the shore, where the data is saved and even partially processed in realtime. The preliminary detector layouts were shown in chapter 2.

Both detectors are constantly growing step-by-step. Sea operations for the deployment of DUs and other infrastructure require a lot of preparation, as chartering boats, submarine and crew, and suffered not only once from bad weather conditions. Currently 10 ORCA and 18 ARCA strings are deployed and taking data, with first results being already published[137, 138]. Each additional string improves the detector capabilities and increases the data growth rate. Both detectors are planned to be completed within the current decade.

4.1.2 Calibration

Measuring charged particles moving faster than light in water requires extremely precise instrumentation. The position and time offset of each PMT has to be known respectively with an accuracy of 10 cm and at the nanosecond level. For this purpose, KM3NeT will deploy at least one calibration units (CUs) at the seabed that contain the

[1] A complete overview about the experiment, including detailed information on the topics discussed in this chapter, is given in [43] and at www.km3net.org.

Figure 4.1: Digital optical module (DOM) at the KM3NeT construction site at NIKHEF, Amsterdam. The multi-PMT design yields a high photocathode area and allows for better trigger conditions and event reconstruction.

instruments for the calibration described below. A detailed description of the KM3NeT CU can be found in [139].

Time calibration The time calibration is performed in 3 steps:

1. The PMTs in the same DOM are calibrated via the time delay between pairs of PMTS from signals of the constant ^{40}K-decay in the sea water.

2. The DOMs of one string are calibrated from the known vertical spacing and the measured time delays after flashing the LEDs located on the top of the DOMs.

3. A Laser Beacon able to fire sub nanosecond pulses is used for synchronising the DUs.

Position calibration The position of the PMTs is affected by the sea current by (i) the horizontal movement of the string and (ii) a twist of the string, causing a rotation of the DOMs. For the first case, a network of acoustic emitters and receivers is deployed in and around the detector. Hydrophones in each DOM are used to determine their position by triangulation from the time difference between emission and detection of the signal. To measure the DOMs rotation, a tilt-meter and a compass are built in.

Water properties Water properties, such es *e.g.* transparency, temperature and salinity have an impact on light and sound propagation and has thus to be monitored. Corresponding probes are attached to an instrumentation base which is connected with the CU.

4.2 Background rates

4.2.1 Optical background

In KM3NeT, typical hit rates are ∼7 kHz per PMT, which are dominated by optical background noise. The three main sources are described below.

Dark counts The dark count rate is an unavoidable issue that all PMTs suffer from. If an electron gets freed from its shell somewhere in the PMT, it may generate the same signal as if it was hit by a photon, depending on where in the electrical field it was freed. This happens mostly due to the thermal energy of the atoms, which is why the dark count rate is strongly dependent on the temperature of the PMT. Another source of dark counts are radioactive decays of ^{40}K within the glass sphere of the DOM. The dark count rate can be suppressed by adjusting the PMT threshold, though it is in general inferior to the background rate from ^{40}K in the seawater.

Decay of ^{40}K in seawater The main source of optical background in seawater origins from the radioactive decay of naturally present (∼0.04 %) ^{40}K isotope. On the one hand, the electron produced in the β-decay

$$^{40}\mathrm{K} \rightarrow {}^{40}\mathrm{Ca} + e^- + \bar{\nu}_e \quad (89.3\,\%) \tag{4.1}$$

is energetic enough to produce Cherenkov light. On the other hand, the photon produced in the electron capture (EC)

$$^{40}\mathrm{K} + e^- \rightarrow {}^{40}\mathrm{Ar}^* + \nu_e \rightarrow {}^{40}\mathrm{Ar} + \gamma + \nu_e \quad (10.7\,\%) \tag{4.2}$$

could scatter on electrons in the water, accelerating them to energies above the Cherenkov threshold.

Bioluminescence Microorganisms like plankton and bacteria, as well as fish and other forms of life in the abyss can produce light in chemical reactions. The wavelengths of the emitted light is similar to that from Cherenkov radiation, and thus create indistinguishable PMT signals. Typically, bioluminescence adds an overall, slowly time varying but uncorrelated hit rate to the detector, which can be filtered by trigger conditions (see next section). But light from bioluminescence can also appear locally in form of short (few seconds) but intense *bursts*. It was found in ANTARES, that the occurrence of these bursts correlate with high sea currents[140, 141], especially in vicinity of the DOMs, where strong water turbulence are created. Data-taking is thus usually stopped during periods of strong sea currents or at least marked as such and treated with special care[2].

[2]Fascinatingly, the calibration data of KM3NeT is also of great interest for marine biologists. For example, whale sounds are recorded by the hydrophones and bioluminescent light from manifold lifeforms is detected by the PMTs. For more information, see https://www.zooniverse.org/projects/reinforce/deep-sea-explorers

4.2.2 Atmospheric muons

In the air showers in which atmospheric neutrinos are produced (see eq. 1.3) also muons are created. Despite the large layer of water above the detector, some of the most energetic muons still manage to reach the detector. The track-like signature they leave in the detector is indistinguishable from muons created in a $\overset{(-)}{\nu}{}_{\mu}^{\mathrm{CC}}$-event. Given the low neutrino cross sections, the number of atmospheric muons that reach the detector is still $\mathcal{O}(10^4)$ times the neutrino event rate. This makes atmospheric muons the most dominant background source in the (filtered) event data.

For studies related to matter effects like oscillation and absorption, only up-going (*i.e.* entering the detector from below) neutrinos are taken into account. Cuts on the reconstructed direction are quite effective to reduce the amount of atmospheric muons, because they are not able to traverse the Earth. It is though possible that atmospheric muons are wrongly reconstructed as up-going in $\mathcal{O}(0.1\%)$ of cases, which happens mostly for faint events at the detector edge. It is thus necessary to make special efforts in order to identify (and remove) atmospheric muon events. The machine learning algorithms that are used to suppress the atmospheric muon background to a reasonable level are discussed in detail in chapter 6.

4.3 Data acquisition and event trigger

The actual data collected by the KM3NeT detectors consists of the analogue signal of the PMTs that pass a preset threshold (typically 0.3 photo-electrons), which is referred to as level-zero filter (L0). The unique PMT address, the time of the leading edge of the signal and the time-over-threshold (ToT) make up a so called *hit*. In addition, the single PMT rates are sampled with a frequency of 10 Hz in order to monitor the general detector status and optical background conditions. All data is digitised and sent to the shore station unfiltered. For one building block, due to the large optical background, the raw data rate amounts to about $25\,\mathrm{GB\,s^{-1}}$ and must therefore be significantly reduced in order to be stored on disk. Therefore, real time filters are applied to the data at the shore station: The level-one filter (L1) requires coincidences of at least two L0 hits of different PMTs of the same DOM within a given time interval, typically $\Delta T = 10\,\mathrm{ns}$. To further decrease the fraction of random coincidences a level-two filter (L2) is applied, that requires a minimum of 4 or 5 L1 hits within a time window of ΔT =10 ns and a maximum space angle between the PMT axes of 90 degrees.

The next step is to select hits originating from a neutrino interaction. The idea of such an event trigger is to combine hits (usually at the L2 level) that satisfy the condition

$$|t_i - t_j| \leq |\vec{x}_i - \vec{x}_j|/c_{\mathrm{water}} + T_{\mathrm{extra}} \tag{4.3}$$

where $t_{i,j}$ and $\vec{x}_{i,j}$ are the time and position of hit $i(j)$ and c_{water} the speed of light in water. Timing uncertainties and photon scattering is accounted for by T_{extra}, which is typically set to 10 ns. In order to reduce the number of background hits, a spatial mask is used to exclude hits far away from the cluster, which reduces the number of PMTs to be considered up to a factor 100. For showers, this mask is typically a sphere with a radius of a few absorption lengths in water around the cluster. For a track-like event it becomes more complicated, as the track direction has to be estimated. A cylinder

around an estimated track trajectory is used, again with a radius of a few absorption lengths. Up to 200 direction hypotheses are tested to cover the whole sky, the one including the most hits is kept. Multiple triggers can be applied at the same time, *e.g.* optimised for different event topologies or neutrino sources.
In summary, triggers are necessary to reduce the needed disk space and and improve the event purity. Eventually, the trigger determines the quality of the data used for top tier analyses and thus the research results of the whole experiment. It is noteworthy that the signal-to-noise ratio at the PMT level is about 10^{-6}, showing the importance of optimal trigger conditions.

Filters and triggers are applied in realtime to all the data sent to the shore station. During the processing, following data packages are send to the respective next CPU in the loop. Eventually, the first CPU should be ready again at the end of the cycle. KM3NeT trigger applications are suitable optimised such that even extremely high trigger rates can be processed with no more than 50 CPU cores. Having in mind that modern mid-range CPUs come already with 6 cores, the "All-data-to-shore" concept can be implemented in a sufficiently cost-effective way.

Chapter 5

Monte Carlo simulation in KM3NeT

Contents

This chapter describes the full Monte Carlo simulation chain of the KM3NeT collaboration. The resulting MC data for both detectors was used in this thesis for sensitivity studies on absorption tomography with ARCA and oscillation tomography with ORCA. The simulation chain starts with the event generation, *i.e.* a neutrino interaction and all secondary particle decays, or an atmospheric muon. Both cause the emission of Cherenkov light, whose production and propagation is simulated in the second step. The photons are then eventually detected by the optical modules. At this step the simulated data corresponds to the raw detector signal. Here the trigger conditions are applied to reduce the number of background signals. The events that pass the trigger are finally reconstructed with different algorithms. In the last step, which is not yet automated, the events get classified and undergo a manual selection for the respective analysis.

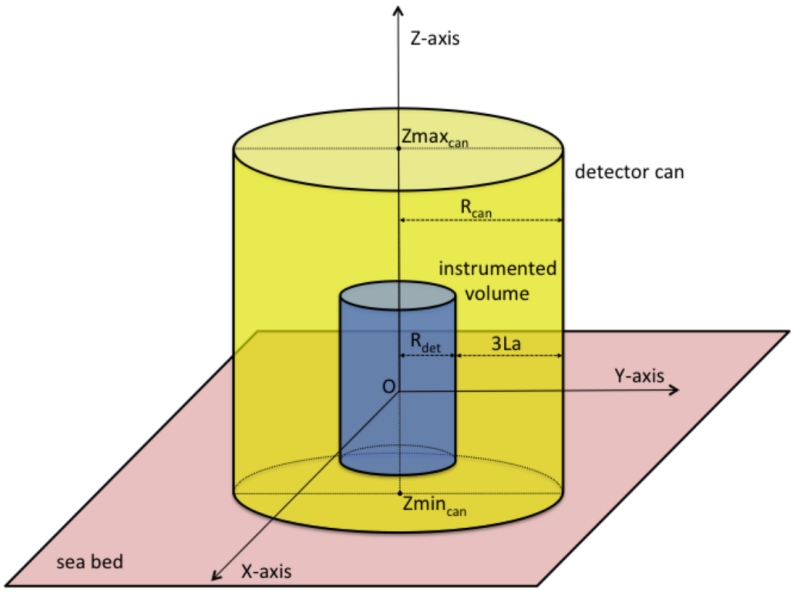

Figure 5.1: Generation volume in gSeaGen[142]. Neutrino interactions are simulated in a generated volume V_{can} (yellow) which radius is extended by three times the absorption length of Cherenkov light in water with respect to the instrumented detector volume V_{det} (blue).

5.1 Event generation

Neutrino interactions in sea water and rock are simulated with the gSeaGen[142] software package, which is based on the GENIE event generator. The energy distribution of generated events can be chosen individually per flavour and interaction channel. An individual calculated event weight can be used later on to obtain a physical event rate. This method ensures that all energy regions are sufficiently sampled in the MC. Simulations include DIS, quasi-elastic scattering and resonance productions, but also the Glashow resonance of $\bar{\nu}_e$ (see sec. 1.4). Tau lepton decays are simulated using TAUOLA[143]. It should be noted here that the mentioned MC weight is not used in our framework, since it includes already an assumption on the absorption probability. Instead, the weighing in our analysis is calculated from the input models described in sec. 7.2.1.

An important aspect of the event generation, which affects the correct weighting in the MC-based detector response, is the generation volume. Neutrino events are generated in a volume V_{can} approximately 3 absorption lengths wider than the instrumented detector volume V_{det} (Fig. 5.1).

For reactions with potential long-range interaction products (muons and taus), events are generated within an extended generation volume $V_{\text{can}}^{\text{ext}}$ (also extending into the seafloor in order to include neutrino interactions in the surrounding rock) and charged particles are propagated to the original V_{can}, where produced Cherenkov light could actually reach V_{det}. For memory reasons, events generated in $V_{\text{can}}^{\text{ext}}$ that do not eventually result in production of Cherenkov light within V_{can} are not saved.

Atmospheric muons (see sec. 4.2.2) are simulated with MUPAGE[144, 145], including

single muons and muon 'bundles' up to hundreds of muons from one primary cosmic ray event, from parameterisations dependent on zenith angle and muon energy.

5.2 Light propagation

All generated particles are propagated with the KM3SIM[146] package, based on GEANT4[1]. It also generates Cherenkov photons from primary and secondary particles and propagates them, taking into account absorption and scattering until they eventually reach a PMT. Finally, PMT hit probabilities are simulated based on characteristics such as photon reflection of its surface, quantum efficiency and transmission in the DOMs glass sphere and optical gel. Typically, the light yield of Cherenkov photons is scaled up during the simulation to enable studies of different water or PMT properties, *i.e.* a higher quantum efficiency, which require more simulated photons.

5.3 Detector simulation and trigger

The PMT response to the incident photon is done with JTriggerEfficiency (JTE) from the KM3NeT intern software JPP, which will be also used on real data. At this stage, optical background is added to the simulation in form of single photon hits at a constant rate (typically conservatively chosen as 10 kHz). The most recent run-by-run simulations use instead the background rate measured at the time of the real data run. Coincident hits of either Cherenkov or background photons are smeared into single pulses with higher ToTs to take into account the limited time resolution of the PMT.

JTE uses the calibrated detector data, *i.e.* PMT position and time offset, for its calculations, but any other detector configuration can be used instead. It is thus easy to create MC data for sub-array of DUs, such as the intermediate 6- or 10-string ORCA phases. It was also used for studying the optimal average horizontal spacing of ORCA strings, which was initially fixed to 23 m and subsequently further reduced to 20 m thanks to the good positioning performance achieved during the deployment of the first lines.

It should be noted here, that all the software packages that are part of the KM3NeT simulation chain are under constant change and improvements. The MC simulations are labeled respectively with an increasing version number. The full ORCA115 MC was made in 2019 with MC v5, while the latest ARCA production was processed with v6, and current production of sub-detectors use v7.

5.4 Event reconstruction

Events are normally reconstructed with two algorithms, one optimised for showers and one for tracks. While the first is more efficient to find the shower vertex (*i.e.* the brightest point) of the event, the second is more likely to find the direction of the outgoing muon (responsible for the track-like event topology). Of course the true topology of a real event is not known, which is why all events are analysed with both a shower-

[1] In newer productions also with JSirene, depending on the energy range and the MC version.

and track reconstruction. What is throughout this thesis called reconstructed energy or direction (E_{reco}, θ_{reco}) refers to the algorithm corresponding to the event classification, *i.e.* for an event classified as track, the output of the track reconstruction is used. Hereunder are presented the current event reconstruction algorithms of KM3NeT.

Aashower `Aashower` is a shower reconstruction for high energy events observed with ARCA[43]. The elongation of a shower-like event increases logarithmically with the neutrino energy and is in the order of $\mathcal{O}(10\,\text{m})$ in the energy range relevant for ARCA analyses. Comparing that to the spacing of ARCA DOMs, one can speak thus of point-like light sources resulting from $\nu_e^{\text{CC}}$and all types of NC interactions.
The algorithm was developed from ANTARES cascade reconstruction algorithm and was updated to make use of the multi-PMT DOM design of KM3NeT. The vertex position of the shower is fitted by minimising the time-residuals between detected L1 hits and expected time-of-arrival under the hypothesis of a spherically expanding light front

$$\delta t_{\text{res}} = t_{\text{int}} - t_{\text{hit}} + d/c_{\text{water}} \; . \tag{5.1}$$

The energy and direction of the shower are reconstructed by maximum-likelihood tests of the probability of a PMT recording a hit from light produced at the vertex. The underlying likelihood model therefore depends not only on the shower characteristics, but also on PMT distance and direction. A time window from $-100\,\text{ns}$ to $900\,\text{ns}$ around the expected time-of-arrival reduces the chance of a random hit from optical background to $\sim 2\,\%$. The latest high energy ARCA analysis reported a median energy and angular resolution of $10\,\%$ and $2\,\text{deg}$ respectively.

Dusj The `Dusj` low-energy shower reconstruction was used for the latest full-ORCA MC simulation of 2019. It is described in detail in sec. 3.3 of the LoI [43] and Chapter 12 of this PhD thesis[147].
In ORCA studies related to matter oscillations, like tomography and NMO studies, the most relevant energies are those with only a few GeV, just slightly over the detection threshold, where triggered events usually only contain a few hits. For a reliable event reconstruction it is thus crucial to reduce the amount of background hits in the time slice of the event.
The approach of `Dusj` is to perform first a prefit for the vertex position on a tight hit selection, *i.e.* not only L1 and L2 hits, but also coincidences between 3 PMTs or PMTs in adjacent DOMs. With this reduction of noise hits, the reconstructed vertex position is very robust versus noise hits and likely to be in vicinity of the true interaction vertex. The result of this prefit is then used as start hypothesis of a more precise second vertex fit, which relies on the robustness of the first fit. Energy and direction as well as the inelasticity y of the shower are then calculated again by maximum-likelihood test on hypotheses of the expected number of photons per PMT, N_γ, with respect to the fitted vertex position. As second quantity, $var(N_\gamma)$ is used to take into account fluctuations due to light from the hadronic shower.
With the departure of the main developer from the KM3NeT collaboration, `Dusj` is no longer maintained, and will not be used for future productions, although showing a great performance.

JShowerFit `JShowerFit` is another low energy shower reconstruction based on JPP which is being developed and used for current MC productions of ORCA sub-arrays. Although `JShowerFit` was not applied to the MC set used for the analysis in this work, it is briefly described here since it played an important role in the development of a KM3NeT event classification (see Chapter 6).
`JShowerFit` starts with two prefits of the vertex position based on time residuals (eq. 5.1) using only L0 and L1 hits. The vertex is then fitted by gradient minimisation of light emission PDFs of `JPP`, that are also used in the consecutive step, a prefit of the shower energy. In contrast to `Dusj`, the `JPP` PDFs do not depend on the inelasticity y.
Energy prefit and reconstructed vertex position are used in the next step for the fit of the shower direction. A scan in all directions is performed and the hit and no-hit likelihoods of a pure electro-magnetic shower are tested with respect to the data.
A final fit is then performed to improve energy and direction reconstruction based on the best results of the prefits.
Since the underlying PDFs used in `JShowerFit` describe only an electro-magnetic shower, a simple linear energy correction is finally applied to take into account the contribution of light from the hadronic shower.

JGandalf JGandalf is a JPP-based track reconstruction used for both KM3NeT detectors[148]. The algorithm is mainly focused on the reconstruction of the muon track, *i.e.* its direction and length, which is again proportional to the muon energy.
A prefit is done to find the approximate track direction. In a grid of constant angles (5° default in ORCA) the track hypothesis is tested vs. the data based on the time-of-arrival. The best fits are processed in the next step, as `JShowerFit` but using hit PDFs of light from muon tracks.
The start position of the track is estimated by projecting the photons of a hit back to the track. The first associated emission point which exceeds the random background level is selected as start position.
Finally the energy is determined by fitting hit and non-hit distributions within a cylinder around the track. Although the energy could be fitted two steps before, it is useful to do it after the fit of the start position, because the total track length is a good indicator for the muon energy. In fact, the track length is used as energy estimator in some early stage analyses. It has to be kept in mind, that the muon can leave the detector so that only a fraction of it's energy is reconstructed.

5.5 Event selection and classification

The event reconstruction is the last step of the data processing stage in KM3NeT. In general, not all MC data is used for high-end analyses, but selection cuts are applied to ensure high data quality and reduce the background due to optical noise and atmospheric muons (which, even after the trigger, is still a factor 1000 above the neutrino rate[92]). And finally, events are classified into classes describing their event topology, namely *track*- and *shower-like*, with the goal to separate at least ν_μ^{CC}events to get some indication about the flavour of the detected neutrino.

ORCA selection

The event selection of the ORCA MC data sample used is described in sec. 10.2 of the PhD Thesis[83]. The selection criteria are:

Valid reconstruction One of the two reconstructions must have succeeded, *i.e.* given a valid output for energy and direction (and track length) of the event.

Up-going direction One of the reconstructed directions must be $\cos(\theta_z) \leq 0$. For tomography it is obvious that only Earth-traversing neutrinos are taken into account. For NMO analysis, this cut is applied to reduce the atmospheric muon background.

Reconstruction quality The intermediate fitting steps of the reconstruction algorithms provide useful information on the fit quality that are used for the event selection. For `JGandalf`, the final reduced χ^2 ($\chi^2_{\text{red}} = \chi^2/\text{n\_deg}$) has to be bigger than -0.5. For `Dusj`, criteria are set on the allowed difference between first and second vertex fit, as well as the number of fits in vicinity of the final result (see sec. 12.2 in [147]).

Geometry cuts The best reconstruction is expected when most of the produced Cherenkov light is caught by the detector. This is most likely the case for events that are fully contained in the instrumented volume. Events are selected when their reconstructed vertex is inside a cylinder a few meters larger than the smallest possible cylinder containing all DOMs. Note that this geometry has to be redefined for each detector configuration, *e.g.* ORCA6. The geometry criteria is actually extended, since light is not only produced at the vertex: Track events are also accepted, when their vertex is contained after being shifted by 30 m in the track direction, *i.e.* the muon flies into the detector. Shower events are accepted, when a sufficient fraction of the volume of a (light) cone starting from its vertex is contained.

ARCA selection

For the ARCA MC v6 of 2020, no official selection cuts were available when I performed the absorption tomography. Only the requirement for at least one valid reconstruction in upgoing direction was used.

Event classification

The KM3NeT design has limited capability to identify the actual flavour and/or interaction channel of events. Instead, events are usually classified according to the light topology they deploy in the detector. While the parameterised detector modelling uses only a track- and a shower-like class, the MC response matrix can be build for multiple classes. Currently, a machine learning algorithm is used to predict a probability between 0 and 1 for a certain event to have a track-like topology. This prediction is referred to as *track score* and is the variable used for the classification. From the design

of the classifier, which is discussed in detail in chapter 6, a reasonable classification cut is

$$class = \begin{cases} \text{track-like} & track\_score \geq 0.5 \\ \text{shower-like} & track\_score < 0.5 \end{cases} \tag{5.2}$$

The cut can of course be optimised for individual analyses. It was also found useful to introduce an "intermediate" class, that contains event that can not clearly be assigned to one of the two topologies, as

$$class = \begin{cases} \text{track-like} & track\_score \geq 0.9 \\ \text{intermediate} & 0.3 \geq track\_score < 0.9 \\ \text{shower-like} & track\_score < 0.3 \end{cases} \tag{5.3}$$

Further, analogue cuts are used based on background classifiers that produce a *muon score* and a *noise score*, predicting the probability for an event to be an atmospheric muon or random noise. The resulting cut criteria are

$$muon\_score < 0.05; \quad noise\_score < 0.1 \tag{5.4}$$

as motivated in [92].

Chapter 6

Particle identification

Contents

The particle identification (PID) is a crucial part for all neutrino experiments. It is used to separate neutrino from background events (see sec. 4.2) and further to distinguish track- and shower-like events, which is used to identify the flavour of the neutrino. Recent KM3NeT analyses used a random decision forest (RDF) trained on a variety of hand-designed training features. I modified and improved the existing code, eventually resulting in a clean and documented framework, accessible by the whole collaboration. The creation of training features as well as the actual training framework were modified fundamentally to use the most up-to date KM3NeT internal software, which enabled for the first time an implementation of the PID into the MC simulation chain. The new framework was build around the `xgboost` library[149] in a python environment, leading to major improvements in the usability and functionality of the software. The first important change is the switch to gradient boosted decision trees (BDTs) that surpasses the efficiency of the RDF. Second, a new tool to evaluate training features has been used to identifying and remove redundant training parameters and has proven to be useful for the development of new features. This chapter gives an introduction on the used machine learning methods. The used training features are introduced and the performance of my adapted framework on the latest ORCA production is presented and compared to the old version. With the generalised shape of the framework, I was further able to create the first PID for ARCA, which I used for my analysis. As a service task, new training features were developed for `JShowerFit`(cf. sec. 5.4), the shower reconstruction used for new productions of ORCA sub-arrays.

6.1 Motivation

Since the neutrino is not detected directly, information about its flavour has to be extracted from the detection of the secondary particles created in the weak interaction process between neutrino and nucleon. The flavour identification of the neutrino is addressed by reconstructing the light signature measured by the detector (as described in sec. 2.1.2). A track-like event topology corresponds to a $\overset{(-)}{\nu}{}_{\mu}^{\mathrm{CC}}$-event, while shower-like events may either origin from $\overset{(-)}{\nu}{}_{e}^{\mathrm{CC}}$ or a NC-event of any flavour. This classification process can be a challenging task, especially at lower ($\sim$GeV) energies where only little Cherenkov light is produced and the muons will not propagate very long.
The most intuitive idea would be to analyse the space and time distribution of the hits. The difficulty here is that not all hits are correlated to the neutrino event, but some of them are produced by optical noise (either from ^{40}K decay or from bioluminescence). More criteria are needed to allow the separation between track and shower events. One way to accomplish that is to cut on output parameters of the event reconstruction that are likely to differ for the the event classes that are to be separated. Doing this by hand can be a very time consuming task, especially when many parameters, sometimes correlated between each other, come into play. Correlations make it necessary to cut on functions of the parameters, instead of the parameter themselves, which further complicates the problem. This task can be automated very efficiently by using machine learning algorithms.

6.2 Introduction to decision trees

Independent of the way of its training, a decision tree tries to predict the true label y of an event based on the input parameters x. At each branch of the tree, one parameter is compared to a certain value. The outcome of the comparison determines the next branch and so on, eventually ending in a leaf, assigning a prediction score to the input variables. An even more powerful prediction can be made by the combination of K trees into a so-called decision forest. The prediction score of a decision forest is given by:

$$\hat{y} = \sum_{k=1}^{K} f_k(x), f \in \mathcal{F} \tag{6.1}$$

where K is the number of trees in the ensemble and $\mathcal{F} = \{f(x) = w_{q(x)}\}(q : \mathbb{R}^m \rightarrow T, \omega \in \mathbb{R}^T)$ the space of classification trees. ω contains the weights per leaf, and q assigns an event to one specific leaf, based on the parameters. The resulting score can now be used as a classification score by choosing a cut value c, so that

$$class = \begin{cases} 1 & \hat{y} \geq c \\ 0 & \hat{y} < c \end{cases} . \tag{6.2}$$

Eq. 6.1 is the basis for the supervised training of our model. For the analysis presented here, the `xgboost`[149] python package was used, where the trees are trained to minimize the objective function

$$obj(f) = L(f) + \Omega(f) \tag{6.3}$$

where L is the training loss function and Ω is the regularization term. L is a metric for the goodness of the prediction, which can be chosen by the user. A common choice for classification tasks is the logistic loss function

$$L(f) = \sum_i [y_i \ln(1 + e^{-\hat{y}_i}) + (1 - y_i) \ln(1 + e^{\hat{y}_i})]. \tag{6.4}$$

The complexity of a tree with T leaves is controlled by the regularization term, which is calculated in `xgboost` as

$$\Omega(f) = \gamma T + \frac{1}{2}\lambda \sum_{j=1}^{T} \omega_j^2 \,, \tag{6.5}$$

where λ and γ are regularization parameters. The first term reflects the preference for small trees over big ones, the second term is in favour of multiple small weights instead of a few big ones.
For the training of a single tree, at each leaf it is checked whether an additional split would improve the objective. The most powerful way to find the best split is to simply evaluate all possible splits. For big data sets this can not be done efficiently and approximate algorithms come into play (*e.g.* [150]). The gradient boosted tree ensembles are trained one tree after another. A new tree is only added to the existing ensemble, if it decreases the objective as defined in eq. 6.3. The regularization term Ω prevents an overfitting by adding trees or leaves as this would increase the model complexity.
The decision trees of RDF used in [92] are in contrast trained in parallel and independent from each other. The number of trees is here specified by the user. In order to avoid that multiple trees grow similar, each tree only sees a random subsample of training features. The training of the BDTs however intrinsically ensures that the trees make complementary use of the training features - identical trees would only increase the model complexity Ω.

6.3 Training parameters

In this section the parameters used for the training of the classifiers introduced in the previous section are described. With the framework I developed, all these features can be extracted directly from the output files of the KM3NeT MC chain and into the proper input format for the training of the classification.

Most basic parameters, like energy, direction of position of interaction of the neutrino are uncorrelated from its flavour. More valuable information arise from intermediate steps of the reconstruction algorithms, *e.g.* measures for the fit quality or differences between different steps during the reconstruction.

Aashowerfit In the current version of the KM3NeT MC chain, the output stored from `aashowerfit` are the reconstructed energy, position and direction of the event, together with the likelihood of the fit and the number of used hits. If the parameter-based PID approach will be used in future for ARCA, it could be worth to investigate if more features can be extracted from `aashowerfit` as was done for the other available shower reconstructions.

Dusj The ORCA MC which I used for my analysis was processed with the `Dusj` shower reconstruction. A long list of parameters were used as described in [92] and more precisely [83], including basic reconstruction outputs but also more advanced features based on differences between different stages of the reconstruction algorithm and expected amount of Cherenkov light in the instrumented detector volume. The most significant improvement arose from the introduction of hit-based variables, that take into account distribution of hits inside the detector and comparing them to PDFs of the expected hit pattern.

JShowerFit `JShowerFit` replaced `Dusj` as shower reconstruction and is currently used for MC simulations of ORCA sub-arrays, which were not used during this thesis. However, during my work on the PID framework for KM3NeT, I developed training features based on `JShowerFit`, which is described at the end of this chapter.

JGandalf Together with the basic reconstructed values (energy, position, direction), the track reconstruction `JGandalf` provides some fit information itself, that are listed in tab. A.2.

6.4 Classifier output

In this section, we will discuss the results of the PID from BDTs for track/shower and ν/μ_{atm} separation, as well as ways to evaluate the quality of the classification. The results shown are obtained by the same method but are discussed separately for each detector (ORCA and ARCA). For ORCA the new BDT classifier is compared to the RDF method.

6.4.1 ORCA

The direct output of the classifier is a prediction score $P \in [0, 1]$. For track/shower separation, we refer to it as *track score* where high(low) values of P means that the event is predicted to be track- (shower-) like. Analog to that, the output of the ν/μ_{atm} classifier is called *muon score*. The *track score* distribution of ORCA is plotted in Fig. 6.1(a) for different interaction channels. It is immediately visible from the histogram, that $\overset{(-)}{\nu}{}_{\mu}^{\text{CC}}$-events are most likely assigned a high track score, while $\overset{(-)}{\nu}{}_{e}^{\text{CC}}$and NC events get low track scores. Note that the $\overset{(-)}{\nu}{}_{\tau}^{\text{CC}}$ sample contains interactions with both event topologies, *i.e.* track- and shower-like event depending on the τ-lepton decay.
Based on this score, one can create a prediction $\hat{y}$ according to eq. 6.2 (here $c = 0.5$) to separate the events into *classified as track/shower* classes. The overall classification efficiency (or accuracy score) is then given by the ratio of correctly classified events (where $\hat{y}_i = y_i$) to the total events (Fig. 6.1(b)). It can be nicely seen how the prediction gets more accurate at higher energies due to the longer muon trajectories.
Figure 6.1(c) shows the fraction of events classified as track for the respective event types. Again the energy dependence is visible, as well as the fact that the $\overset{(-)}{\nu}{}_{\tau}^{\text{CC}}$sample contains $\sim$17 % of track-like events.
The last quantity in Fig. 6.1(d) is the so called *separability* which was already used in

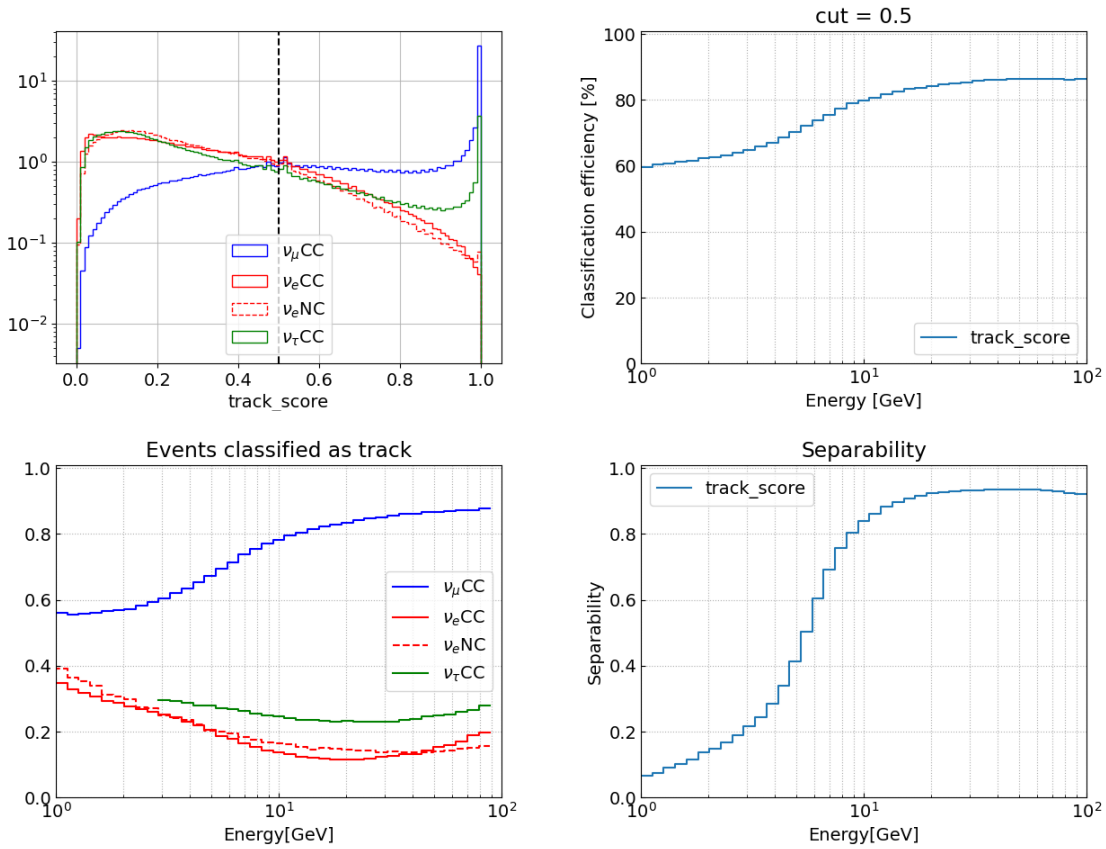

Figure 6.1: Output of the track/shower classifier for ORCA, trained with BDT. **Upper left:** Prediction score per interaction channel. Events with *track score* > 0.5 are classified as track-like. **Upper right:** Fraction of correctly classified events as a function of energy. **Lower left:** Fraction of events of different types classified as track. **Lower right:** Separability of $\overset{(-)}{\nu}{}_\mu^{\text{CC}}$ and $\overset{(-)}{\nu}{}_e^{\text{CC}}$-events, as defined in eq. 6.6.

an earlier thesis[151] on machine learning in KM3NeT, and is defined as

$$S(\Delta E) = 1 - C(\Delta E) = 1 - \frac{\sum_i P^{\nu_\mu}_{i,\text{track}}(\Delta E) \times P^{\nu_e}_{i,\text{track}}(\Delta E)}{\sqrt{\sum_i (P^{\nu_\mu}_{i,\text{track}}(\Delta E))^2 \times (P^{\nu_e}_{i,\text{track}}(\Delta E))^2}} \,. \tag{6.6}$$

Here C is the correlation factor between the classifier output for true track and shower events, calculated from the binned probability $P^{\nu_x}_{i,\text{track}}$ for a neutrino of flavour x to be classified as track (only CC-events are used).
While the *accuracy score* gives no information about the confidence with which the event is classified and may vary strongly for different values of the cut c if most of the predicted values $\hat{y}$ are in close vicinity to it, the *separability* is completely independent from the chosen cut c. The *separability* is an efficient quantity to compare the efficiency of different classifiers. Naturally many other metrics are used in the machine learning community, each having pros and cons for evaluating the quality of a classifier.

For analyses of the full ORCA detector with SWIM, the MC production of 2019 is used. For this production no atmospheric muons were processed, which is why no ν/μ_{atm} classifier is available for this MC. This is because from earlier productions it was

found that a combination of selection cuts, *e.g.* on the reconstructed vertex position, and decision trees is able to reduce the contribution of atmospherics muons in the final data to 3 %, while keeping 95 % of neutrinos[92]. The same holds true for noise events. By using the same selection cuts on the current dataset it is therefore justified to neglect background sources in the analysis.

6.4.2 ARCA

Since ARCA detects neutrinos with much higher energies than ORCA, muons will propagate for tens or even hundreds of meters before decaying. This is expected to simplify the classification into track- and shower-like events but also the reconstruction of the muon direction, which is the main criteria to distinguish (up-going) neutrinos from atmospheric muons.
During this thesis, the first KM3NeT PID for ARCA was created with BDTs. A publication about the comparison of other classification frameworks for ARCA using Graph- and Convolutional Neural Networks is in planning. Since no official analysis for the ARCAv6 production was released, no selection cuts were applied (apart from requiring the event being reconstructed as up-going by at least one of the reconstruction algorithms) were applied. The first necessary step is the rejection of background events. The output of a first ν/μ_{atm} classifier is shown in (Fig. 6.2). Although being very efficient in selecting μ_{atm} , the overall muon contamination $(n_\mu/(n_\mu + n_\nu))$ is still large due to the huge amount of μ_{atm} in the sample.
The reason is that in first order it is very easy to identify atmospheric muons at these energies. As it can be seen in Fig. 6.2, the overwhelming majority of muons get assigned probabilities of $> 90\%$ by the classifier, most likely by simple cuts on the reconstructed vertex of the event (far above the instrumented volume $\rightarrow \mu_{\text{atm}}$). Like this, the classifier reaches a high efficiency very fast and stops the training process.
In order to further reduce the muon contamination, the output of this first superficial muon classifier can somehow be interpreted as a measure of quality of the direction reconstruction and thus be used as selection criteria. A very loose cut which selects all events with a muon score smaller than 0.95 removes almost 90% of muon events, while keeping 98% of neutrino events.
A second classifier being trained on the remaining events has now to find finer differences between neutrinos and muons. The result of this second classifier (labeled as "muon score2") is also shown in Fig. 6.2. The muon contamination can now be reduced to a few percent, while keeping the majority of neutrinos.
Using a pre-selection on the data, as done for ORCA, would probably make the first classifier redundant, since most μ_{atm} can be easily removed by simple cuts. One could however bring up again the argument why we use machine learning in the first place - to automatise the manual search for selection criteria. Learning from this example it may be interesting to let a BDT decide which events are well enough reconstructed to be taken into account for analysis.

The example of the ν/μ_{atm} classification discussed above shows, that neither the *accuracy score* nor the *separability* are sufficient metrics for the quality of the classifier. Both would look excellent in this case, since most atmospheric muons are easily recognised by the low likelihood of their direction reconstruction and by the fact that

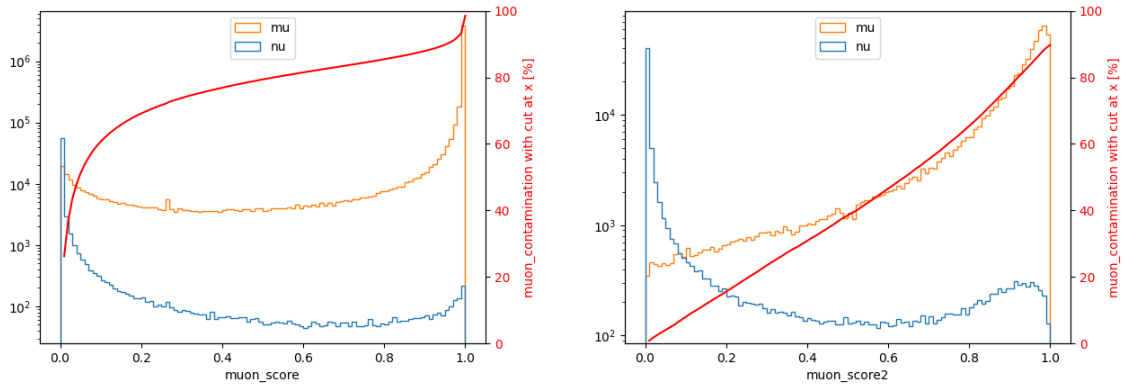

Figure 6.2: Left: Output of the ν/μ_{atm} classifier without selection cuts. The remaining muon contamination after a cut on the muon score at x is marked in red. **Right:** Output of second classifier, using the selection cut "muon score< 0.95".

no hadronic shower is observed. The goal is to reduce the muon contamination to a few percent while keeping as many neutrino events as possible. Figure 6.3 shows that a muon contamination of <5 % can be achieved while keeping ∼80 % of up-going neutrinos. Muons from down-going neutrino interactions are however barely distinguishable from atmospheric muons.

The track/shower classification turns out to be very efficient without any selection cuts or additional training features (Fig. 6.4). The plots show the same quantities as described above for ORCA.

6.5 Feature evaluation

Although improvements of the classifier could probably be achieved by technical adjustments (tree architecture, evaluation metric) its efficiency mostly depends on the parameters used for its training. For a better understanding of the features and their efficiency to distinguish event classes, the `scikit-learn` package[152] provides tools to evaluate the importance of features used to train a classifier, which I implemented in the KM3NeT framework. This is especially useful when the calculation of the training features is computing-intensive itself and could be reduced to the minimum of necessary features. By recursively training of classifiers, evaluating the feature importance and retraining with a reduced list of most efficient parameters, one can exclude features that bring no improvement to the PID. Figure 6.5 shows the separability as in equation 6.6 for such a recursive evaluation. The integer of the plot legends gives the number of used features. Although drastically reducing the features from 225 (blue) to 63 (green), the separability remains unaffected. Even another reduction by 50 % (red) still provides good separation power.

The most efficient training features require detailed technical knowledge of the reconstruction algorithm[1] and are thus not listed explicitly here. Most of them are comparisons between different steps of the algorithm or, as described in [92], are based

[1]This knowledge is even partially lost because the author of the code left the collaboration.

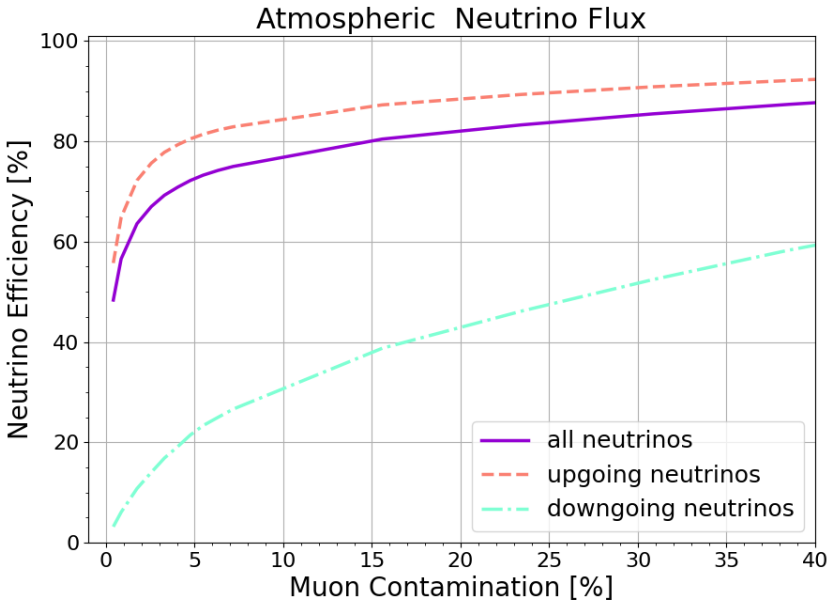

Figure 6.3: Neutrino efficiency vs. muon contamination of the ν/μ_{atm} classifier in ARCA. Since all μ_{atm} enter the detector from above, the classifier is much more efficient when only up-going events are present in the data set.

on PDFs of the expected hit distribution.

Comparison with RDF The MC for ORCA that is used for the analysis of this thesis was using `Dusj` for the shower reconstruction. The PID was created from a RDF that was trained with the SGClassifier[153] from ANTARES. The software is neither maintained nor documented and is further unpractical to handle, as it does not work directly with the format of the MC files. This was the main motivation to switch to `xgboost`, a widely used python library which is maintained and documented and provides a lot of extra functionality, as the modification of the machine learning method. The track/shower classification was improved by switching to BDTs. Also, the number of training features was reduced by ∼80 %, by removing the non-beneficial variables I identified.

Fig. 6.6 shows the comparison between BDTs (blue) and RDFs (red), and the usage of hit-based features (solid). The BDT uses only 31 training variables, where the RDF used more than two hundred. The comparison of solid and dashed lines show the increase of *separability* by adding the hit-based features, while the the improvement of the red curves respective to the blue ones origins from the change from RDF to BDT.

Since I developed the PID framework in parallel to my main analysis, I did not used it for the results I present in Part III. It showed however that the improved classifier affects the result only marginally, when only two PID classes are used (eq. 6.2). A

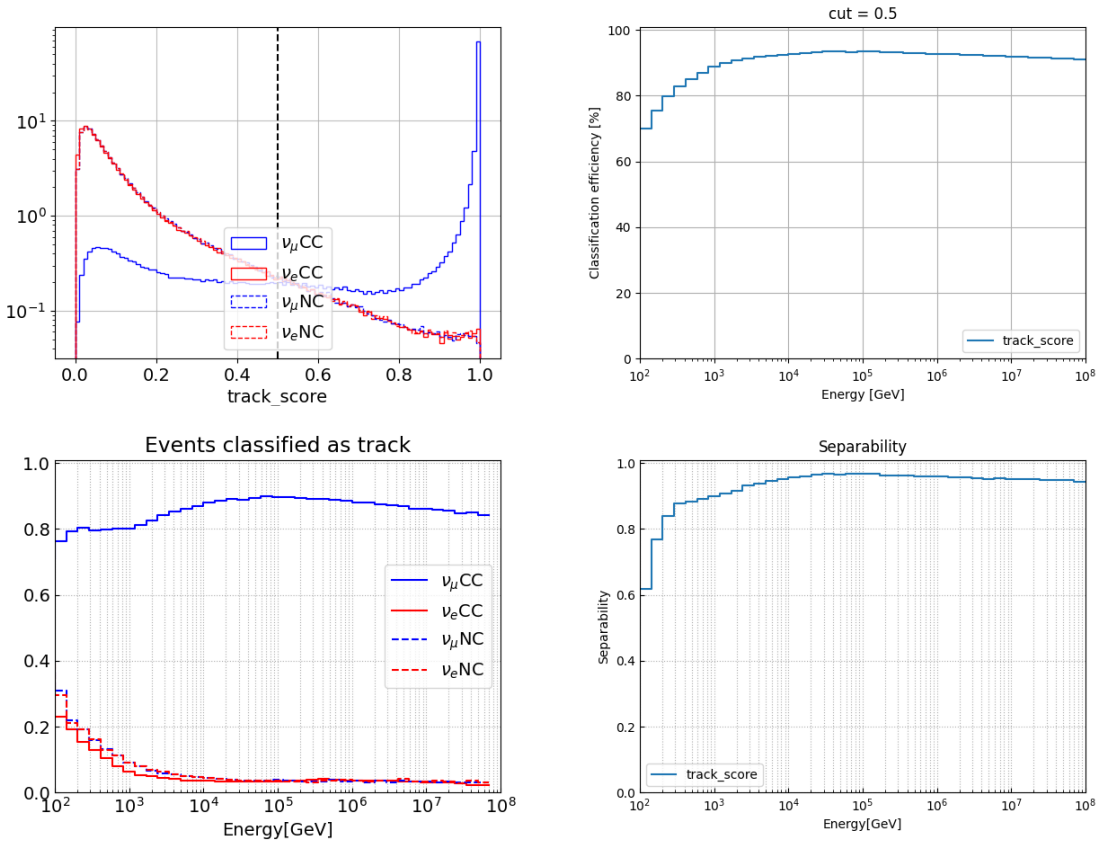

Figure 6.4: Output of the track/shower classifier for ARCA, trained with BDT. **Upper left:** Prediction score per neutrino interaction channel. Events with *track score* > 0.5 are classified as track-like. **Upper right:** Fraction of correctly classified events per energy. **Lower left:** Fraction of events classified as track. **Lower right:** Separability of $\overset{(-)}{\nu}{}_\mu^{\text{CC}}$ and $\overset{(-)}{\nu}{}_e^{\text{CC}}$-events, as defined in eq. 6.6.

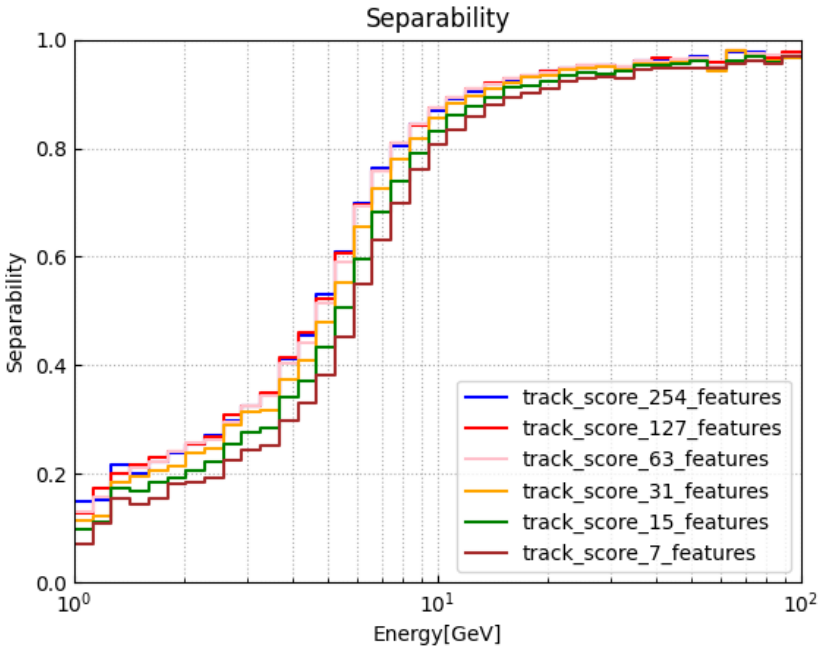

Figure 6.5: Feature evaluation of ORCA track/shower classifier. The classifier is evaluated after each training and the least important 50% of features are removed recursively. With this method one can minimise the number of necessary features while keeping its efficiency high.

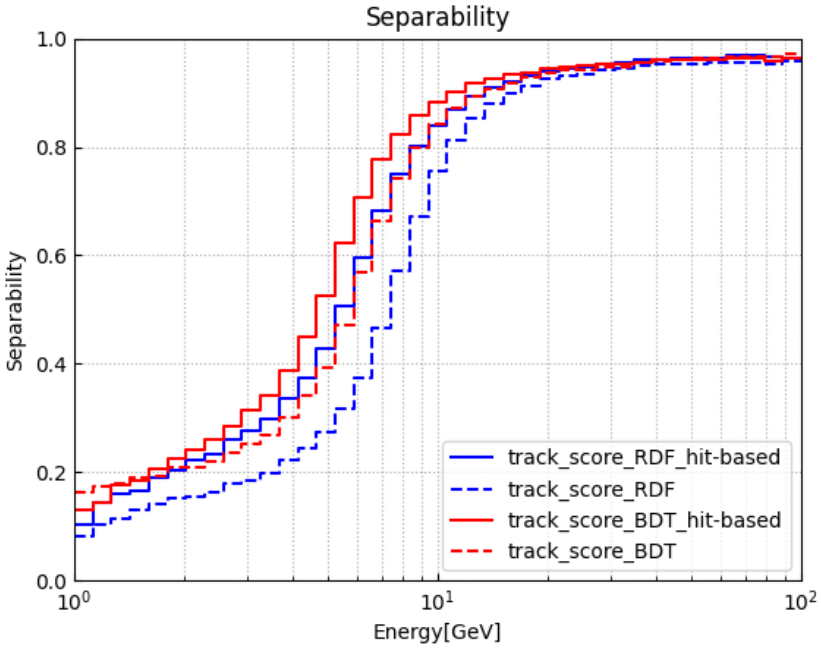

Figure 6.6: Separability of several track/shower classifiers for ORCA. The classification efficiency is significantly increased by adding the hit-based training features and additionally by training BDTs instead of an RDF.

more significant efficiency gain is emerging from the use of multiple PID classes, *e.g.*

$$\text{PID class} = \begin{cases} 1 \quad \geq & \text{track\_score} \geq 0.9 \text{ good tracks} \\ 0.9 > & \text{track\_score} \geq 0.5 \text{ bad tracks} \\ 0.5 > & \text{track\_score} \geq 0.3 \text{ bad showers} \\ 0.3 > & \text{track\_score} \geq 0 \quad \text{good showers} \end{cases} \tag{6.7}$$

which is tested in new analyses.

6.6 Development of `JShowerFit` training features

New MC simulations of ORCA sub-arrays, that are processed in parallel to the growing detector, are reconstructed with `JShowerFit` instead of `Dusj`. As a service task for the KM3NeT collaboration, I developed new training features with the aim to mimic the most important features that were based on the `Dusj` reconstruction.

Fit information `JShowerFit` goes through multiple fit steps, each of them optimised for a certain event information, *i.e.* interaction vertex position, incident neutrino direction, and neutrino energy, using the output of a previous fit step as input. At each step, all intermediate fits are saved, which enables the calculation of several training parameters. Together with the author of `JShowerFit` I implemented such features similar to those based on `Dusj`. Due to intrinsic differences between the two reconstruction algorithms, it is however not possible to reproduce the exact same training features of `Dusj` with `JShowerFit`. The most efficient features found for `JShowerFit` are the distances of the vertex positions found in different reconstruction steps, and the fraction of fits per step that found a vertex position close to the best fit.

Hit features A big amount my work related to the PID went into the development of hit-based features for `JShowerFit`. While the `Dusj` hit-PDFs were created from the reconstructed MC events, the PDFs used for the features of this extraction are taken from `JPP` and based on physical models only. This assures that no MC information is used to train – and thus wrongly improve – the classifier. Further it allows to easily calculate the hit-based features under new physical assumptions, as water properties or light yield from charged secondary particles, which could be used in future to estimate their impact on the PID.
The basic idea of the hit-based features is to compare the measured hit distribution with the hit distribution expected from the PDFs for both a shower- and a track-like hypothesis.

The so called JPDFs try to estimate the likelihood of a given event to trigger a PMT signal. The JPDF is based only on physical parameters, like light production and transmission, and technical parameters describing the light detection, like trigger efficiency of the PMT (see [154]). For each event, the triggered PMTs within a certain volume around the reconstructed vertex position are selected. For showers, the volume is a sphere with radius R, for tracks a cylinder of radius R and height corresponding to the reconstructed track length + 20 m. R is currently set to 70 m, the approximate

absorption length of Cherenkov light in water. The likelihood of detecting a photon, given an incident neutrino E_{reco}, and $\vec{dir}_{reco}$ at $\vec{pos}_{reco}$ is then calculated for each PMT in the selected volume as

$$LLR = -\ln\left(\frac{P(\text{signal + background})}{P(\text{background})}\right) \tag{6.8}$$

where the probability of detecting a photon x ns after an interaction is obtained from the PDF as

$$P(\text{PDF}, x) = \exp\left(-\int_{x_{\min}}^{x} \text{PDF}\ dx\right) \times \frac{\text{PDF}(x)}{1 - \exp(-\int_{x_{\min}}^{x_{\max}} \text{PDF}\ dx)} \tag{6.9}$$

with a time window of [-50,450] ns. The background hypothesis P(background) is calculated for a constant background rate of 7 kHz.

This is done for all 4 combinations of reconstruction (`JShower` or `JGandalf`) + geometry (sphere or cylinder). The sum of the likelihoods is then saved for all 4 cases. Additionally, the JPDFs are also evaluated for shifted vertex positions. The idea is, that a shower reconstruction is likely to fit the vertex position centered between all hits, which for a track-like event is somewhere along the muon track. The interaction vertex is thus shifted respectively by 1 m, 20 % and 40 % of the track length along the track trajectory. If the sum of the likelihoods is higher for a shifted vertex than for the actual reconstructed vertex, it is a hint that the event might actually be track-like.
The same JPDFs are also used to extract features based on no-hit information. Here one calculates the probability of being triggered (equation 6.8) either by a neutrino or a background (R=7 kHz) event for all (triggered or not) PMTs within the selected volume around the reconstructed interaction vertex to estimate the number of expected hits. Finally, the number of hits assigned to the event by the respective reconstruction, as well as the number of PMTs (in the chosen volume, respectively) are stored to the output file. The ratio of expected to actual hits may in future replace containment cuts based on the reconstructed vertex position, which have to be adapted for each detector configuration.

Result The latest ORCA MC was produced for a sub-array of 6 strings. This production was used as benchmark to test the `JShowerFit` features I developed. Fig. 6.7 shows the output of three different classifiers on the ORCA6 production: The blue benchmark curve is obtained using all developed features. Without the hit-based features the separability is only marginally worse. Removing however the fit information has a large impact, proving their classification power.

Currently the performance stated in [92] could not be achieved with the features based on `JShowerFit`. However, the underlying MC production was produced in 2019, which makes it hard to make a fair comparison to the latest production of 2022, where not only basic steps in light generation etc. were upgraded, but also the `JShowerFit` reconstruction was constantly improved.

Generally, as for all machine learning techniques, it is never obvious whether the peak performance is reached or other approaches, *e.g.* in this case more powerful features, could bring further improvement to the classification. Especially the lack of improvement from the `JShowerFit` hit-based features is worth investigating in future.

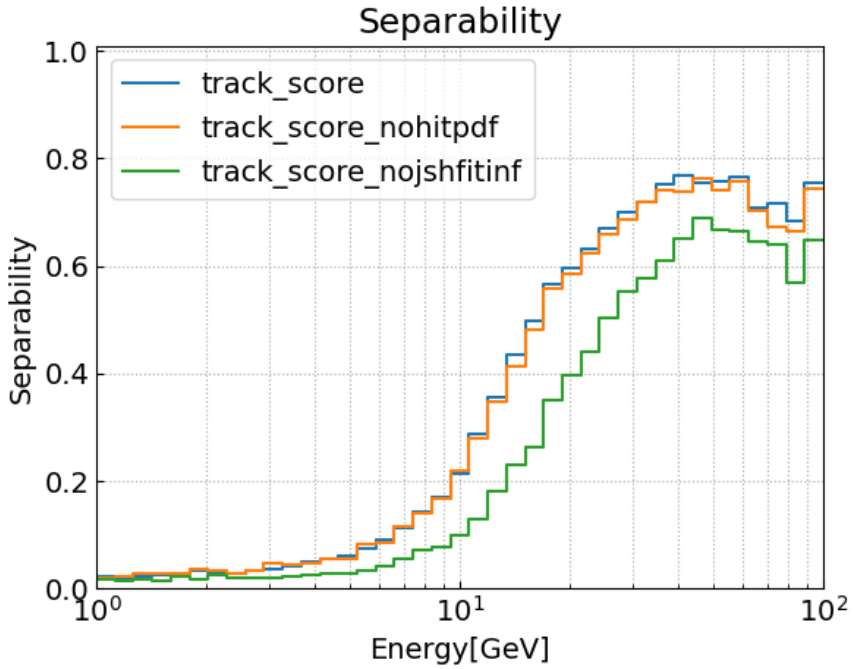

Figure 6.7: ORCA6 PID with `JShowerFit`. The blue benchmark curve is obtained using all developed features. Removing the hit-based features (orange) or the fit information (green) reduces the separability, depending on the classification power of the respective features.

However, the tools I developed provide a solid base for future work on the KM3NeT PID and are in fact already used by other collaborators[3]. They are summarized in detail in a technical internal note (Appendix B).

Chapter 7

Software/Analysis framework

Contents

This chapter covers the two software and analysis frameworks that were used to perform the studies presented in this thesis. During my time in KM3NeT I became the main responsible for maintaining these frameworks, contributing strongly to their development and usability within the collaboration. Two tomography-specific adaptations that I realized are the implementation of a fit procedure for flexible and customizable 3D Earth models, and the simulation of neutrino absorption. These functionalities are integrated in the computation of the rate of interacting events at the detector site described in sec. 7.2. The core difference between the two frameworks lies in the way the detector response is modelled: either based on MC simulations of the detector or by an approximate parameterisation of the detector properties. Both are discussed in sec. 7.3. Sec. 7.4 describes the state-of-the-art statistical methods and hypothesis tests used to compare the resulting event distributions of different simulations of experiments, in order to draw conclusions about the sensitivity to a given input model. This includes the treatment of systematic uncertainties and statistical fluctuations.

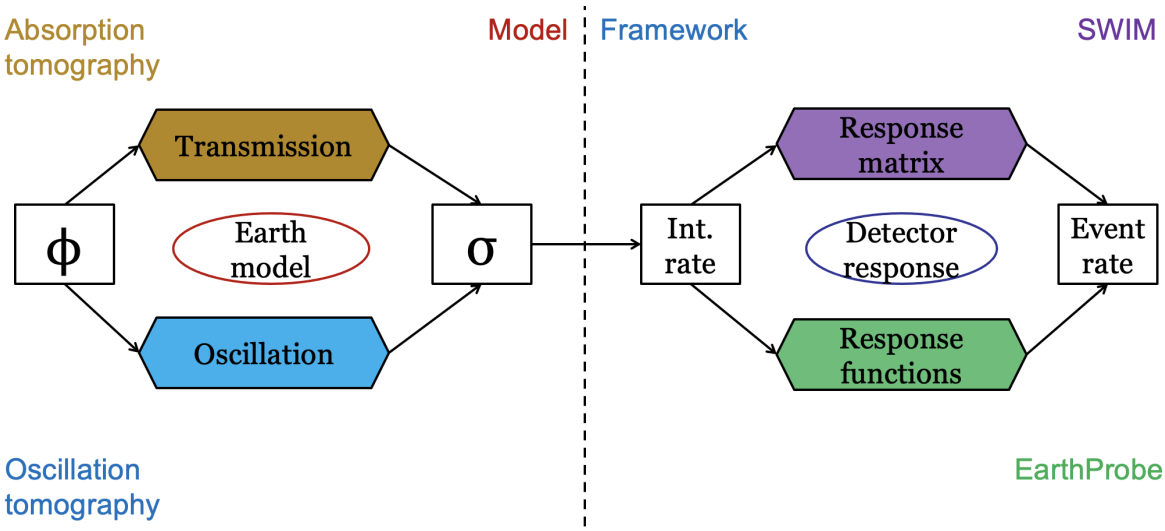

Figure 7.1: Event simulation chain for absorption and oscillation tomography. The interacting event rate at the detector site is calculated based on the input models of neutrino flux, Earth model and neutrino cross section. The detector response is simulated with parameterised response functions in `EarthProbe` or with a Monte Carlo based response matrix in `SWIM`.

7.1 Introduction

Since none of the detectors studied here (see chapter 2) is built yet, their performances have to be estimated from simulations. A sketch of the whole simulation chain is shown in Fig. 7.1. The first step consists in the calculation of the event rates at the detector site (sec. 7.2). The initial atmospheric neutrino flux is either attenuated by absorption or its flavour components are mixed by oscillation. The type and strength of the effect depends on the simulated energy range and the underlying Earth model – our parameter of interest. Finally, the oscillated/attenuated flux is only detectable if the neutrinos interact with matter at the detector site, for which the probability depends on the neutrino cross section. The rate of interacting events obtained by combining all these ingredients represents the signal that would be measured by a perfect detector. A real detector has first of all a limited size and resolution of energy and direction, but also other detector-related parameters as its size, the detection threshold and PID performance play an important role. This will eventually lead to a smearing of the interacting event distributions and has thus a major impact on the results of the experiment (sec. 7.3). During my thesis work I have explored two different approaches for the modelisation of the detector response:
One possibility is to use a MC simulation in order to mimic the detector response on a statistical basis, which is - at least in theory - the more accurate approach, since it aims at simulating all physical processes relevant for the neutrino detection and is based on the most realistic detector configuration. The second method approximates the detector resolution with parameterised functions. The flexibility allowed by this approach is especially helpful when different detector types are under investigation.

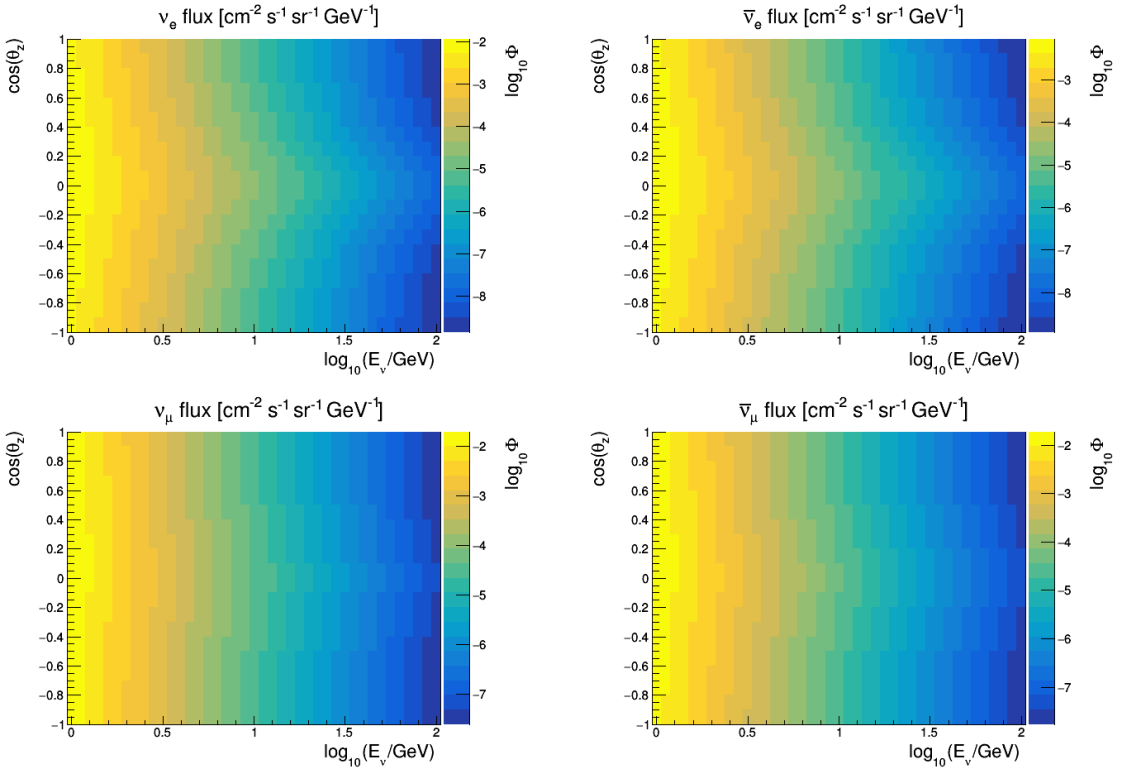

Figure 7.2: 2D Honda flux histograms as used in simulations of oscillation tomography. Data taken from [38].

7.2 From source to detector

7.2.1 Neutrino flux

The origin and properties of atmospheric neutrinos, that are used for the tomography of the Earth, were introduced in sec. 1.2. In both simulation frameworks used in this work, the initial neutrino flux is stored in 2D histograms with $\cos(\theta_z)$ on the y-axis and $\log_{10}(E_\nu)$ on the x-axis (Fig. 7.2). The neutrino flux used in all the studies presented in this manuscript is the all-year average at the Gran Sasso site (for minimum solar activity and without mountain), as calculated by the HKKM group[37].

The Honda flux tables are calculated in bins of $\cos(\theta_z)$ with a relatively coarse width of 0.1. In the simulation framework, intermediate values are interpolated from the 2D histograms. It turned out that the `ROOT` interpolation performs more accurately on logarithmic values of the flux, due to its steep decrease with energy over many orders of magnitude. Fig. 7.3 shows the interpolation of the Honda flux at $\cos(\theta_z) = -0.9$ for the whole used energy range and compares the interpolation of logarithmic and normal values. The artefacts of the interpolation, which are best visible for the ν_μ flux, disappear by using logarithmic histograms.

The choice of binning of the HKKM group is somehow unlucky for the horizontal flux. Values are only available for the bins $[-0.1, 0.0]$ and $[0.0, 0.1]$, but not for $\cos(\theta_z) = 0.0$, where the peak in the flux is located. This was already visible in Fig. 1.3, where the curve is flattened around the horizon. This is a result from the intrinsic interpolation

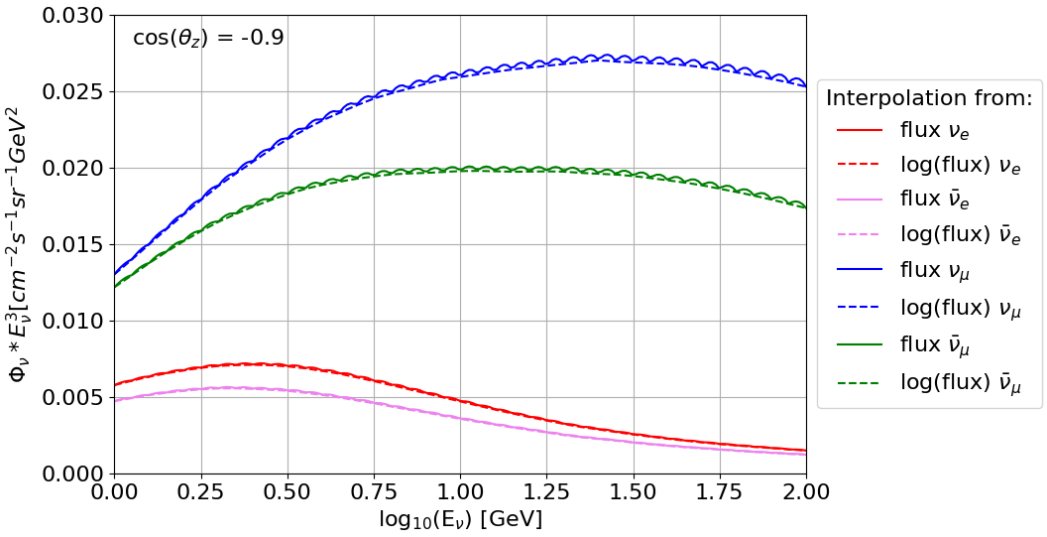

Figure 7.3: Flux interpolation from histograms with linear scale (solid lines) and logarithmic scale (dashed lines). The first case creates artefacts due to the bilinear interpolation approach used by ROOT.

technique of ROOT, which uses a bilinear approach. To visualize the effect, Fig. 7.4 shows the interpolation of the Honda values done with Python, once using a linear interpolation (as in ROOT) and once a cubic interpolation. The latter describes the flux function at the horizon in a more realistic way. However, since horizontal neutrinos play close to zero role for neutrino tomography, this has no impact on the work presented here but is just mentioned for completeness.

Absorption of neutrinos effectively takes place only above 30 TeV. The parameterisations that were used in the LoI (see Fig. 1.5), including conventional and prompt components, are used to create input histograms for the absorption tomography analysis in the same way as for oscillation tomography (Fig. 7.5). As a benchmark for the astrophysical flux, I use the latest publication from the analysis of 9.5 yr of IceCube data[155]

$$\phi^{\overleftrightarrow{\nu_\mu}}_{@100\,\mathrm{TeV}} = 1.44 \times 10^{-18} \times E^{-2.37} \tag{7.1}$$

for the energy range from 15 TeV to 5 PeV, as indicated by their paper.

7.2.2 Earth Models

Of great importance for Earth tomography is the flexibility of the underlying Earth model, which is necessary to properly account for both absorption and oscillation. As default, PREM is approximated with a radial symmetric density profile of 44 layers of constant density (as in Fig. 3.4) and Z/A, that together give the electron density according to eq. 3.8. The approximation of constant layers simplifies the calculations and was tested to be precise enough with the chosen 44 layers. As an input the framework takes a table containing radii, densities and values of Z/A to define the layers. It is thus possible to modify not only the properties but also the number of layers. This allows for an accurate replication of radial Earth models from the literature

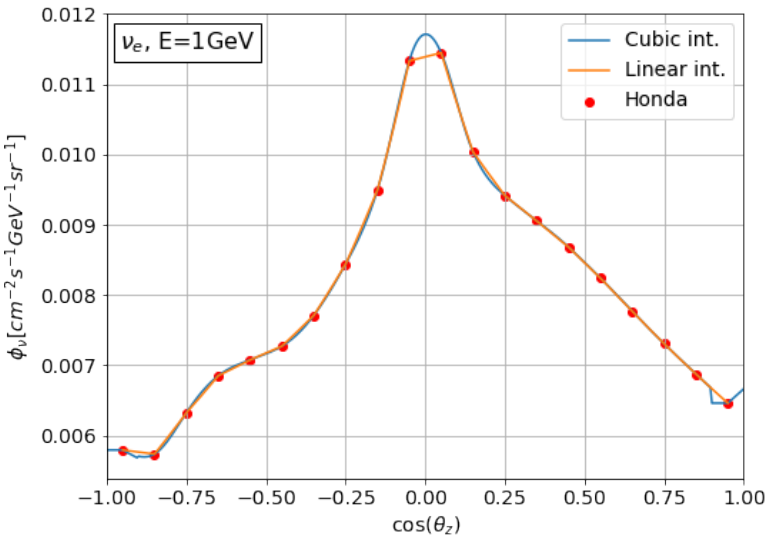

Figure 7.4: Interpolation of the data from Honda flux tables with Python using a cubic interpolation technique and a linear one as in ROOT. The expected peak at $\cos(\theta_z)$ is estimated more accurately with the cubic interpolation.

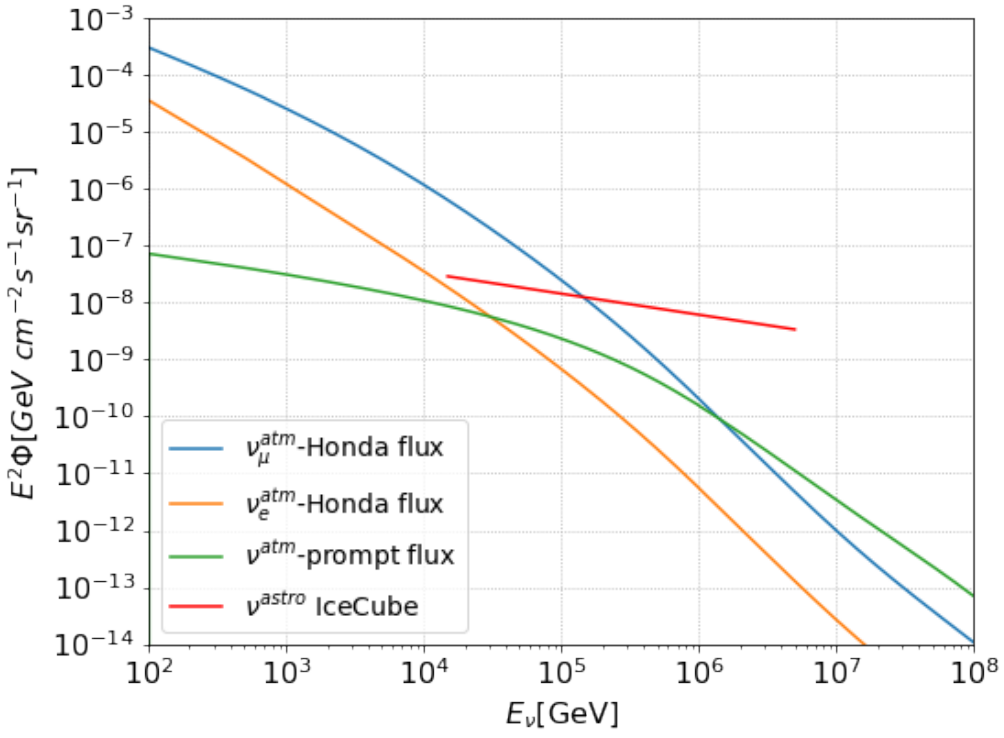

Figure 7.5: 1D fluxes used for the analysis of neutrino absorption. The atmospheric component is obtained by the same parameterisation as Fig. 1.5, namely HKKM (conventional) and Enberg (prompt). For the astrophysical flux, the latest publication of IceCube is used (eq. 7.1[87]).

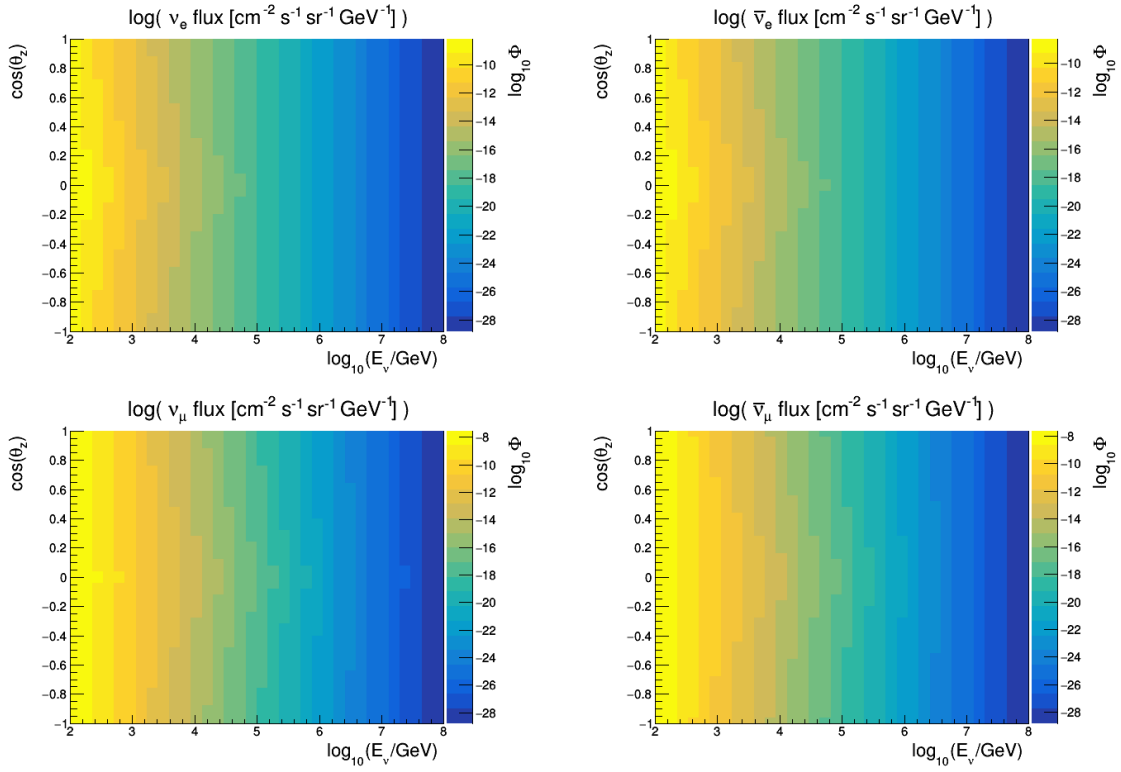

Figure 7.6: Conventional + prompt component of the atmospheric flux for $\overset{(-)}{\nu}_e$ and $\overset{(-)}{\nu}_\mu$ per cm^2, second, sr and GeV, with logarithmic colorscale. The energy range corresponds to that used in simulations of absorption tomography.

including specific layers of the Earth like *e.g.* D", but also for the simulation of possible variations of the CMB or other layer boundaries.

Once the Earth model is set, for a neutrino with energy E and incident zenith angle θ_z, the resulting baseline

$$L \simeq -2\cos(\theta_z)R_{\oplus} \tag{7.2}$$

is subdivided into n path segments of constant density ρ and Z/A, with $R_{\oplus} = 6371\,\mathrm{km}$ (Earth + water). For a radial symmetric model with N layers, a straight up-going neutrino path would consist of $n = 2N - 1$ segments, since all layers but the innermost are traversed twice. The respective intersection length l is calculated geometrically for the radially symmetric case.

The resulting vector containing the information of the path segments can then be used for the calculation of oscillation and absorption probabilities, as will be shown in the following sections.

For the study of inhomogeneities in the Earth's structure that break the radial symmetry, a new method for the calculation of the neutrino path had to be found. The geometry package `TGeoManager` of `ROOT`[156] is designed to build detector geometries, visualize them and track particles within. From a basic set of 3D geometrical objects, *e.g.* cubes, spheres and cylinders, that can be combined, rotated and translated, one can build complex shapes and geometries. An example object built with `TGeoManager` containing the Earth core, a cross section of the mantle, and an additional volume representing the inhomogeneity is shown in Fig. 7.7. It is modeled as a segment of a sphere with a thickness d and an opening angle ϕ, that is rotated by an angle Θ_L away from the detector. One can further assign custom matter densities and material mixtures to each part of the geometry, which determines the Z/A. Additionally, an object of the `TGeoManager` class can be built within milliseconds with adapted matter properties, but also geometrical parameters like size and position of hypothetical inhomogeneities, which allows for on-the-fly calculations of oscillation probabilities, and thus the fit of Earth-related parameters.

The segments of the neutrino path are derived geometrically by `TGeoManager` by testing how long a given trajectory needs to be extended until another node is reached. Contrary to the radial symmetric case, the matter distribution along the neutrino path now depends on the chosen azimuth angle, *e.g.* an inhomogeneous region would be only traversed by neutrinos coming from a certain range of azimuths. The output object has the same digital structure as in the method described above and can equivalently be used for the calculation of oscillation and absorption probabilities. This makes `TGeoManager` a practical package to study asymmetrical and complex Earth models, as it can be easily used with the existing analysis software.

7.2.3 Oscillation

The ratio of neutrino flavours at the detector site is modified with respect to the original neutrino flux due to neutrino oscillations. Within the KM3NeT collaboration, the default tool used for the calculation of oscillation probabilities for all (anti-)neutrino flavours is `OscProb`[157]. As input the neutrino path devided into n segments containing information about its length, density and Z/A is used. The default oscillation

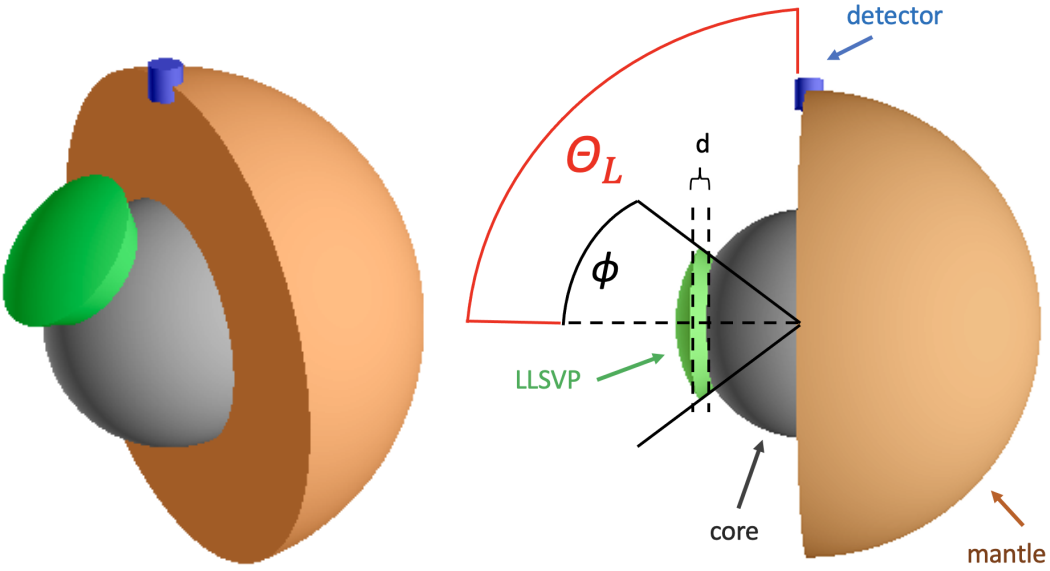

Figure 7.7: Example 3D Earth model created with the `TGeoManager` class in oblique and side view. The core (grey) and mantle (brown, cross section for visualisation) are two distinct layers with unique density and chemical composition. Same holds for the inhomogeneity (green), that can be shaped and positioned freely with the three parameters d, ϕ and Θ_L, the latter changing its relative position to the detector site (blue, enhanced).

parameters used throughout the whole thesis are taken from NuFit5.0 [55] as listed in Tab. 1.1, assuming the normal mass ordering.

`OscProb` calculates the Hamiltonian of the neutrino propagation, as described in sec. 1.3, for each of the path segments and integrates over for the final oscillation probability $P_{\text{Osc}}(\nu_l \to \nu_x)(E, \cos\theta)$ (Fig. 7.8).

It is computationally convenient to perform the calculation of all oscillation probabilities for a set of baselines once at the beginning of the simulation chain. The results are then stored in two dimensional *oscillograms* that can be used later without the need for repeating the calculation. Obviously the oscillograms have to be recalculated if the input parameters, *i.e.* oscillation parameters or the Earth model, change. Three of these oscillograms are shown in Figure 7.9, for the sake of visualisation for three extreme matter profiles: vacuum, an Earth without core, and PREM. Especially the presence of the steep CMB in PREM is visible at $\cos(\theta_{z,\text{CMB}}) \approx -0.84$.

7.2.4 Absorption

At energies above ~1 TeV oscillation effects are negligible due to the low L/E ratio. Instead, neutrino-matter interactions have to be taken into account, due to the increasing neutrino cross section. This includes mainly DIS scattering with nuclei, but also coherent scattering on nuclei, elastic/diffractive scattering on nucleons as well as interactions with shell electrons[158]. Furthermore, one has to consider scattered neutrinos from NC-interactions, which will lose energy and change their direction, or the regeneration of ν from the decay of τ's created in ν_τ^{CC} interactions.

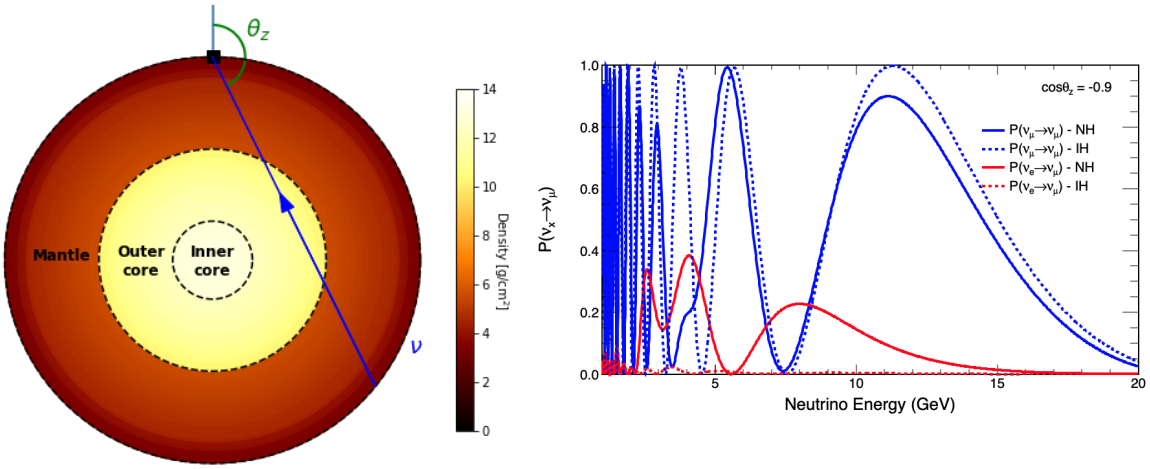

Figure 7.8: Oscillation probability $P(\nu_x \rightarrow \nu_\mu)$ calculated with `OscProb` as represented on the left panel (Normal and inverted hierarchy).

In this section, different frameworks which are able to simulate attenuation effects of neutrinos traversing the Earth are introduced and compared with each other, concerning both their physical accuracy as well as their usefulness for the planned studies of the Earth's interior.

OscProb

The simplest approach to neutrino absorption is to assume an exponential attenuation based on particle density n, neutrino cross section σ and neutrino path length L:

$$P_{\text{Trans}} = \exp(-n \cdot L \cdot \sigma) \tag{7.3}$$

where $n = \frac{\rho}{N_A}$ with the matter density ρ and the Avogadro constant N_A. P_{Trans} is used to scale down the flux, *i.e.* the number of neutrinos reaching the detector. The neutrino absorption probability is given by $P_{\text{Abs}} = 1 - P_{\text{Trans}}$.

I created an absorption class for `OscProb` in which the neutrino trajectory is again separated into path segments by one of the two methods described in sec. 7.2.2 and P_{Trans} is calculated for each of them. Similar to the oscillograms one can now plot P_{Trans} vs. θ_z and neutrino energy (Fig. 7.10).

NuPropEarth

Another framework that makes use of `TGeoManager` is `NuPropEarth`[158], partially written by members of KM3NeT to simulate neutrino propagation through the Earth. Instead of averaging the neutrino flux attenuation per layer of the Earth model, the neutrino-matter interactions are precisely simulated with `GENIE`[74]. This includes the calculation of the Lorentz vector of all decay products of the interaction. For the purpose of Earth tomography studies with neutrino absorption, it is however enough to know whether the neutrino interacts with matter or not. By simulating a large number of neutrinos propagating through the Earth, the transmission probability is equivalent to

$$P_{\text{Trans}} = \frac{\phi_{\text{out}}}{\phi_{\text{in}}} \tag{7.4}$$

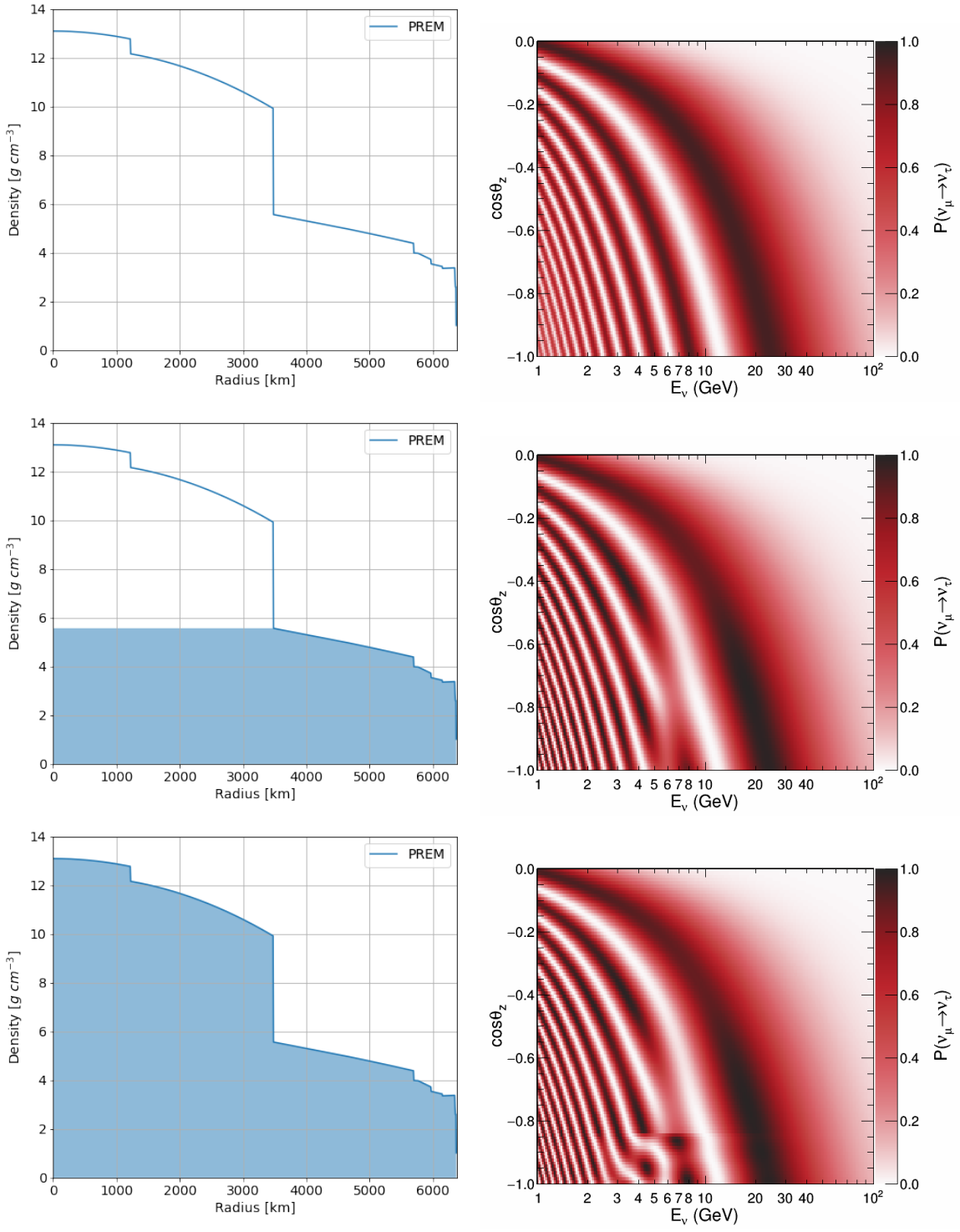

Figure 7.9: Oscillograms for $\nu_\mu \to \nu_\tau$ for vacuum (top), a coreless Earth (middle) and PREM (bottom). The matter effects become visible especially below the CMB at $\cos\theta_z \approx -0.84$.

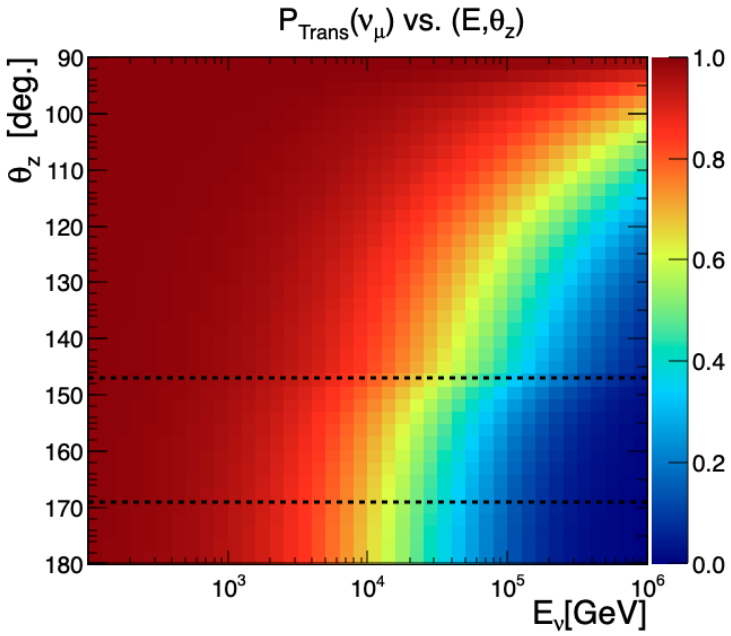

Figure 7.10: Transmission probability of a ν_μ depending on zenith angle and energy. It decreases with the neutrino energy and its pathlength through the Earth. In the energy range considered here, the transmission probability does not depend on the neutrino flavour.

where ϕ_{in} is the total number of simulated neutrinos and ϕ_{out} the number of non-interacting neutrinos.

The biggest difference between `NuPropEarth` and `OscProb` is expected to come from neutrinos that undergo a NC interaction with a nucleus, but continue propagating with a lower energy. At the energies in consideration for absorption tomography ($E_\nu \gtrsim 10\,\text{TeV}$), the scattering angle is very small ($\lesssim 0.3°$, see Fig. 7.11). However, a neutrino which is scattered at that angle *e.g.* in the Earth's core, *i.e.* $\sim 6368\,\text{km}$ away from the detector, would still be deflected enough to miss the detector by $>30\,\text{km}$. On the other hand, neutrinos that would not reach the detector regarding their original direction could be scattered towards it. Since the angular deviations in question are about an order of magnitude below the detectors angular resolution, one would not be able to distinguish between these two cases. It is thus justified to include NC scattered events into the expected event rate at the detector site, leading to an effective increase of the transmission probability.

Since `NuPropEarth` performs an explicit simulation of the neutrino propagation of the Earth, the calculation of an actual *absorbogram* like Fig. 7.10 is quite time- and CPU-expensive ($\mathcal{O}(h)$). The result is subject to statistical fluctuations, which is why a large amount of neutrinos has to be simulated ($\mathcal{O}(10^6)$ for each value of $\cos(\theta_z)$). Afterwards, the transmission probability has to be calculated from eq. 7.4 and the results have to be combined into a single 2D histogram by hand. It is thus not possible to use `NuPropEarth` for fits of Earth parameters.

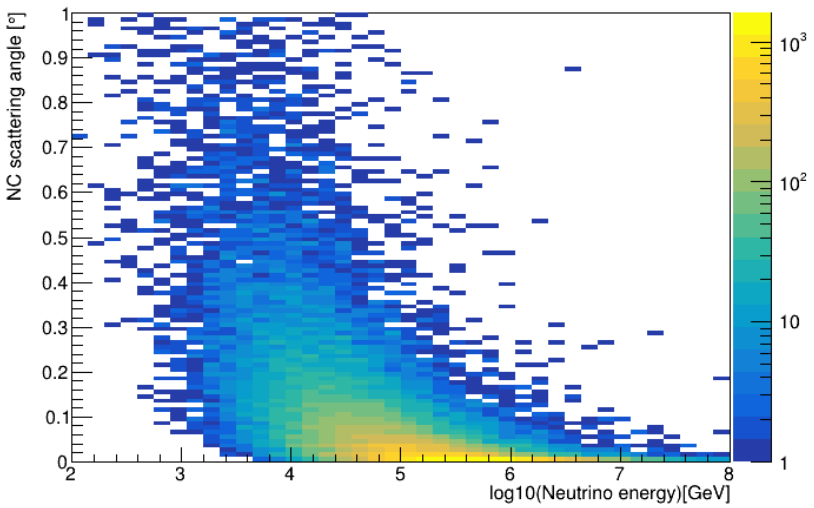

Figure 7.11: Angular deviation of NC scattered neutrinos for $\cos(\theta_z) = -0.9$ as obtained from `NuPropEarth` assuming a flux spectrum $\sim E^{-2}$. The colorscale shows the absolute number of simulated neutrinos.

NuSquids

The third framework that was considered for the simulation of neutrino absorption is ν−`SQuIDS`[159, 160], which was also used by other tomography studies in the literature [136, 130]. Similar to `OscProb`, it solves the evolution of a neutrino ensemble analytically. The advantage of ν−`SQuIDS` is that instead of solving the Schrödinger equation (1.10) it can solve the quantum Boltzmann equation

$$\frac{\delta\hat{\psi}_i}{\delta x} = i[H, \hat{\psi}_i] + A, \hat{\psi}_i + O(\hat{\psi}_i, \hat{\psi}_J) \tag{7.5}$$

where $\hat{\psi}_i$ represents the neutrino state at $E_\nu = E_i$, H is the Hamiltonian, A is a non-unitary operator, and O is an operator that contains the interactions between neutrino states of energies E_i and E_j. This includes effects of neutrino-matter interactions and especially the regeneration of NC-scattered neutrinos (and ν from τ-decay)[161]. It is hence expected, that ν−`SQuIDS` performs very similar as `NuPropEarth`. The analytical method of ν−`SQuIDS` is however much faster than `NuPropEarth` and in fact comparable to `OscProb`.

The underlying Earth model of ν−`SQuIDS` is similar to the original `OscProb` implementation - spherically-symmetric concentric shells with user-defined radii and matter properties. It is in principle possible, to implement `TGeoManager` into ν−`SQuIDS`, although this would require the inclusion of `ROOT`.

Comparison of absorption frameworks

Fig. 7.12 shows the comparison of the respective frameworks for two different values of $\cos(\theta_z)$ and a neutrino flux $\phi \sim E^{-2}$. No ν-recreation from ν_τ^{CC}-events are taken

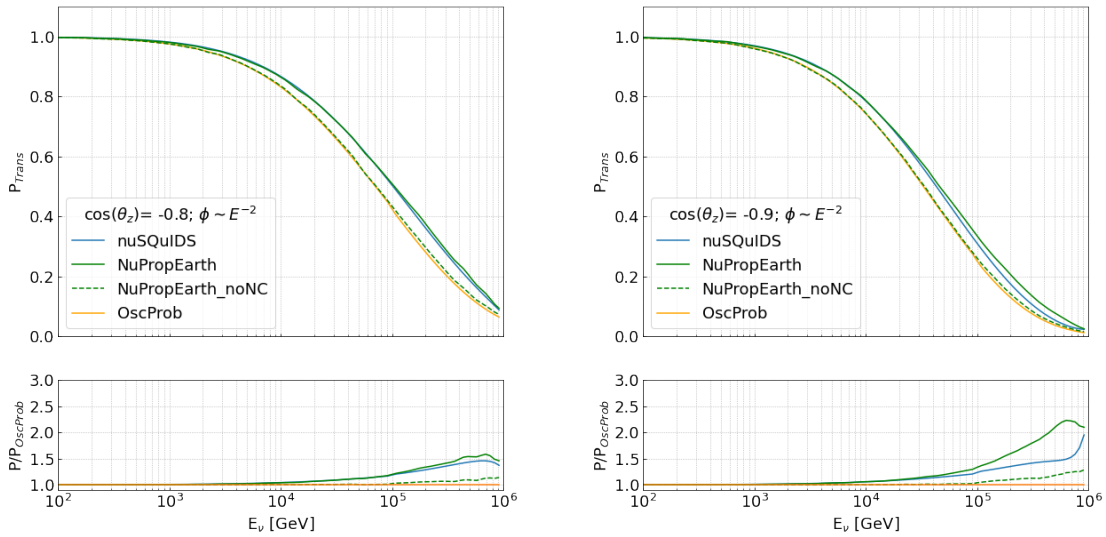

Figure 7.12: Transmission probability calculated with different frameworks, at $\cos(\theta_z) = -0.8$ (left) and -0.9 (right) and a neutrino flux $\phi \sim E^{-2}$. The bottom panel shows the relative deviation to the exponential attenuation (`OscProb`, eq. 7.3). When excluding NC scattered neutrinos, `NuPropEarth` and `OscProb` are in great agreement. `NuPropEarth` and ν−`SQuIDS`show similar results, depending on $\cos(\theta_z)$.

into account[1]. The transmission probability was calculated for the two cases with `NuPropEarth`, with (solid) and without (dashed) NC-scattered neutrinos. Without taking into account NC-scattered neutrinos, `NuPropEarth` and `OscProb` show very similar results, while the inclusion of NC scattered events increases the transmission probability, since neutrinos can reach the detector even after an interaction. The additional events per energy bin are indeed events from higher energy bins, shifted down due to the energy loss from the NC scattering. The effect therefore increases with higher energies and consequently higher NC cross sections, as seen in the lower panel of Fig. 7.12, but also decreases again when the cross section reaches values where no neutrino reaches the detector at all. `NuPropEarth` and ν−`SQuIDS` show very good agreement for $\cos(\theta) = -0.8$ but diverge at higher energies for $\cos(\theta) = -0.9$.

Next to the physical precision of the different frameworks, their functionality in combination with our analysis framework has to be taken into account. All frameworks are able to create a 2D histogram of transmission probabilities, which can be simply read by the analysis software and included into the calculation of the interacting event rate. For `NuPropEarth` however, each adjustment of Earth related parameters would take hours of computing time, making it impractical for the use of Earth tomography. Complex Earth models on the other hand can so far not be handled with ν−`SQuIDS`. Finally, I decided to keep using `OscProb`, although it does currently not include NC-

[1]From Fig. 4.1 in [158] it can be assumed that τ-regeneration has a non-negligible impact on the transmission probabilities of ν_τ. The effect has nevertheless not be studied here, as due to technical limitations, which are discussed in chapter 8, the contribution of ν_τ can only simulated to a limited extent in our framework for ARCA.

	Computing time	Adaptive Earth model	NC-scattering & τ-regeneration
`OscProb`	$\mathcal{O}$(ms)	✓	to implement
`NuPropEarth`	$\mathcal{O}$(h)	✓	✓
ν−`SQuIDS`	$\mathcal{O}$(ms)	to implement	✓

Table 7.1: Comparison of functionality of absorption frameworks. Criteria are the calculation speed (needed for fitting), the complexity of the underlying Earth model (*i.e.* the possibility to analyse inhomogeneities) and the treatment of neutrinos from NC-scattering and τ-regeneration.

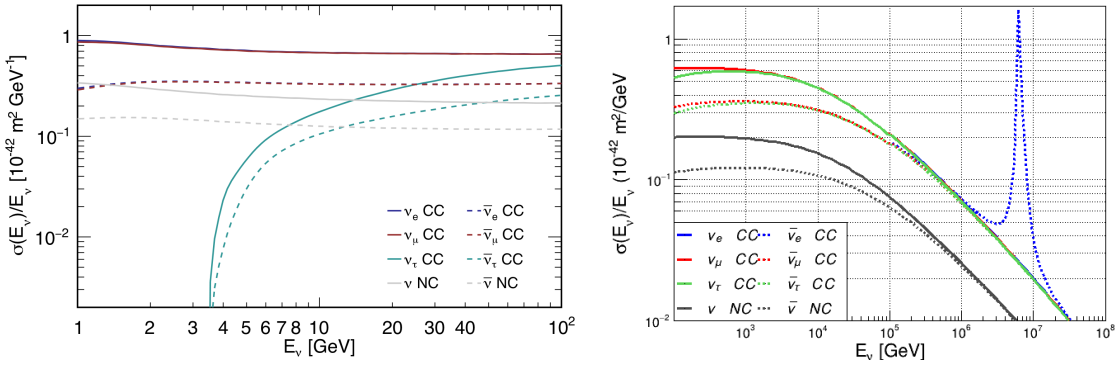

Figure 7.13: Total neutrino cross section for scattering off water, in the energy ranges relevant for neutrino oscillation tomogrpahy (left, from [162]) and absorption tomography (right) and per interaction channel. Calculated from `GENIE` table GHE19_00b[74].

scattered neutrino events and τ-recreation and is thus underestimating the transmission probability.

7.2.5 Cross section models

Following eq. 1.44 the differential neutrino cross section is calculated as

$$\frac{d\sigma_\nu}{dy}(E, y) = \sigma(E_\nu) \times P_E(y) \tag{7.6}$$

where $\sigma(E)$ is the total cross section and $P_E(y)$ a normalised probability distribution for an interaction inelasticity y for a neutrino with energy E_ν. The total cross sections are interpolated from graphs (Fig. 7.13) that are derived by data from `GENIE`[74] by calculating the weighted sum of cross sections for a hydrogen and oxygen target

$$\sigma = \frac{2\sigma(^1_1\mathrm{H}) + \sigma(^{16}_8\mathrm{O})}{18}. \tag{7.7}$$

The Bjorken-y distribution can either be interpolated according to Fig. 1.10 or taken from the ORCA MC simulation (Fig. 7.14). Although implemented, the Bjorken-y dependency on the cross section is not used in the presented analysis. As we will discuss in sec. 7.4, only one bin is used for the Bjorken-y, which means that effectively only the total cross section is used.

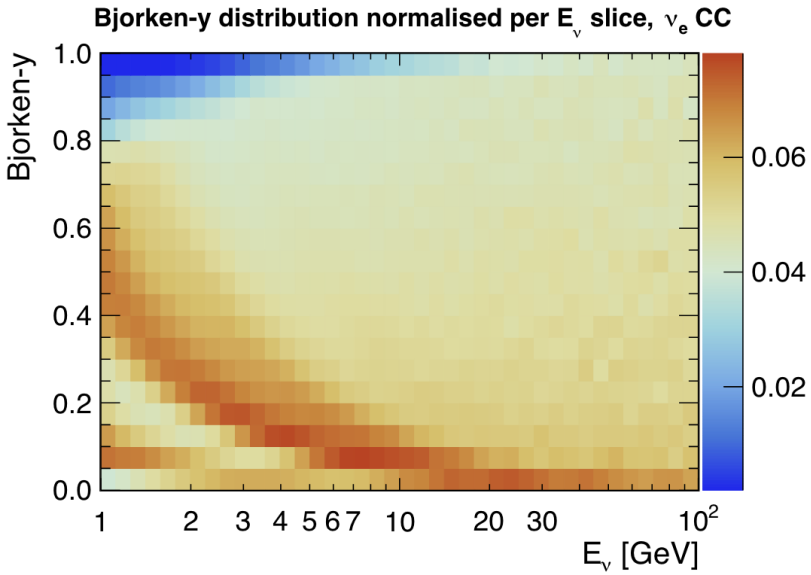

Figure 7.14: Bjorken y distribution of ORCA MC. Figure taken from [162].

7.2.6 Interacting event rates

Folding the initial neutrino flux with the probability of oscillation or absorption and with the interaction cross section, one obtains the differential rate of interacting events per unit exposure (product of the target mass M and detection time t) for each flavor:

$$\frac{\mathrm{d}^2 N_\alpha^{\mathrm{int}}}{\mathrm{d}M\mathrm{d}t}(E,\theta_z) = \sum_{\beta=e,\mu} 2\pi \cdot \Delta E \cdot \Delta\theta_z \frac{\mathrm{d}^2\Phi_{\nu_\beta}}{\mathrm{d}E\mathrm{d}\theta_z}(E,\theta_z)\cdot \\ P_{\mathrm{Osc}}(\nu_\beta \to \nu_\alpha)(E,\theta_z)\cdot P_{\mathrm{Trans}}(E,\theta_z)\cdot \frac{\sigma_{\nu_\alpha}^{\mathrm{int}}(E)}{m_N} \tag{7.8}$$

where β denotes the initial neutrino flavour and α its final state $\nu_{\alpha,\beta} \in \{\overset{(-)}{\nu}_{e,\mu,\tau}\}$. ΔE and $\Delta\theta_z$ are the respective bin widths of energy and zenith angle, the factor 2π comes from the integration over the whole azimuth range. To save computation time, the approximations

$$P_{\mathrm{Osc}}(\nu_\beta \to \nu_\alpha) = \delta_{\alpha\beta}; \qquad E_\nu > 100\,\mathrm{GeV}$$
$$P_{\mathrm{Trans}} = 1; \qquad E_\nu < 100\,\mathrm{GeV}$$

are used. Note that P_{Trans} intrinsically depends on the cross section of the inital state (σ_{ν_β}) while the explicit cross section ($\sigma_{\nu_\alpha}^{\mathrm{int}}$) corresponds to the oscillated state. In theory the oscillation could also have an effect on the absorption probability during the propagation trough the Earth. Since the energy ranges where oscillation and absorption effects are visible do not overlap, here either oscillation or absorption is used at one time.

The resulting 2D histograms for the interacting event rates in the range from 1 GeV to 100 GeV are shown in Fig. 7.15. The oscillation patterns are clearly visible for upgoing neutrinos. ν_τ only appear for energies greater than 3.35 GeV($\approx 2m_\tau$). Note the different color scales, that approximately fit the expectations for the ratio of the unoscillated flux $\nu_e : \nu_\mu : \nu_\tau = 1 : 2 : 0$.

From 10^2 GeV to 10^8 GeV the interaction rates are shown in Fig. 7.16, for better visualisation in logarithmic scale. The effect of neutrino absorption is slightly visible by comparing straight up- and straight downgoing neutrinos at the highest energy bins.

7.3 Modeling of detector response

In this part of the simulation we model the experiments ability to reconstruct the true characteristics $\mathbf{x}$ of a neutrino event in the way

$$N_{\text{reco}}(\mathbf{x'}) = \sum_{\mathbf{x}} f(\mathbf{x}, \mathbf{x'}) \times N_{\text{int}}(\mathbf{x}) \ , \tag{7.9}$$

where $\mathbf{x'}$ denotes the reconstructed event characteristics, *i.e.* the energy E_{reco} and the zenith angle θ_z, and f the projection between truth and reconstruction, that can be interpreted as a probability to reconstruct $\mathbf{x'}$ from $\mathbf{x}$. In this work two different approaches for the definition of f were used, which are discussed below.

7.3.1 MC based detector response

A first approach (historically developed by a former PhD student at APC[162]), is to define the detector response in form of a multi-dimensional matrix, filled only by the output of a MC simulation. The motivation, implementation and functionality of this so called *response matrix* R is described in great detail in [162] and is briefly summarised here.

The response matrix has to contain information about the probability of a neutrino with any energy E, direction θ and interaction channel ν_x (flavour, CC/NC) to be reconstructed with E_{reco}, θ_{reco} and classification channel i. Such a probability can be expressed by the ratio of MC events that are selected for the final analysis to the total number of generated MC events in the corresponding 'true' bin, by[2]

$$R^{[\nu_x \to i]}(E, \theta, E_{\text{reco}}, \theta_{\text{reco}}) = \frac{N_{\text{sel}}^{\text{MC}}[\nu_x \to i](E, \theta, E_{\text{reco}}, \theta_{\text{reco}})}{N_{\text{gen}}^{\text{MC}}[\nu_x](E, \theta)} \ . \tag{7.10}$$

One consequently gets one 4-dimensional response matrix for each classification channel. In reality R has the form of a 5-dimensional `THnSparse` matrix from `ROOT`, where the additional dimension holds the flag F, a discrete integer from the bijective projection $[\nu_x \to i] \leftrightarrow F$. In this work, only a track and shower class were used, but the design of the response matrix allows the definition of more than two PID classes, *e.g.* as in [92] where a 'middle' class is defined.

Since the generation volume V_{gen} in the MC, and thus the number of generated neutrinos, is an arbitrary choice (V_{can} in sec. 5.1), for the proper event weighting a scaling for the reference mass M_{ref} has to be applied. For that we choose a reference volume $V_{\text{ref}} \leq V_{\text{gen}}$, in which the event generation is uniform for all neutrino flavours. $N_{\text{gen}}^{\text{MC}}$ are only drawn from V_{ref}, whose mass is given by

$$M_{\text{ref}} = \rho_{\text{water}} \times V_{\text{ref}}. \tag{7.11}$$

[2]Note that in comparison to [162] the Bjorken-y is not explicitly mentioned here, as only one bin is used in that dimension.

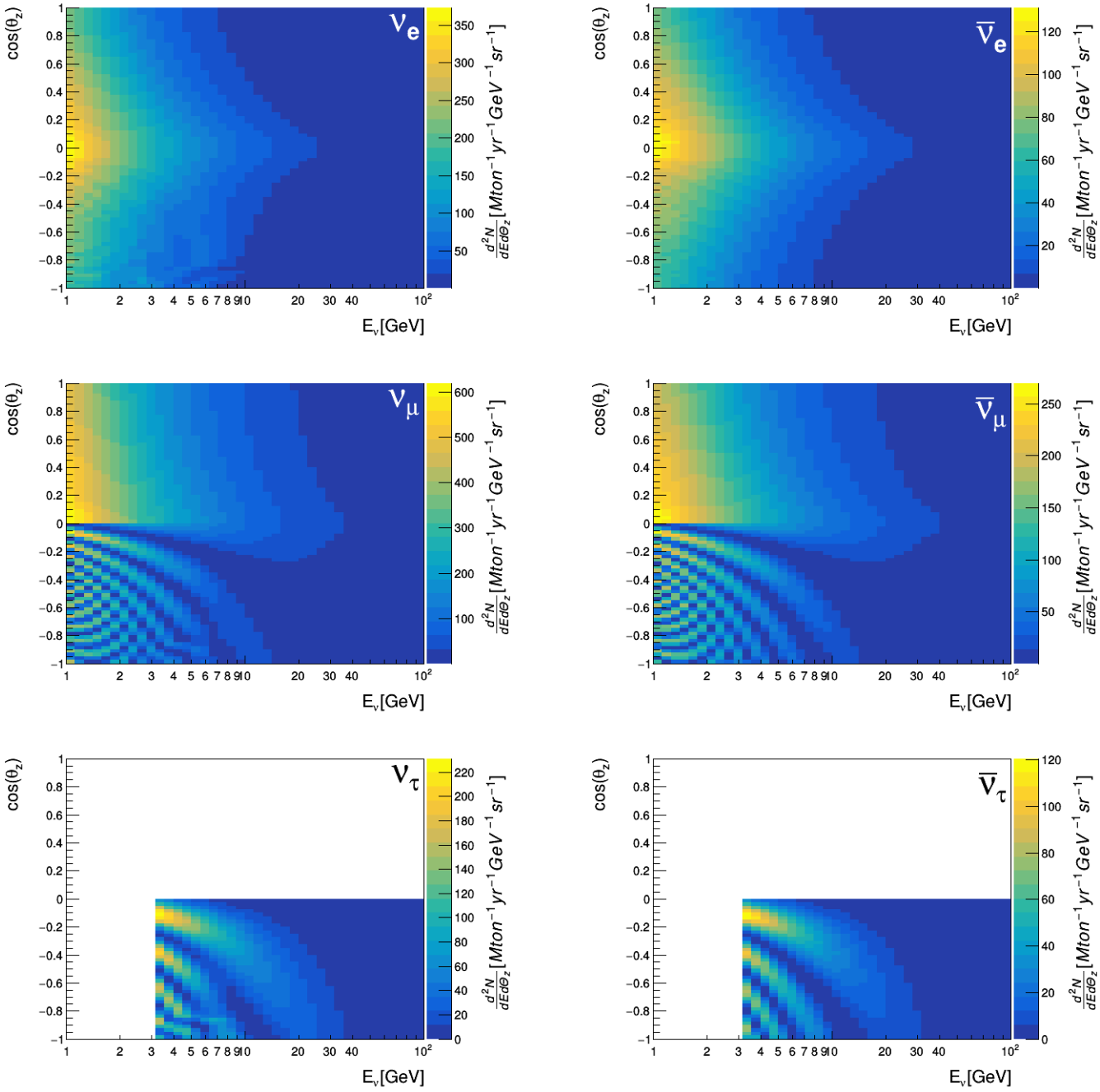

Figure 7.15: Interaction rates from 1 GeV to 100 GeV per Mton-yr, GeV and sr for $\overset{(-)}{\nu}_e$, $\overset{(-)}{\nu}_\mu$ and $\overset{(-)}{\nu}_\tau$.

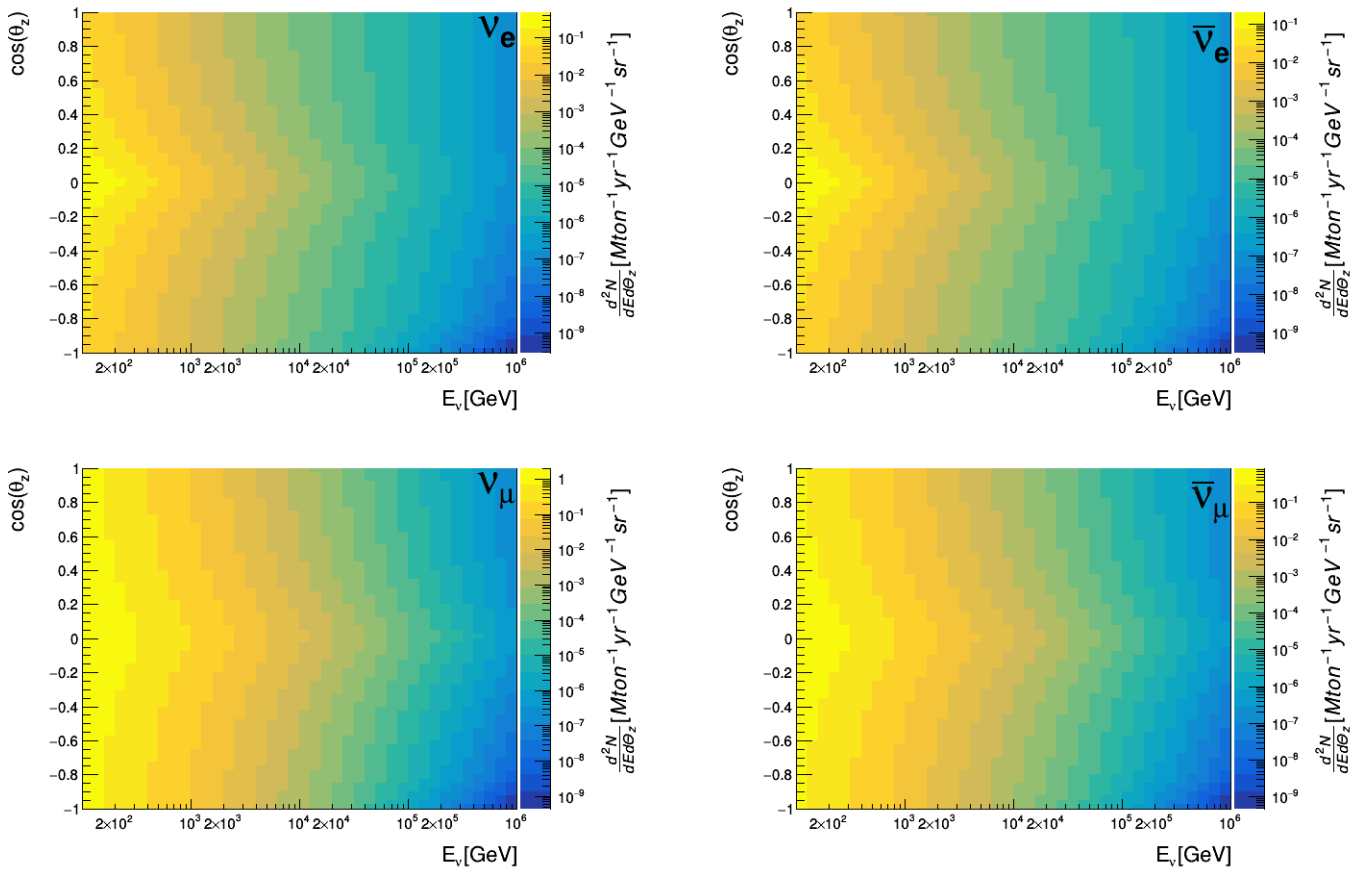

Figure 7.16: Interaction rates from 10^2 GeV to 10^8 GeV per Mton-yr, GeV and sr for $\overset{(-)}{\nu}_e$ and $\overset{(-)}{\nu}_\mu$.

The simulated event distributions are then obtained based on the MC response as

$$N^{[i]}_{\text{reco}}(E_{\text{reco}}, \theta_{\text{reco}}) = \sum_{\nu_x} \sum_{E,\theta} R^{[\nu_x \to i]}(E, \theta, E_{\text{reco}}, \theta_{\text{reco}}) \times M_{\text{ref}} \times N^{\nu_x}_{\text{int}}(E, \theta) \tag{7.12}$$

with $N^{\text{int}}_{\nu_x}(E, \theta)$ being the interacting event rates per unit exposure in the interaction channel ν_x, according to eq. 7.8.

For a better physical intuition about the response matrix, its correspondence to the event smearing and classification and the effective detection mass is pointed out now. These quantities will also be used in the parameterised detector modelling of sec. 7.3.2

Event smearing and classification

The classification efficiency defined as

$$\varepsilon^{[\nu_x \to i]}_{\text{class}}(E, \theta) = \sum_{E_{\text{reco}}, \theta_{\text{reco}}} R^{[\nu_x \to i]}(E, \theta, E_{\text{reco}}, \theta_{\text{reco}}) \tag{7.13}$$

describes the probability for a ν_x event to be selected and classified into one of the defined PID classes. Further, the probability of a selected and classified event with true E, θ to be reconstructed with $E_{\text{reco}}, \theta_{\text{reco}}$

$$p^{[\nu_x \to i]}_{\text{reco}}(E, \theta, E_{\text{reco}}, \theta_{\text{reco}}) = \frac{R^{[\nu_x \to i]}(E, \theta, E_{\text{reco}}, \theta_{\text{reco}})}{\varepsilon^{[\nu_x \to i]}_{\text{class}}(E, \theta)} \tag{7.14}$$

serves as PDF for the smearing of the true interacting event histograms (see examples for ORCA and ARCA in Fig. 7.17 & 7.18). For a reliable analysis it is crucial to keep the sparseness of the response matrix due to limited MC statistics in mind and adapt the binning accordingly[3]. The choice of the binning used during this analysis is further discussed in section 7.4.

Effective detection mass

The amount of data collected by a neutrino detector is connected to its volume V. However, not all events that take place inside the detector are actually detected. One thus characterises a detector by its effective volume

$$V_{\text{eff}} = V \times \varepsilon_{\mathbf{det}} \ . \tag{7.15}$$

The detection efficiency $\varepsilon_{\mathbf{det}}$ typically scales with the amount of produced Cherenkov light and thus with the neutrino energy. In our MC based response, the detection efficiency for a given neutrino interaction channel ν_x is defined as

$$\varepsilon^{\nu_x}_{\mathbf{det}}(E, \theta) = \sum_i \frac{N^{\text{MC}}_{\text{sel}}[\nu_x \to i](E, \theta)}{N^{\text{MC}}_{\text{gen}}(E, \theta)} \tag{7.16}$$

[3]Methods for an artificial smearing of the response PDFs have been discussed in [162] but were not used during the scope of this thesis.

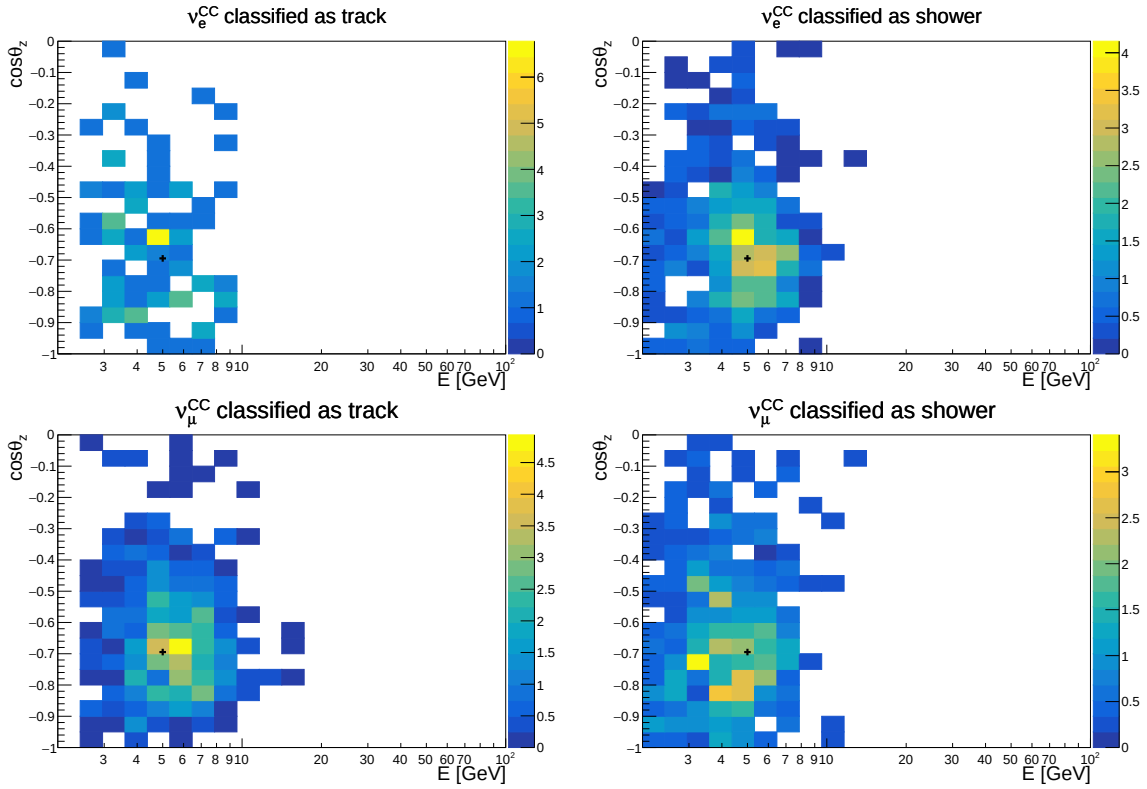

Figure 7.17: 2D response PDF $p_{\text{reco}}^{[\nu_x \to i]}$ (in %) based on the ORCA MC simulation, for ν_e/ν_μ-CC events and two PID classes. The true energy (E=5 GeV) and direction (θ_z=134°) is marked with a black cross on each plot.

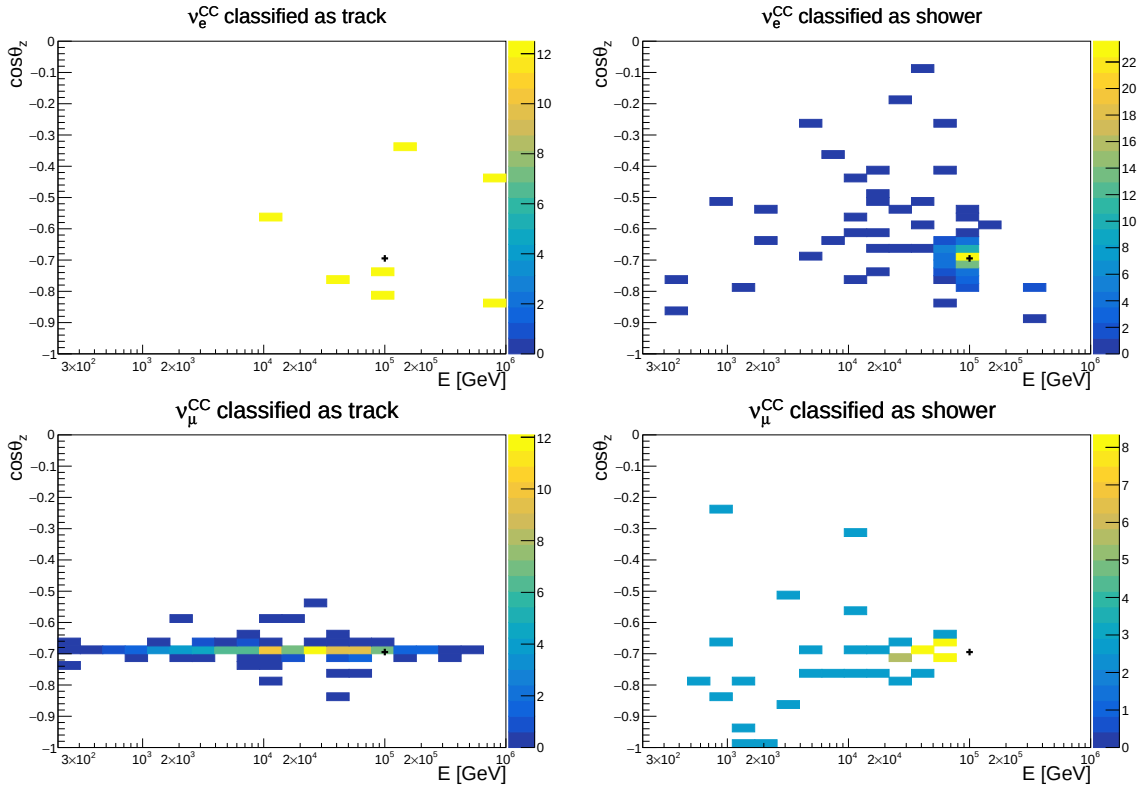

Figure 7.18: 2D response PDF $p_{\text{reco}}^{[\nu_x \to i]}$ (in %) based on the ARCA MC simulation, for ν_e/ν_μ-CC events and two PID classes. The true energy (E=10^5 GeV) and direction (θ_z=134°) is marked with a black cross on each plot.

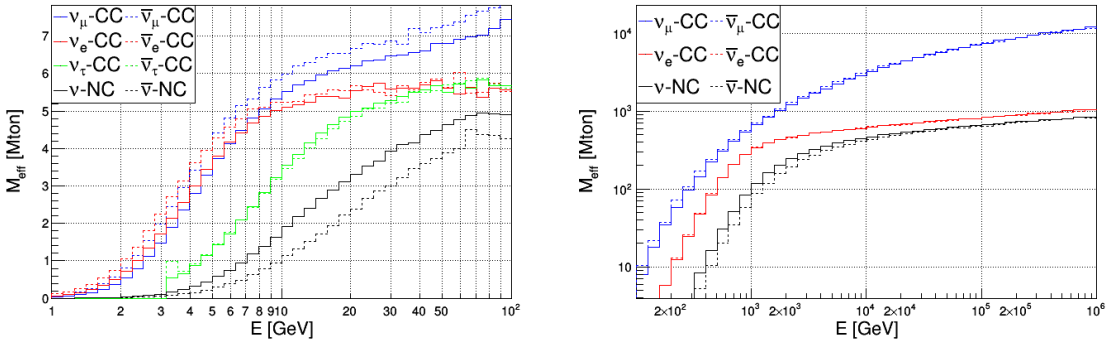

Figure 7.19: Effective mass of ORCA(left) and ARCA(right), computed from the response matrix (eq. 7.17).

Usually one does not refer to the effective volume, but to the effective mass

$$M_{\text{eff}}^{\nu_x}(E,\theta) = M_{\text{ref}} \times \varepsilon_{\mathbf{det}}^{\nu_x}(E,\theta). \tag{7.17}$$

Note here that the generated events are drawn from within the reference volume V_{ref} defined above, but the number of selected events is independent of the chosen reference volume, from which follows that the $\varepsilon_{\mathbf{det}}^{\nu_x}(E,\theta)$ can be greater than 1. This means that for whatever choice of V_{ref}, M_{eff} will be scaled correctly to account also for events that are generated outside of V_{ref}, but nevertheless are selected. This shows nicely in the effective mass of $\overset{(-)}{\nu}{}_{\mu}^{\text{CC}}$events in Fig. 7.19, that is constantly growing even after reaching the saturation energy of the other interaction channels, due to the prolonged muon tracks.

7.3.2 Parameterised detector response

During this thesis, a main aspect of the analysis was to test what type of neutrino detector will be the most sensitive to Earth parameters. The caveat of the MC-based model of a detector response is first of all the limited access to simulation data of other experiments and second the lack of flexibility.

The comparison of different detectors requires a more practical approach, which is easily adaptable to new detectors. This is challenging, as detection techniques and analysis techniques can differ fundamentally between different experiments. A fair comparison has to be based on a common ground without oversimplifying the actual performances. In this work we are modelling neutrino detectors by the following core attributes (plotted in Fig. 7.20):

- The **effective mass** $M_{\text{eff}}(E)$ is the product of the instrumented target mass M of the detector and its detection efficiency, *i.e.* the probability for a neutrino interaction to be successfully detected as an event. M_{eff} typically increases with the neutrino energy, until reaching a plateau that saturates approximately at the instrumented mass of the detector. We have conservatively neglected here a potential increase in M_{eff} for $\overset{(-)}{\nu}{}_{\mu}^{\text{CC}}$events at high energies, corresponding to through-going muons created in neutrino interactions outside of the detector

Detector	M (Mton)	E_{th} (GeV)	E_{pl} (GeV)	$\sigma(E)/E$	σ_θ (deg)	E_{th}^{class} (GeV)	E_{pl}^{class} (GeV)	P_{max}^{class}
ORCA-like	8	2	10	25%	$30/\sqrt{E}$	2	10	85%
HyperKamiokande-like	0.40	0.1	0.2	15%	$15/\sqrt{E}$	0.1	0.2	99%
DUNE-like	0.04	0.1	0.2	5%	5	0.1	0.2	99%
Next-Generation	10	0.5	1.0	$5\% + 10\%/\sqrt{E}$	$2 + 10/\sqrt{E}$	0.5	1	99%

Table 7.2: Inputs for the response functions of the detectors considered in this study: total target mass; threshold and plateau energy for the detection efficiency curve; energy and zenith resolutions; threshold and plateau energy for the classification efficiency curve; maximal classification probability achievable.

target volume. The threshold for detection is mainly driven by the density (and intrinsic efficiency) of sensors. We approximate $M_{\text{eff}}(E)$ by a sigmoid function of $\log(E)$ with two adjustable parameters E_{th} and E_{pl}, which correspond to energies where the detection efficiency reaches 1 % and 99 %, respectively.

- The **energy resolution** parameterises the relative error on the reconstructed neutrino energy in the form of a Gaussian probability density function (PDF) with energy-dependent width: $\sigma_E(E)/E = A_E + B_E/\sqrt{E}$.

- The **angular resolution** parameterises the error on the measured zenith angle in the form of a von Mises-Fisher PDF on a sphere[163] marginalized with respect to azimuth. For water Cherenkov detectors we take into account the dependence of σ_θ on the energy as $\sigma_\theta(E) = A_\theta + B_\theta\sqrt{E}$.

- The **classification efficiency** $\varepsilon_{\textbf{class}}(E)$ describes the probability for a neutrino event of energy E to be correctly classified into one of the topological channels observable by the detector. We model it with a sigmoid as a function of $\log(E)$ with adjustable threshold (E_{th}^{class}) and plateau (E_{pl}^{class}) energies, maximal identification probability P_{max}^{class} and minimum probability of 50 %. With only one classification efficiency, we can only model 2 PID classes, *i.e.* track and shower. This classification is done by all oscillation experiments with the goal to identify the flavour of the detected neutrino based on the event signature and is thus suited for a comparison between the investigated detectors.

For absorption tomography, due to the low flux of TeV to PeV neutrinos, the only detectors currently feasible are water Cherenkov detectors with huge instrumented volumes, and thus similar performances. Regarding this lack of alternative detectors for absorption tomography, the study of different detector layouts is restrained only to oscillation tomography. Among the neutrino detectors that are principally able to perform oscillation tomography by the detection of GeV atmospheric neutrinos, we chose to analyse ORCA, HyperKamiokande and DUNE. The parameters related to their respective response functions are listed in Tab. 7.2. The entry Next-Generation refers to a hypothetical neutrino detector that may be built in the future. For now, the reader can imagine a detector that overcomes the trade-off between detector size and resolution and combines best of both worlds. Concepts on the potential design of such a NextGen detector, and a motivation for the values listed here are discussed in detail in chapter 10.

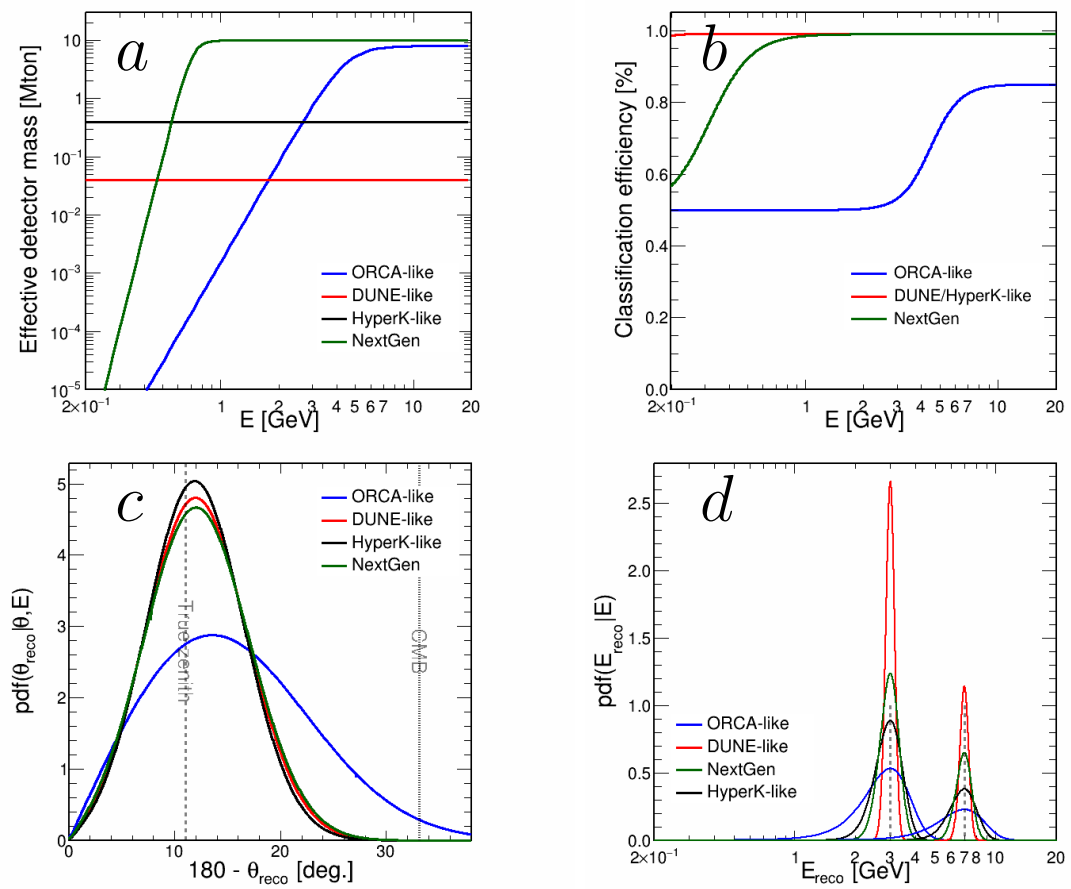

Figure 7.20: Examples of response functions used for the modelling of the neutrino detectors. **(a)** Effective mass (M_{eff}) as a function of the neutrino true energy. **(b)** Classification efficiency ($\varepsilon_{\text{class}}$) as a function of the true neutrino energy. **(c)** Probability distribution function for the reconstructed zenith angle for a neutrino with true energy $E = 10\,\text{GeV}$ and true zenith angle $\theta = 11.05°$ (corresponding to a neutrino trajectory grazing the ICB). **(d)** Probability distribution function for the reconstructed energy for two specific values of the true neutrino energy ($E = 3$ and $5\,\text{GeV}$).

In this parameterised approach, the simulated detector output can be calculated in the form of 2D histograms of detected events in a given observational channel (*tracks* or *showers*), as a function of the reconstructed energy and direction. Such histograms are obtained by looping over the (E, θ) bins of the interacting event rates and smearing them with the response functions, according to eq. 7.18. The rate is weighted with the appropriate detection efficiency at each energy E. The expected signal in a realistic experiment is computed by a convolution of the interacting rate at energy E and incident at zenith angle θ over the (E, θ) plane according to the energy and zenith resolution $PDFs$. The reconstructed events for each interaction channel are distributed into the two observational channels (*tracks* and *showers*) according to the classification efficiency function $\varepsilon_{\text{class}}(E)$. Every bin in the final, $(E_{\text{reco}}, \theta_{\text{reco}})$ event oscillogram for a given topological channel therefore
(i) contains a certain fraction of misreconstructed events coming from other (E, θ) bins;
(ii) misses some events that end up misreconstructed into different $(E_{\text{reco}}, \theta_{\text{reco}})$ bins;
and the same holds true for misclassified events which end up in the wrong topological channel histogram.

$$\begin{aligned} N_{\text{tracks}}(E_{\text{reco}}, \theta_{\text{reco}}) = \sum_{E,\theta} [N^{\text{int}}_{\text{tracks}}(E, \theta) \times \varepsilon_{\text{class}}(E) + N^{\text{int}}_{\text{casc}}(E, \theta) \times (1 - \varepsilon_{\text{class}}(E))] \\ \times PDF_{\text{angle}}(\theta_{\text{reco}}; E, \theta) \times PDF_{\text{energy}}(E_{\text{reco}}; E) \\ \times \Delta E \times \Delta\theta \times M_{\text{eff}}(E) \end{aligned} \tag{7.18}$$

This expression is now indeed similar to eq. 7.12, which uses the response matrix. For a given set of true energy and direction (E, θ), the 2D PDF looks like shown in Figure 7.21. Since our parameterisation does not include a flavour dependency, this 'smearing' is applied to all neutrino flavours equally, independent on their interaction channel. This is obviously a simplification, but reduces significantly the needed parameters per detector and allows for a more understandable comparison between different experiments.

7.4 Statistics

7.4.1 Binning

The choice of the binning of both the response matrix and the final event histograms is crucial for the whole analysis, as it affects the final result as well as the reliability of the simulation. The correct choice for the number of bins is a trade-off: On the one hand, mathematically the sensitivity can only increase with the number of bins. And from the physical point of view a fine binning is necessary to resolve *e.g.* the oscillation pattern, or absorption effects around Earth layer boundaries. On the other hand we have seen that depending on the available statistics from a MC simulation, the response matrix can be very sparse. Empty bins in the response functions (Fig. 7.17 & 7.18) due to small statistics should be prevented by reducing the number of bins. Larger bins bring also the benefit of a decrease in computation time, which is especially noticeable

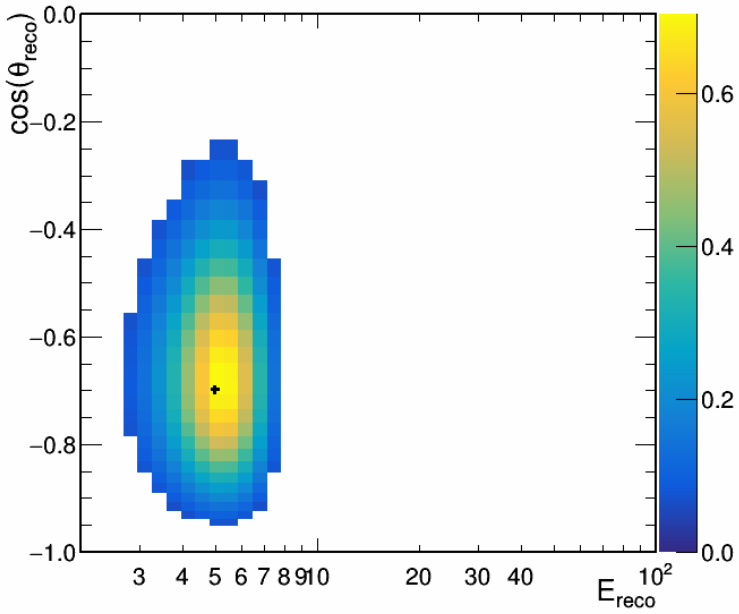

Figure 7.21: 2D parameterised response function in reconstructed energy E_{reco} and direction $\cos(\theta_{\text{reco}})$ corresponding to the ORCA-like detector, for the true energy E=5 GeV and direction θ_z=134° (indicated by the black cross). The same distribution is used for all flavours.

during fitting, where the simulation has to be done several hundred times. A good practice is to choose the bin widths to be similar to the resolution of the detector, in order to (i) ensure smooth response functions and (ii) make use of the full detector capabilities. The parameterised response functions are by definition always smooth and apart from the computation time there are no limits on the number of bins.

Further considerations about the binning concern the presentation of results. Since the atmospheric neutrino flux covers many orders of magnitude, the energy axis is binned logarithmically. For the y-axis there exist two possibilities: the most common method is to use a binning in $\cos(\theta_z)$, spanning the whole angular range of -1 to 1, which after eq. 7.2 corresponds to a linear change of length of the neutrino baseline. For neutrino tomography studies it is more convenient to chose a binning directly in θ_z for the following reason: As was shown in Fig. 3.6, the inner core boundary (ICB) is already at $\cos(\theta_z) = -0.98$ and the CMB at $\cos(\theta_z) = -0.84$. An (already fine) binning of 100 $\cos(\theta_z)$ bins (= bin width of 0.02) would thus mean, that all events that traverse the inner core are included in only one bin. Since we are interested in the properties of the three chemical layers in the Earth, a θ_z-binning ensures that each layer is covered by at least a few baselines.

7.4.2 Sensitivity studies

Log likelihood ratio test

A common practice in particle physics for measuring the level of compatibility between an experimental output d and a given hypothesis is to compute its likelihood $\mathcal{L}(\mathbf{d}|\mathbf{\Theta})$,

where $\boldsymbol{\Theta}$ is a set of parameters $\boldsymbol{\Theta} = (\Theta_0, \Theta_1, ..., \Theta_{N_{\text{syst}}-1})$ that present the hypothesis.

The observed data $\mathbf{d}$ contains the reconstructed event histograms of each PID class:

$$\mathbf{d} = (\mathbf{n}^0, \mathbf{n}^1, ..., \mathbf{n}^{N_{\text{class}}-1}) \tag{7.19}$$

where $\mathbf{n}^i = (n_0^i, n_1^i, .., n_{N_{\text{bins}}-1}^i)$ contains the number of events per bin in the final event histogram for PID class i. Since we are dealing with independent event counts, one can assume a Poisson-distributed number of events in each E-θ_z bin and consequently write:

$$\mathcal{L}_{\text{stat}}(\mathbf{d}|\boldsymbol{\Theta}) = \prod_{i=0}^{N_{\text{class}}-1} \prod_{b=0}^{N_{\text{bins}}-1} \frac{[\mu_b^i]^{n_b^i} e^{-\mu_b^i}}{n_b^i!} \tag{7.20}$$

with μ_b^i the expectation value in bin b for PID class i under the hypothesis $\boldsymbol{\Theta}$. In practice one often refers to $-2\ln\mathcal{L}$, the log-likelihood (LnL), where the natural logarithm is used to get rid of the exponential and avoid very small values of the likelihood. The minus is mostly convention to turn the maximum into a minimum, which is usually easier to find by fitting algorithms. The factor 2 eases the conversion to a confidence interval. The log-likelihood function is also a common approach for hypothesis tests: Assuming known log-likelihood profiles for a "null hypothesis" $\boldsymbol{\Theta}_0$ and a "test hypothesis" $\boldsymbol{\Theta}$ we define the log-likelihood ratio (LLR)

$$\lambda(\boldsymbol{d}|\boldsymbol{\Theta}) = -2\ln\frac{\mathcal{L}(\mathbf{d}|\boldsymbol{\Theta})}{\mathcal{L}(\mathbf{d}|\boldsymbol{\Theta}_0)}. \tag{7.21}$$

In the following we assume a fixed null hypothesis, *e.g.* the global best fits of oscillation parameters in Tab. 1.1. Inserting 7.20 into 7.21 one obtains

$$\lambda_{\text{stat}}(\boldsymbol{d}|\boldsymbol{\Theta}) = \sum_{i=0}^{N_{\text{class}}-1} \sum_{b=0}^{N_{\text{bins}}-1} 2[\mu_b^i - \mu_{b,0}^i + \mu_{b,0}^i \times \ln\left(\frac{\mu_{b,0}^i}{\mu_b^i}\right)] \tag{7.22}$$

For large sample sizes, the Poisson distribution is well approximated by a normal distribution and $\lambda(\boldsymbol{d}|\boldsymbol{\Theta})$ approaches a χ^2-distribution (Wilk's theorem)

$$\lambda_{\text{stat}}(\boldsymbol{d}|\boldsymbol{\Theta}) \approx \sum_{i=0}^{N_{\text{class}}-1} \sum_{b=0}^{N_{\text{bins}}-1} \frac{(\mu_{b,0}^i - \mu_b^i)^2}{\mu_{b,0}^i} = \Delta\chi^2\ , \tag{7.23}$$

which allows for a conversion into a confidence interval in terms of σ. The general frequentists approach is to simulate many pseudo-experiments, *i.e.* where the bin entries in the event histogram are drawn from a Poisson distribution, for both hypothesis and determine the p-value for the rejection of the test hypothesis from the $\Delta\chi^2$ distributions. The computation of many pseudo-experiments is however computationally expensive, especially if high significance is under investigation, which would require an accurate sampling of the tails of the likelihood profiles. An estimation made in [162] shows that up to $\mathcal{O}(10^8)$ pseudo-experiments may be necessary to reach 5σ. Instead, in this analysis the so called Asimov-approach is used, where the event histograms for each hypothesis are filled with its expectation value μ. Therefore $\Delta\chi^2$ is only computed once and yields an Asimov-significance $S = \sqrt{(\Delta\chi^2)}$ with which the test hypothesis

can be rejected. This chi-square method is equivalent to the LLR of Gaussian likelihoods, where in order to state a confidence interval of *e.g.* 68 %, one searches the values $\Theta_{L/U}$ for which $-2\mathcal{L}$ increases by one unit. This confidence interval corresponds to the frequentist approach, meaning that 68 % of identical experiments would find a parameter range $[\Theta_L, \Theta_U]$ that includes Θ[164].

Treatment of systematic uncertainties

The equation 7.20 is a measure for the statistical likelihood $\mathcal{L}_{\text{stat}}$. It is however possible to use external constraints on the parameters Θ, *e.g.* measurements of the oscillation parameters by other experiments, by adding Gaussian priors of the form

$$\mathcal{L}_{\text{syst}}(\boldsymbol{\Theta}) = \prod_{s=0}^{N_{\text{syst}}-1} \exp(-\left(\frac{\hat{\Theta}_s - \Theta_s}{\sigma_{\Theta_s}}\right)^2) \tag{7.24}$$

where $\hat{\Theta}$ is usually the global best fit value of that parameter, and σ_Θ its uncertainty, or in other words the mean and the width of the Gaussian. Calculating again the LLR for both the statistical and systematic likelihood

$$\mathcal{L} = \mathcal{L}_{\text{stat}} \times \mathcal{L}_{\text{syst}} \tag{7.25}$$

we find the expression

$$\lambda(\boldsymbol{d}|\boldsymbol{\Theta}) = \lambda_{\text{stat}}(\boldsymbol{d}|\boldsymbol{\Theta}) + \prod_{s=0}^{N_{\text{syst}}-1} \left(\frac{\hat{\Theta}_s - \Theta_s}{\sigma_{\Theta_s}}\right)^2 . \tag{7.26}$$

The contribution of the Gaussian term to the total log-likelihood can be interpreted as a penalty term, that is added when the fitting algorithm drifts parameters to values, that are already physically excluded by other experiments. The Asimov significance is again given by

$$S = \sqrt{\lambda(\boldsymbol{d}|\boldsymbol{\Theta})} . \tag{7.27}$$

Monte Carlo statistical uncertainties

In the case of a MC-based detector response (sec. 7.3.1) also the entries of the response matrix R are subject to statistical fluctuations. Our simulated output $\mu(R)$ from one possible realisation of R, is connected to the output $\mu'(R')$ coming from the 'true' detector response R' (which would be obtained by infinite MC statistics) via

$$\mu'_k = \beta_k \mu_k \tag{7.28}$$

with a normally distributed $\beta_k = \mathcal{N}(1, \sigma_k^2)$, with k running over the number of bins in $R = N_{\text{class}} \times N_{\text{bins}}$-1. This approximation is known as "Beeston and Barlow light method"[4]. In our case, our likelihood ratio of eq. 7.26 is extended by one additional term

$$\lambda(\boldsymbol{d}|\boldsymbol{\Theta}) = \lambda_{\text{stat}}(\boldsymbol{d}|\boldsymbol{\Theta}) + \lambda_{\text{syst}}(\boldsymbol{\Theta}) + \sum_k \frac{(\beta_k - 1)^2}{\sigma_k^2} . \tag{7.29}$$

[4]For more details see sec. 6.4 in [162] or [165].

Fitting process

In order to find the true underlying parameters form real data, $\mathbf{\Theta}$ is fitted to $\mathbf{d}$ by minimising the LLR $\lambda(\boldsymbol{d}|\mathbf{\Theta})$. In our frameworks, a fitter class was build around `Minuit2`[166] which is implemented in `ROOT`. The implemented fit parameters include oscillation parameters and systematic uncertainties of the atmospheric flux, detector properties and Earth related parameters. The user can define individually which parameters are fitted and which priors to apply. Typically, increasing the number of free parameters leads to a decrease of the resulting sensitivity, which can again be counteracted with stringent priors. The fitter stores one 'data experiment' with the true (pseudo-)data, and a 'model experiment' with variable parameters. In each step of the fitting process, the model experiment is resimulated while varying the values of the fit parameters, *i.e.* the Earth model and consequently the oscillation and absorption probabilities are updated, until the minimum LLR is found.

In case of a fit to an Asimov dataset, the best fit value of $\mathbf{\Theta}$ equal its input values. For the investigation of a single parameter, like the Z/A of the outer core, confidence intervals can be identified by computing the LLR by hand for some values of the parameter in order to draw the LLR-profile. For a fit of multiple correlated parameters the `Minuit2` provides an algorithm (`MINOS`[5]) to scan the multidimensional parameter space starting from their best fit values in order to find their confidence levels. This function is used here for the error estimation of multi-layer fits to the density profile of the data experiment.

Constraining global Earth parameters

By applying priors to fitting parameters, one wants to ensure that the fit result is in agreement with the results of other experiments or theoretical constraints. When we fit the densities of an Earth model with N layers, we can additionally add the constrain of the Earths total mass and inertia, which both depend on the density of all individual layers:

$$M_{\oplus} = \sum_{i=1}^{N} \frac{4\pi}{3} \times (R^3_{\text{outer},i} - R^3_{\text{inner},i}) \times \rho_i \tag{7.30}$$

and

$$I_{\oplus} = \sum_{i=1}^{N} \frac{8\pi}{15} \times (R^5_{\text{outer},i} - R^5_{\text{inner},i}) \times \rho_i \ , \tag{7.31}$$

where $R_{\text{outer/inner}}$ refer to the boundaries of the respective layer and ρ to its density. In practice, both are not touched by the fitter itself, but are calculated from the intermediate fit results of $\rho_{(1,2,\dots,N)}$ and compared in each step to the prior (sec. 3.1.2) as in eq. 7.26.

[5] More information is provided in the manual[167].

Part III

Results

Chapter 8

Absorption tomography with KM3NeT/ARCA

Contents

This first chapter presenting results of my doctorate contains several original studies on KM3NeT at once: the first analysis on absorption tomography with KM3NeT, using SWIM for the first time with an ARCA MC dataset, specially created during the scope of this thesis and briefly analysed here. I evaluated the sensitivity on the Earth's matter density due to neutrino absorption towards the possibility of constraining the Earth's radial density profile and find comparable results as for the similar study of IceCube data by [136]. I studied further the feasibility of detecting heterogeneities in the mantle, using the 3D model I designed for that purpose.

8.1 The first ARCA dataset for SWIM

With the motivation of studying the feasibility of absorption tomography with ARCA, a data sample in a compatible format for `SWIM` was created from the latest MC(v6), which was produced in autumn 2021. This is a very tedious task, since hundreds to thousands of MC files have to be processed in the KM3NeT computing cluster at CC-Lyon, with special care on the completeness of data. Cancelled jobs or missing files lead eventually to a mismatch of selected to generated events, which result in an unphysical response matrix with efficiencies > 1 (more selected than generated events in single bins).
The MC files do not intrinsically contain a PID, which I created following the procedure described in chapter 6. Further, at the time this study was executed, no ν_τ events were processed in the ARCA MC, which means that the detector response for ν_τ could not be simulated for ARCA. The results in this chapter were thus obtained by considering only the conventional atmospheric flux and the prompt component of ν_e and ν_μ. The contribution of prompt ν_τ is however subdominant. In sec. 8.2 the effect of ν_τ and astrophysical neutrinos is briefly studied using an approximate detector response.

The preparation of an analysis dataset is a long-lasting procedure with many details to be figured out, mainly concerning the data quality. Since the used MC was relatively new at the time I carried out the study of absorption tomography with ARCA, no such dataset was available in the collaboration. The only loose selection cut applied on the MC is the requirement of at least one successful reconstruction output with $\cos\theta_z < 0$, *i.e.* a neutrino reconstructed as up-going. The results presented in this chapter should therefore be considered, for now, as a first insight into the potential of ARCA contributing to Earth science with room for optimisation.

In a first step the general detector performances are studied, namely the expected event rates and the reconstruction capabilities. The reconstruction output of `JGandalf` (tracks) and `aashower` (showers) are plotted vs. the true MC value in Fig. 8.1 (normalised per energy/$\cos(\theta_z)$ bin). The angular resolutions are very high in the track channel, as expected from the long muon tracks. The energy resolution decreases with higher neutrino energies. This behaviour is likely to origin from events with interaction vertices outside the instrumented volume and could probably be countered with cuts on the reconstructed position of the event, to ensure that (a) the hadronic shower and (b) the muon track – which length is a main indicator for the muon energy – are contained in the instrumented volume.
The expected annual event rates classified as tracks and showers is shown in Fig. 8.2. Respectively ∼30k and ∼10k events are expected per PID class. Note that the MC simulation was made for one building block of ARCA. Since the second block will be identical to the first one, doubling the event rate or the simulated livetime of the used MC equals the result of two building blocks, which was done for all analyses with `SWIM` presented here.

The PID of ARCA, *i.e.* the track-shower separation and atmospheric muon suppression, was already presented in chapter 6. The conclusion was, that the muon background can be sufficiently removed with a cut on the classification output, which is applied in all presented results. A study of the contribution of background events from random noise was not carried out, but as for ORCA, noise events by random

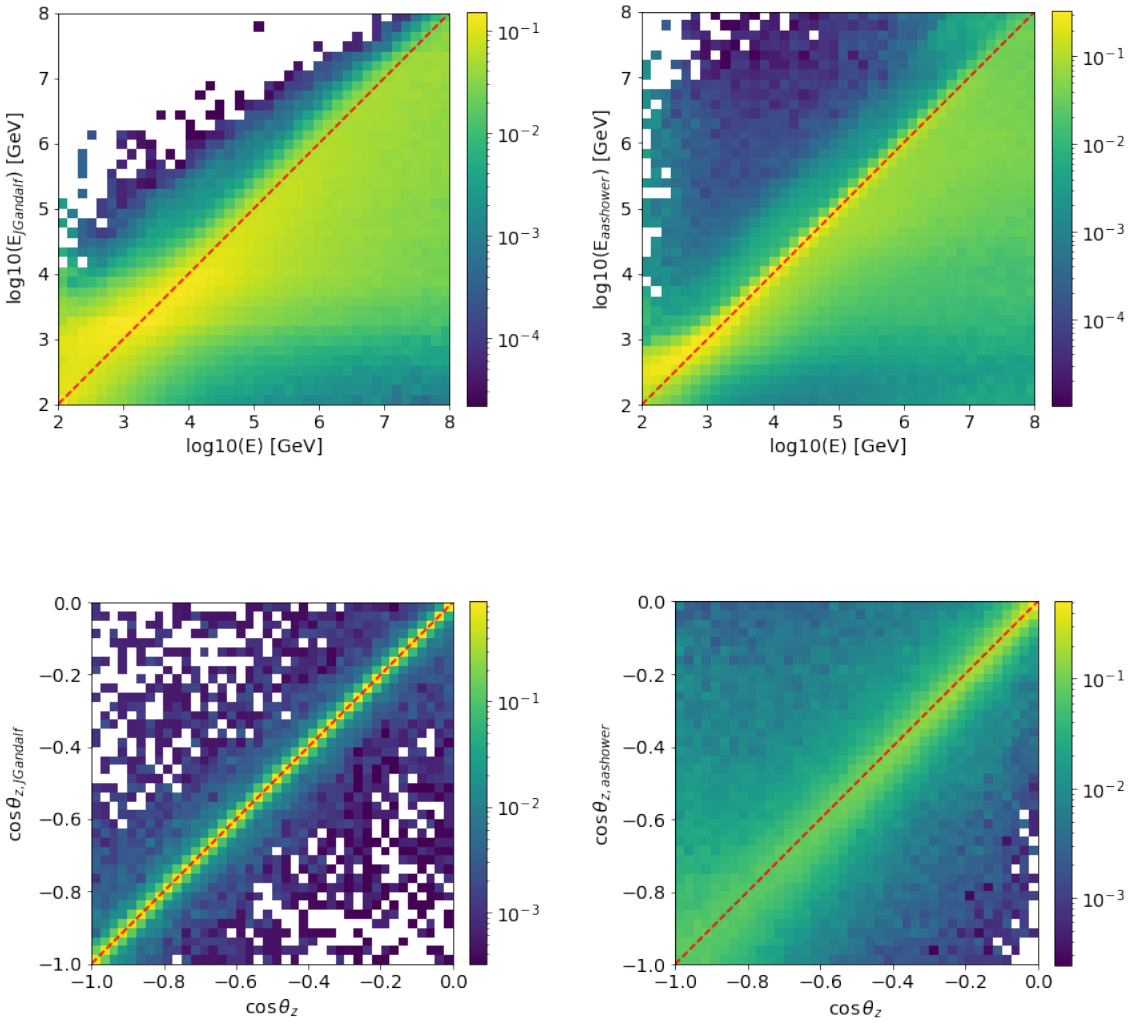

Figure 8.1: Energy (top) and angle (bottom) reconstruction of ARCA with `JGandalf` (left, for tracks) and `aashower` (right, for showers), normalised per energy bin.

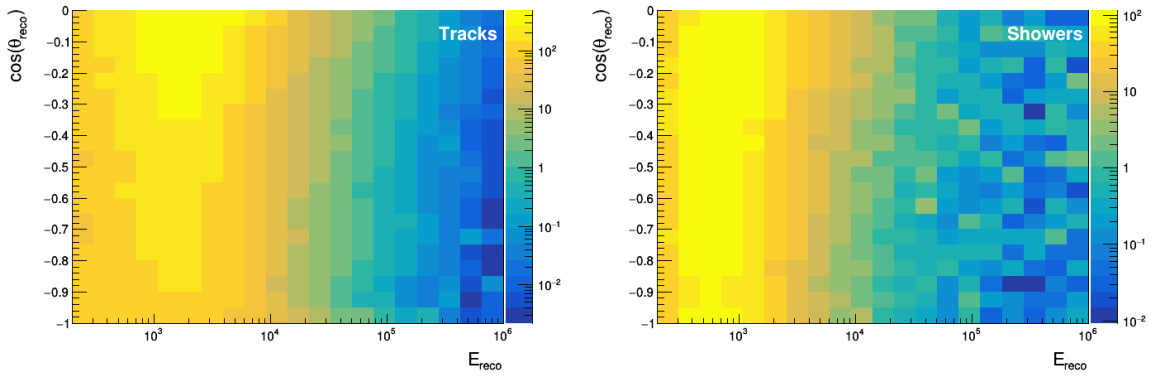

Figure 8.2: Annual atmospheric event rates per year and PID class for one ARCA building block.

coincidences are expected to be efficiently removed by selection cuts and classifier algorithms, especially at the high energies relevant for absorption tomography. The classification into track- and shower-channels comes close to a perfect accuracy. It is however not expected to have a high impact on the study, since both ν_e and ν_μ are affected almost equally by absorption effects, due to their similar cross sections.

`SWIM` is designed in such a way, that with the correct input data from MC and input models of flux and cross sections matching the energy range in question a complete experiment can be simulated within ms. The calculated detector response yields directly the effective mass of the detector (eq. 7.17), shown in Fig. 7.19.

Finally, the correct implementation of the neutrino absorption has been verified. Fig. 8.3 shows the interacting event rates of ν_μ^{CC} for different cuts on the neutrino energy, relative to the total rate. Apart from the decrease of event rates due to the lower initial flux at higher energies, the effect of the absorption in the Earth core becomes more and more visible at higher energies. For ν_μ with $E > 10^5\,\mathrm{GeV}$ the drop at the CMB at 33.13° is clearly visible, confirming the proper modelling of absorption effects.

Although being a preliminary dataset with plenty of room for improvements, in addition to the implementation of neutrino absorption to SWIM it opens the possibility for the whole KM3NeT collaboration to use a new alternative analysis framework for ARCA. This has been already exploited by Nadja Lessing, a master student at ECAP, Erlangen who studied decoherence effects in neutrino oscillations with both KM3NeT detectors with SWIM. The preparation of the ARCA dataset may also motivate people to study other detectors. An obvious extension would be to use ANTARES MC data, which has a similar structure as that from ORCA and ARCA.

8.2 Density profiling

The first approach towards density profiling by measuring the absorption of atmospheric neutrinos was inspired by the work of *Donini et al.* [136], who fitted an Earth model with 5 layers of constant density, using one year of IceCube data (Fig. 3.10).

In order to repeat that study with ARCA, I developed a new functionality to the

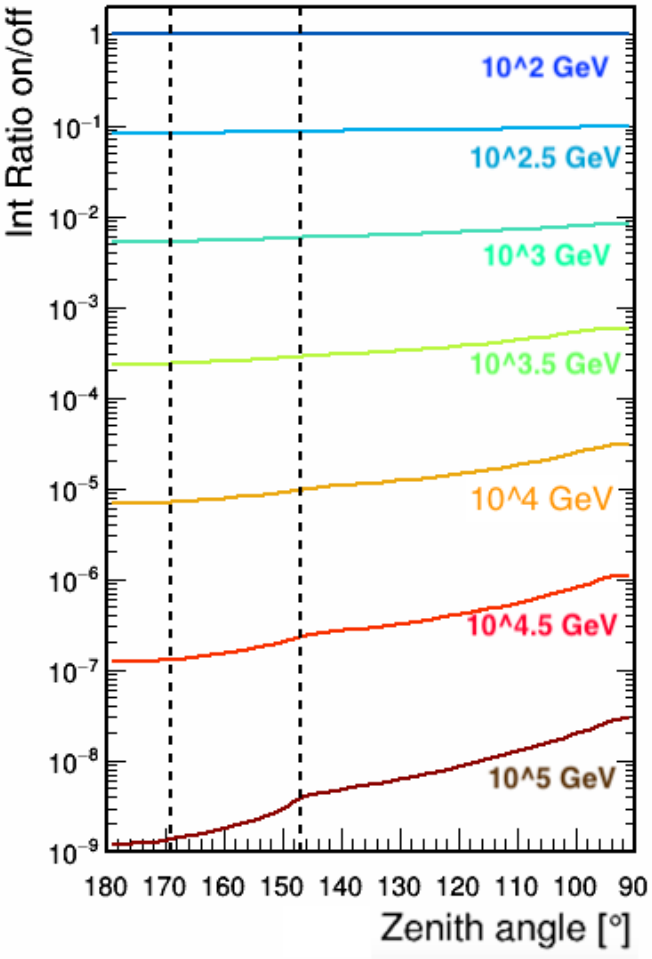

Figure 8.3: Interacting rates of ν_μ^{CC} for different cuts on the neutrino energy, relative to the total rate. The ICB and CMB are indicated with dashed lines. (Figure analogue to [134].)

analysis frameworks, for fitting the densities in different customizable layers of the underlying Earth model (instead of using a fixed PREM profile). To that aim the "data experiment" is calculated once using the 42-layer PREM as described in sec. 7.2.2. Due to the binning, the mass and inertia of our input PREM $M_{\oplus,\mathrm{PREM}} = 6.03 \times 10^{24}\,\mathrm{kg}$ and $I_{\oplus,\mathrm{PREM}} = 8.09 \times 10^{37}\,\mathrm{kg\,m^2}$ slightly differ (<1 %) from the gravitational measurements. As we will see in the following, this discrepancy is much smaller than the sensitivity from neutrino tomography and can thus has no impact on the results.
In the "model experiment" the layer boundaries from the data experiment are kept in order to avoid mismatches that could affect the fit result, especially at the CMB where a large density jump is present.

As in [136] I assign each of the 42-layers to one of the 5 layers $\hat{l}_i$; $i \in (1, .., 5)$, one for the inner core and respectively two for the outer core and the mantle, with the explicit boundaries $\hat{r}_i \in [1221.5, 2400, 3480, 5000, 6368]$ km. Principally, the number and radii of the layers can be customized in the framework. The density in each layer $\hat{l}_i$ is fixed for all sub-layers from the 42-layer model to $\hat{\rho}_i$, which are the fit parameters. The Z/A values do not affect the absorption probability and thus have no impact on this study, since neutrino oscillations are neglected here.

Hypothesis test of two different Earth models As a start we test how exploiting neutrino absorption with ARCA could allow to distinguish between two different Earth models. Fig. 8.4 shows our PREM model with 42-layers and an example model with 5-layers. Simulating the expected event rates resulting from each of the two models allows to construct absorbograms and statistics histograms of the absolute difference ΔN, the relative difference $\Delta N/N$ and the signed χ^2, as shown in Fig. 8.4 for track-like events and in Fig. 8.5 for shower-like vents. The distributions are consistent with what was expected: First, the transmission probability differs the most (up to 4 %) for neutrinos coming from zenith angles $\theta_z < 130°(\equiv R > 5000\,\mathrm{km})$, *i.e.* with long trajectories crossing the mantle, where our two Earth models diverge the most. The sign of ΔN (and thus $\Delta N/N$ and χ^2) is the same as the sign of the density variation between both models. Above ∼6000 km where the 5-layer model is denser than PREM ($\delta\rho > 0$) we see more events in PREM ($\Delta N > 0$), and vice versa, between 5000 km and 6000 km where both $\delta\rho$ and ΔN have negative values.
Second we observe that the highest ΔN is expected at lower energies, where the neutrino flux is the highest, *i.e.* where most events are detected. The relative difference $\Delta N/N$ on the other hand peaks at higher energies, where only few events are detected at all, and thus small differences in event numbers make a large relative difference. The χ^2 is mathematically the product of $|\Delta N| \times \Delta N/N$ and thus peaks in between the energy regimes, *i.e.* at energies from 10^3 GeV to 10^5 GeV. Finding this main energy range for absorption tomography justifies to neglect the prompt τ-neutrino flux, as its contribution to the total flux is only relevant above 10^6 GeV (see Fig. 1.5). It should be noted that the χ^2 calculated from the histogram corresponds to the statistical LLR only (eq. 7.23). Including the MC error as in eq. 7.29 (with $\lambda_{\mathrm{syst}} = 0$) significantly decreases the resulting sensitivity. The LLR for which the 42- and the 5-layer Earth model can be distinguished is $\lambda = 1.67$ without MC error and decreases to $\lambda_{\mathrm{stat}} = 0.59$ when it is included. Due to the higher $\overset{(-)}{\nu}_\mu$ flux (Fig. 8.2), ∼95 % of the contribution comes from the track channel in both cases. From that one can conclude, that a larger

	ARCA				IceCube			
	10 yr		10 yr no MCerr		1 yr data		10 yr forecast	
Layer 1	+20.11	−13.12	+12.33	−11.92	+26.11	−13.66	+10.78	−11.75
Layer 2	+6.56	−6.25	+3.88	−3.82	+16.64	−13.71	+6.55	−6.85
Layer 3	+3.28	−3.23	+2.03	−2.00	+9.14	−3.87	+3.92	−3.51
Layer 4	+1.16	−1.13	+0.72	−0.72	+5.87	−2.40	+0.78	−1.01
Layer 5	+0.48	−0.48	+0.29	−0.29	+1.56	−1.99	+0.06	−0.29

Table 8.1: Comparison of the 68 % posterior on the respective layer density with ARCA and IceCube (data extracted from Fig. 3.10 (Fig. 10 in [136])).

MC sample and thus a more precise modeling of the detector response could increase the sensitivity.

Fit of a 5-layer model to PREM Now that the procedure to perform a hypothesis test between two Earth models has been described, one can proceed with the actual fit of the densities in each respective layer of the 5-layer model. As start value all 5 layers are set to $5\,\mathrm{g\,cm^{-3}}$, close to the average Earth density of about $5.5\,\mathrm{g\,cm^{-3}}$. No systematics uncertainties are considered. The result of the fit together with the 68 % posterior found by `Minos` is shown in Fig. 8.6 for simulated data of 10 yr with both ARCA building blocks. The fact that the fit converges can be seen as a first proof of concept of determining the Earth's density profile by absorption tomography. The density jump between outer core and mantle region is resolved, as the posterior of the neighbouring layers do not overlap. The decrease of uncertainty per layer with the radius is a logical consequence of the growing statistics: whereas all neutrinos pass through the mantle, the inner core is only seen by those with a almost straight up-going trajectory. The mass of our fitted 5-layer Earth corresponds to $M_{\oplus,\nu} = 6.00^{+1.54}_{-1.46} \times 10^{24}\,\mathrm{kg}$, its inertia to $I_{\oplus,\nu} = 8.02^{+1.43}_{-1.40} \times 10^{37}\,\mathrm{kg\,m^2}$, and thus match our input PREM. The total mass and momentum of inertia was not constrained in this fit. The strong limits on these parameters result in a (multidimensional) likelihood profile with multiple local minima. The approach of `Minos` to scan the profile until the requested posterior is found gives in that case no valid results.

Comparison with IceCube performance The resolution in terms of the widths of the posteriors on the Earth's density profile with ARCA can be compared to that from IceCube published by *Donini et al.* (Fig. 3.10) , which are read by eye and presented in tabular form in Tab. 8.1.

With one year of data they find $M_{\oplus,\nu} = 6.00^{+1.6}_{-1.3} \times 10^{24}\,\mathrm{kg}$ and $I_{\oplus,\nu} = 6.9 \pm 2.4 \times 10^{37}\,\mathrm{kg\,m^2}$. However, the comparison is subject to some caveats:

- **Modelling of absorption** The neutrino propagation through the Earth was modelled with ν−`SQuIDS`, extending the standard attenuation effect by the inclusion of NC-scattered neutrinos and neutrino regeneration from tau lepton decays, as discussed in sec. 7.2.4. This effectively decreases the absorption probability, as more neutrinos survive the propagation through Earth.

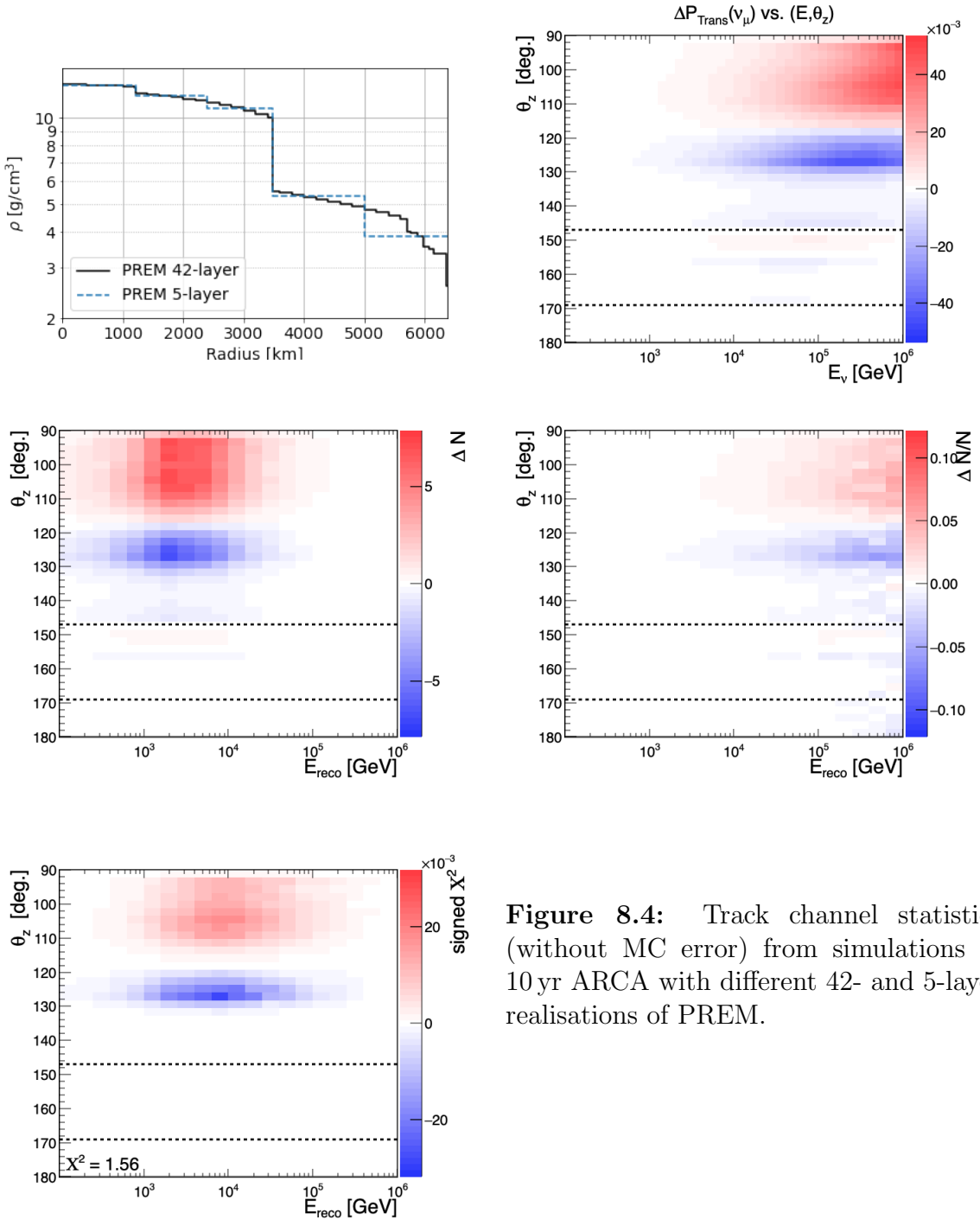

Figure 8.4: Track channel statistics (without MC error) from simulations of 10 yr ARCA with different 42- and 5-layer realisations of PREM.

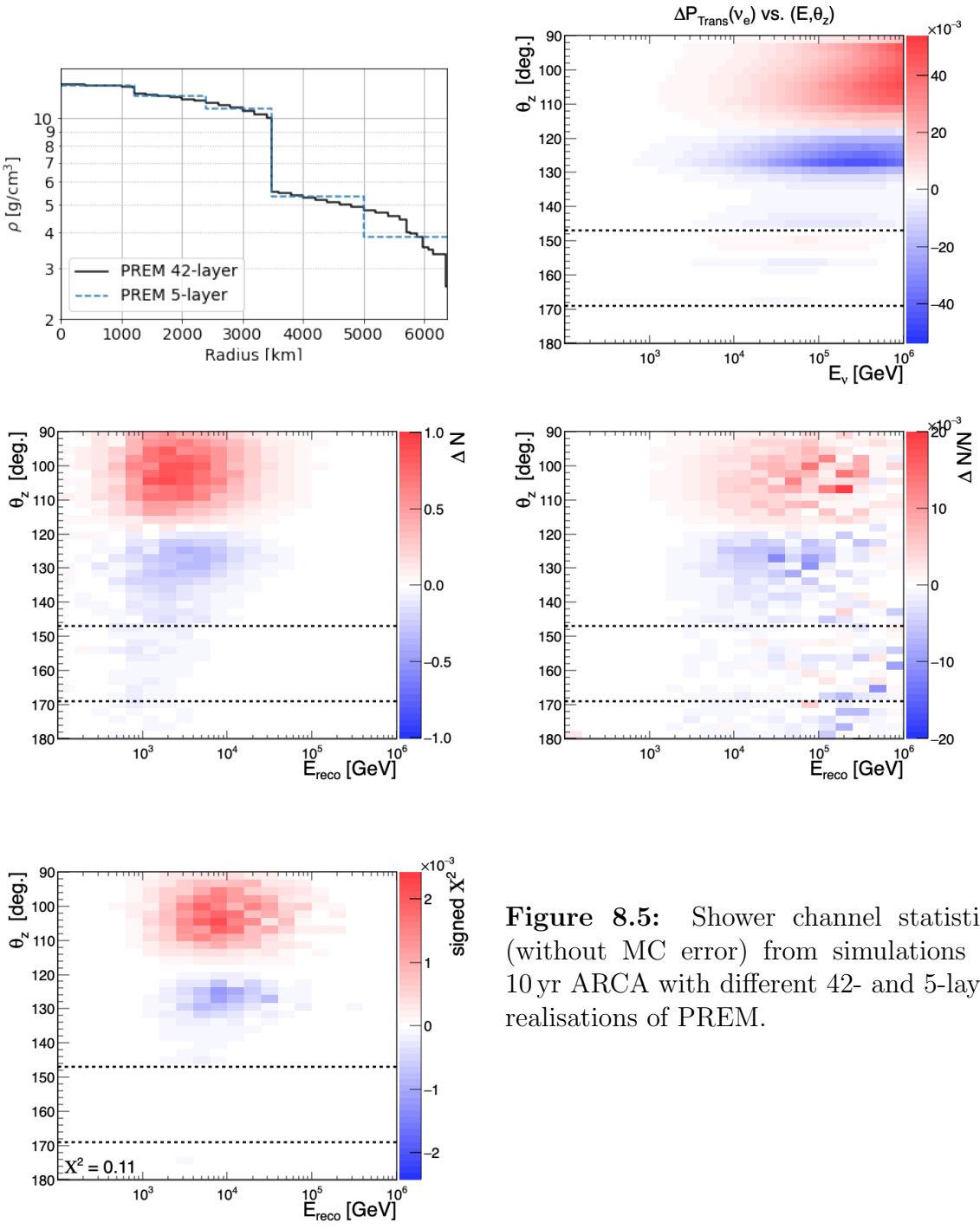

Figure 8.5: Shower channel statistics (without MC error) from simulations of 10 yr ARCA with different 42- and 5-layer realisations of PREM.

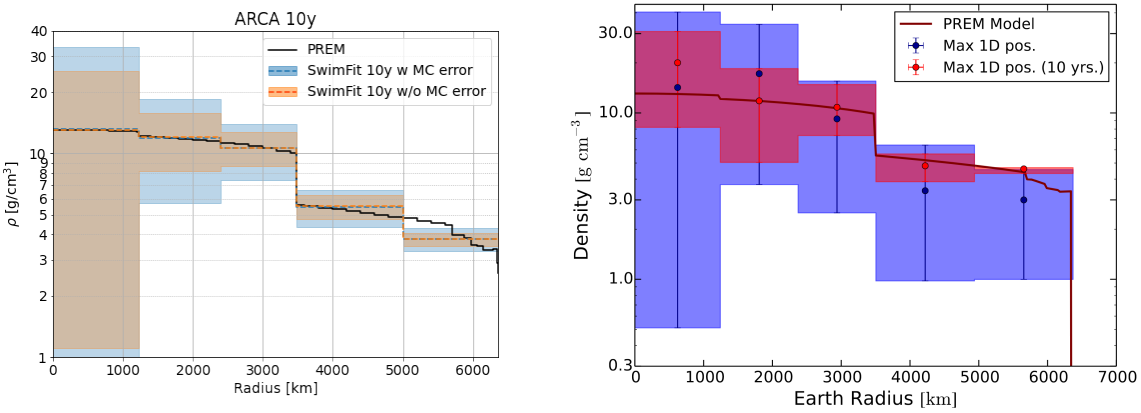

Figure 8.6: Left: Density profiling with ARCA with 10 years of data with two building blocks, with and without MC error. **Right:** The red curve shows the reference result from [136]. Note that their best fit does not match PREM.

- **Systematics** The fit on the IceCube data included 4 nuisance parameters: (1) The overall flux normalization, (2) The pion-to-kaon ratio in the hadronic air showers in which atmospheric neutrinos are created, (3) The spectral index of the atmospheric neutrino flux, (4) The efficiency of the optical modules.
  Free nuisance parameters generally loosen the constraints on the actual parameters of interest. Approximately 30 % of their derived errors on $M_{\oplus,\nu}$ and $I_{\oplus,\nu}$ are due to nuisance parameters.

- **Posterior calculation** The Posteriors in [136] are based on marginalized posterior probability distributions and therefore don't include correlations, contrary to the error estimation by `Minos`, which is thus the more conservative approach. When fitting multiple layer densities in parallel one sees that they are strongly correlated with each other (more on that in chapter 9). Higher densities in one layer can be equalized by lowering the density elsewhere, which eventually broadens the error bands compared to a fit of a single layer. It also means that not all combinations of densities that are allowed by simply looking at the posterior are actual valid 'solutions' of the fit.
  It is also not clear whether they took MC uncertainties into account and consequently if their result should be compared to that with or without including the MC error.

By eye, our result appear much worse for the innermost layer, which comes from the logarithmic y-axis and the higher best fit value of IceCube. In absolute values the width of the errorbands are somewhat converging. Surprisingly, the IceCube forecast predicts very tight limits on the outer mantle region and also surpasses ARCA in the inner core, even without taking into account the MC error. These are however also the two layers, where the IceCube forecast is far off the PREM density, making a direct comparison complicated.

Impact of cosmic- and τ-neutrinos In the above presented results, two simplifications were made concerning the neutrino flux. First, only atmospheric neutrinos

(ν^{atm} =conventional + prompt) were used as input model to calculate the event rates, following the approach made by *Donini et al.*. It seems indeed to be a reasonable approximation, as the contribution of astrophysical neutrinos (ν^{astro}) only becomes dominant at $\gtrsim 2 \times 10^5$ GeV (see Fig. 7.5), where almost all core-traversing neutrinos get absorbed anyway (as visible in the absorbogram in Fig. 7.10). Second, no ν_τ were simulated due to the missing MC simulation and thus the lack of a proper detector response function. Both the prompt component of the atmospheric neutrino flux as well as the astrophysical flux are thought to consist of an approximate flavour ratio $\overset{(-)}{\nu}_e : \overset{(-)}{\nu}_\mu : \overset{(-)}{\nu}_\tau = 1 : 1 : 1$. When only taking into account atmospheric neutrinos, neglecting a third of the anyway small contribution of the prompt flux is reasonable. The ν_τ contribution of the cosmic neutrino flux on the other hand should not be neglected, as it indeed represents a third of the overall flux (at high energies, where $\nu^{\text{astro}} \gg \nu^{\text{atm}}$).

In order to test a potential impact of cosmic neutrinos, their flux ϕ^{astro} was modeled after the latest publication of IceCube, as described in sec. 7.2.1. Next, `SWIM` was modified to use also a contribution of ν_τ in the neutrino flux[1]. One reason why no MC simulation of ν_τ-interactions were available in the first processing run is the complexity of the decay chain as discussed in sec. 2.1.2. ν_τ are thus not generally belonging to either one of the typical classification channels shower- or track-like. Due to the lack of a proper ν_τ response for ARCA, they were here approximately treated like NC events. This estimate accounts for the fact that most tau decays end up in an electronic shower and that a ν_τ is created which carries away energy, as in all NC interactions.

The impact of adding ν_τ and cosmic neutrinos on the sensitivity of the Earth's density profile is shown in Fig. 8.7, compared to the previous case (both with MC error). The improvement is only marginal, confirming the original assumption that astrophysical neutrinos can be neglected due to the high overall absorption probability at the energy range where they get dominant over the atmospheric neutrino flux.

8.3 Probing 3D density heterogeneities

After studying the whole Earth as a radial symmetric body, this section is dedicated to the investigation of possible 3D heterogenities in the deep Earth, namely the LLSVPs introduced in sec. 3.1. For the first trials, I simulated the neutrino propagation through Earth with `NuPropEarth`, once for a radial symmetric Earth according to PREM and once with an additional heterogeneous region of constant density. As already discussed in sec. 7.2.1, the disadvantages of `NuPropEarth` for the purpose of a flexible LLSVP model made me search for an alternative. `OscProb` in combination with `TGeoManager` provided a faster and more accessible approach for this task, with the major advantage that the exact same framework can be used for oscillation studies, by simply switching `OscProb` to calculate oscillations instead of absorption.

A 3D Earth model holds in general an azimuth dependence. Strictly spoken this would require to adapt the complete framework by extending all input models, oscillation and absorption probabilities and the final results by one dimension. Moreover it would further increase the sparseness of the response matrix, making even more MC

[1] Since `SWIM` was intentionally designed for oscillation studies with atmospheric neutrinos, it was explicitly forbidden to use ν_τ, as there are not present in the conventional flux.

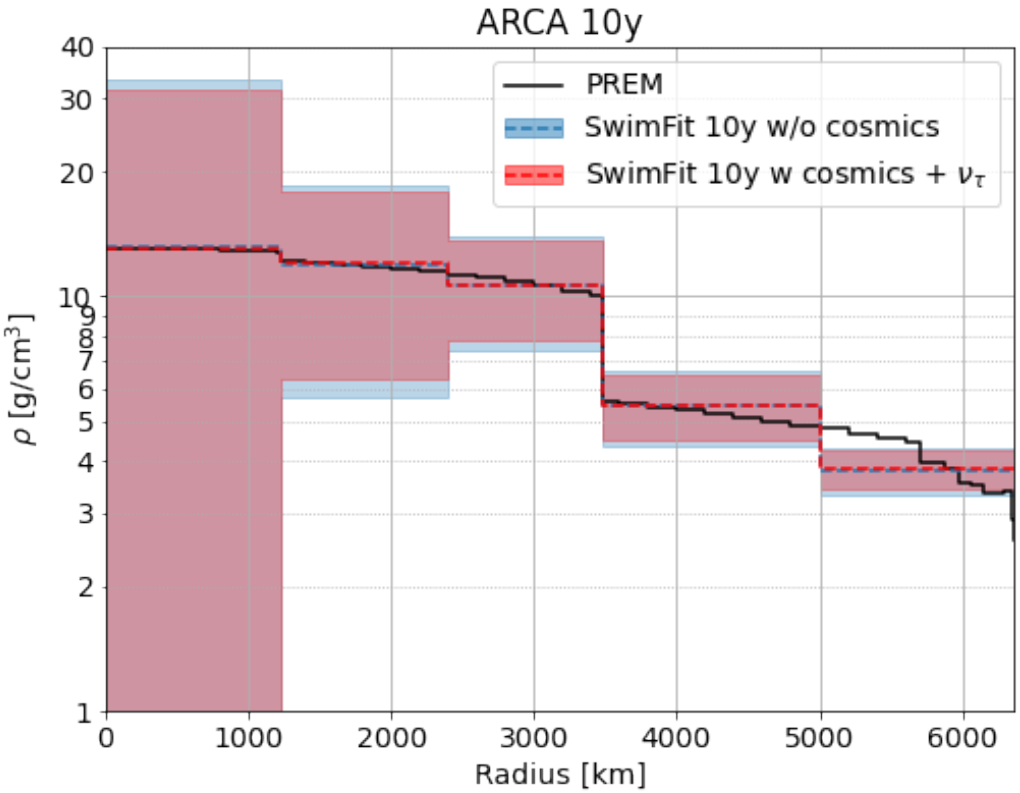

Figure 8.7: Density profiling with ARCA with 10 years of data with two building blocks, with atmospheric neutrinos only and in combination with cosmic neutrinos, including the contribution from ν_τ.

statistics necessary for a reliable model of the detector response. Instead, the azimuth dependency was accounted for in a different way, based on the functionalities available in the `TGeoManager` package.
The baselines for `OscProb` are calculated for a fixed azimuth angle ϕ and thus for a 1D Earth profile. In the previous studies it was always assumed that the Earth model is radially symmetric, which justified the simulation over the integrated range $\phi \in [0, 2\pi[$. Instead, for the analysis of a local density anomaly, the experiment is simulated n times, once for each azimuth bin

$$\phi_1 \in \left[0, \frac{2\pi}{n}\right[\,,\ \phi_2 \in \left[\frac{2\pi}{n}, 2\frac{2\pi}{n}\right[\,, ...,\ \phi_n \in \left[(n-1)\frac{2\pi}{n}, 2\pi\right[\,. \tag{8.1}$$

and the baselines for `OscProb` are reevaluated at the center value of each bin. Each azimuth will correspond to a different cross section through the LLSVP (Fig. 8.8). For each azimuth bin, the likelihood $\mathcal{L}_i$ can be compared to the previously used homogeneous Earth model. The total $\mathcal{L}$ is then given by

$$\mathcal{L} = \frac{1}{n} \sum_{i=1}^{n} \mathcal{L}_i \,. \tag{8.2}$$

The weight of $1/n$ has to be applied to properly scale down the neutrino events, since the underlying flux model is averaged over the whole azimuth range. Note that in this approximation, the flux is still homogeneous for all azimuth angles, *i.e.* the East-West-effect is not taken into account. In this analysis, the chosen step size of $\phi_{\text{step}} = 5$ leads to $n = 72$. Since most of the azimuth bins have no cross section with the LLSVP, these do not have to be computed (as they are identical to PREM).

First tests performed with a reasonably-sized LLSVP of $\sim 10^{10}\,\text{km}^3$ volume, but a large density variation compared to PREM ($\delta\rho_{\text{PREM}} = +10\,\%$) showed barely any effect to the expected ARCA event rates, shown for tracks in Fig. 8.9 and for showers in Fig. 8.10. The difference in absorption probability (with respect to the PREM model) P_{Abs} increases by up to 2.5 % for the small window in θ_z that goes through the LLSVP. Due to the overall low flux at these energies, this barely affects the expected event rates, leading to only small values of ΔN, $\Delta N/N$ and χ^2 (even without the weight of $1/n$ being applied to the shown scales). Despite of an optimal choice for the LLSVP location with respect to ARCA (see chapter 9 for more details on this aspect), the low atmospheric neutrino flux and the small fraction of neutrinos crossing the density heterogeneity finally lead to the conclusion that absorption tomography is not feasible for the study of LLSVPs.

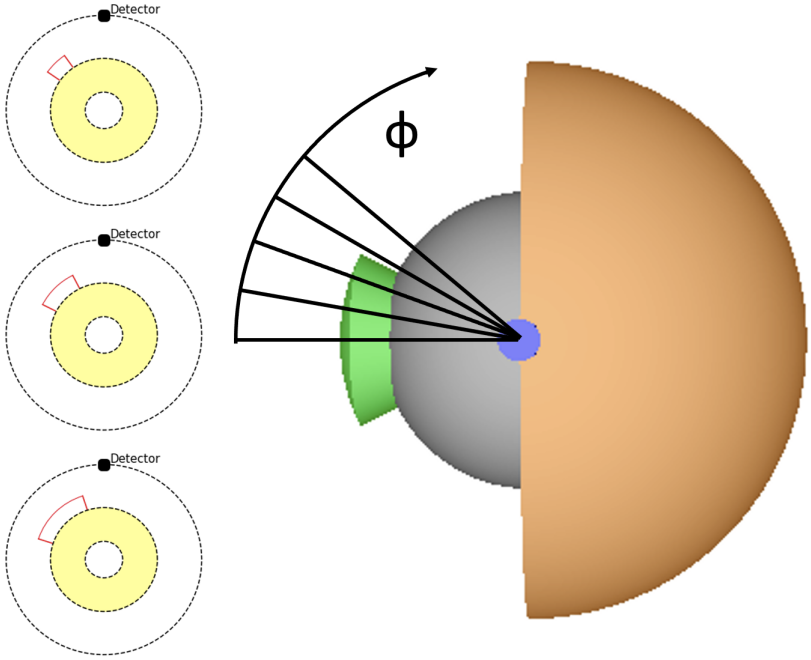

Figure 8.8: Visualisation of the azimuth dependence in the LLSVP analysis. The right figure shows the top view of the 3D Earth model, with the detector on the top. n experiments are simulated for different slices through the model at various azimuth angles ϕ. Neutrinos at different directions see thus different cross sections of the LLSVP (three examples are shown on the left).

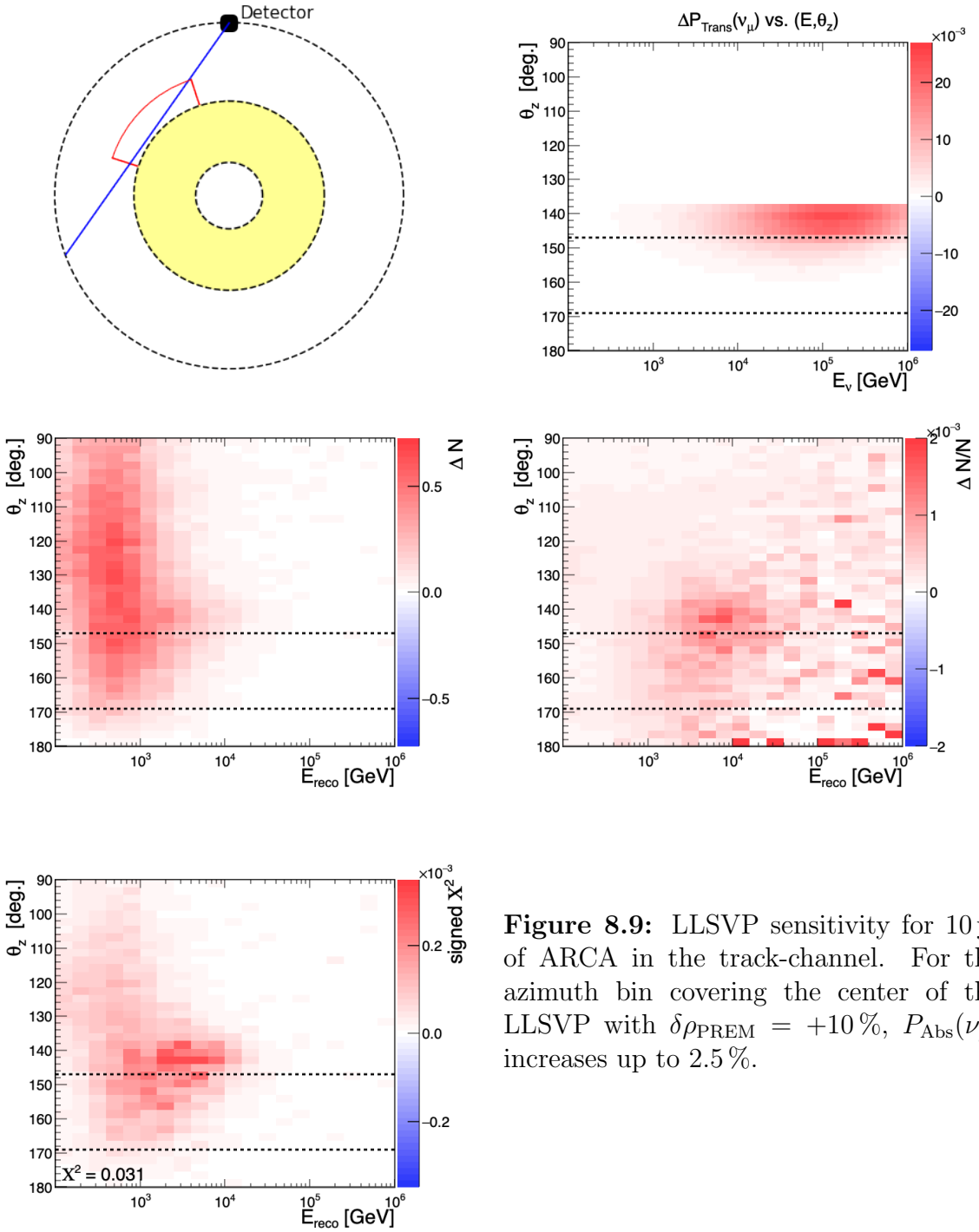

Figure 8.9: LLSVP sensitivity for 10 yr of ARCA in the track-channel. For the azimuth bin covering the center of the LLSVP with $\delta\rho_{\mathrm{PREM}} = +10\,\%$, $P_{\mathrm{Abs}}(\nu_\mu)$ increases up to 2.5 %.

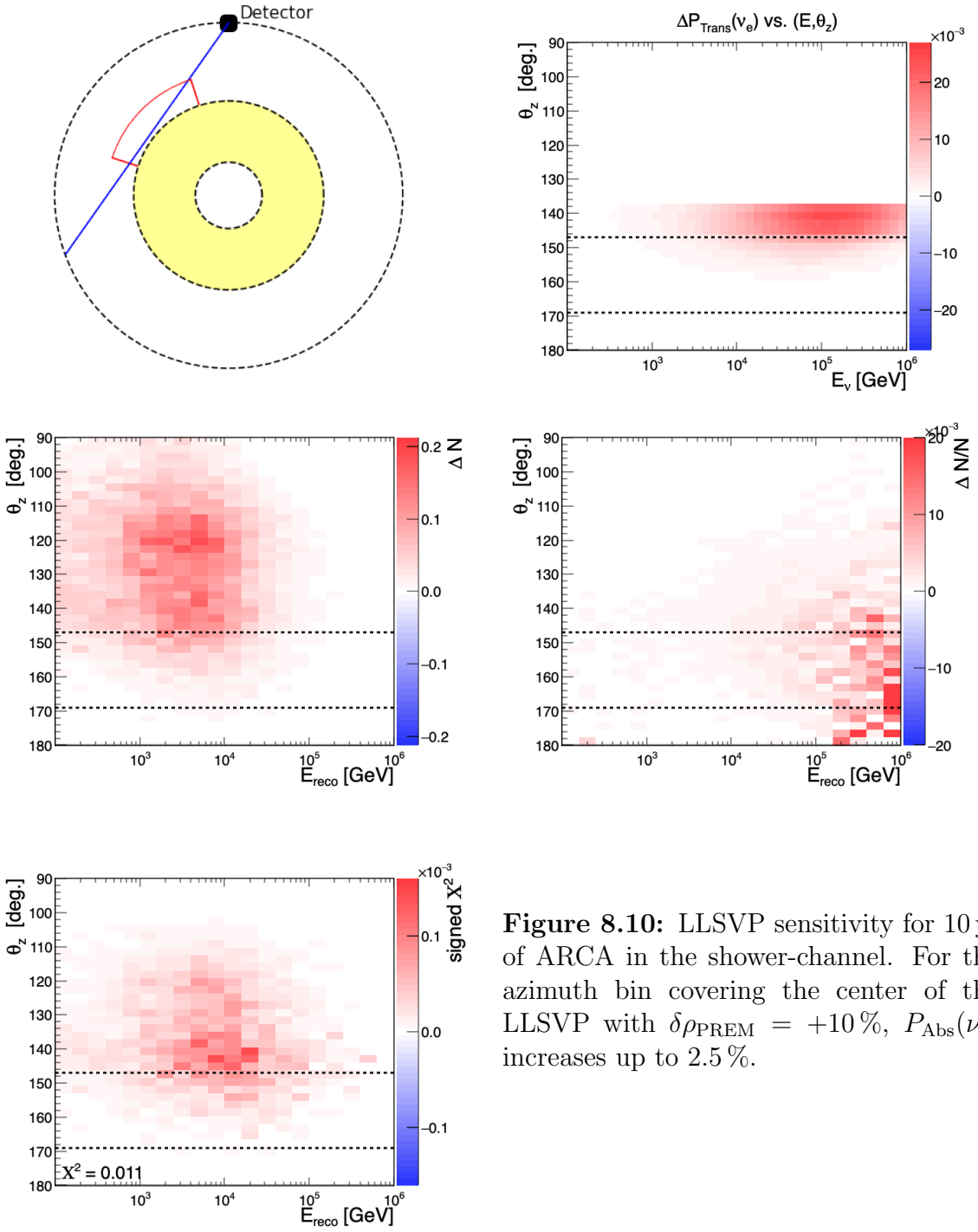

Figure 8.10: LLSVP sensitivity for 10 yr of ARCA in the shower-channel. For the azimuth bin covering the center of the LLSVP with $\delta\rho_{\mathrm{PREM}} = +10\,\%$, $P_{\mathrm{Abs}}(\nu_e)$ increases up to 2.5 %.

Chapter 9

Oscillation tomography with KM3NeT/ORCA

Contents

All density analyses presented in chapter 8 can be executed also with ORCA by studying neutrino oscillations in matter under the assumption of a known Z/A. We find that ORCA performs significantly better in all aspects compared to ARCA, which is why the studies presented in this chapter are extended into more detail and are further set into context of the geophysical state of the art.

In addition to density studies, the connection of neutrino oscillations in matter to the Z/A allows the study of the chemical composition of the Earth's deep interior, an interesting complement to seismic methods that cannot by themselves disentangle the respective contributions of temperature and chemistry. This provides a strong motivation for oscillation tomography. The focus lies here on the outer core, whose matter density is well constrained by PREM, but whose chemical composition remains the object of intense debates about geophysical and geochemical models.

9.1 The ORCA MC sample

The latest Monte Carlo simulation for the full ORCA detector was produced in 2019. It was used in the most recent publications on the determination of the neutrino mass ordering with KM3NeT [92, 168] and is discussed in the first reference in terms of resolution and classification performances. The energy and angular reconstruction for the track and shower class are shown here in Fig. 9.1. The PID was already discussed in chapter 6. In order to get an intuition about the expected event statistics, as in chapter 8, the annual event rates per PID class are shown in Fig. 9.2, with ∼10k track- and ∼20k shower-like events.

9.2 Density profiling

9.2.1 Constant densities

The analysis of the 1D density profile of the Earth with absorption tomography (sec. 8.2) is now repeated with ORCA with oscillation data. For this and all consecutive analyses of matter densities with oscillation tomography, the Z/A is assumed to be known and fixed to 0.4661 (pure FeNi alloy) for the whole core and to 0.4961 (pyrolite) for the mantle.

Hypothesis test of two different Earth models The first exercise, *i.e.* comparing the signal resulting from a 5-layer PREM towards our default 42-layer model, is shown in Fig. 9.3 for the shower channel, which appears to contain the dominant distribution to the overall signal, and in Fig. 9.4 for the track channel. The difference in the neutrino oscillation probabilities between the two radial models are shown in Fig. 9.5. At this point it should be remembered that I assume the normal mass ordering, leading to matter effects only in the neutrino oscillations, while antineutrino oscillations (Fig. A.4) are about one order of magnitude lower. Here, because of the high component of ν_μ in the atmospheric neutrino flux, the main sensitivity towards the density profile will come from the $\nu_\mu \to \nu_x$ oscillations. Indeed, the difference of interacting event rates of $\overset{(-)}{\nu}{}_e^{\mathrm{CC}}$ and $\overset{(-)}{\nu}{}_\mu^{\mathrm{CC}}$ (*i.e.* the main contribution to the shower- and track PID class) interactions show the same pattern as the $\nu_\mu \to \nu_e$ and $\nu_\mu \to \nu_\mu$ oscillation, respectively. Oscillations into ν_τ play only a small role, due to the low ν_τ cross sections below ∼20 GeV.
After taking into account the detector response, the fast $\nu_\mu \to \nu_\mu$ oscillations are smeared in the statistics histograms, while the pattern in the shower channel is more coarse and can be better resolved. This explains the high contribution of about 80 % from the shower channel to the total significance with which ORCA can distinguish between both density profiles. The highest sensitivity contribution appears above the CMB at $\theta_z > 147°$, from neutrinos that cross only the mantle, where the density difference between the two radial models is the most significant, similar to what we have seen with absorption tomography.
Combining the $\Delta\chi^2$ of both PID classes gives the total sensitivity of $\Delta\chi^2_{\mathrm{stat}} = 6.36$. Taking into account the MC error reduces this to $\Delta\chi^2 = 4.99$. If one compares these

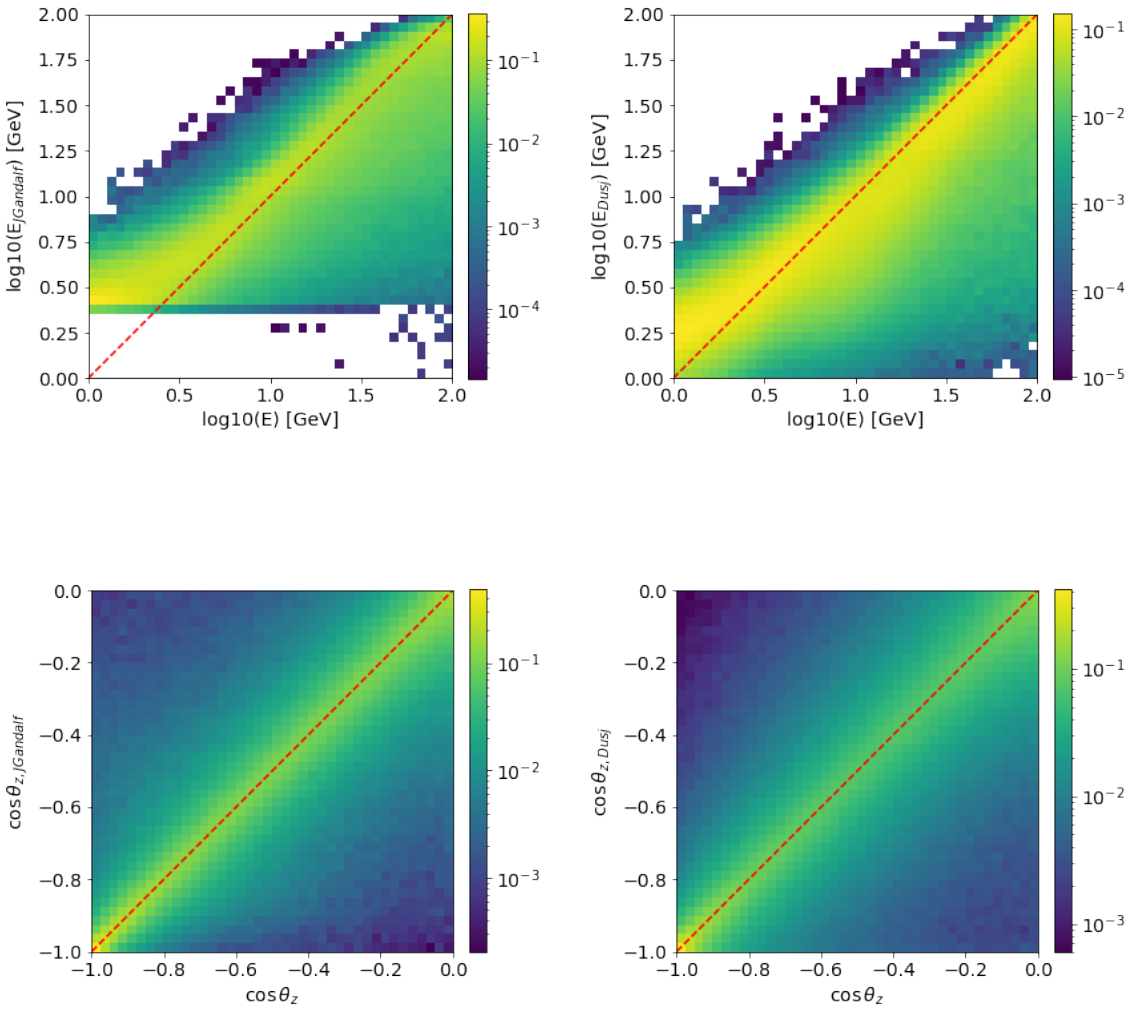

Figure 9.1: Energy (top) and angle (bottom) reconstruction of ORCA with `JGandalf` (left, for tracks) and `Dusj` (right, for showers), normalised per energy bin.

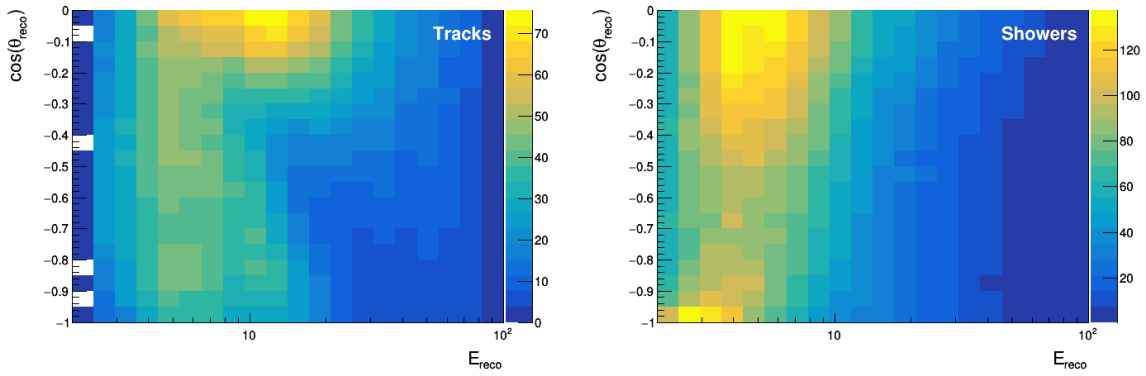

Figure 9.2: Annual atmospheric event rates per year and PID class for ORCA.

numbers with the corresponding ones obtained with ARCA, it appears that ORCA performs at least 4 times better than ARCA when taking into account the MC error. The main reason for this is the much higher neutrino flux at GeV energies and thus the overall higher event rates in the energy range of neutrino oscillations. In contrast to ARCA, the dominant areas of the absolute and relative differences in event rates (ΔN & $\Delta N/N$) overlap in the ORCA simulation, yielding a higher $\Delta\chi^2$.
The fact that the impact of the MC error is significantly smaller for ORCA is a consequence of the underlying MC production, that covers only three orders of magnitude in energy (with a higher sampling in the energy range of matter oscillations) instead of six orders of magnitude in the ARCA MC, consequently yielding more statistic per bin in the response matrix.

Fit of a 5-layer model to PREM The good performance of this first test of the method is also seen in the results of fitting the Earth's density profile, shown in Fig. 9.6. Again the start values of the layer densities were set to $5\,\mathrm{g\,cm^{-3}}$ and no systematics were used (their impact is discussed in sec. 9.4).

The quality of the fit is much better than for absorption tomography. Only the average density of the outer part of the mantle appears to be overestimated with oscillation tomography, where the fit yields a minimum at $\Delta\chi^2_{\text{free}} = 1.45$, almost 3 times lower than for test hypothesis in Fig. 9.6.

One way to force the fit towards more reasonable densities is to constrain the total mass and inertia of the Earth (or rather our 42-layer realisation of PREM). This also decreases the error bars (Fig. 9.7) as the inertia constraint reduces the possibility to compensate *e.g.* for missing matter in one layer by adding it in another layer. The effect of the constraints is the strongest in the outermost layer of the outer core and the mantle, since they contribute the most to the mass and inertia, due to their large volumes relatively far from the rotation axis.

We can now set limits on the Earth's mass based on oscillation tomography: for the unconstrained fit of our 5-layer Earth model we find $M_{\oplus,\nu} = 6.19^{+0.39}_{-0.39} \times 10^{24}\,\mathrm{kg}$ and $I_{\oplus,\nu} = 8.53^{+0.45}_{-0.45} \times 10^{37}\,\mathrm{kg\,m^2}$. Relative to the mass of our input PREM, this reads as $M_{\oplus,\nu} = (1.027 \pm 0.065) M_{\oplus,\mathrm{PREM}}$, which is comparable to the reported $M_{\oplus,\nu} = (1 \pm 0.084) M_{\oplus,\mathrm{PREM}}$ of a 10 year simulation of DUNE in [129]. It is interesting to note, that the superior event resolution capabilities of DUNE seem to compensate the large difference in size compared to ORCA. We will also observe this in chapter 10.

For the constrained case we obtain $M_{\oplus,\nu} = 6.03^{+0.23}_{-0.23} \times 10^{24}\,\mathrm{kg}$ and $I_{\oplus,\nu} = 8.09^{+0.18}_{-0.18} \times 10^{37}\,\mathrm{kg\,m^2}$, obviously matching our input PREM. Using the constraints of the Earth parameters yields $\Delta\chi^2_{\text{constrain}} = 4.18$, which is again similar to the test hypothesis in Fig. 9.6. From that one can conclude that ORCA can reject the hypothesis of a 5-layer Earth with a CL of 96.8 % with the help of gravitational limits on Earth mass and inertia. However, with the tight limits from oscillation tomography, the approach of using only 5 layers of constant densities seems to be an oversimplification. It even prevents us to find the accurate average density in the outer part of the mantle, due to the absence of transmission zones that appear to have some impact on the observed oscillations. In principle one could increase the number of bins for fitting a finer density profile, but not only would the necessary computing time increase significantly with

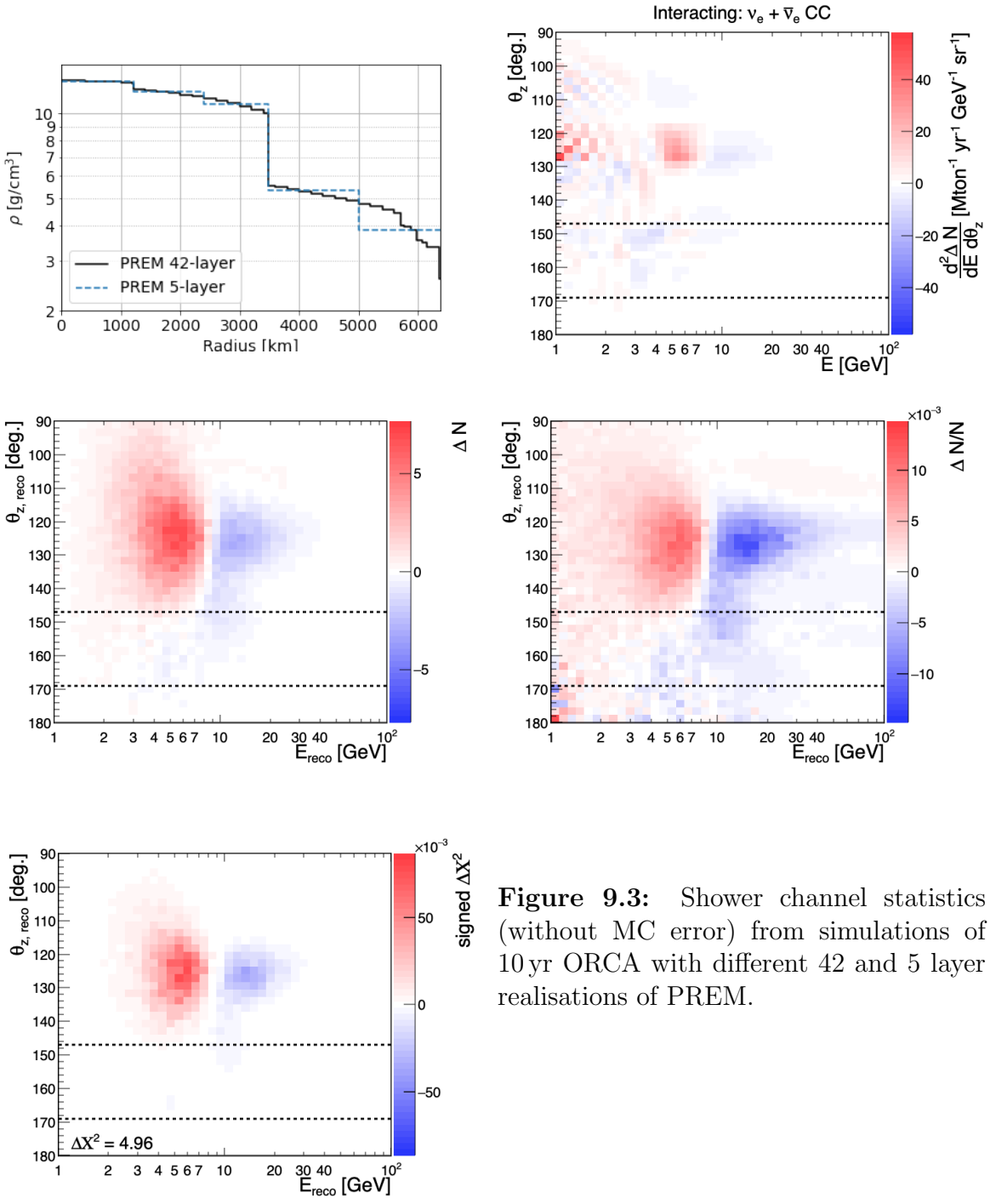

Figure 9.3: Shower channel statistics (without MC error) from simulations of 10 yr ORCA with different 42 and 5 layer realisations of PREM.

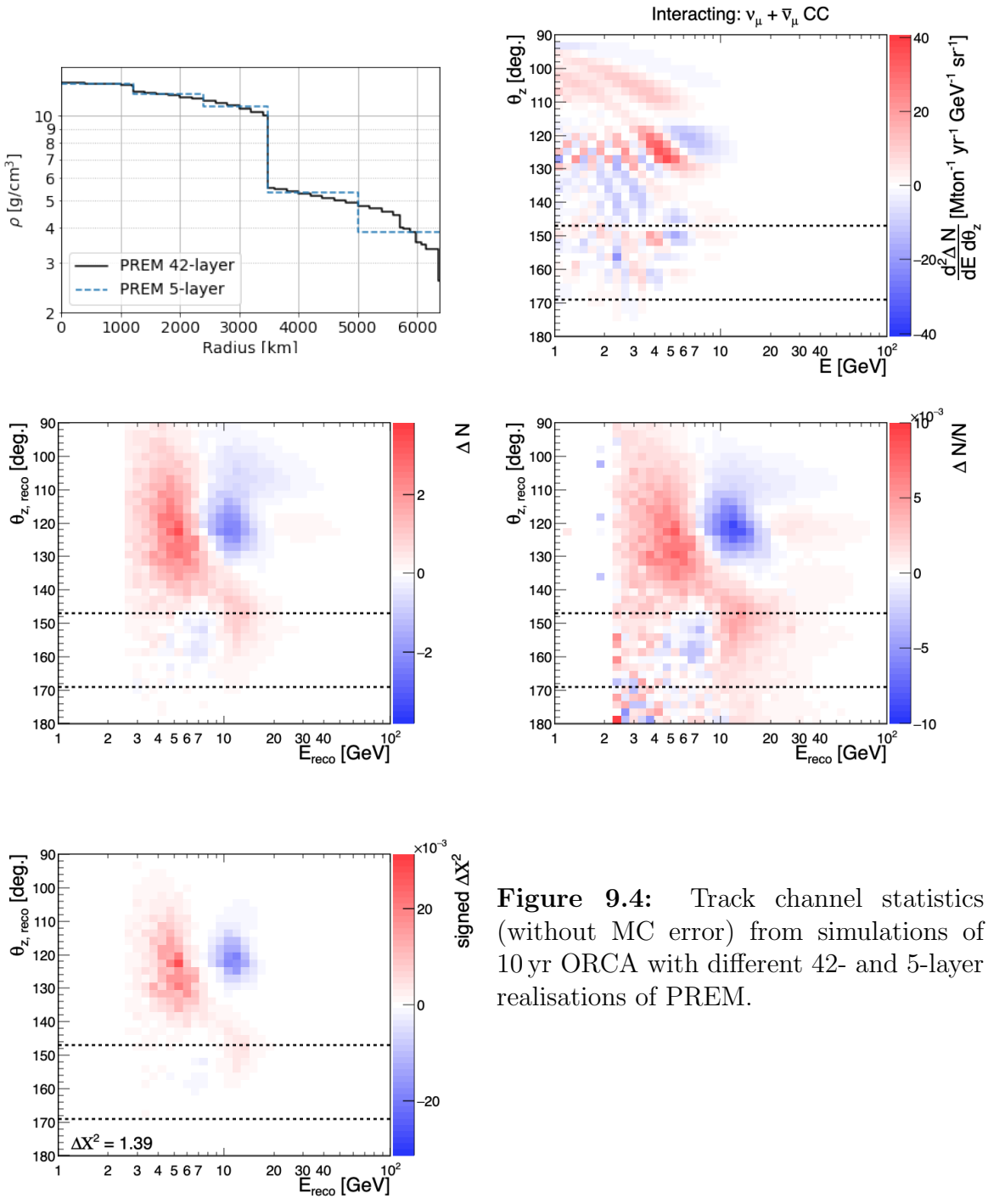

Figure 9.4: Track channel statistics (without MC error) from simulations of 10 yr ORCA with different 42- and 5-layer realisations of PREM.

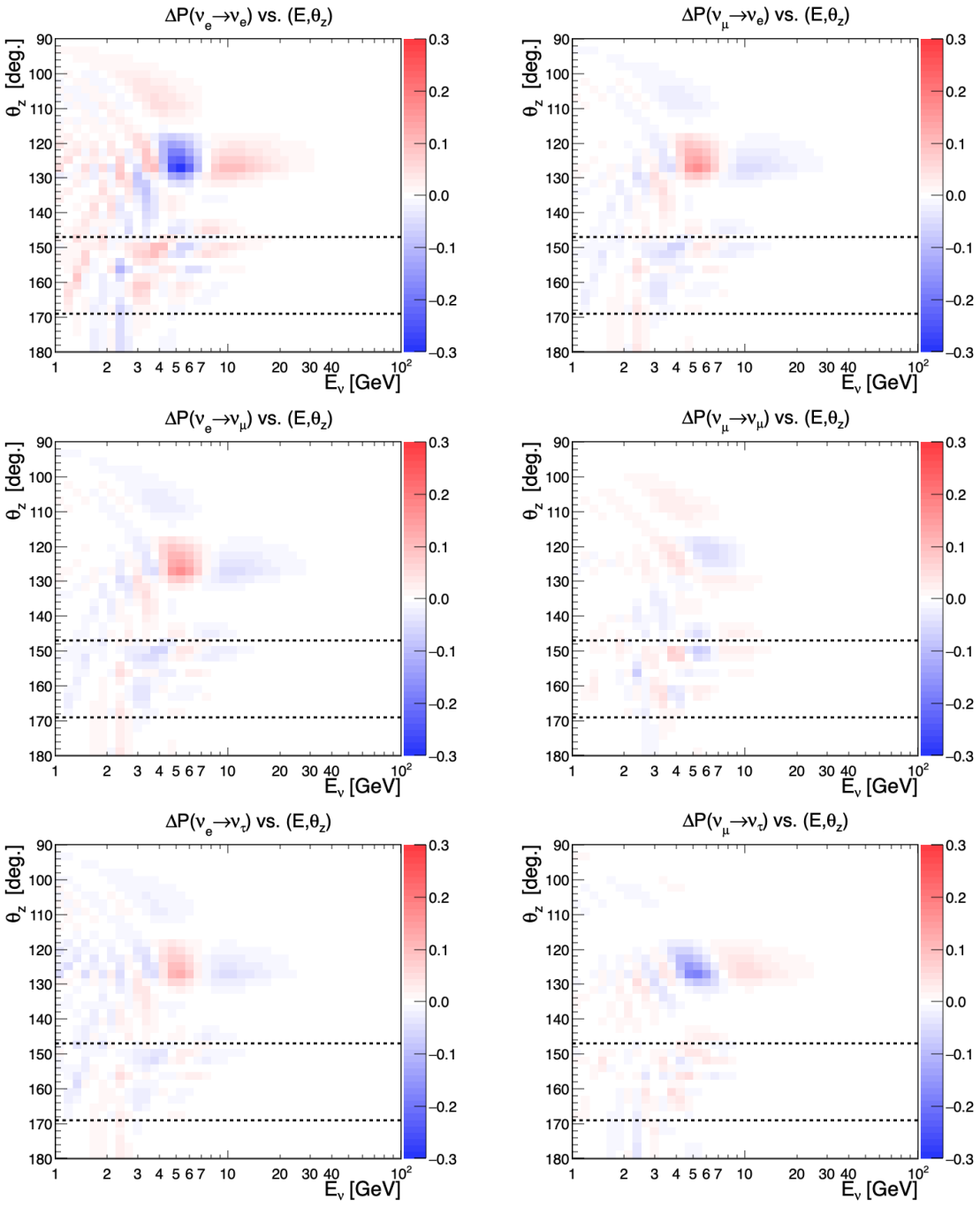

Figure 9.5: Differences in ν oscillation probabilities between 42- and 5-layer PREM.

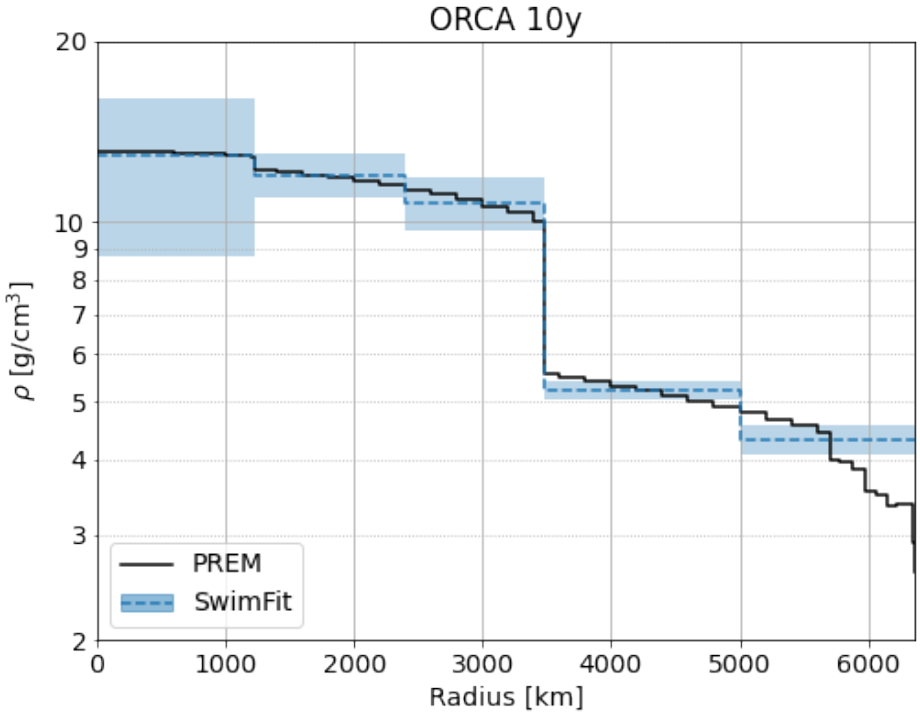

Figure 9.6: Density profiling with 10 years of ORCA. The error bands correspond to the 68 % posterior.

the number of bins, also the errors would get bigger due to the strong correlations between all layers. These drawbacks motivate the development of a slightly different approach, described below.

9.2.2 Relative densities

In Earth science it is common to measure density not in absolute values but as variations relative to PREM. Technically this can here be done in a similar way as follows: we reuse our 5 defined layers $\hat{l}_i$ but instead of setting each layer to a constant density $\hat{\rho}_i$ (which was the fit parameter before) the new density is now $\rho_j = \rho_{j,\mathrm{PREM}} \times \hat{s}_i$ with $j \in (1, .., 42)$ corresponding to the 42-steps and $\hat{s}_i$ a scaling parameter that is fitted for each of the 5 layers. The illustration in Fig. 9.8 shows how a density profile based on PREM changes with a relative change of 3 % in the inner core (layer 1) or outer core (layer 2 & 3).

The result of fitting the Earth's density profile relative to PREM with this method is shown in Fig. 9.9 (without constraints on the Earth parameters). The resulting 68 % posterior interval on Earth's mass and inertia are $\delta M_{\oplus,\nu} = +0.39/-0.38 \times 10^{24}\,\mathrm{kg}$ and $\delta I_{\oplus,\nu} = 8.53^{+0.49}_{-0.49} \times 10^{37}\,\mathrm{kg\,m^2}$. The error bars (and consequently the limits on mass and inertia) are of comparable size for both approaches, the constant and the relative density profiling, which shows the robustness of the analysis towards eventual mismatches between the shape of our model PREM and the real Earth density profile.

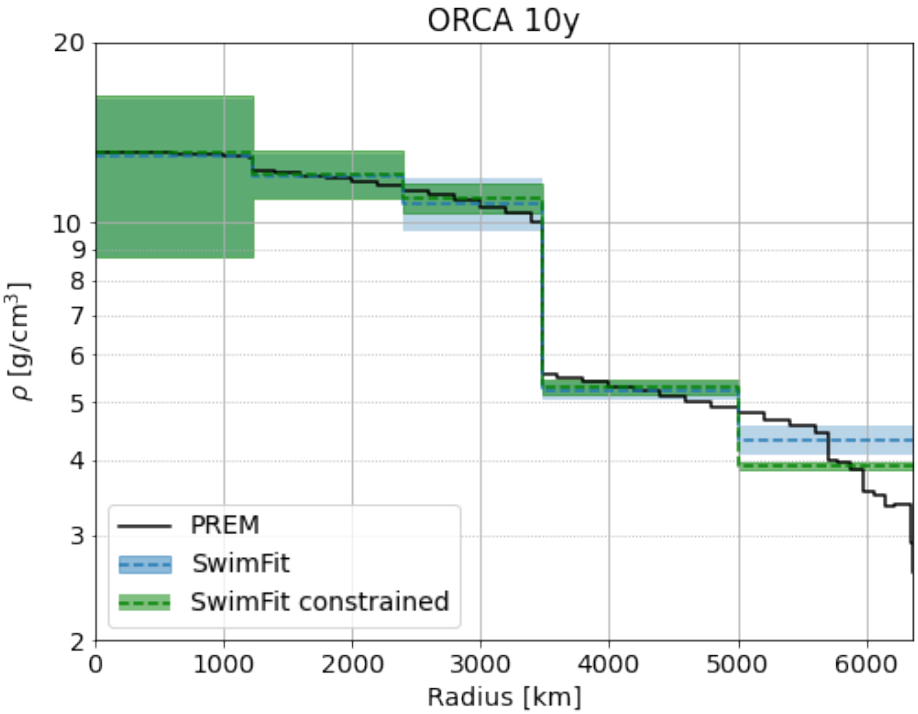

Figure 9.7: Density profiling with 10 years of ORCA. Overlayed in green are the errors when the total mass and inertia are constrained to the "true" value, which is calculated from the 42-layer PREM. The errorbands give the 68 % posterior.

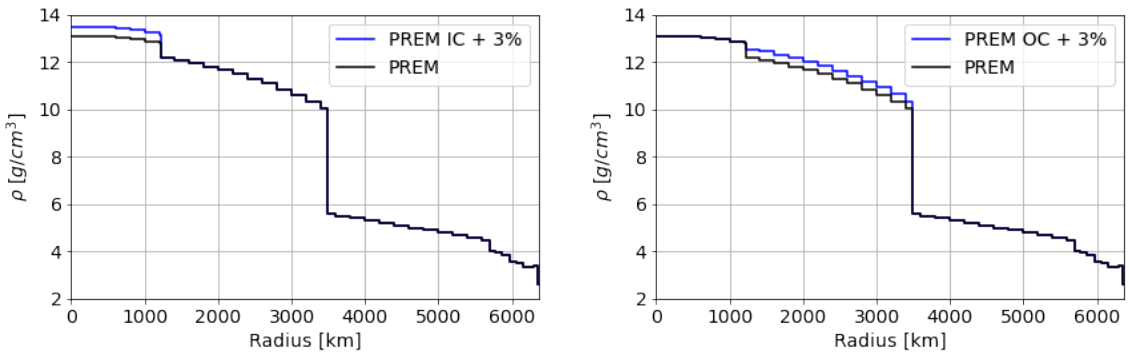

Figure 9.8: Example of a density scaling of 3 % relative to PREM in the inner (left) and outer (right) core.

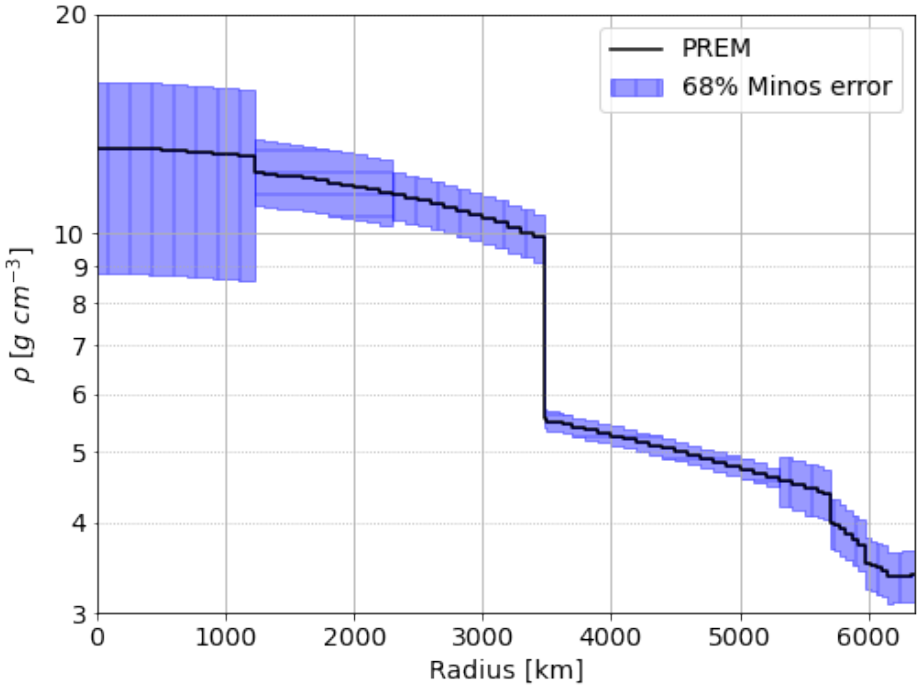

Figure 9.9: Density profiling with 10 yr ORCA by fitting variations to PREM for whole layers.

Combination with normal mode tomography Despite the great improvement obtained by using oscillations instead of absorption tomography for the density profiling of the Earth, the resolution of ORCA is still not competitive with the sub-percent uncertainties on PREM. In the last months of my doctorate we have been starting a collaboration with a seismology Professor at University of Utrecht, Netherlands and her PhD student, who study the Earth's interior using seismic wave data from whole-Earth oscillations (normal mode tomography), to search for a combined use of the results from neutrino tomography and seismology. Normal mode frequencies depend on three main parameters: S and P wave velocities and the matter density. They can be reconstructed from seismic measurements using the least-squares inversion method as described by [169], which is used by our collaborators and described *e.g.* in [170]. Because it is not possible to draw conclusions on a single parameter from those seismic measurements, but only their interplay, one could use the uncertainties on the density profile determined with neutrino tomography as a prior to the seismology framework. The precondition is however, that the priors are of a Gaussian shape. To verify that, I scanned the log-likelihood profile for all possible combinations of two layers, for density variations up to 10 % (Fig. 9.10).

Multiple options exist to determine the actual value of the prior. Fig. 9.11 shows the 1D log-likelihood profile, the lower and upper `Minos`-error, as well as the parabolic error interval extracted from the covariance matrix per layer. During the minimisation of the LLR by `Minuit2` a first estimation of the uncertainty interval of the fit parameter is made under the assumption of a parabolic log-likelihood profile which is zero at

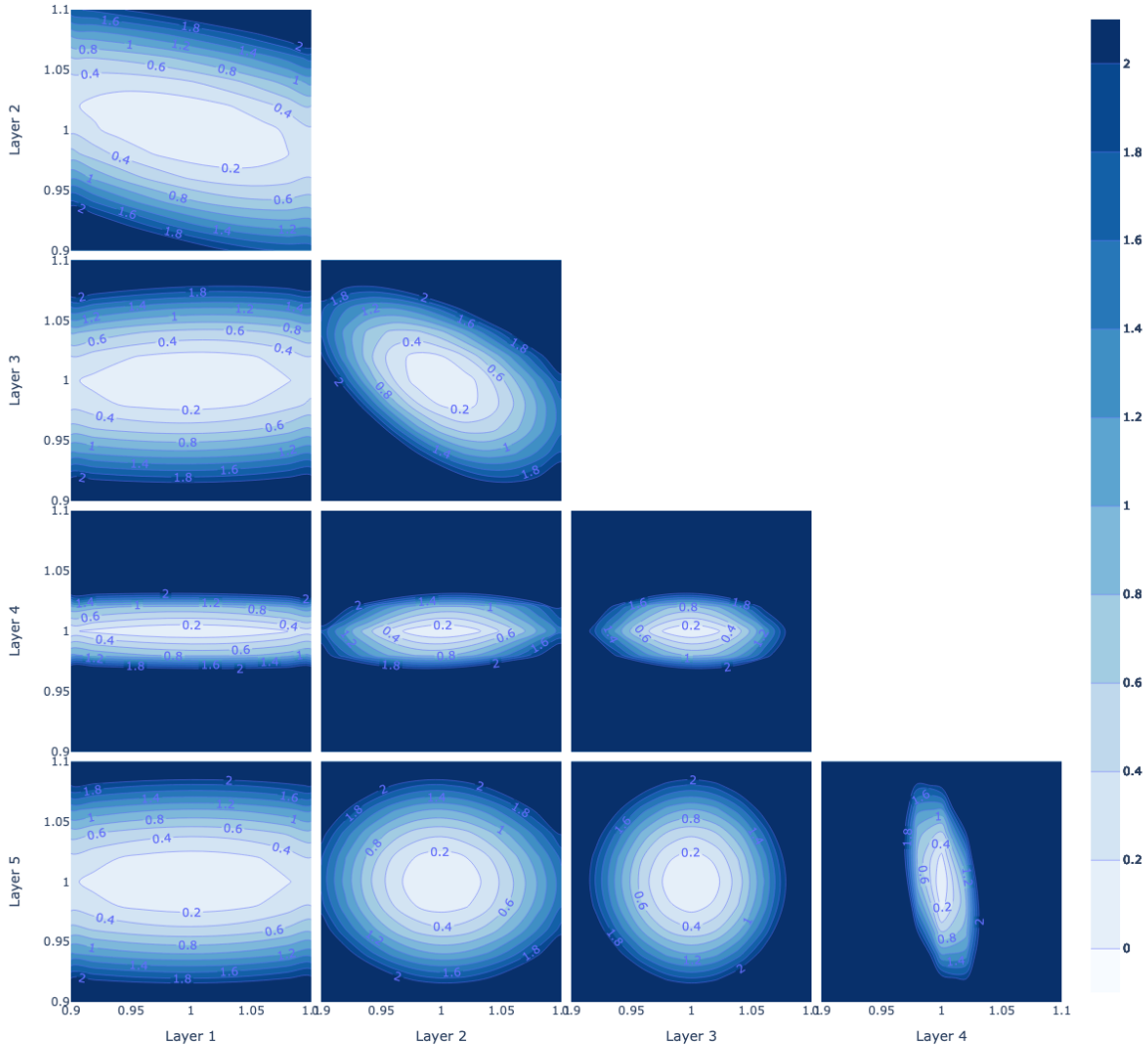

Figure 9.10: 2D likelihood profiles of the density profiling with 10 yr ORCA between respective two layers, visualising their correlations. The axes are the density scaling $\hat{s}_i$ relative to PREM for the indicated layer i. The upper limit of the color scale was set to 2, as we are only interested in the region of the 1σ interval. Higher values of $\Delta\chi^2$ are in dark blue. The profiles show a 2D Gaussian shape, which qualifies them for being used as priors for the HMC method.

the fit minimum. The inverse of the second derivative of the found parabola is stored in the covariance matrix, which is in this case given by

$$\mathbf{C}_M = \begin{pmatrix} 0.03825 & & & & \\ -0.00773 & 0.00581 & & & \\ 0.00069 & -0.00226 & 0.00319 & & \\ -0.00033 & 0.00022 & -0.00012 & 0.00054 & \\ 0.00021 & -0.00020 & -0.00003 & -0.00055 & 0.00389 \end{pmatrix}.$$

The slope of the 2D profiles is related to the values at the respective position in the covariance matrix (below the diagonal). Strong anti-correlations are visible between layer 1 & 2, and between layer 2 & 3, thus in the Earth's core that is sampled the least. Also layers 1 to 3 are thinner than layer 4 & 5 in the mantle. A general observation about the density profiling, is that the error bars grow quickly if the number of fitted layers is increased, due to the enhanced correlations between thin neighbouring layers. The error estimation by `Minos` does not use the simplification of a parabolic log-likelihood profile, but instead samples the likelihood in order to find where the LLR equals a user specific value (here $\Delta\chi^2 = 1$). It is thus surprising that the `Minos` error does not match the manually derived log-likelihood profile but instead the parabolic one from the covariance matrix. The discrepancy may arise from internal algorithms of `Minos`. It is however convenient that the `Minos` errors are in good agreement with the covariance matrix, as it fulfills the condition for Gaussian priors and thus the direct use for the HMC. As the mentioned collaboration only started recently, no results from the combination of neutrino and seismic data can be presented yet.

9.3 Probing LLSVPs with oscillation tomography

For the study of LLSVPs with oscillation tomography in ORCA we use the same methods as described in chapter 8 and the same model LLSVP (*i.e.* $\delta\rho_{\text{PREM}} = +10\,\%$) for which the results as shown in for tracks Fig. 9.12 and for showers in Fig. 9.13. The oscillation probabilities (Fig. 9.14) differ by up to 20 % around 7 GeV, where the MSW-resonance for mantle-like electron densities is expected. The range of θ_z fits the location of the LLSVP. The differences in the interacting event rates in the track- and shower class are again dominated by the $\nu_\mu \to \nu_\mu$ and $\nu_\mu \to \nu_e$ oscillation, respectively. Consequently, the distributions of ΔN, $\Delta N/N$ and consequently $\Delta\chi^2$ are centered around this energy and this zenith angle. The total significance level, *i.e.* summed over all azimuth bins and divided by n (eq. 8.2), with which ORCA can detect this specific LLSVP is $\Delta\chi^2 = 0.45$[1], and thus almost 100 times higher than with absorption tomography. Although the tested LLSVP position was chosen as the one yielding the strongest signal, ORCA still does not reach the 1σ CL, even with the extreme density variation used.

An interesting observation is that here, contrary to the study of the Earth's radial density profile, both PID channels contribute almost equally to the total significance,

[1]Note that in the figure, (i) the $\Delta\chi^2$ is unweighted with the inverse of the number azimuth bins and (ii) the maximal value is obtained for the azimuth direction with the largest path length through the LLSVP.

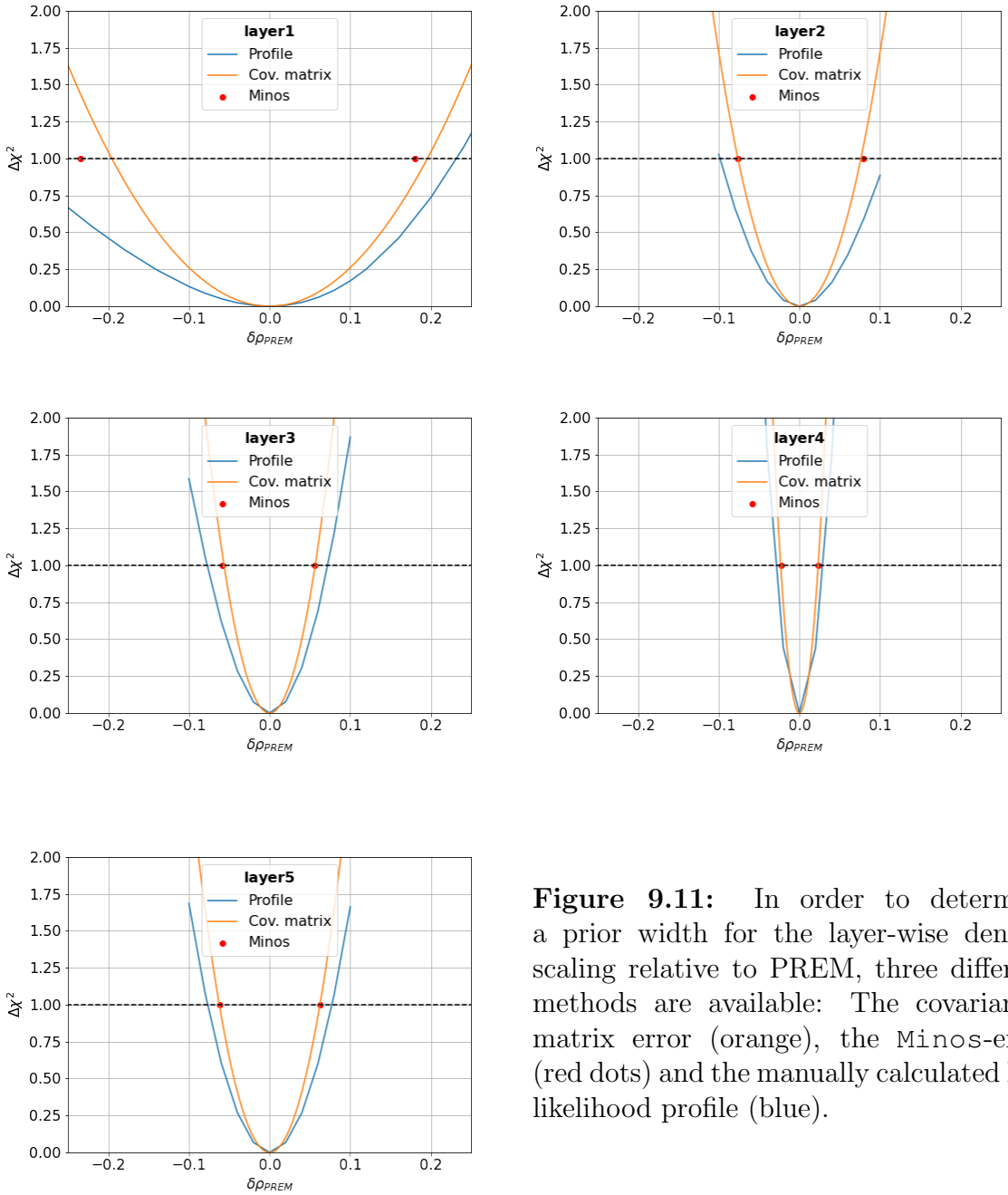

Figure 9.11: In order to determine a prior width for the layer-wise density scaling relative to PREM, three different methods are available: The covariance-matrix error (orange), the `Minos`-error (red dots) and the manually calculated log-likelihood profile (blue).

with even a slight excess in the track channel. This can be related to the fact, that only neutrinos in a small angular region traverse the LLSVP. Therefore the angular resolution becomes more important, which is better for track-like events. Also, the energy resolution is not sufficient to resolve the expected signal in the shower channel. The fact that different applications of neutrino tomography appear to depend on different detector capabilities is also observed when different detectors are investigated in chapter 10.

The estimation of the impact of changing LLSVP positions, densities and shapes was done by profiling the LLR while varying each of these parameters respectively. First, the positional dependence of the LLSVP is tested, by changing the relative angle Θ_L between its center and the detector (Fig. 9.15, left panel). We see that the most favourable position corresponds to an angular rotation 40° to 60° away from the detector. In that case, the zenith angle window in which neutrinos cross the LLSVP would be only of a few degrees width, but the neutrino path length across LLSVP would be maximal. For angles $\Theta_L > 90°$ on the other hand, where more neutrinos cross the LLSVP, but only over a short pathlength, the LLSVP would be almost transparent for ORCA.
Another reason why LLSVP positions opposite to the detector location are disfavoured is the zenith dependency of the atmospheric neutrino flux, that results in more neutrinos reaching the detector from the horizon and less straight up-going neutrinos.
It is interesting to compare the optimal configuration between detector and LLSVP found here, with the actual position of the Pacific and African LLSVPs as described in chapter 3: With a relative angle of $\Theta_L \approx 45°$ the African LLSVP is perfectly located to be seen by ORCA. The Pacific LLSVP on the other hand has a relative angle of $\Theta_L \approx 127°$ with respect to ORCA, which will make it hardly detectable.

Second, the impact of the shape of the LLSVP is investigated, in terms of its thickness and lateral extension. The LLSVP shell-shape used so far, with a thickness $d = r_2 - r_1 = 1000\,\text{km}$ and an opening angle $\phi = 27°$ yields a volume of $\sim 1 \times 10^{10}\,\text{km}^3$, using

$$V = \frac{2\pi}{3}(r_2^3 - r_1^3)(1 - \cos\phi)\ . \tag{9.1}$$

Fixing V for a fair comparison between different shapes, one can derive a relation between the thickness d and the opening angle ϕ as

$$d(\phi)|_V = \sqrt[3]{\frac{3V}{2\pi(1-\cos\phi)} + r_1^3} - r_1\ . \tag{9.2}$$

Using that relation, I calculated the sensitivity for different LLSVP shapes, *i.e.* pairs of d and ϕ, while keeping V fixed (Fig. 9.15, right panel). Starting from thin LLSVPs that extend over a large surface of the core, and moving towards narrower and thicker shapes, I found that the latter case is strongly favoured, with a gain of a factor $\sim$10 between the two extreme cases tested. Note that all shapes were set to $\Theta_L = 45°$, assuming that it is the optimal spot for all shapes. Although this is an interesting and innovative finding of the thick but narrow shape being detectable the best, I kept the initial thickness and width based on seismic measurements for the rest of the LLSVP analysis.

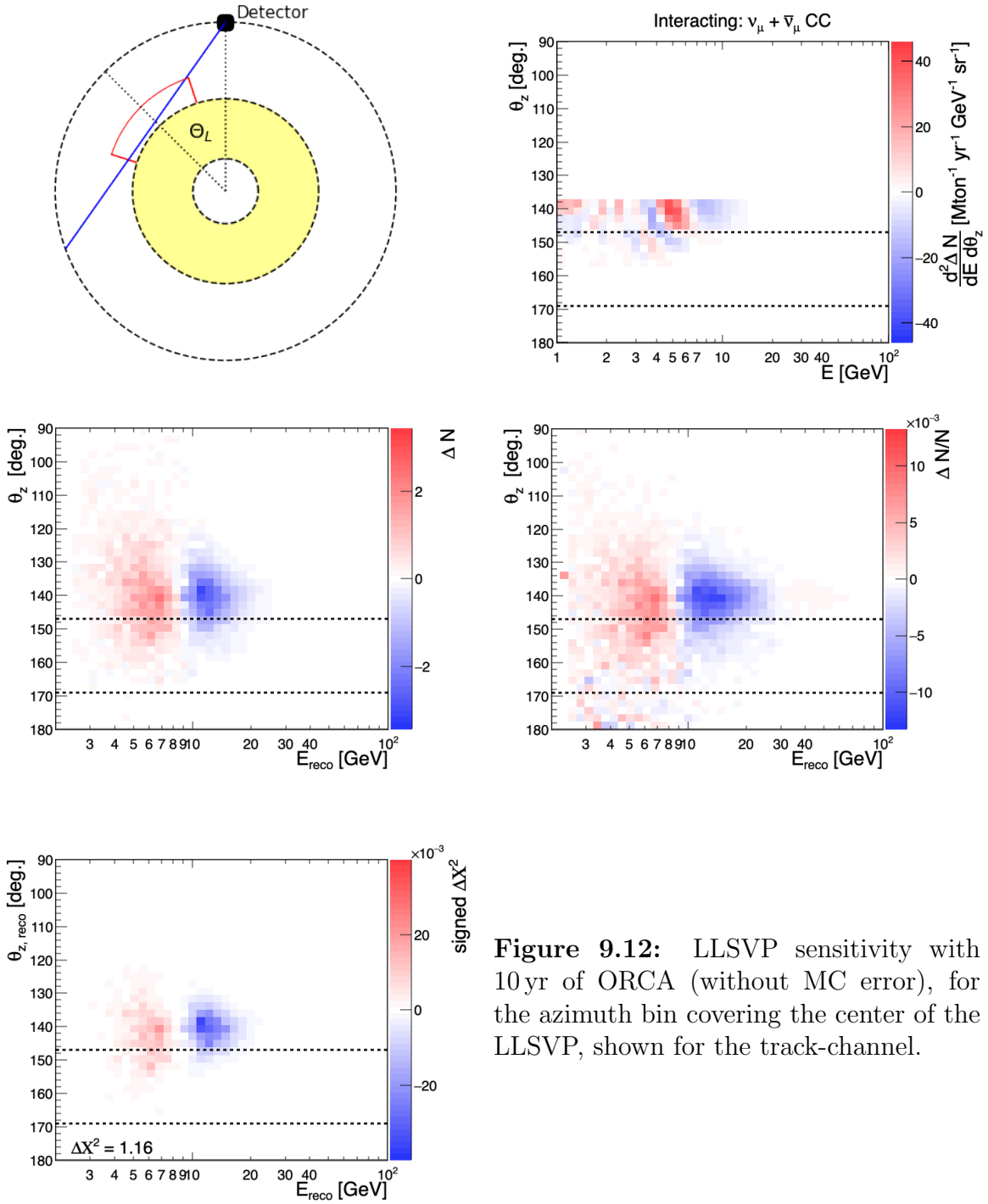

Figure 9.12: LLSVP sensitivity with 10 yr of ORCA (without MC error), for the azimuth bin covering the center of the LLSVP, shown for the track-channel.

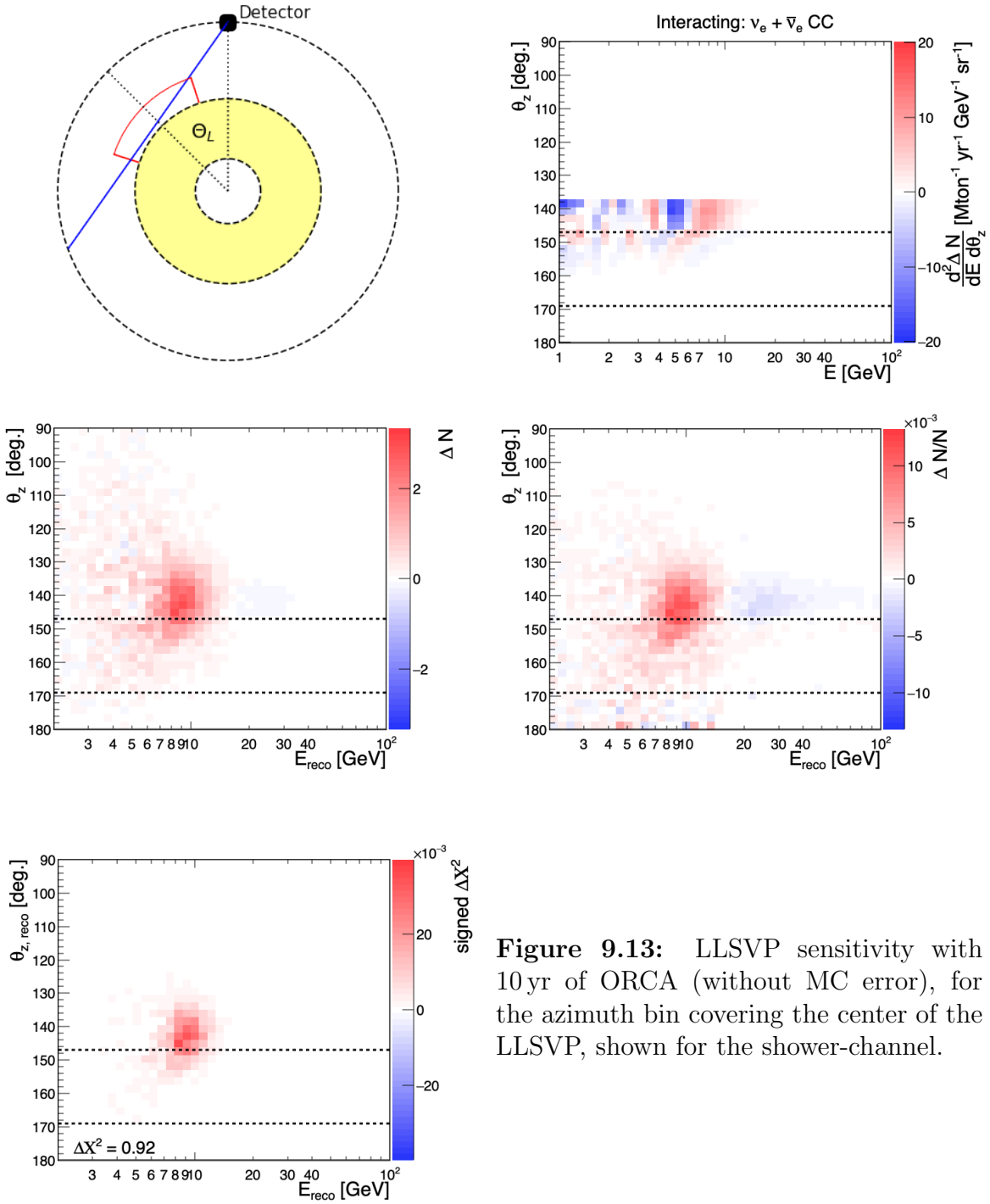

Figure 9.13: LLSVP sensitivity with 10 yr of ORCA (without MC error), for the azimuth bin covering the center of the LLSVP, shown for the shower-channel.

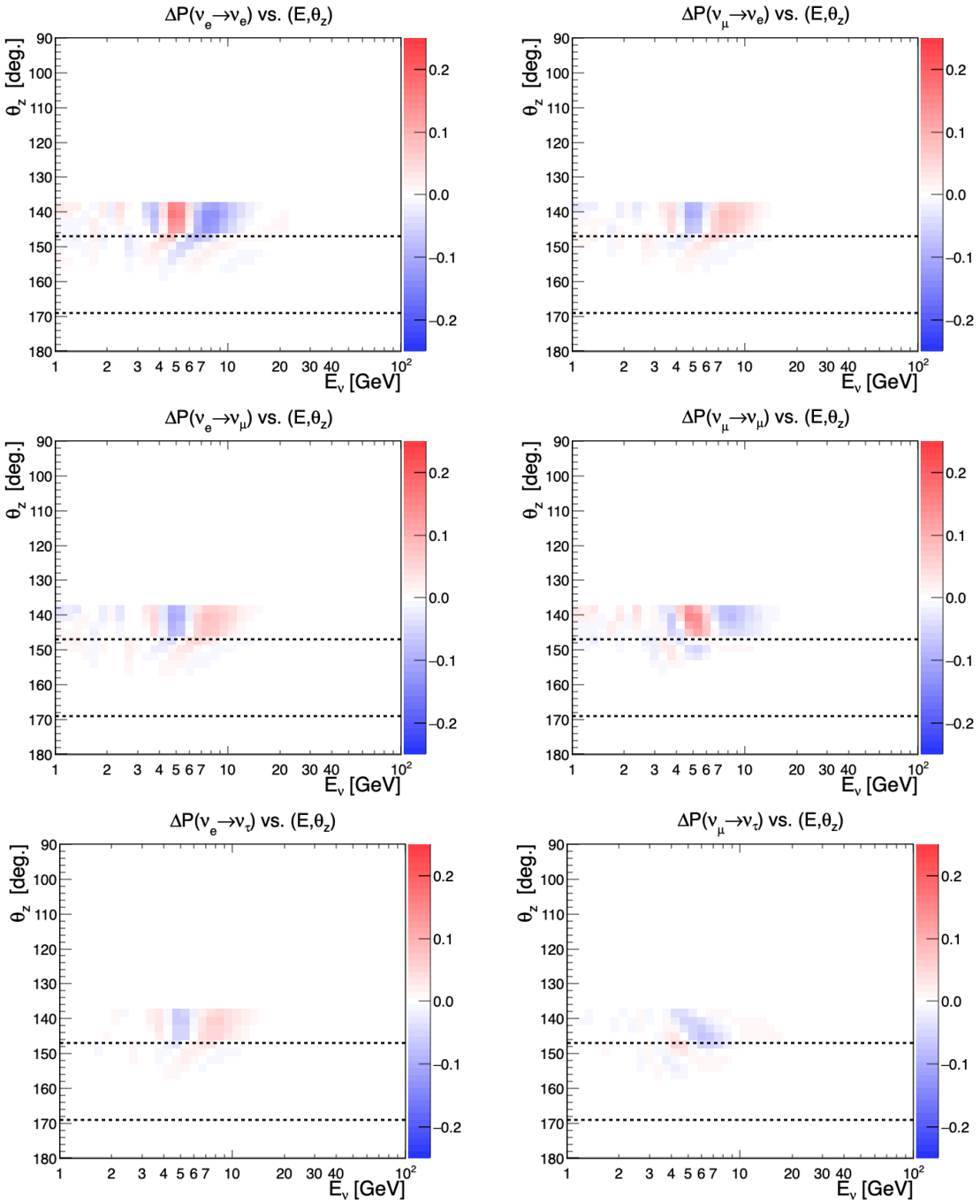

Figure 9.14: Differences in ν oscillation probabilities between homo- and heterogene mantle.

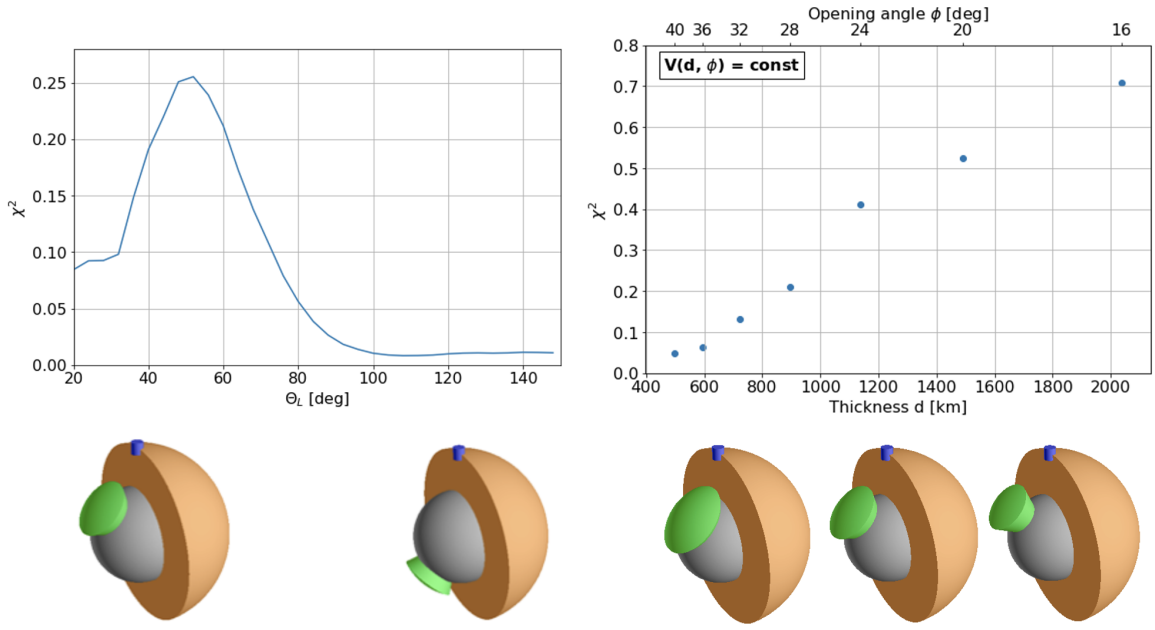

Figure 9.15: Analysis of the LLSVP visibility as a function of its relative position Θ_L to the detector (left) and its shape, parameterised by the thickness d and the opening angle ϕ for a fixed volume V (right).

Finally, the log-likelihood profile from different LLSVP densities is drawn (Fig. 9.16). The density could only be constrained within about +24 %/-20 % precision at the 1σ level, or in other words, only a LLSVP 24 %(20 %) denser(lighter) than the mantle could be detected with ORCA. These numbers are too large to be of geophysical interest for now and require more advanced detectors, as studied in chapter 10.

9.4 Outer core composition

In this section, I release the previously made assumption of knowing the Z/A, and instead I fix the matter density to the PREM values. This allows us to study the electron density in the Earth, with the aim to draw conclusions about its chemical composition. That is not possible with absorption tomography and thus a strong motivation to study oscillation tomography with ORCA. Technically, the analysis is identical to that of the matter density, since it makes no difference for the electron density, whether a scaling is applied to the matter density or the Z/A(eq. 3.8). The only difference is the interpretation of the result and – with respect to the interest of geophysicists – the Earth regions of interest. For the chemical composition of the Earth, the outer core is of special interest. Thus, instead of fitting the whole Earth, I simplify the analysis by fixing the inner core and mantle composition (i.e. Z/A) and use only one variable Z/A for the outer core.

This kind of analysis was already executed in [162] (cf. section 9.2) and is here to some extent repeated with the following adaptations that reflect the evolution of our global knowledge of the neutrino oscillation parameters thanks to new measurements, and also the improvements achieved on the simulation tools and methods within the

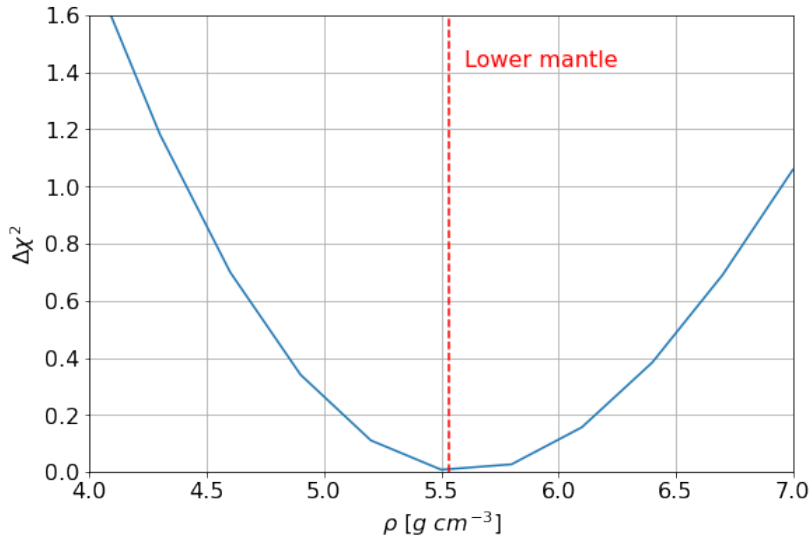

Figure 9.16: $\Delta\chi^2$ profile of the sensitivity towards the LLSVP density, for the optimal position ($\Theta_L = 45°$) with 10 yr of ORCA data.

ORCA collaboration itself:

- Using updated oscillation parameters from NuFit5.0[55]
- Using as the true value of $\theta_{23} = 49.2°$
- Switching from ORCA MC 2016 to the latest MC from 2019
- Increasing the binning to 40 bins in $\log(E)$ and θ_z due to higher MC statistics

Figure 9.17 shows the expected signal from a +5 % variation, respectively in the outer core or in the whole mantle Z/A, for the track- and the shower-channel, for 10 yr operation of ORCA. Compared to Fig. 9.6 in [162], the same smeared oscillation patterns are visible, although here with a finer resolution due to the increased binning. Also the total sensitivity $\Delta\chi^2$ increased by a factor of 2 to 3 due to the above mentioned changes in the analysis.

The increase in the Z/A sensitivity compared to Fig. 9.7 in [162][2] can also be seen in the likelihood profiles shown in Fig. 9.18, that were calculated for different assumptions of systematic uncertainties, as well as the impact of the MC error. The systematics with priors that were used are listed in tab. 9.1. A detailed description together with the technical implementation in `SWIM` is given in [162], chapter 7. Next to the oscillation parameters, the studied nuisance parameters affect the shape and the normalisation of the neutrino flux as follows:

NC scale Normalisation factor for the NC interaction rate.

Energy and Zenith slope Adds a linear tilt to the flux along either the energy or angular axis. The overall flux normalisation is kept constant.

[2]The plot was reproduced during the scope of this thesis for sanity checks, see Fig. A.6.

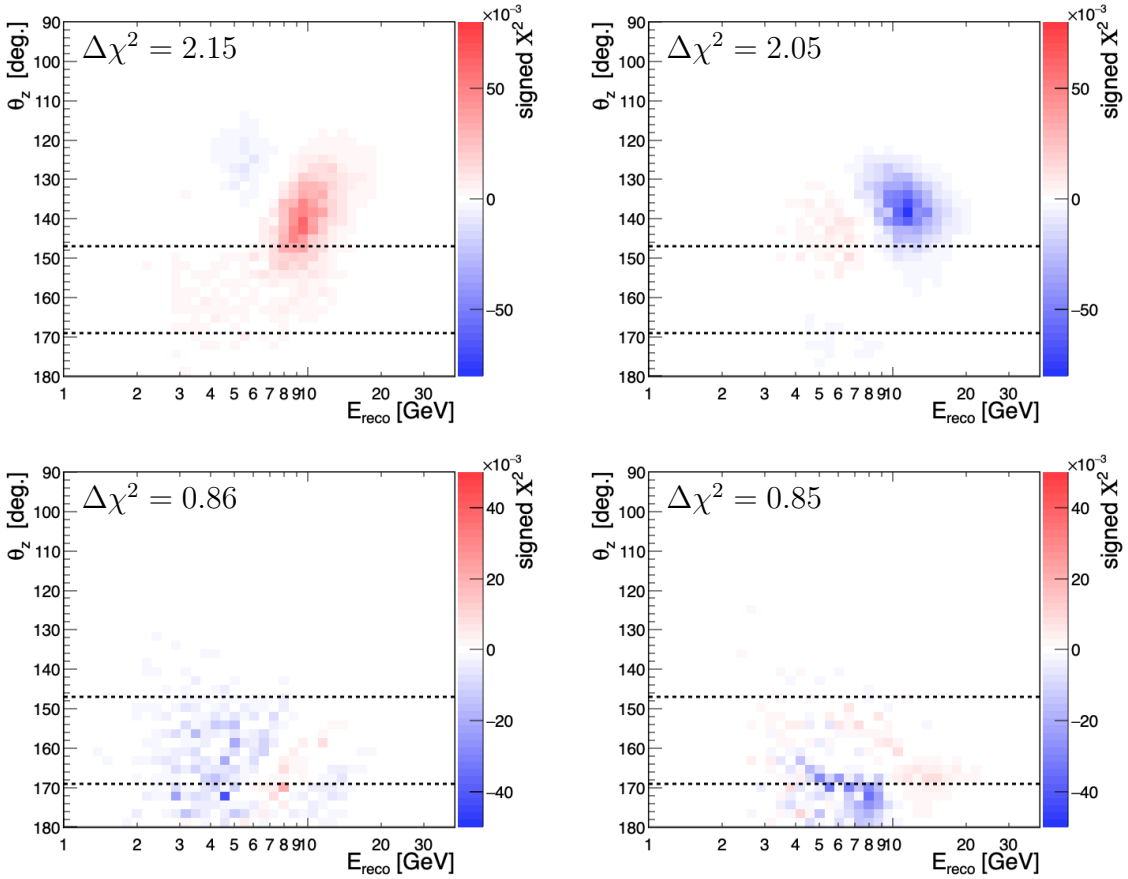

Figure 9.17: Expected signal in the shower-(left) and track-(right) channels for a respective +5 % variation of the Z/A in the mantle (top) and outer core (bottom).

Parameter	Mean	Prior
Z/A mantle	0.496	0.02
δ_{CP}	0	-
θ_{23}	49.2°	-
Δm^2_{31}	$2.517 \times 10^{-3}\,\mathrm{eV}^2$	-
θ_{13}	8.57°	0.15°
NC scale	1	0.1
EnergySlope	0	-
ZenithSlope	0	-
$\nu_e/\bar{\nu}_e$-skew	0	0.05
$\nu_\mu/\bar{\nu}_\mu$-skew	0	0.05
$\overset{(-)}{\nu}_\mu/\overset{(-)}{\nu}_e$-skew	0	0.05
TrackNorm	1	-
ShowerNorm	1	-

Table 9.1: Systematic uncertainties and priors used for Z/A likelihood profiles in Fig. 9.18 (motivated from [162]). Horizontal lines mark the additional nuisance parameters used for the likelihood profiles shown.

Skew-parameters Modifies the normalisation of the neutrino flux per flavour so that the ratio of the new integrated flux $\tilde{I}$ differs from the ratio of the original fluxes I by the skew parameter $s_{a,b}$: $\tilde{I}_a/\tilde{I}_b = I_a/I_b + s_{a,b}$. The overall flux normalisation is kept constant.

Track and Shower norm Normalisation factors for the track and shower PID classes, respectively.

We find that the MC error has a big impact on the result. The nuisance parameters on the other hand barely affect the sensitivity of the outer core Z/A. A plausible explanation is that the parameters are constrained by neutrinos that traverse only the mantle. In a sense, variations of the outer core Z/A can not be completely mimicked by oscillation parameters, as this would also affect mantle traversing neutrinos, where no shift in the oscillations are expected. This assumption was confirmed in studies with `EarthProbe`, see Fig. 10.8 in the following chapter.

I could show that ORCA is able to measure the Z/A of the Earth's outer core with the precision of a few percent. The expected 1σ intervals are listed in tab. 9.2, together with the corresponding result of the analysis in [162]. The precision must be nevertheless improved in order to distinguish between the example models that were introduced in chapter 3, visualized by the zoomed-in likelihood profile (Fig. 9.17 right). It is interesting to note that the likelihood-ratio profile decreases again at higher values of Z/A. As pointed out in [128], the peak in the oscillation probability that is responsible for ORCAs sensitivity to the electron density in the outer core appears also in the oscillation probability at a $\sim$55 % higher Z/A($\approx$ 0.7). This leads to the small asymmetry in the error intervals quoted in tab. 9.2, and can also be seen in Fig. 9.16. This asymmetry is however not detected by the error estimation by `Minos`, which is nicely visible in Fig. 9.11 (especially for layer 2).
The here presented study was done in a similar form by Capozzi and Petcov[132], using

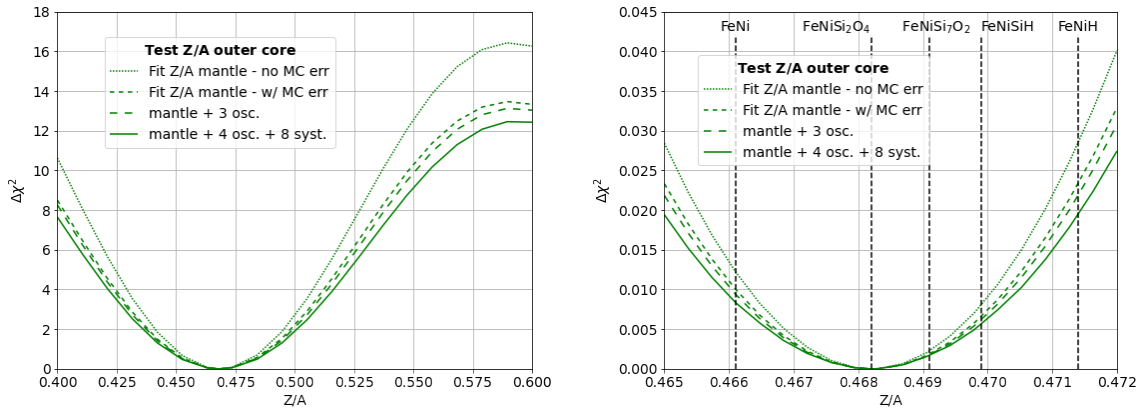

Figure 9.18: Likelihood profile Z/A outer core, with different sets of systematics, described in Tab. 9.1 (Wide and narrow Z/A range). Updated analysis of Fig. 9.7 in [162].

	This work		[162] Table 9.1	
	low	up	low	up
no MC err.	-3.5	4.4	-6.0	5.7
w/ MC err.	-4.0	4.8	-6.7	6.5
+ 3 osc.	-4.1	5.0	-6.9	6.8
+ 4 osc. + 8 syst.	-4.3	5.3	-7.2	7.3

Table 9.2: Relative widths (in %) of the expected 1σ intervals for the measurements of the Z/A scaling in the outer core, corresponding to Fig. 9.18. Corresponding results of the previous analysis of [162] are shown as reference.

analytical functions to simulate the detector performance. Although theses authors present their LLR-profiles as a function of the matter density instead of the Z/A, both results can be translated one into another based on eq. 3.8 and can thus be compared and discussed. By reading out the plots of their Figure 6 for $\sin^2(\theta_{23}) = 0.50$ and the most optimistic uncertainty estimations, I find an approximate 1σ CL of $\pm 8.3\,\%$. Comparing that with tab. 9.2 shows good agreement with the result of [162], whose analysis was based on the same dataset that [132] give as reference for their simulations. For $\sin^2(\theta_{23}) = 0.58$ they find that the outer core density can be constrained by up to $\sim 7.2\,\%$ at the 1σ confidence level, while my analysis with the most up-to-date MC simulation yields -4.3 %/-5.3 % for $\sin^2(\theta_{23}) = 0.572$, a significantly better result than that by [132]. This illustrates again how a better understanding of the detector and consequent improvements of *e.g.* the event reconstruction and classification can yield a gain in sensitivity.

Finally, the results of oscillation tomography with ORCA can also be shown in a more general way, in terms of a sensitivity towards the electron density within the different regions of the Earth. So far we have been focusing on either the Z/A or the matter density ρ, while assuming the other parameter to be known from Earth science. Rearranging eq. 3.8 gives the relation between both quantities

$$Z/A(\delta\rho_{\mathrm{PREM}})|_{n_e=\mathrm{const.}} \sim \frac{n_e}{\delta\rho_{\mathrm{PREM}}} \,. \tag{9.3}$$

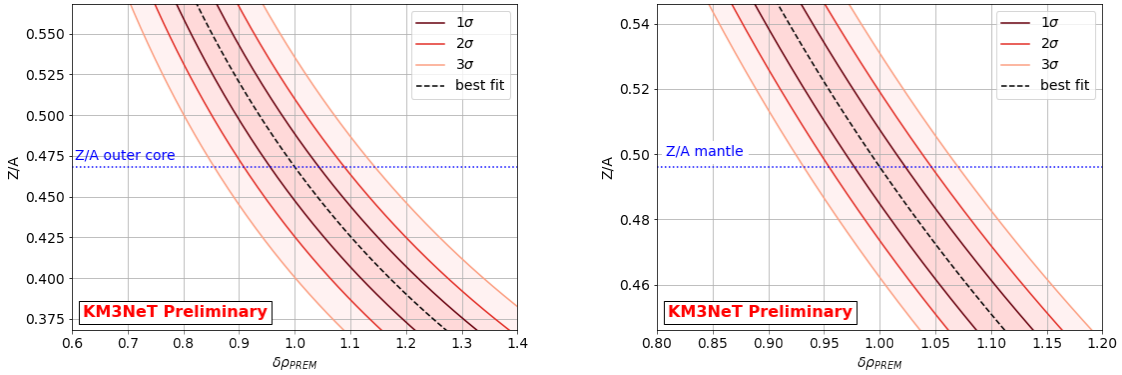

Figure 9.19: Contour plot Z/A vs. $\delta\rho_{\mathrm{PREM}}$, drawn from the `Minos` error intervals of the electron density of the outer core and the mantle, respectively, for 10 yr of ORCA. The contours indicate constant values of n_e, according to eq. 9.3.

Figure 9.19 shows the sensitivity contours for both parameters for the outer core and the mantle with 10 yr of ORCA. The contours are here obtained by calculating the 1, 2 and 3σ intervals of n_e with `Minos` and drawing the lines according to eq. 9.3 for constant values of the electron density n_e, for which the open and hyperbolic shape follows.
The wide contour plots shown above should be a reminder that all statements made about Z/A and the matter density rely strongly on inputs from geoscience, in order to constrain either one of the two variables. Regarding that these geophysical constraints are much stronger than the current sensitivity of oscillation tomography, it appears reasonable to make statements directly on either Z/A or ρ, instead of on the product of both (*i.e.* the electron density). These constraints could also come from absorption tomography, which would effectively "close" the contours in Fig. 9.19 along the x-axis, and enable a completely independent way of studying the deep Earth.

Chapter 10

Further perspectives for oscillation tomography with atmospheric neutrino detectors

Contents

In this final chapter of my dissertation, I loosen the focus on the KM3NeT experiment and consider the broader picture of neutrino physics. Although the found capabilities of performing Earth tomography with ARCA and ORCA are innovative and exciting, the qualitative benefit it could bring to geophysics is very limited yet. Therefore I switch now from the MC-based KM3NeT detector response to the parameterised one (as described in sec. 7.3.2), which allows for an approximate simulation of any kind of neutrino detector. The results can also be projected on existing – or planned – detector configurations, as those introduced in chapter 2. For ORCA, this approach shows comparable results as the ones found in chapter 9. Further I find that a detector like HyperKamiokande yields the best results for the study of the outer core. This may further help future experiments with a focus on Earth tomography with atmospheric neutrinos to design a detector that matches the specific requirements. One such hypothetical detector is evaluated in this chapter, and I find that it is capable to efficiently discriminate between FeNiH and $FeNiSi_xO_y$ models in less than 15 years. This particular NextGen detector could also constrain the density of our model LLSVPs up to 2 %, although it should be noted that the optimal detector configurations are different for studies of mantle chemical heterogeneities and for the outer core composition.

Model Label	FeNi	$FeNiSi_2O_4$	$FeNiSi_7O_2$	FeNiSiH	FeNiH
	-	Badro et al. [116]	Kaminski & Javoy [117]	Tagawa et al. [118]	Sakamaki et al. [119]
Composition	95 wt% Fe	89 wt% Fe	86 wt% Fe	88.2 wt% Fe	94 wt% Fe
	5 wt% Ni	5 wt% Ni	5 wt% Ni	5 wt% Ni	5 wt% Ni
	-	2 wt% Si	7 wt% Si	6.5 wt% Si	1 wt% H
	-	4 wt% O	2 wt% O	0.3 wt% H	-
Z/A	0.4661	0.4682	0.4691	0.4699	0.4714

Table 10.1: Models of Earth's outer core composition. For each model, the weight fraction of the different elements is shown as well as the corresponding average Z/A. In all models the Ni content is set to 5 wt% and Fe is the complement to 100 % once light elements have been taken into account. All elements considered in the different compositions have a Z/A between 0.46 and 0.50, except Hydrogen whose Z/A = 1 and increases the bulk Z/A of the alloy. All these models fit equally well the seismic constraints.

10.1 Outer core Z/A

The chemical composition of the Earth's outer core is constrained (1) by seismic velocities in the core and the density jump at the inner/outer core boundary, and (2) by geochemical models of light elements incorporation in metal during the formation of the Earth. Since its composition controls many aspects of its dynamics, as well as in the interplay between core and mantle, precise information on the amount and type of light element in the outer core is of great interest for geophysicists (as discussed in sec. 3.1.3). The fact that seismic measurements are not sufficient to fully constrain chemical composition gave rise for a growing interest towards neutrino oscillation tomography as possible solution for this problem. In contrast to similar publications (see sec. 3.3). I try to keep this work close to the point of view of a geophysicist and to go beyond a simple proof of concept by considering explicit outer core models introduced in Tab. 10.1, with a specific focus on hydrogen. The results obtained in this study are presented in an article recently submitted to Frontiers in GeoScience [2]. Since this chapter is meant to give an outlook on the perspectives of oscillation tomography, the simulated livetime is extended to 20 yr (or even more if indicated so) for all shown results.

10.1.1 Underlying signal and detector smearing

The concept of constraining outer core compositions is illustrated in Fig. 10.1 for the track channel. The top panels show the relative change in the expected $\nu_\mu+\bar{\nu}_\mu$-event rates for each indicated core composition with respect to FeNi over the true neutrino energy, at an incident zenith angle of $\theta_z = 165°$ and $\theta_z = 160°$. The amplitude of the relative difference of event numbers $\Delta N/N$ increases with the difference between the Z/A of the underlying model and the Z/A of FeNi (= 0.466). Although the oscillation pattern in dependency of the true neutrino energy is nicely visible, it is important to notice that the shape of the pattern can strongly vary for different values of θ_z, due to the dependency on the neutrino baseline (eq. 7.2), *e.g.* the peak at $E \approx 5\,\mathrm{GeV}$, which flips its sign. It is therefore necessary to consider the signal of neutrino data in the two-dimensional (θ_z, E) plane, as shown in the bottom panel.

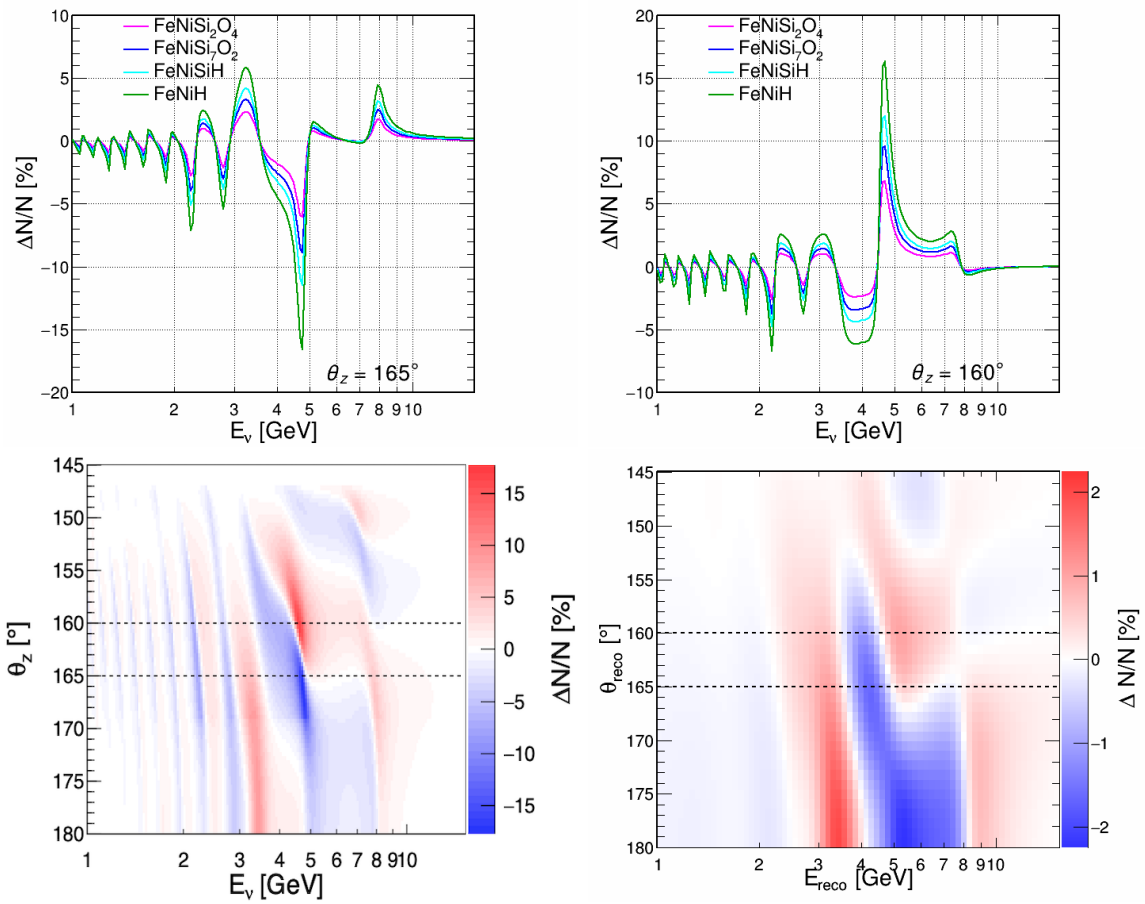

Figure 10.1: Analysis concept for the outer core chemical compositions. The top panel plots show the theoretical $\Delta N/N$ of $\nu_\mu + \bar{\nu}_\mu$ over the true neutrino energy between the respective model and FeNi for different incident angles. The bottom left histogram shows the same quantity for the composition models FeNiH vs. FeNi. In the bottom right histogram the detector resolution of the NextGen detector (Tab. 7.2) is applied, leading to a smearing of the fine signal pattern.

The lower left histogram shows the theoretical $\Delta N/N$ from the comparison of FeNiH and FeNi. In a realistic model with limited angular and energy resolution the fine differences in the respective oscillation patterns will smear out, leading to a significant decrease of separability. One example is shown in the bottom right histogram, where the detector response of the NextGen detector was applied (see Tab. 7.2). The same plots are shown for the shower channel in Fig. 10.2.

10.1.2 Comparing detectors

The statistical measure with which the two tested hypotheses (FeNiH and FeNi) can be distinguished is again given by the $\Delta\chi^2$, as described in sec. 7.4. For the comparison FeNi vs FeNiH and 20 yr of data taking with the NextGen detector it is shown in Fig. 10.3 for the track- and shower-channel. Note that only the absolute value of $\Delta\chi^2$ change if different models are tested against each other, but not the pattern of the histogram, which is why only this result is shown here.

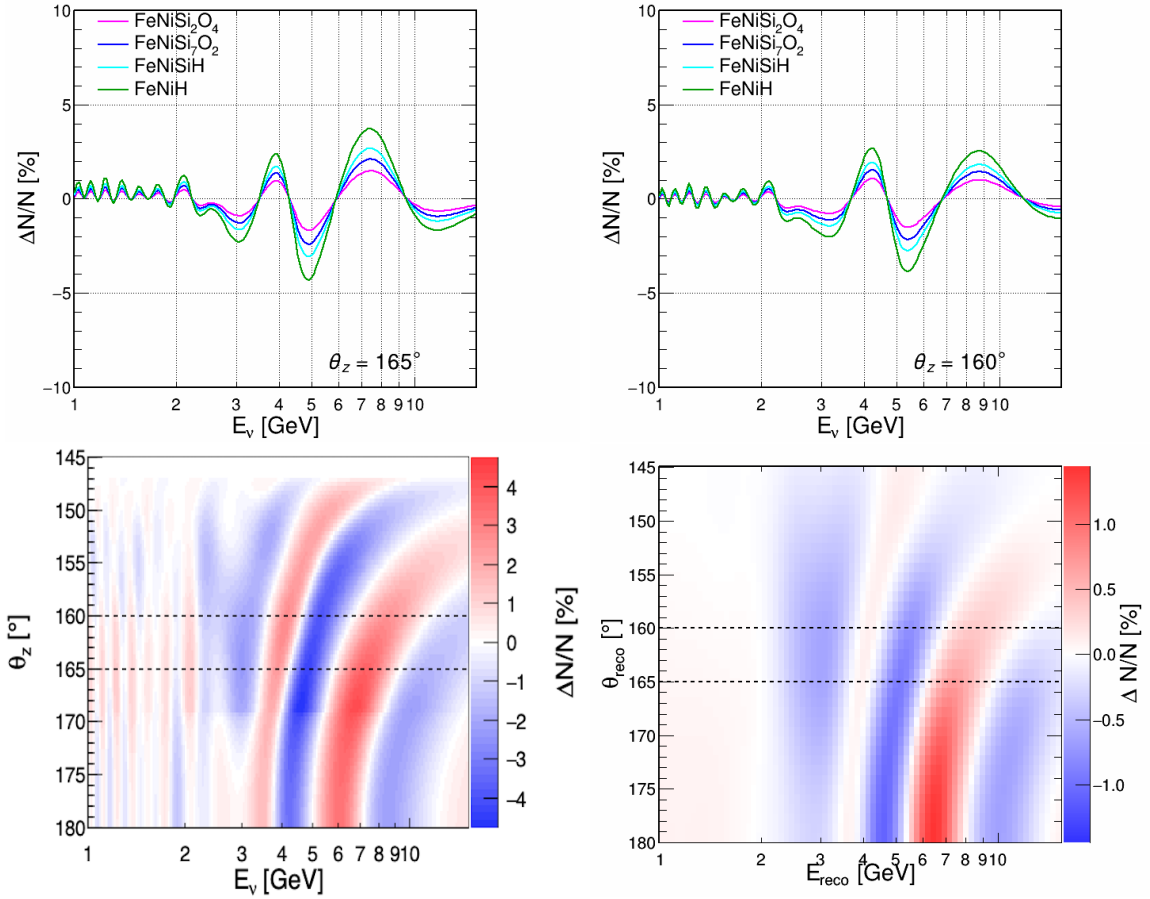

Figure 10.2: Analysis concept for the outer core chemical compositions. The top panel plots show the theoretical $\Delta N/N$ of $\nu_e + \bar{\nu}_e$ over the true neutrino energy between the respective model and FeNi for different incident angles. The bottom left histogram shows the same quantity for the composition models FeNiH vs. FeNi . In the bottom right histogram the detector resolution of the NextGen detector (Tab. 7.2) is applied, leading to a smearing of the fine signal pattern.

What does in fact change the measured signal – with a big impact on the final result – is the used detector. In Fig. 10.4 the $\Delta\chi^2$ maps are shown again for the comparison FeNi vs. FeNiH and 20 yr of data taking, but for the upcoming detectors DUNE, ORCA and HyperKamiokande. The colorscale was changed for better visibility, as the expected signal is much lower as simulated for the NextGen detector. In the direct comparison one can clearly see the impact of the different detector resolutions. While DUNE will be able to identify even fine oscillations, ORCA will blur out the periodic pattern and eventually detect only two big regions where the oscillations differ between the two composition models. Yet, the large detector volume of ORCA seems to compensate for the low resolution, as the combined $\Delta\chi^2$ matches that expected from DUNE. Another finding is that the sensitivity distribution between the PID channels changes with the different detectors, due to the different capabilities of resolving the respective oscillation patterns. Finally, the best result is expected neither for the small but high resolution detector DUNE, nor for the large but less precise ORCA detector, but for HyperKamiokande which represents a compromise between DUNE and ORCA

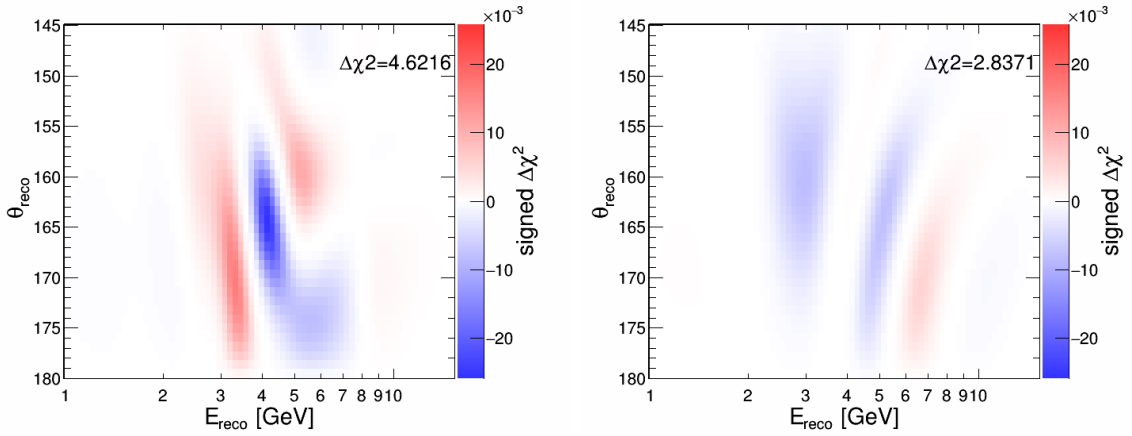

Figure 10.3: Sensitivity of the NextGen detector for discriminating between FeNi and FeNiH outer core compositions after 20 years data taking. The plots show the signed $\Delta\chi^2$ maps as a function of the reconstructed energy and zenith of the neutrinos, respectively for track- and shower-events.

in terms of scale and accuracy.

The method used above for calculating the statistical separation power between two explicit values of the outer core Z/A was further used to draw the $\Delta\chi^2$ profile in the left panel of Fig. 10.5 for all detectors under investigation. The x-axis shows the ΔZ/A between two respective models. In the narrow region of interest that is studied here, the shape of the $\Delta\chi^2$ profiles are identical for each model hypothesis and the found Z/A sensitivity, *i.e.* the with of the parabola at $\Delta\chi^2 = 1\,(\equiv 1\,\sigma)$ is somewhat a universal detector property[1].
The vertical lines indicate the necessary sensitivity in order to distinguish a pure FeNi outer core from FeNiH and $FeNiSi_2O_4$, respectively. As already seen above, none of the upcoming neutrino detectors will be able to resolve the fine differences in Z/A from the outer core model compositions under investigation. Only the NextGen detector achieves the required precision, which is – as will be shown hereafter – not a coincidence but a direct consequence of the definition of its model parameters.

The just discussed $\Delta\chi^2$ profiles are also computed for 20 yr of data taking with each detector. The evolution of the detectors confidence level (in σ and $\Delta\chi^2$) over time is shown in the right panel of Fig. 10.5, where the dashed lines correspond again to the test of FeNi and the solid one to $FeNiSi_2O_4$, both with respect to FeNiH . Note that only one curve is shown for ORCA and DUNE, as their curves are almost indistinguishable by eye. While a detector lifespan of 10 yr to 20 yr is a reasonable assumption, the extension to 50 yr is drawn here to visualize the general evolution of statistical confidences. From the definition of $\Delta\chi^2$ in eq. 7.23, it is obvious that it grows linearly with the number of events and thus with the detector livetime. From the relation $\sigma = \sqrt{\Delta\chi^2}$ it follows that the actual C.L. for an observation grows fast only in the first few years of an experiment and that the growing rate decreases with the duration of the experiment. Hence even unrealistic experiment duration of many

[1]The result for ORCA is compared with that obtained with `SWIM` in Fig. A.7. The two frameworks are in good agreement.

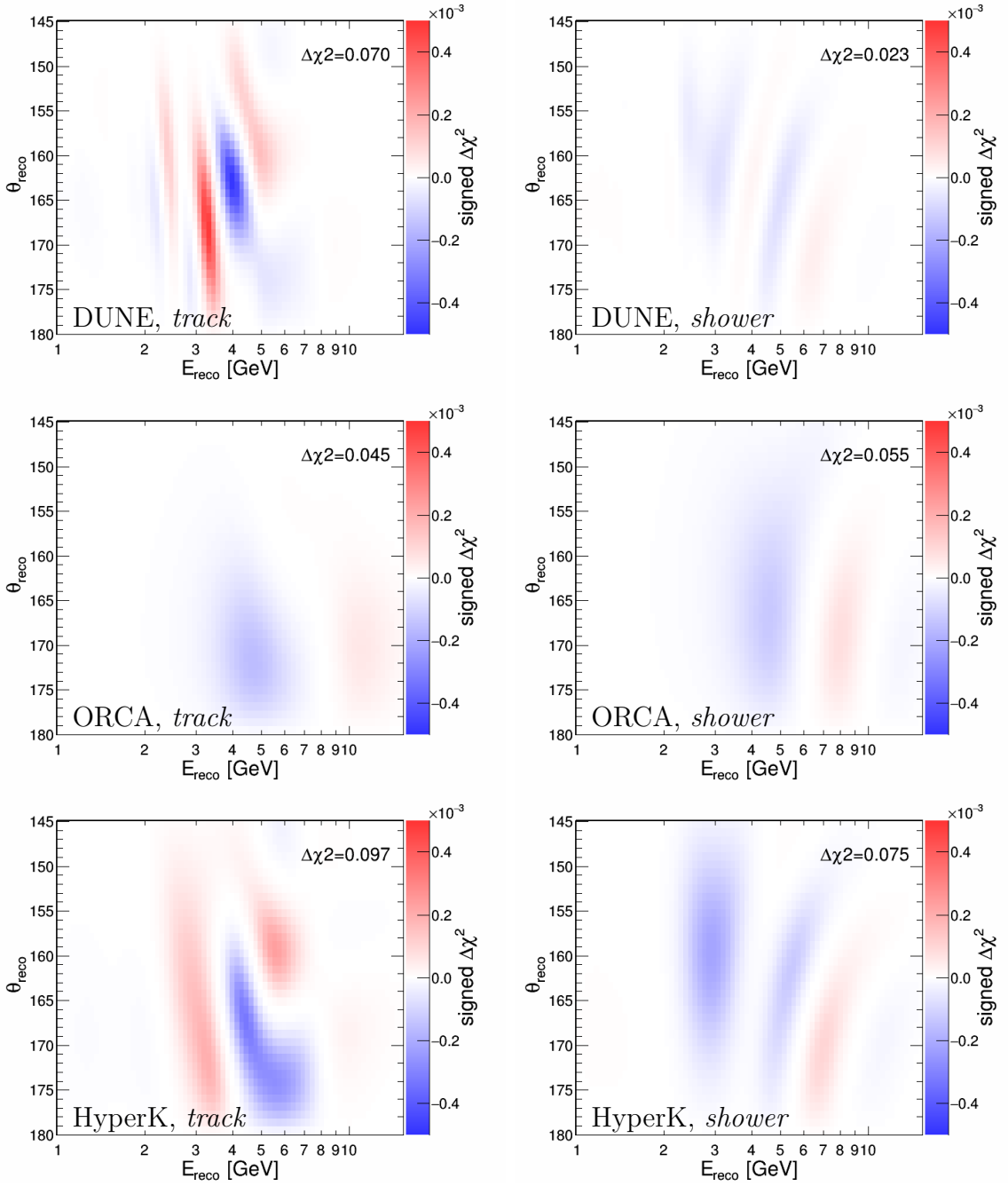

Figure 10.4: $\Delta\chi^2$ sensitivity for discriminating between FeNi composition and FeNiH model in 20 years livetime of upcoming detectors. From top to bottom, the panels are for DUNE, ORCA and HyperKamiokande, for track- (left) and shower-events (right).

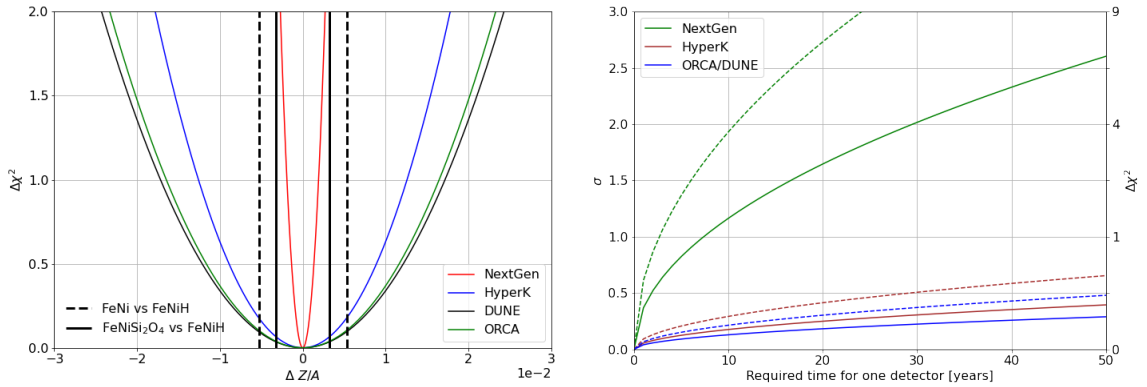

Figure 10.5: Left: The outer core sensitivity in terms of $\Delta\chi^2$ is shown vs. the difference in Z/A between two tested model hypotheses per detector for a 20 yr livetime. The vertical lines show the actual ΔZ/A for the comparison of FeNiH and $FeNiSi_2O_4$ vs. FeNi , respectively. **Right:** The evolution of σ and $\Delta\chi^2$ over detector livetime, again for both model comparisons. The lines for the ORCA and DUNE detectors, which are indistinguishable by eye, are combined in the right panel.

decades will not be sufficient to better constrain the core composition.

10.1.3 The search for the optimal detector

In the previous parts of this section the sensitivity of the Earth's outer core Z/A was tested for explicit detector configurations or rather approximate parameterisations of them. Doing so we found that the HyperKamiokande detectors yields the best results compared to the other current generation detector DUNE and ORCA, although still below the 1σ C.L. This was in no way obvious or predictable, as all these detectors where designed for a purely particle physics orientated research, with oscillation tomography being only a side feature to that. The here used analysis framework which is based on a parameterised detector response is the optimal tool to investigate any detector characteristics – realistic or not. In our framework, in order to capture the relevant characteristics of the different families of detectors, we use a set of 8 different parameters to model a detector (see sec. 7.3.2). Although all parameters contribute to set the final detector performance, in our search for the best suited detector characteristics we focused on the interplay between size and event resolution, as they differ the most between our selection of detectors.
In the same procedure as the one used earlier, the $\Delta\chi^2$ value for the comparisons $FeNiSi_2O_4$ vs. FeNiH was calculated for hypothetical detectors with various combination of energy and angular resolutions constant in the true neutrino energy, for an exposure of 200 Mt yr (Fig. 10.6, left). All other parameters were fixed to the value given in Tab. 7.2 for the Next-Generation detector, that were chosen to be in between the values of ORCA and DUNE/HyperKamiokande. The color code depicts the areas for $\sigma < 1$ (red), $1 < \sigma < 2$ (yellow) and $\sigma > 2$ (green). The rough positions of the detectors in the angular and energy resolution grid are overlayed, where error boxes correspond to resolutions in between $E = 3$ GeV to 7 GeV due to the energy dependencies. The detector livetimes that would be necessary to reach an exposure of 200 Mt yr

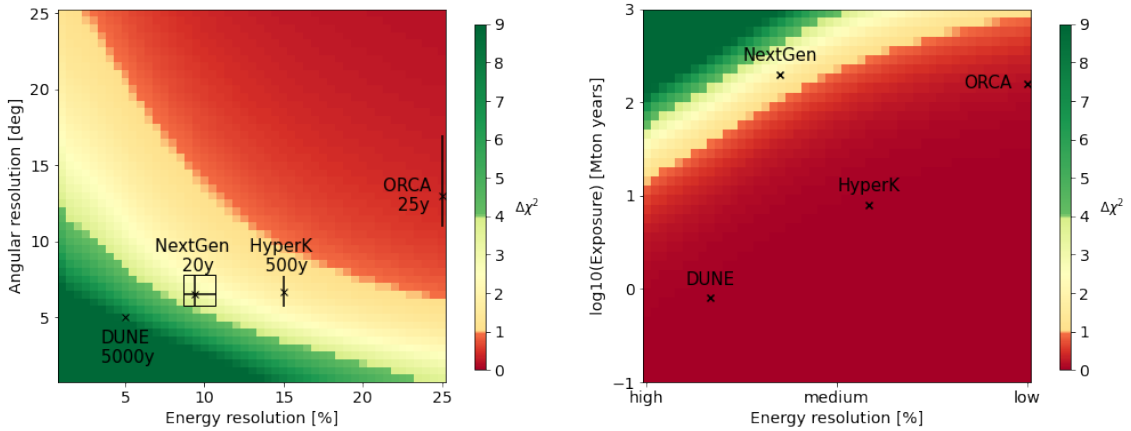

Figure 10.6: $\Delta\chi^2$ discrimination power for $FeNiSi_2O_4$ vs. FeNiH for various combinations of detector configurations. **Left:** Dependency on angular and energy resolution (constant in true neutrino energy) for 200 Mt yr exposure. The respective resolution ranges of the investigated detectors are superimposed together with the necessary livetime to reach the assumed exposure. The error boxes indicate their resolutions in the energy interval of 3 GeV to 7 GeV. **Right:** Exposure vs. overall resolution, where a linear dependency between angular and energy resolution is estimated from the left plot. All other parameters were set to the value listed for the NextGen detector in Tab. 7.2 for both plots.

is also given. Note that the actual sensitivity results of the detectors are not directly the values in the histogram, due to the contribution of the other 6 detector parameters. The drawn histogram helps to estimate the resolution a detector would need in order to be able to distinguish between outer core compositions with such fine differences in Z/A as between $FeNiSi_2O_4$ and FeNi. In fact, this map was the motivation for the choice of detector resolution, which we labeled as NextGen.

The conclusion we have reached may sound a bit confusing at first sight, as one could consider DUNE as the perfect detector, because it is deep in the green area. However one should not ignore the assumption made about the exposure. In order to find a complementary way to present the result, an approximate linear relation between angular and energy resolution of a detector was derived from a fit to the 4 detector positions in the $\Delta\chi^2$ resolution map: $(\sigma_\theta \approx 0.42 \times \sigma_E + 2.2)$. Using that relation allows to draw a second $\Delta\chi^2$ map with the logarithmic exoposure on the y-axis and a somewhat "overall" resolution on the x-axis (Fig. 10.6, right). That choice of presentation allows now for a more intuitive interpretation of the detector performances. All current detectors are far from the 1σ region, as either the exposure or the resolution are insufficient.
In order to reach the green or even yellow region, one of these quantities has to be increased. Moving one of the detector locations in the map up the y-axis which represents the exposure, the instrumented detector mass needs to be increased, assuming that > 20 yr of detector livetime is not feasible. In the case of DUNE, the instrumented mass is limited by the size of the TPC, which is somehow limited to the electron drift

length and photon absorption length in liquid Argon – two key parameters for the event reconstruction and thus the overall detector resolution. The only way to increase the total detector volume would thus be – as it is already planned – to build more than one LArTPC. From the $\Delta\chi^2$ map we can estimate, that a $\sim$25 Mt yr exposure with a DUNE-like detector would be required to reach a 1σ discrimination power between $FeNiSi_2O_4$ and FeNi, which corresponds to 250 single DUNE chambers, or $\sim$60 DUNE detectors with 4 TPCs each.
An analogue estimation can be made for a HyperKamiokande-like detector, where 30 water tanks would be necessary. An exceptional case is a ORCA-like modular water Cherenkov detector, that could be extended almost limitless by simply adding more modules.

In conclusion, the favourable detector design to reach (i) sufficient statistics by a Mt instrumented mass with a sub-GeV detection threshold and (ii) enhanced detection, reconstruction and classification capabilities is that of a large and scalable water Cherenkov detector. Its photodetection layout can be either 3D, as in ORCA, or 2D, as in HyperKamiokande, as long as it provides good angular coverage for neutrinos crossing the Earth's outer core.
Such a NextGen detector could contribute significantly to better constraining the outer core composition, as is summarized in Fig. 10.7. Here, the Z/A resolution of the NextGen detector is shown as an evolution in time, together with the required limits to distinguish respectively two models of composition. A hydrogen-rich outer core (FeNiH) could be excluded with respect to zero hydrogen content after no more than 15 years. Models with smaller amounts of hydrogen (FeNiSiH) lead to only small changes in the overall Z/A and could be identified only after up to 35 years, even with the proposed NextGen detector.

10.1.4 Side discussion: Systematics

During the studies of the outer core Z/A with `EarthProbe`, the effect of uncertainties of *e.g.* oscillation parameters was not taken into account. First of all, the necessary detector livetimes for oscillation tomography is $\mathcal{O}(10\,\mathrm{yr})$. One can thus assume that most oscillation parameters will be much better constrained at the point where neutrino experiments can contribute to geoscience. Reactor neutrino experiments like JUNO can provide constraints independent from atmospheric neutrino experiments and are thus perfectly suited to be used as limits for *e.g.* ORCA or HyperKamiokande.
Secondly, when only studying the Earth's core, effects of systematic uncertainties are also limited by neutrinos that pass only the mantle, as they are unaffected by variations of the core properties. A simple test to confirm this theory was executed in the following way: Fig. 10.8 shows two fits of the outer core Z/A for respectively 20 yr operation of the NextGen detector, once with fixed systematics as in the sections before and once with allowed free variations of θ_{23}, Δm^2_{31} and δ_{CP}. The shown curve of $\Delta\chi^2$ was once calculated using all neutrinos and once only for zenith angles $\theta_z \in [180°, 150°]$, *i.e.* core-traversing neutrinos. While the result with fixed systematics is (almost[2]) identical, the effect of the uncertainties, *i.e.* a decrease in $\Delta\chi^2$, is bigger if only core-traversing

[2]As the bin edges are not perfectly aligned with the CMB, a few core-traversing neutrinos are missed by the used cut.

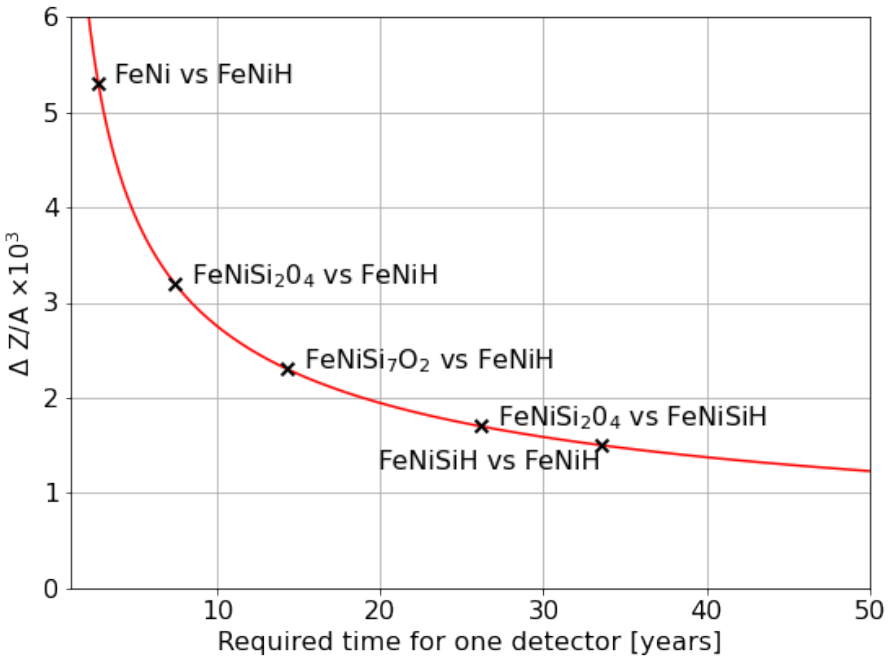

Figure 10.7: Precision of the Z/A measurement achievable at 1σ with the NextGen detector as a function of running time. The crosses indicate the separation in Z/A between pairs of models considered in this study. Not shown in the graph is the time required to distinguish $FeNiSi_7O_2$ vs $FeNiSi_2O_4$ ($\simeq$90 yr) and $FeNiSi_7O_2$ vs FeNiSiH ($\simeq$120 yr). If n identical NextGen detectors were running in parallel, the time scale would be reduced by that same factor n, *i.e.* $FeNiSi_7O_2$ vs. $FeNiSi_2O_4$ could be distinguished in about 20 years if 4 NextGen detectors would be taking data simultaneously.

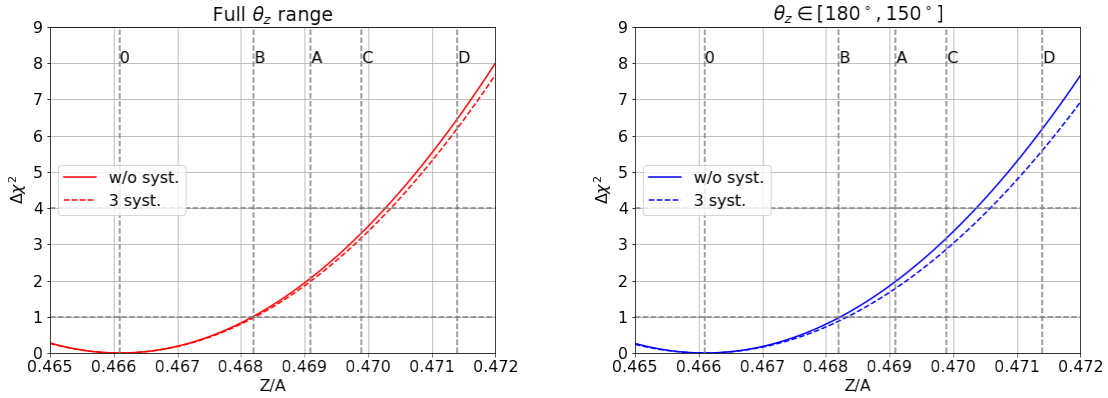

Figure 10.8: Evaluation of systematic effects for an example fit of the core Z/A. The Z/A sensitivity is calculated for the full range of θ_z (left) and for $\theta_z \in [180°, 150°]$, *i.e.* core-traversing neutrinos (right), with and without accounting for systematic uncertainties of θ_{23}, Δm^2_{31} and δ_{CP}. When the full neutrino sample is considered, the effect of systematics is weakened by the information from neutrinos that cross only the mantle but not the core.

neutrinos are taken into account.

10.1.5 Side discussion: NC events in EarthProbe

During the scope of this thesis, an adaption was made within the `EarthProbe` framework concerning the treatment of NC events. As discussed in sec. 1.4, a NC interaction of a neutrino with a nucleon does only produce a hadronic shower, the neutrino itself leaves the detector. The fraction of the energy transferred from the neutrino during the scattering is given by the Bjorken-y (eq. 1.43). The visible energy E_{vis} is thus by a factor y smaller than the actual neutrino energy E. Originally the detector response, *i.e.* the smearing of energy and direction, is applied directly to the true neutrino energy. In the case of NC events, E_{vis} should be used instead.
The probability density function for the appearance of a hadronic shower with E_{vis} after a NC scattering of a neutrino with energy E is approximated from the differential cross sections in eq. 1.45, *i.e.* the appearance of a constant term plus one dependent on $(1-y)^2$, as

$$P(E_{\text{vis}}, E) = \left(a + b\left(1 - \frac{E_{\text{vis}}}{E}\right)^2\right) \Big/ \left(a + \frac{b}{3}\right) / E \tag{10.1}$$

where a and b are approximated form the bjorken-y distribution (Fig. 1.10) as

$$\begin{cases} \nu: & a = 1;\ b = 0.2 \\ \bar{\nu}: & a = 0.2;\ b = 1 \end{cases} \tag{10.2}$$

The PDF is shown in Fig. 10.9 (left).

Effectively, the energy of a 5 GeV neutrino is smeared as shown in Fig. 10.9, right. The energy reconstruction of CC events is as previously assumed to be Gaussian distributed. For NC events, the smearing due to the detector response is folded with the smearing due to the energy transfer or the scattering process.

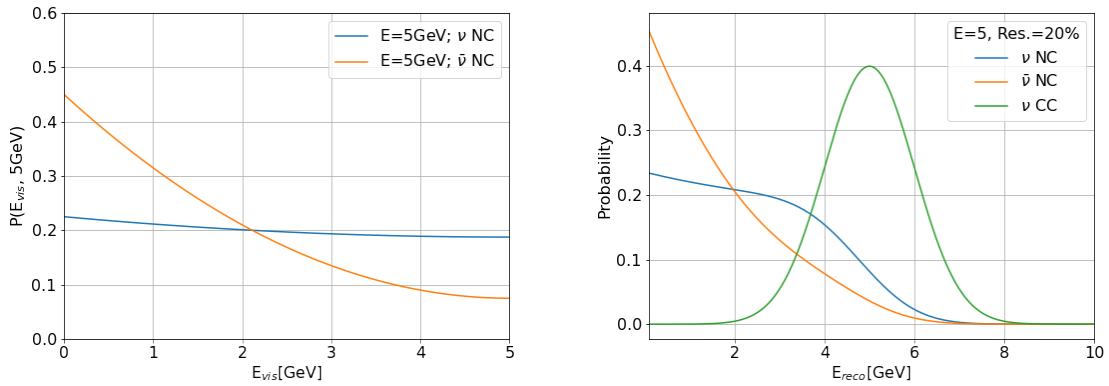

Figure 10.9: Left: PDF of E_{vis} for NC scattering of a 5 GeV (anti-)neutrinos. **Right:** Energy reconstruction probability for a Gaussian resolution with $\sigma = 20\,\%$. While CC events are reconstructed around the true energy, NC events appear less energetic.

The energy of NC events is smeared according to eq. 10.1 during the calculation of the reconstructed event rates. As a consequence of the NC energy smearing, NC events are reconstructed at lower energies as before. Since the neutrino flavour can usually not be reconstructed from NC events, they add only background to the experiment. As can be seen in Fig. 10.10, with the new treatment NC events appear at lower energies in the final simulated event rates and thus out of the relevant energy range for oscillation tomography or even fall below the detection threshold leading to an overall reduction of background through NC events.

The application of the NC smearing is not only physically more accurate but also leads to an effective reduction of background and thus an improvement of the final result. It was used in all shown results of this chapter. The gain is however relatively small, a comparison with previous results without NC smearing is shown in Fig. 10.11.

Further I explored the possibility of a complete suppression of the NC background, which will be to some extent possible in DUNE[101]. The theoretical gain is shown in Fig. 10.12.

As a final example of the best possible outcome of neutrino tomography with the upcoming detector generation, Fig. 10.13 shows the sensitivity towards the outer core Z/A for a potential combination of the results from ORCA, DUNE and HyperK, again together with the possible gain due to the suppression of NC events. In this very optimistic scenario, that would require a careful treatment of the correlated systematic effects between the different experiments, the pure FeNi model could be distinguished from FeNiH after 50 years of concomitant data taking.

10.2 A new avenue to study LLSVPs?

The analysis of LLSVPs as done with `SWIM` in sec. 9.3 were repeated for the parameterised detectors in `EarthProbe`. I find that dependency of the signal on the LLSVP shape and position are comparable (Fig. A.8). The sensitivities towards the density

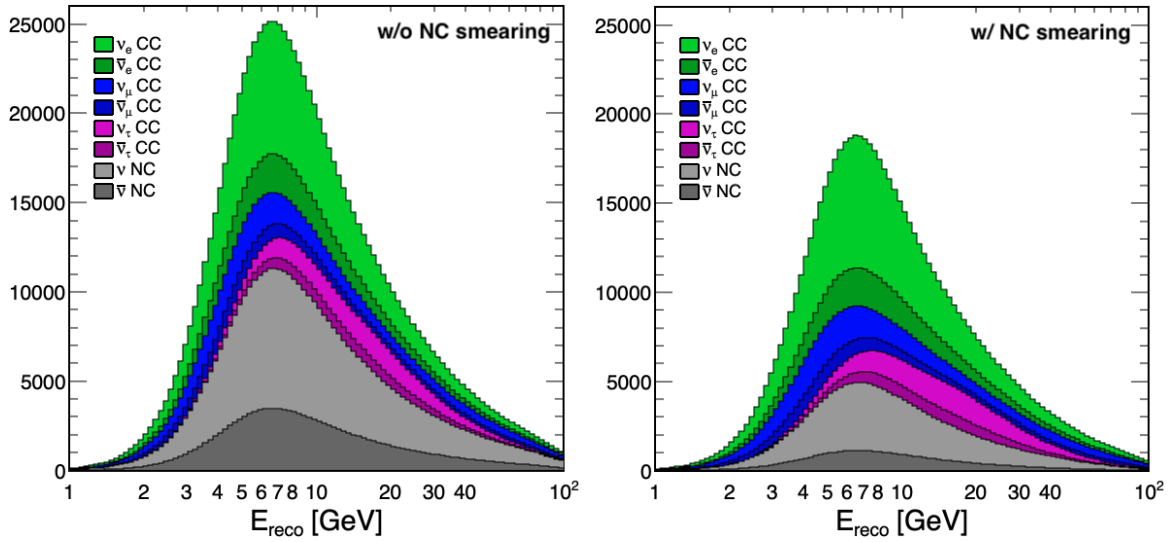

Figure 10.10: Shower-like event rates calculated for ORCA with `EarthProbe` before (left) and after (right) introduction of the NC smearing. As only the visible energy is reconstructed now in a NC interaction, many events fall below the plateau of the detection efficiency, which leads to an effective reduction of NC events in the final data sample.

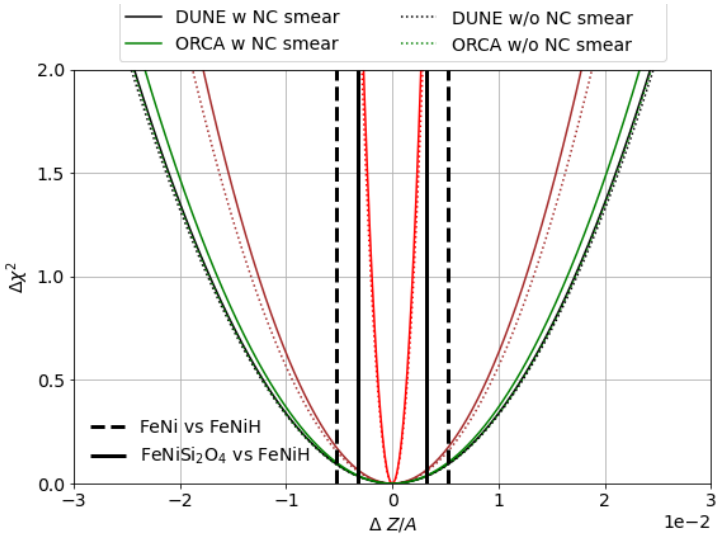

Figure 10.11: Gain in outer core Z/A sensitivity (shown in Fig. 10.5) by smearing NC event energies (dotted to solid curves).

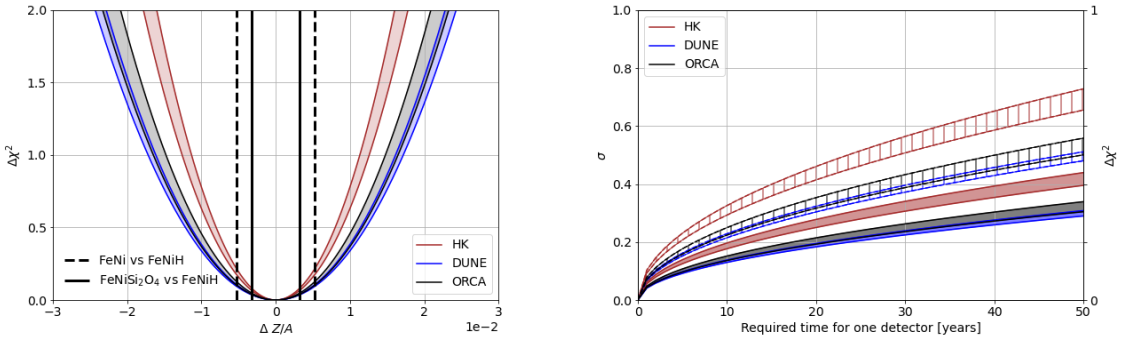

Figure 10.12: Outer core sensitivity vs. $\Delta Z/A$ and detector livetime, as in Fig. 10.5. The bands indicate the possible gain by a complete supression of NC events.

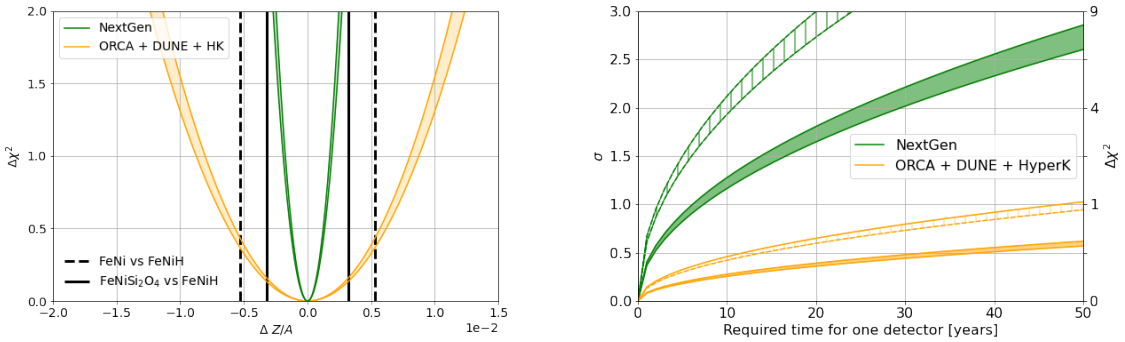

Figure 10.13: Sensitivity on outer core Z/A (as in Fig. 10.5), for the NextGen detector and a combination of ORCA, DUNE and HyperK. The bands indicate the possible gain by suppressing NC events.

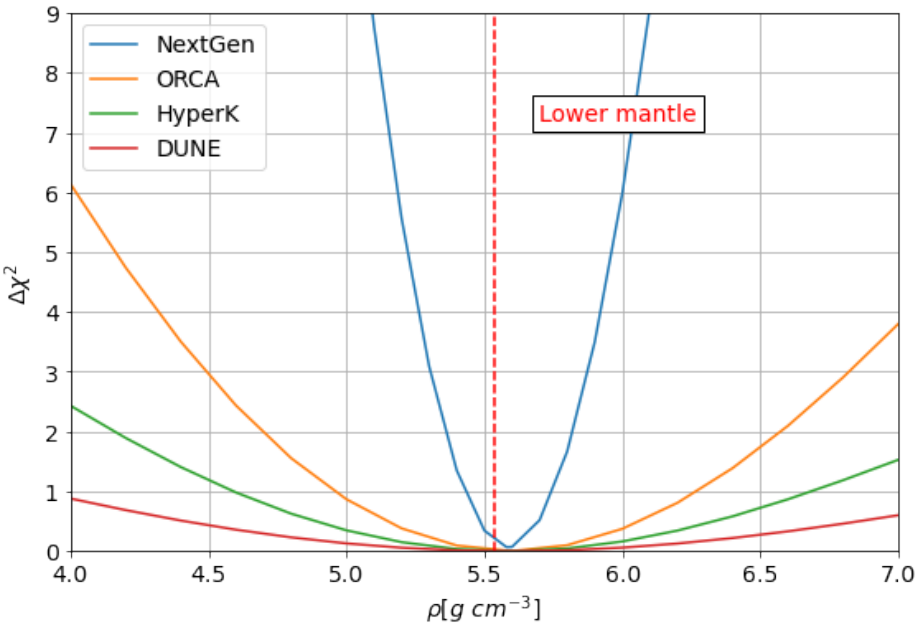

Figure 10.14: Sensitivity towards the LLSVP density (as in Fig. 9.16) for different detectors simulated with `EarthProbe` and 20 yr livetime.

of the LLSVP are shown for the different detectors in Fig. 10.14. The results found with the parameterised response of ORCA are significantly higher than with the MC response.
Interestingly, the ranking in performance of the studied detectors is very different compared to the Z/A study of the outer core, where ORCA and HyperKamiokande showed similar results, and slightly worse as DUNE. Here, ORCA outperforms both detectors by a long way and DUNE shows even worse results than HyperKamiokande.
To some extend this trend is expected from the switch from core to mantle studies, as the MSW resonance appears at higher energies in the mantle and are thus better seen by ORCA with a higher energy detection threshold. Another explanation may be that the small volume of the LLSVP means low statistics. It appears that the saturation of the likelihood, that appears in counting experiments when a lot of data is collected, is not reached even after 20 yr of DUNE and HyperKamiokande.
This leads to the conclusion, that possible future neutrino detectors that are build for geoscientific research have not only to be adapted to neutrino tomography in general, but can be further optimised for the specific task of interest, mantle vs. core study.

Summary and outlook

Main results In the hope of getting a glimpse beyond the standard model, various neutrino experiments are being build around the globe, surpassing the previous detector generation in size and performance. This does not only open fascinating insights into particle physics but may also open a new window for investigating the interior of the Earth. The potential of doing so by studying the matter dependent oscillation and absorption of neutrinos was investigated in this thesis.

One part of this thesis focused on the KM3NeT experiment, which is currently building an array of water-Cherenkov detectors in the Mediterranean Sea. KM3NeT/ORCA is designed for the detection of GeV-energy neutrinos produced in the atmosphere, while KM3NeT/ARCA is optimised to measure neutrinos in the TeV range and higher, including both atmospheric and astrophysical neutrinos. KM3NeT is thus a perfect candidate for performing both oscillation and absorption tomography. As the detectors are still under construction, their performances are simulated with a specially developed analysis framework of the collaboration which uses Monte Carlo simulations. The software – originally designed for sensitivity studies on oscillation parameters – was adapted by me to be used with ARCA and to calculate oscillation and absorption effects based on varying modifiable Earth models in 1D and 3D. The new functionality enabled multiple pioneer studies with KM3NeT.

Absorption tomography, being sensitive to the matter density along a neutrino trajectory, can be used to scan the Earth's density profile in an approximate model consisting of 5 layers, each with a constant density calculated according to the preliminary reference Earth model (PREM). The principal analysis concept could be demonstrated, showing ARCA's potential to detect the Earth's core, with overall comparable performances to a similar study of IceCube on a forecast of 10 years of data acquisition. A possible improvement of sensitivities by exploiting the astrophysical neutrino flux was investigated, but shows only a small effect as the Earth gets opaque for neutrinos in that high-energy range. Studying small density heterogeneities in the lower mantle of the Earth, the so called large low shear velocity provinces (LLSVPs), appears to be out of reach with absorption tomography in the context of existing high-energy atmospheric neutrino detectors like ARCA.

Oscillation tomography is sensitive to the electron density n_e in the propagation medium of a neutrino, which is proportional to the product of the matter density ρ and the proton-to-nucleon ratio Z/A. Assuming that one of these quantities is known from Earth science, one can measure the other. Repeating the analysis of the Earth's density profile with ORCA yields significantly stronger resolution power, up to a precision of $+24\,\%/-32\,\%$ for the inner core and $\pm 5\,\%$ for the lower mantle with 10 years of ORCA data. The improvement is due to the higher flux of neutrinos in the oscillation

energy range. Using gravitational constraints on the Earth's mass and inertia further improves the result, as correlation effects between the layers are suppressed. However, the approximation of a 5-layer model appears to be too simplified concerning the obtained resolutions, especially in the outer mantle region with various small transition zones of different density. In a next step, instead of fitting constant densities, ρ was measured relative to PREM. This approach is also commonly used in geophysics and opens the door for a combined use of neutrino with *e.g.* seismic data. The study on oscillation and absorption tomography are subject of my ICRC proceeding[171].
Studying LLSVPs appears more feasible with oscillation tomography. An evaluation of the signal from LLSVPs at different locations in the Earth relative to the detector position revealed that long neutrino intersections through a LLSVP in a narrow angular window are favoured over short ones with a wide angular window. In the concrete case of ORCA, this condition on the LLSVP position is fulfilled almost perfectly for the African LLSVP. However, only LLSVPs with relative densities $+24\,\%/-21\,\%$ compared to the surrounding mantle can be detected, which is about 10 times the density anomaly estimates based on seismic measurements. Interestingly, the contributions of the two PID channels, namely track- and shower-like events, differ strongly between the study of the outer core and mantle heterogeneities, indicating that neutrino detectors can in fact be optimised for specific geophysical questions.
The last presented analysis of KM3NeT focused on the Z/A of the outer core, assuming its density is known from PREM. The sensitivity to the Z/A in the outer core was found to be $\pm 5\,\%$. This result is obtained in the same manner as in an earlier PhD thesis on oscillation tomography with ORCA. Improvements in the Monte Carlo simulation and new assumptions on oscillation parameters based on the updated global results show a clear gain in sensitivity with respect to the old analysis, which shows how the potential of neutrino oscillation tomography can still benefit from better knowledge of the detector.

In order to distinguish between realistic models of the outer core composition and to identify the light elements it contains, sub-percent accuracy is necessary due to the similar Z/A values of *e.g.* Iron, Silicon or Oxygen. In the second part of this thesis, detectors of different designs and detection techniques are evaluated regarding their performance power on constraining the outer core composition, with the goal to define requirements for a potential next-generation detector (NextGen) that would be capable of actually excluding realistic model compositions. Chronologically, most of the work presented in that chapter was done during the first year of my PhD and led to several contributions in conferences and workshops, a publication in Europhysics News [1] and a paper submitted to Frontier Geoscience [2], all with a focus on the chemical composition of the outer core. Instead of using a specific MC simulation to simulate a detector, parameterised responses are used for a flexible tuning of the basic detector properties, as size and resolution. The detector types under investigation include an ORCA-like large volume water-Cherenkov detector, a water-tank design with improved resolution at the cost of instrumented volume à la HyperKamiokande and a DUNE-like experiment using a TPC filled with liquid Argon. The DUNE- and ORCA- like detector configuration yield similar results, while HyperKamiokande achieves a precision of $\sim 2.5\,\%$ after 20 years of running time. The trade-off effects between size and detector performance is one of our most robust conclusions.

Based on these findings, a NextGen configuration was defined with similar resolution power as HyperKamiokande but with an instrumented volume about 30 times larger. Such a detector would be able to exclude a hydrogen-rich outer core model within 15 years. Although such a detector may seem unattainable at the moment, one has to be aware that the technology already exists and is used right now. With appropriate budget and manpower, such a powerful neutrino tomography detector could be built, while the theoretical limitation of seismology to directly constrain chemical compositions will never be overcome.

Outlook Neutrino tomography shows the general potential to contribute to a better knowledge of the interior of the Earth. However, the current detector generation does not yet reach the precision to tackle open questions of geosciences alone. The starting collaboration with the seismologists at University of Utrecht, Prof. Arwen Deuss and her PhD student Rûna van Tent, bears great potential regarding the combination of neutrino- and seismic data.
The tools developed during my doctorate can be seen as a solid base for future neutrino physicists with the aim of doing neutrino tomography. Especially the implementation of a 3D Earth model opens new, interesting possibilities, such as the modeling of more complex 3D heterogenities in the mantle, and more generally 3D neutrino tomography of the Earth using multiple neutrino detectors.

`EarthProbe` and `SWIM`, the two frameworks used during this thesis, were originally created by a former PhD student of APC, Simon Bourret. In fact they share many classes and the overall design is similar. It would be worthwhile to implement the parameterised detector response from `EarthProbe` into `SWIM`, to ease the development and avoid potential mismatches due to slight divergences in the code, by focusing on only one software environment.

Additional work Parallel to the actual analysis, both the parameter-based framework `EarthProbe` and the MC-based framework `SWIM` were extended by multiple functionalities regarding neutrino tomography, but were also maintained and improved on all levels of software development. This is especially true for `SWIM` which evolved to one of the main analysis frameworks in the oscillation working group of KM3NeT. The implementation of absorption effects and input models at higher energies together with a proper input file built from the ARCA MC also opens the opportunity to use `SWIM` for ARCA and further demonstrates how in principle any MC can be used to simulate the respective detector – one of the motivations to develop `SWIM` in the first place. `EarthProbe` was used by the M1 student Romain van den Broucke for a study on ARCAs sensitivity to the high-energy neutrino cross-section, using the new tools I developed.

`ParamPID`, the python based machine-learning package for the event classification, developed into an important pillar of oscillation analysis and will be further maintained and improved by other collaborators. Together with my framework for the creation of training features (both described in the technical note B) it provides a powerful tool to further improve the KM3NeT PID by adding and evaluating more features. Its performance was presented as a poster in the Neutrino2022 conference [3].
I used `ParamPID` to train the first PID for ARCA for the track/shower- and neu-

trino/muon classification. A paper comparing different machine learning techniques (Deep learning, graph/convolutional neural-networks) for event classification in ARCA is in planning. Efforts are made in order to distinguish atmospheric and astrophysical neutrinos.
Moreover, in a mini production of ORCA4 with alternate PMT-efficiencies, thanks to my adapted framework, the PID was for the first time automatically created as a part of the MC chain.

Abbreviations

AGN Active Galactic Nuclei 8
ARCA Astrophysical research with cosmics in the abyss 31

BBN Big Bang nucleosynthesis 7
BDT boosted decision tree 67

CC charged current 6
CMB core-mantle boundary 41
CP charge-parity 6
CU calibration unit 54

DIS deep inelastic scattering 22
DOM digital optical module 28
DU detection unit 31

EC electron capture 56

ICB inner core boundary 107

JB junction box 54
JTE JTriggerEfficiency 61

LLR log-likelihood ratio 108
LLSVP large low shear velocity province 43
LnL log-likelihood 108

NC neutral current 6
NextGen next-generation 49
NMO neutrino mass ordering 16

ORCA Oscillation research with cosmics in the abyss 31

PDF probability density function 104
PID particle identification 67
PMT photomultiplier tube 54
PREM preliminary reference Earth model 40

QE quantum efficiency 34

RDF random decision forest 67

SM standard model 6
SN supernova 8
SSM standard solar model 7

ToT time-over-threshold 57
TPC time projection chamber 35

ULVZ ultra light velocity zone 43

Z/A proton-to-nucleon ratio 42

Appendix A

Additional plots and tables

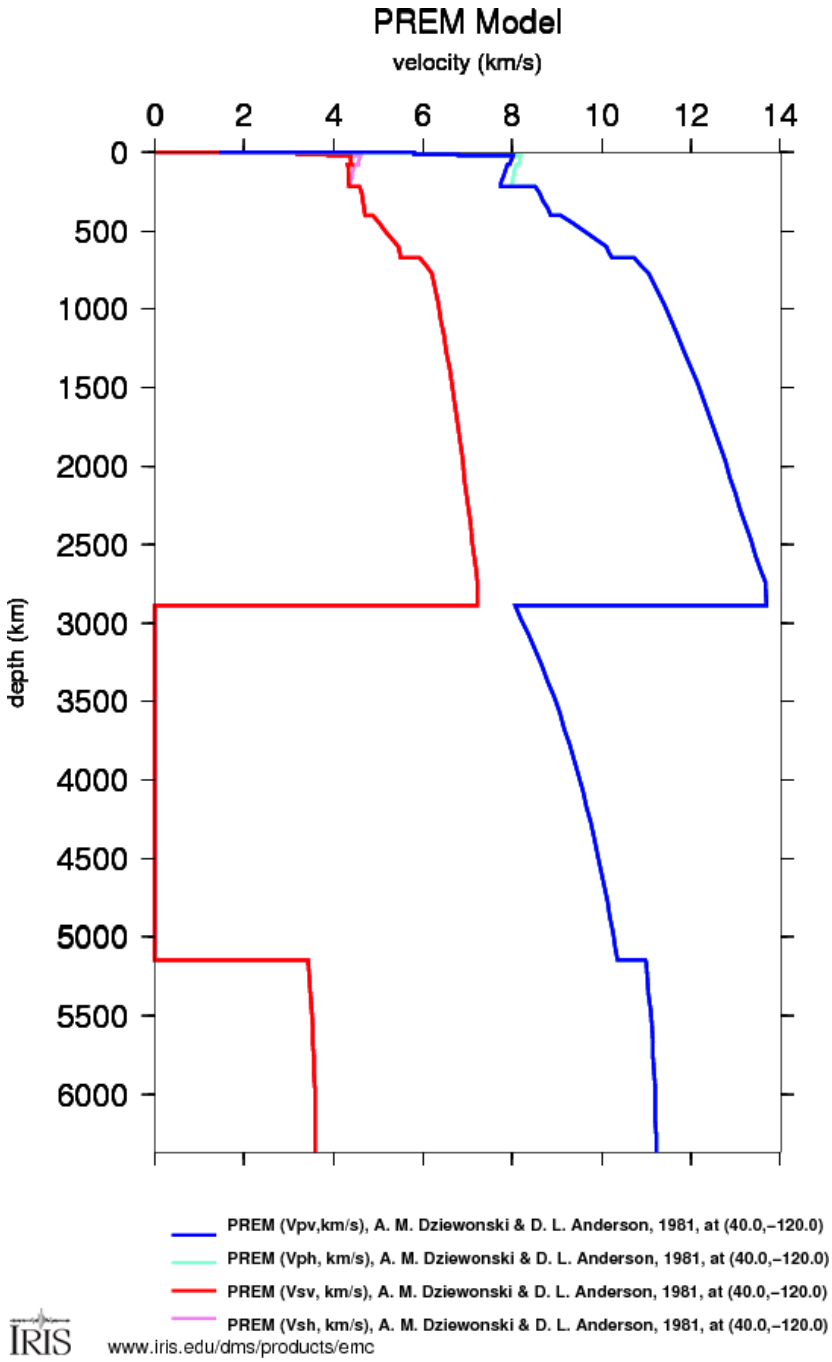

Figure A.1: PREM S and P wave velocities. (From http://ds.iris.edu/ds/products/emc-prem/.)

Radius [km]	ρ [g/cm^3]
0.0	13.0884
200.0	13.0884
400.0	13.0797
600.0	13.0536
800.0	13.0100
1000.0	12.9491
1200.0	12.8707
1221.5	12.7749
1400.0	12.1663
1600.0	12.0692
1800.0	11.9468
2000.0	11.8090
2200.0	11.6547
2400.0	11.4831
2600.0	11.2929
2800.0	11.0833
3000.0	10.8532
3200.0	10.6015
3400.0	10.3272
3480.0	10.0294
3600.0	5.5664
3630.0	5.5064
3800.0	5.4914
4000.0	5.4068
4200.0	5.3072
4400.0	5.2071
4600.0	5.1059
4800.0	5.0029
5000.0	4.8978
5200.0	4.7898
5400.0	4.6784
5600.0	4.5630
5701.0	4.4431
5771.0	3.9921
5871.0	3.9758
5971.0	3.8498
6061.0	3.5432
6151.0	3.4895
6221.0	3.3595
6291.0	3.3671
6346.6	3.3747
6356.0	2.9
6368.0	2.6

Table A.1: 42-layer PREM used as default in all analyses. Horizontal lines mark the borders between inner- and outer core and mantle.

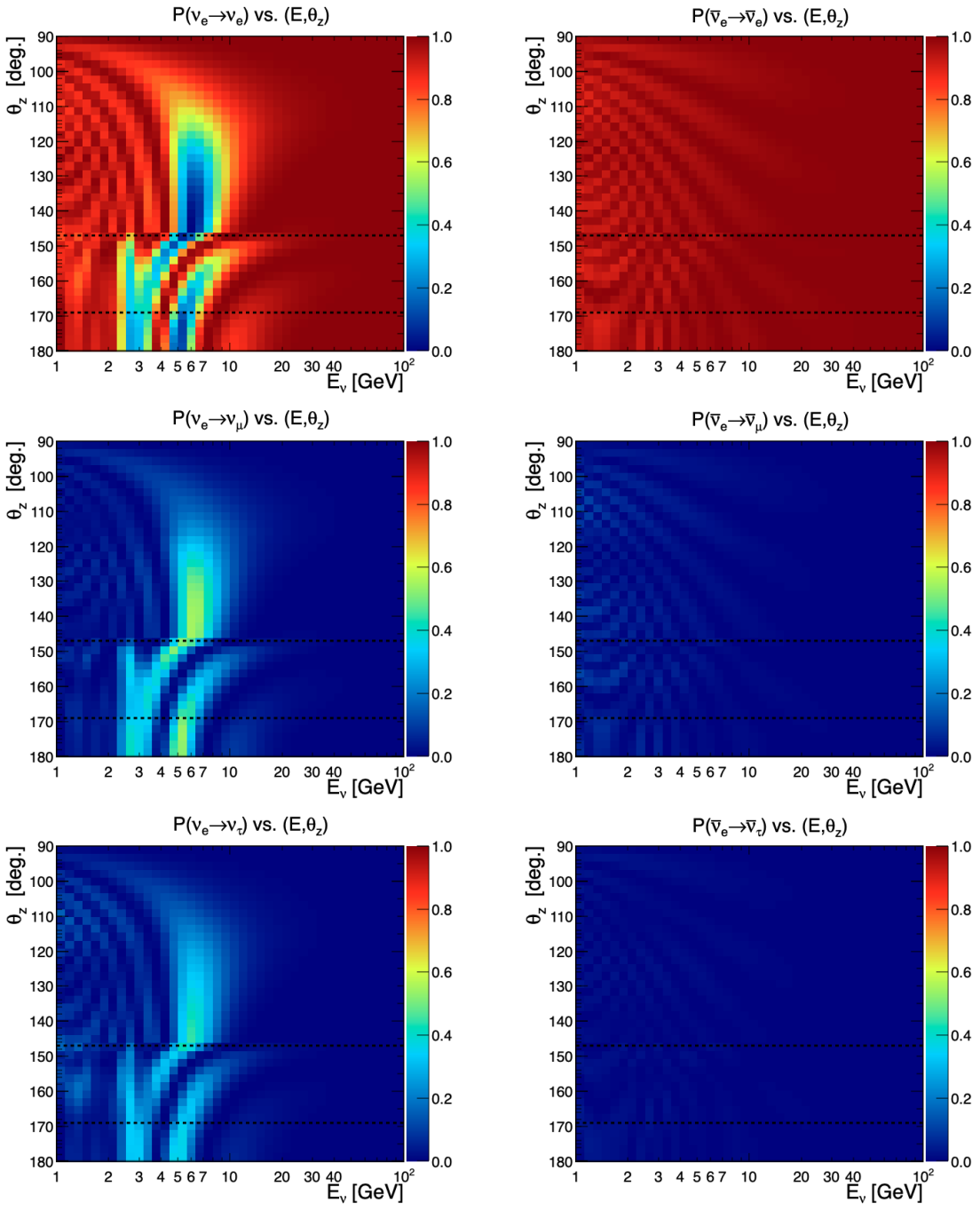

Figure A.2: $\overset{(-)}{\nu}_e$ oscillation probabilities for PREM calculated with `OscProb`.

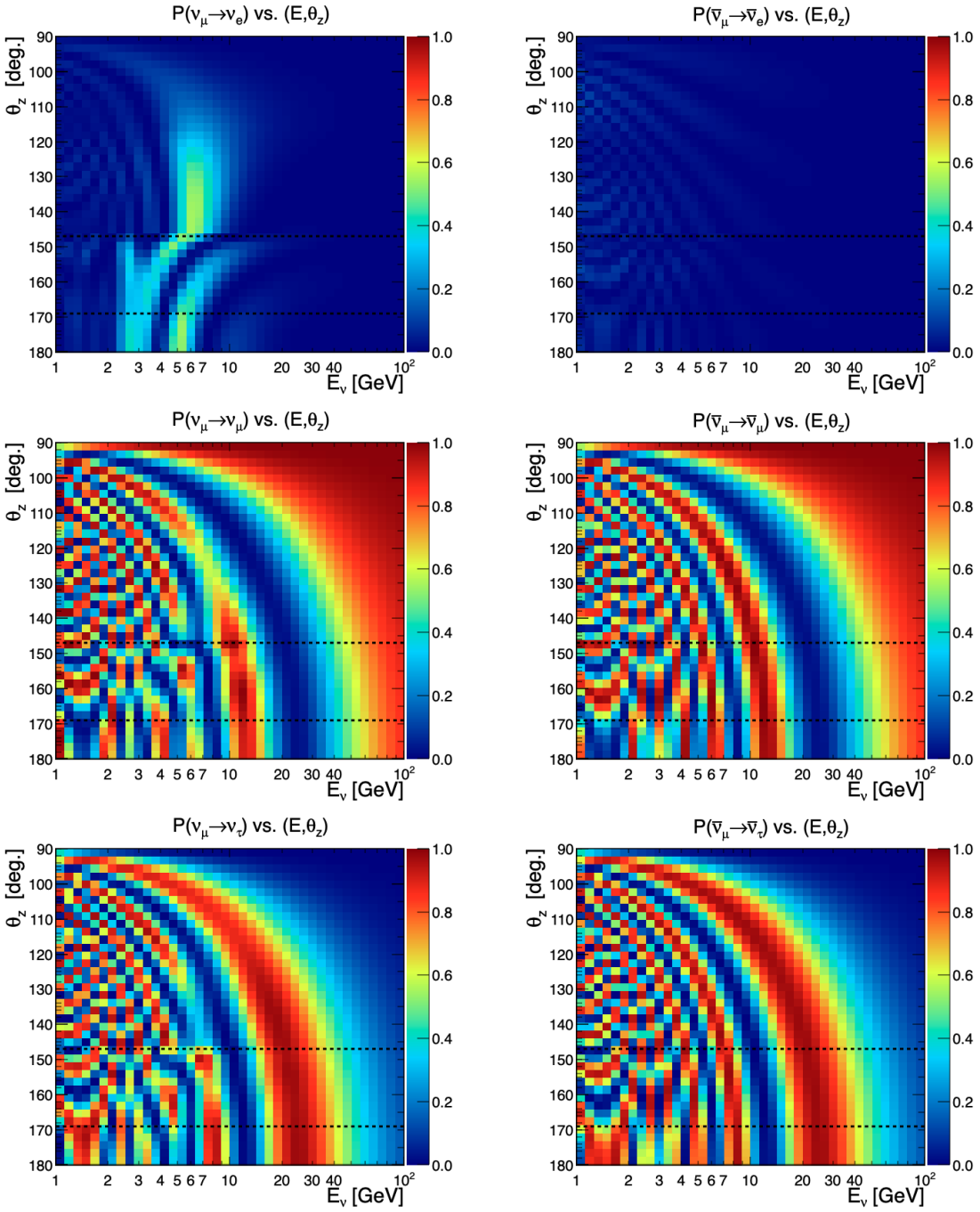

Figure A.3: $\overset{(-)}{\nu}_\mu$ oscillation probabilities for PREM calculated with `OscProb`.

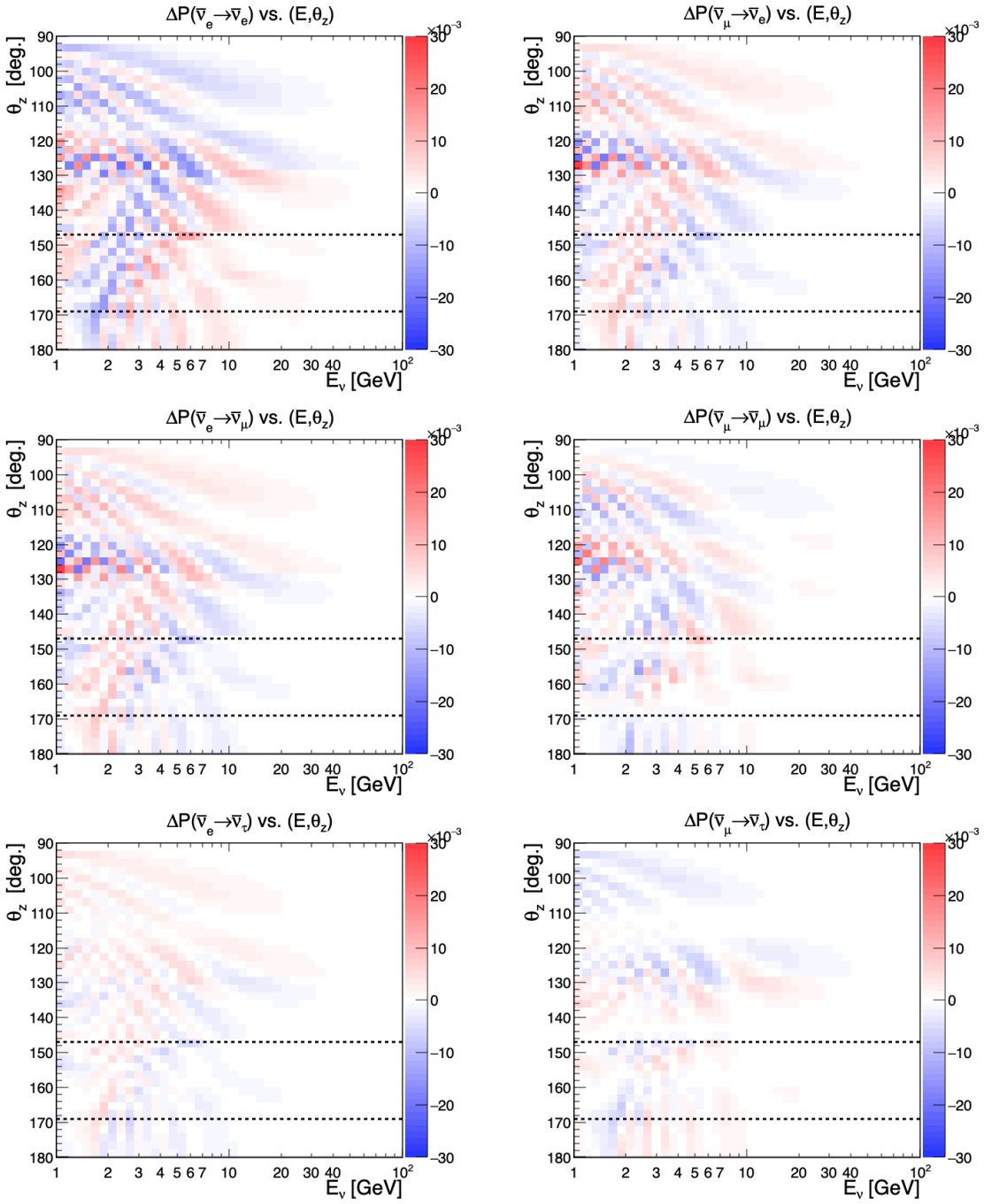

Figure A.4: Differences in $\bar{\nu}$ oscillation probabilities between 42- and 5-layer PREM.

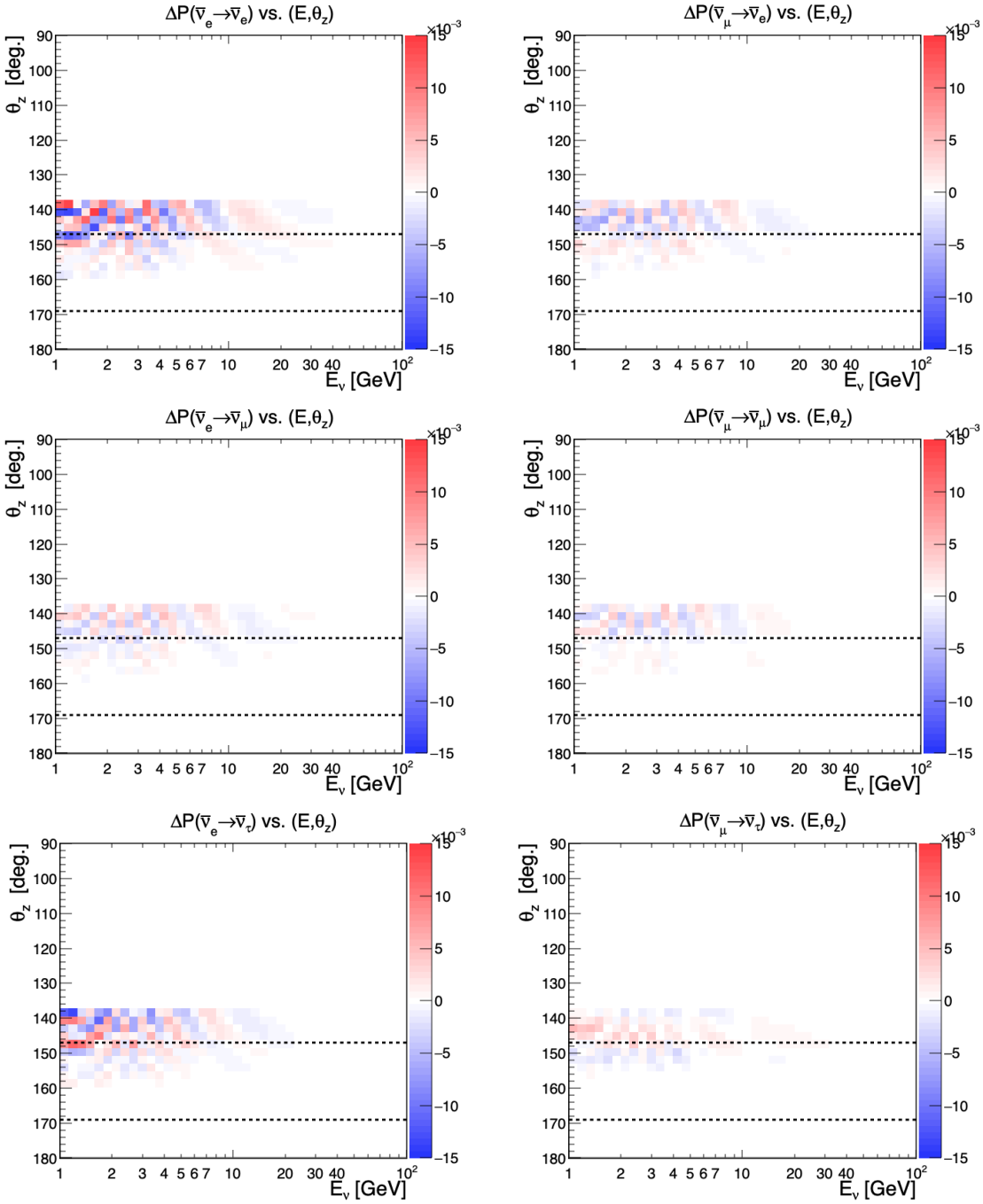

Figure A.5: Differences in $\bar{\nu}$ oscillation probabilities between homo- and heterogene mantle.

Feature	Description
JGANDALF_BETA0_RAD	angular resolution [rad]
JGANDALF_BETA1_RAD	angular resolution [rad]
JGANDALF_CHI2	chi2
JGANDALF_NUMBER_OF_HITS	number of hits
JENERGY_ENERGY	uncorrected energy [GeV]
JENERGY_CHI2	chi2
JGANDALF_LAMBDA	control parameter
JGANDALF_NUMBER_OF_ITERATIONS	number of iterations
JSTART_NPE_MIP	number of photo-electrons up to the barycentre
JSTART_NPE_MIP_TOTAL	number of photo-electrons along the whole track
JSTART_LENGTH_METRES	distance between first and last hits in metres
JVETO_NPE	number of photo-electrons
JVETO_NUMBER_OF_HITS	number of hits
JENERGY_MUON_RANGE_METRES	range of a muon with the reconstructed energy [m]
JENERGY_NOISE_LIKELIHOOD	log likelihood of every hit being K40
JENERGY_NDF	number of degrees of freedom
JENERGY_NUMBER_OF_HITS	number of hits
JCOPY_Z_M	true vertex position along track [m]
JPP_COVERAGE_ORIENTATION	coverage of dynamic orientation calibration
JPP_COVERAGE_POSITION	coverage of dynamic position calibration
JENERGY_MINIMAL_ENERGY	minimal energy [GeV]
JENERGY_MAXIMAL_ENERGY	maximal energy [GeV]

Table A.2: List of intrinsic information of the `JGandalf` track-reconstruction, that are used as features for the parameter-based PID.

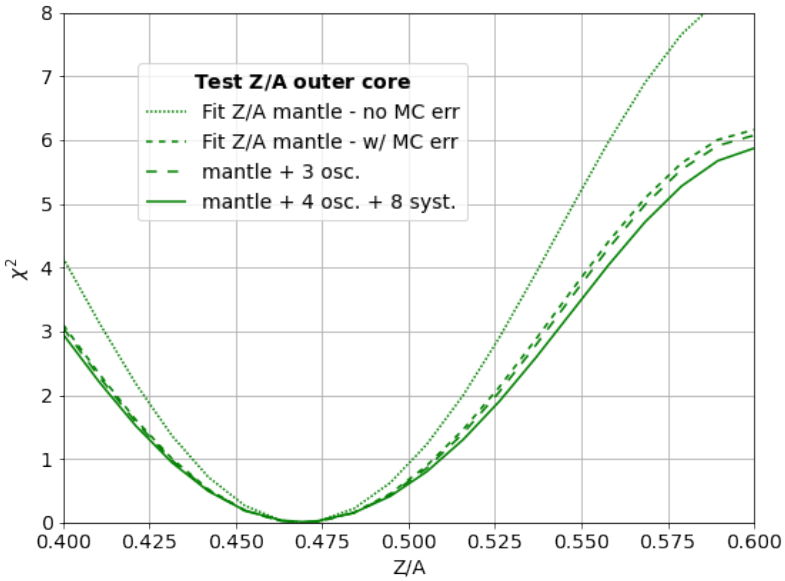

Figure A.6: Reproduction of Fig. 9.7 in [162] using oscillation parameters from NuFit 3.2, 20 bins per axis and the KM3NeT MC from the LOI of 2016.

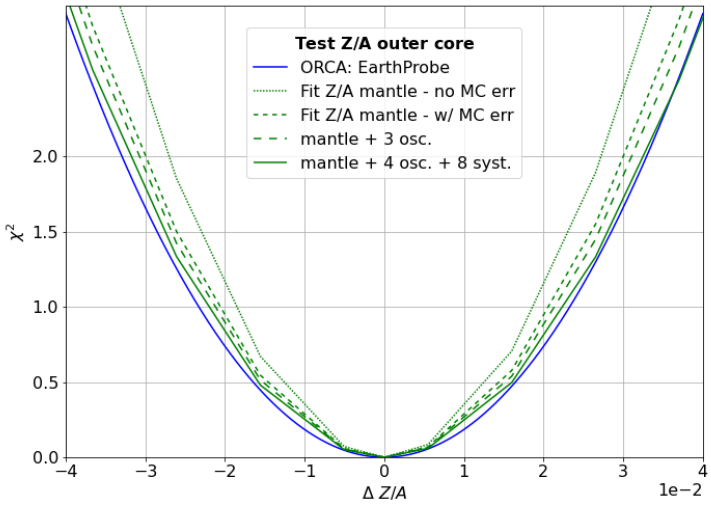

Figure A.7: Comparison of the outer core Z/A sensitivity between `SWIM` and `EarthProbe` (10 yr).

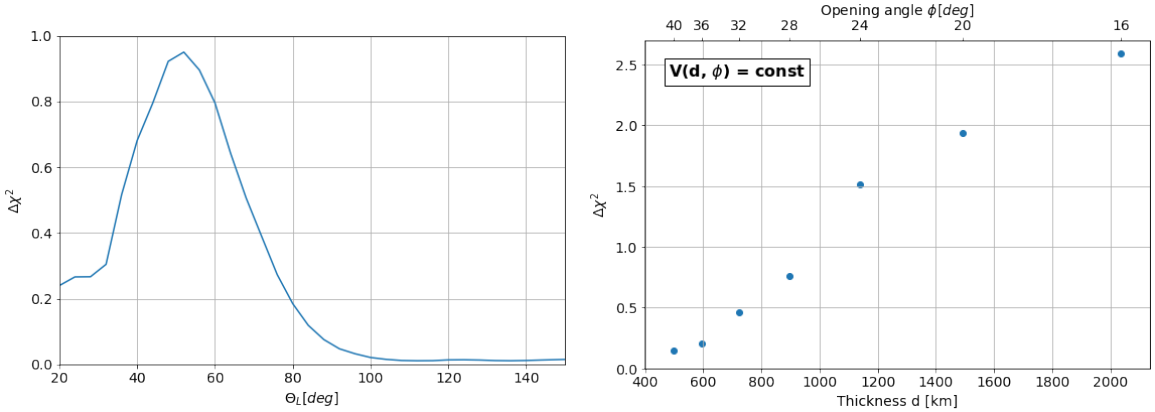

Figure A.8: Analysis of the LLSVP shape performed with `EarthProbe` (as for `SWIM` in Fig. 9.15).

Appendix B

Parameter-based PID

This document provides a manual and technical information on the preparation of a parameter-based PID from offline files. This includes the conversion from offline files to pandas DataFrames, the extraction of training parameters and the training itself. It is further explained how the final h5 file containing the PID can be converted to the SWIM input format. This document refers to the tags v1.0.0 of the **ParamPID** and **newhitfeatures** repositories in the KM3NeT Git.

B.1 Offline file conversion and feature extraction

The preparation of the PID starts after the full mass-production chain, including the simulation of neutrino interaction, light propagation, event trigger, and event reconstruction. The final output of the MC simulation is saved in the ROOT based *offline file* format. Since the machine learning application described here is Python based, the files have first to be converted. The KM3NeT internal *km3pipe*[172] was created for exactly this task, and is the backbone of the feature extraction. The code for the feature extraction is available on the KM3NeT Git: `https://git.km3net.de/parapid/newhitfeatures`. It can be simply installed by creating a virtual environment with

```
python -m venv pyvenv
. pyvenv/bin/activate
```

and

```
make
```

NOTE: the installation requires JPPY The main script is *scripts/extractor.py* that, after parsing some input arguments (use *./extractor.py -h* for help) starts the pipeline. Its default modules are explained below.

B.1.1 WriteSummary

WriteSummary.py contains the modules *create_key* and *write_table*, which create the **summary** DataFrame in which all extracted features are stored and which is the output of the Pipeline.
NOTE: Most of the feature names are hardcoded within the respective modules! Their names are chosen to fit the scripts of the PID training.
NOTE: The dtypes of each processed *blob* (=event) have to be consistent! Otherwise the event won't be written out. Since some values in the offline files can be of *NoneType*, each module puts a **dummy value** for each of its features.

B.1.2 McTrackInfoModule

It extracts general MC information of the event

- True energy
- True position
- True direction
- pdgid
- is_cc
- decay_muon (bool indicating muon in decay channel)

and some values to identify the event

- run_id
- trigger_counter
- frame_index

B.1.3 SelectorBestModule

Calls *km3io.tools.best_track()* to extract

- Reconstructed energy
- Reconstructed position
- Reconstructed direction
- Reconstruction likelihood

of the best track of the respective reconstruction (which are chosen as input arguments for *extractor.py*). A boolean parameter *RECO_is_good* indicates whether the reconstruction was successful, i.e a best track was found. For further processing, only events should be used with at least one good reconstruction available.

B.1.4 WeightModule

Extracts

- w1, w2, w3
- num_sec [numberOfSeconds]
- n_gen [numberOfEvents]
- n_files_gen

According to the wiki (https://wiki.km3net.de/index.php/Neutrino_generator_weights) the correct event weight per year (**weight_one_year**) is given by

$$w[yr^{-1}] = w2 * \phi * \frac{365.25 * 24 * 3600}{\mathbf{num\_sec} * \mathbf{n\_gen}} \tag{B.1}$$

NOTE: When combining multiple files, the event weight w has to be divided by the number of files (per flavour). If you are sure how many files you will use, **n_files_gen** can be given as argument to *WeightModule*. Otherwise, the default is 1. The value of **n_files_gen** used for

$$\mathbf{weight\_one\_year} = \frac{w}{\mathbf{n\_files\_gen}} \tag{B.2}$$

is however saved to the output file.

B.1.5 FitInfExtractor

The available fit information (FitInf) of each reconstruction algorithm are listed in https://git.km3net.de/common/km3net-dataformat/-/blob/master/definitionfitparameters.csv according to the current KM3NeT-dataformat.
NOTE: The FitInf are extracted by their indices. However, the indexing may change in the future! Carefully check, if the list of FitInf that are to be extracted matches the current KM3NeT-dataformat!

B.1.6 UpDownFeatureModule

Currently this module only calculates

$$\frac{\text{JENERGY\_CHI2}}{max(\text{JENERGY\_NUMBER\_OF\_HITS}, 1)} \tag{B.3}$$

the reduced likelihood of the best reconstructed track by JGandalf. The original idea was to compare e.g. the likelihood of the best up-going and the best down-going reconstructed track, as additional quality cut on the direction reconstruction.

B.1.7 JSHFeaturesExtractor

This module extracts features based on the output of JShowerFit and its intermediate stages (prefit, ptsimples, posfit).

distance_stageA_stageB Difference in reconstructed vertices between stage A and B

dt_stageA_stageB Difference in reconstructed time between stage A and B

stageX_fits_near_best Number of fits in stage X in vicinity of best fit

ratio_stageX_fits_near_best Ratio of fits in stage X in vicinity of best fit

mean_tres_hits_around_10deg_Cherenkov_angle

mean_abs_tres_hits_around_10deg_Cherenkov_angle

mean_tres_weighted_hits_around_10deg_Cherenkov_angle

nhits_around_10deg_Cherenkov_angle

angle_dirprefit_shfit Angle between direction prefit and final fit

Note: For each offline file, the corresponding detx file has to be provided.

B.1.8 HitPdfModules

The two following modules were aiming to mimic the HitPdfFeatures that were used by former analysis [92] based on DUSJ reconstruction. In that work, the event reconstruction was compared with PDFs of hit distributions for shower-like events, which helped to significantly increase the PID efficiency. While the DUSJ HitPdfs were created from the reconstructed MC events, the PDFs used for the features of this extraction are taken from JPP [173] and based on physical models only. **Note:** For each offline file, the corresponding detx file has to be provided.

Hit features

The so called JPDFs try to estimate the likelihood of a given event to trigger a PMT signal. The JPDF is based only on physical parameters, like light production and transmission, and technical parameters describing the light detection, like trigger efficiency of the PMT (see [154]). For each event, the triggered PMTs within a certain volume around the reconstructed vertex position are selected. For showers, the volume is a sphere with radius R, for tracks a cylinder of radius R and height corresponding to the reconstructed track length + 20 m. R is currently set to 70 m, the approximate absorption length of Cherenkov light in water. The likelihood of detecting a photon, given an incident neutrino E_{reco}, and $\vec{dir}_{reco}$ at $\vec{pos}_{reco}$ is then calculated for each PMT in the selected volume as

$$LLR = -\ln\left(\frac{P(\text{signal + background})}{P(\text{background})}\right) \tag{B.4}$$

where the probability of detecting a photon x ns after an interaction is obtained from the PDF as

$$P(\text{PDF}, x) = \exp\left(-\int_{x_{min}}^{x} \text{PDF } dx\right) \times \frac{\text{PDF}(x)}{1 - \exp(-\int_{x_{min}}^{x_{max}} \text{PDF } dx)} \tag{B.5}$$

with a time window of [-50,450] ns. The background hypothesis P(background) is calculated for a constant background rate of 7 kHz.

This is done for all 4 combinations of reconstruction (JShower or JGandalf) + geometry (sphere or cylinder). The sum of the likelihoods is then saved for all 4 cases.
Example: To calculate *llh_shower_jshower* one uses the output of JShower for $\vec{pos}, \vec{dir}, E$ of an event. All hits within a sphere of radius R around $\vec{pos}$ are selected, and the likelihood to trigger these PMTs with an event of $\vec{dir}, E$ at $\vec{pos}$ are calculated. On the other hand, for llh_track_jshower the likelihoods are calculated for all PMTs within a cylinder. For *llh_track/shower_jgandalf* the output of JGandalf is used for the geometry cut and the evaluation of the JPDF.
Additionally, the JPDFs are also evaluated for shifted vertex positions. The idea is, that a shower reconstruction is likely to fit the vertex position centered between all hits, which for a track-like event is somewhere along the muon track. The interaction vertex is thus shifted respectively by 1 m, 20% and 40% of the track length along the track trajectory. If the sum of the likelihoods is higher for a shifted vertex than for the actual reconstructed vertex, it is a hint that the event might actually be track-like. The extracted features are thus:

- llh_track/shower_RECO
- llh_track/shower_shifted1m_RECO
- llh_track/shower_shifted0p2_RECO
- llh_track/shower_shifted0p4_RECO

for all 4 combinations of track/shower + RECO.

No-hit features

The same JPDFs are also used to extract features based on no-hit information. Here one calculates the probability of being triggered (equation B.4) either by a neutrino or a background (R=7 kHz) event for **all** (triggered or not) PMTs within the selected volume around the reconstructed interaction vertex to estimate the number of expected hits. Finally, the number of hits assigned to the event by the respective reconstruction, as well as the number of PMTs (in the chosen volume, respectively) are stored to the output file. The ratio of expected to actual hits may in future replace containment cuts based on the reconstructed vertex position, which have to be adapted for each detector configuration.

The extracted features are thus:

- n_exp_hits_track/shower_RECO
- n_exp_hits_background_track/shower_RECO
- n_hits_track/shower_RECO
- n_pmts_track/shower_RECO

for all 4 combinations of track/shower + RECO.

B.1.9 Remarks

CPU time A table of the CPU time needed per module for the processing of an offline file with $\sim$ 19 k ORCA6 events is attached (Tab. B.1). The HitPdfModules take by far the most time, followed by JSHFeaturesExtractor. Both are not needed for ARCA productions (no JShowerFit), making their processing much faster than ORCA productions. **It is in any case recommended to test the extractor script on a single file, before launching multiple jobs.**

Run multiple jobs The *extractor.py* script will automatically submit a job to CC-Lyon when the option -b is given. Since there are usually thousand of MC files, it is convenient to use a script to launch all jobs at once. A DRAFT for such a script is available *submit.py* but has to be used very carefully. I.e. the file locations of offline and .detx files have to be adapted. The options for *extractor.py* have to be set in *submit.py*. Also the number of files to be processed per job can be set (in *chunked_iterable*). E.g. for ORCA6 MC more than 9000 offline files were produced, which exceeds the usual job limit. It is very much recommended to study the timing information of km3pipe as well as the needed resources (memory, CPU time) on a CC-Lyon cluster of a single job, before launching a full production.

Concatenating files The output files can be combined with the *concat.py* script. It can be also used to add additional columns (like the respective filename). Be aware that for big productions you may run into memory errors at this point (any hints to work around this problem are welcome).

B.2 Parameter-based PID

This ParamPID repository (https://git.km3net.de/parapid/parampid) provides the package for the training of track/shower and nu/mu classifiers. It can also be installed via

```
python -m venv pyvenv
. pyvenv/bin/activate
make
```

Its main script is called *APC_PID.py*, which also provides a help menu for the required input arguments (option -h). Its functionality is best explained by looking at the three main classes of the package.

B.2.1 PidTuple

The PidTuple class prepares the input file for the training. This basically includes the declaration of the PID classes and the choice of the events that will be used for training.

Select training classes

For the first task the input DataFrame has to contain the columns **is_neutrino**, **pdgid** and **is_cc**. The list of class names can be extended if needed. The currently implemented classifiers are:

track/shower track: ν_μ-CC; shower: ν_μ-NC, ν_e-CC/NC
Note: ν_τ events are not yet separated into track and showers (based on the produced lepton)

nu/mu mupage vs $\nu_{e,\mu,\tau}$-CC/NC

The classifier will try two separate events with label 0 and label 1. Simply switching the labels of the PID classes would therefore allow to train e.g. pure_noise vs ν, or ν_τ vs $\nu_{e,\mu}$ etc. The corresponding lines of code in *APC_PID.py* are:

```
pidTuple.SetLabelsByEventClasses({"elec_cc":0,
                                  "elec_nc":0,
                                  "muon_nc":0,
                                  "muon_cc":1,
                                  "mupage":2,
                                  "tau_cc":3,
                                  "pure_noise":4})
```

Draw training sample

In order to draw a training sample one could simply choose random events of each class. However in ParamPID the default approach is to choose a training sample with homogeneous energy distributions in each training class. This is achieved by binning

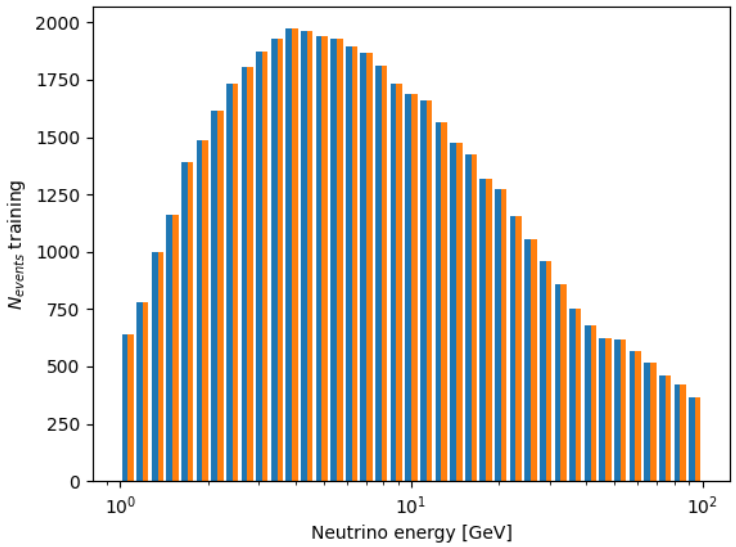

Figure B.1: Energy distribution of training samples of class1 (blue) and class2 (orange)

the data in $log(E)$ and draw a random sample of size $n_i = min(\text{class1}(E_i), \text{class2}(E_i))$ per bin i. The number of training events N to be used for the training (per class) is passed to *APC_PID.py* with the option -n N. If $N > \sum n_i$, all n_i will be scaled by the factor $\frac{n_i}{N}$[1]. The energy distribution of the training sample for two classes may then look like in Fig. B.1.

The motivation - or even the necessity - of homogenising the training sample is that otherwise one risks to train the classifier on the event distribution of the sample, which relies only on the parameters of the MC. E.g. if atmospheric muons are only produced at energies above 10 TeV, a classifier would reject 100% of muons by cutting on the energy. The energy distribution of training events is thus an important information to correctly interpret the output of the classifier.
Note: This homogenisation function is a relic of the original ECAP scripts. The usage of *sklearn* allows for the weighting of training events, which also allows to homogenise the training sample without rejecting events.

B.2.2 ParamPID

This class is the heart of the parameter-based PID and contains the actual training function. At this point, the DataFrame is in the right shape for the training. It is now recommended (but optional) to apply selection cuts.

[1] Actually, the integer of this value is taken, because one can not use a fraction of an event. Thus the total number of training events may be smaller than the input N.

Event selection

Some cuts, based on the respective event reconstruction, are defined in the ParamPID class and can be applied by using the options --jsh, --gandalf, --aashower and/or --dusj. An event passes the selection if the criteria for at least one of the reconstructions is full-filled. In the past, selection cuts on containment, fit likelihood etc. showed to be quite efficient in order to increase the PID efficiency. It is of course possible to apply selection cuts on the input file before launching *APC_PID.py*. In order to test different selection cuts it is however convenient to keep one file with all events, and apply cuts only directly before the training step.
Note: The current selection cuts in ParamPID are neither optimised nor official, but simple examples. They all contain a cut on events reconstructed as up-going.

Training

Event classification based on a list of parameters, is hardly doable by hand, especially given the high number of available parameters. Machine learning tools like decision forests are optimised for tasks like this. A decision forest contains a number of decision trees, that calculate a prediction y based on the input parameters x. At each branch of the tree, one parameter is compared to a certain value. The outcome of the comparison determines the next branch and so on, eventually ending in a leaf, assigning a prediction score to the input variables $y_i = f(x)$. An even more powerful prediction can be made by the combination of n trees to a so called decision forest. The prediction score of a decision forest is given by:

$$y = \sum_{k=1}^{K} f_k(x) \tag{B.6}$$

where K is the number of trees in the ensemble. This score can now be used as a classification score by choosing a cut value c, so that

$$class = \begin{cases} 1 & y \geq c \\ 0 & y < c \end{cases} \tag{B.7}$$

There are multiple methods on how to train the decision forest. Earlier version of this package used random decision forests (RDF), were each tree is trained independently from each other, assigning an event either to class 0 or class 1, and where the final prediction score is simply the fraction of trees voting for class 1 (or 0). It is common (like in [92]) that each of these randomly trained trees only sees a fraction of the available training parameters. Overall this method is less likely to be overtrained, e.g. due to unknown systematic effects in the MC, making it generally more reliable.
The current version of ParamPID uses instead boosted decision trees (BDT) that are trained one after the other, aiming to optimise an objective function, a combination of training loss and regularization term. The XGBoost library [149] provides a python package which is used by ParamPID to train the BDT. Their documentation also includes a nice introduction to Boosted Trees, which is highly recommended for the reader who is new to the field of decision trees.
After the declaration of the classifier, the actual training is started. The resulting classifier is stored with the *pickle* package and can be used in the future. The classification

is than applied to all events that were not used for training. However, each event of the training sample gets also a PID score assigned, using the *cross_val_predict* function of the *scikit-learn* package[152]. Cross-validation means that the training sample is divided into n sub samples and successively n-1 samples are used to predict the class of the remaining sample.

Feature evaluation

As in most machine learning applications, one can never be sure to have reached the maximum possible performance. Each additional feature could improve the classification. It comes thus in handy that *sklearn* provides a function to rank the training features by their importance to the classifier. New parameters can be evaluated and may help to understand what kind of features is helpful for the respective classification. Equally useful is to exclude features, that do not help the classifier, in order to reduce memory and CPU usage. The optional --eval option will run the recursive feature evaluation. Here, after each training, the least important parameters are removed, and a new classifier is trained with the remaining features. The features and PID-output of each step are stored for analysis.

B.2.3 PidPlotter

In a final step, some plots are produced for an immediate evaluation of the track/shower PID (Fig. B.2). Those are:

Energy distribution of training sample As described above and in Fig. B.1

Accuracy score The fraction of correctly classified events per energy

PID efficiency The fraction of events per PID class that are classified as track. Note that the classifier may perform significantly worse for event types that weren't present in the training sample.

PID score The distribution of the classifier output for each PID class.

Separability The separability is defined as 1 - correlation factor of the PID score distribution of two classes:

$$S(\Delta E) = 1 - c(\Delta E) = 1 - \frac{\sum_i P^{\nu_\mu}_{i,\mathrm{track}}(\Delta E) \times P^{\nu_e}_{i,\mathrm{track}}(\Delta E)}{\sqrt{\sum_i (P^{\nu_\mu}_{i,\mathrm{track}}(\Delta E))^2 \times (P^{\nu_e}_{i,\mathrm{track}}(\Delta E))^2}} \tag{B.8}$$

where P_track is the probability with that an event is classified as track. This definition of separability was used in earlier studies on the KM3NeT PID ([151]) and is useful to check at which energies the classifier can actually distinguish between the two classes. In contrast to the accuracy score or the PID efficiency, the separability does not rely on a cut value on the PID score.

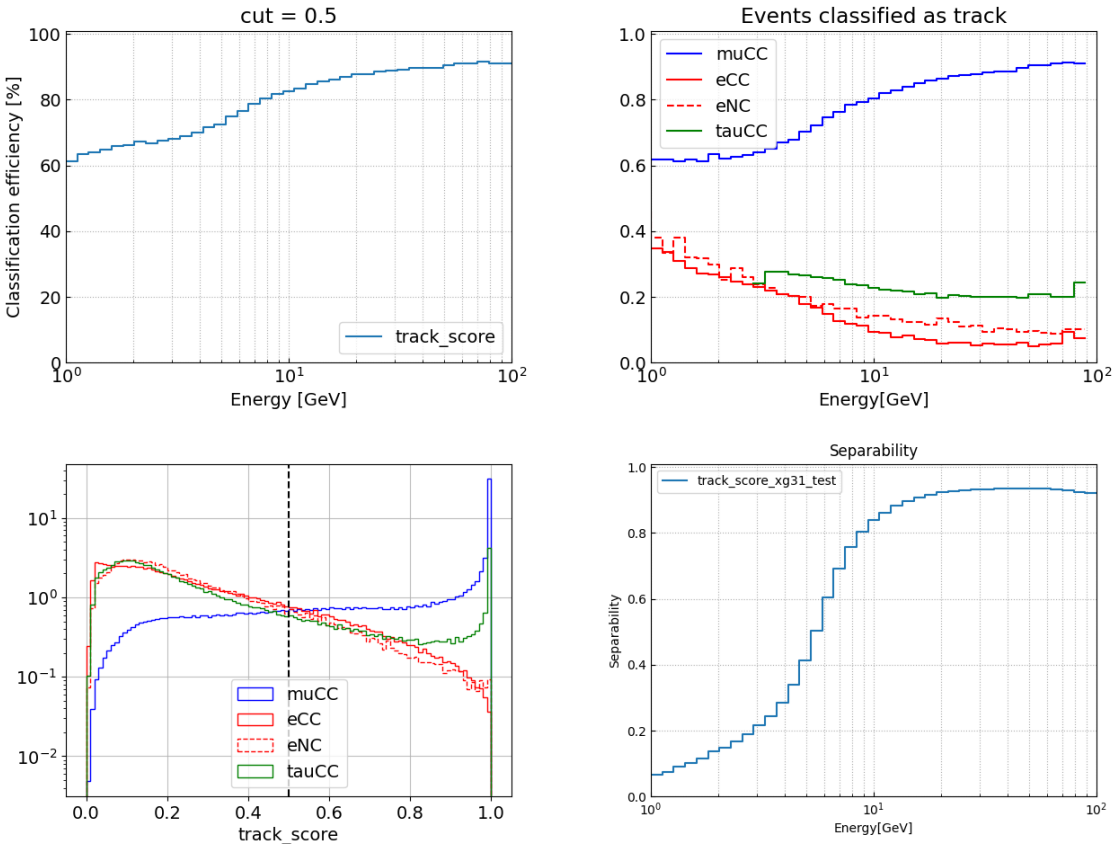

Figure B.2: Example output plots of *APC_PID.py* for full-ORCA, produced by the *PidPlotter* class.

B.2.4 Remarks

The output file "PID_output.h5", the classifier "SCORE_NAME.rdf" and all plots are saved in the directory, that was given to *APC_PID.py* with the option -w. Note that "PID_output.h5" contains only the selected events!
The classifier can now be applied on other events with *parampid/scripts/applyRDF.py*. The column table that were used for the training of the classifier has to be provided, and the DataFrame that stores the events must contain all these columns. The user should ensure, that no events of the training sample are classified this way!
The decision trees of the classifier can be inspected with *misc/rdf_to_text.py* which will provide all decision paths in text form, and a graphic of one tree (Fig. B.3).
Note: For historical reasons, a lot of functions and output files are labeled with "RDF", although ParamPID is using BDTs now.
The output file from ParamPID can easily converted to the SWIM format. Use *misc/h5_to_root.py* for the conversion into a ROOT file. Since most of the training parameters are not used by SWIM, it is possible to pass a list of columns to be kept, in order to reduce the conversion time. Finally, convert the ROOT file to SWIM format with the respective script in the SWIM repository.

Attachments

Module Name	**CPU time[s]**
OfflinePump	59.501
create_key	0.313
McTrackInfoModule	51.460
SelectorBestModule	247.459
WeightModule	0.911
FitInfExtractor	340.752
JSHFeaturesExtractor	1596.960
UpDownFeatureModule	120.790
HitPdfModule	4480.658
NoHitPdfModule	24877.863
write_table	49.947
HDF5Sink	239.920

Table B.1: CPU time of newhitfeatures for offline file (19043 events).

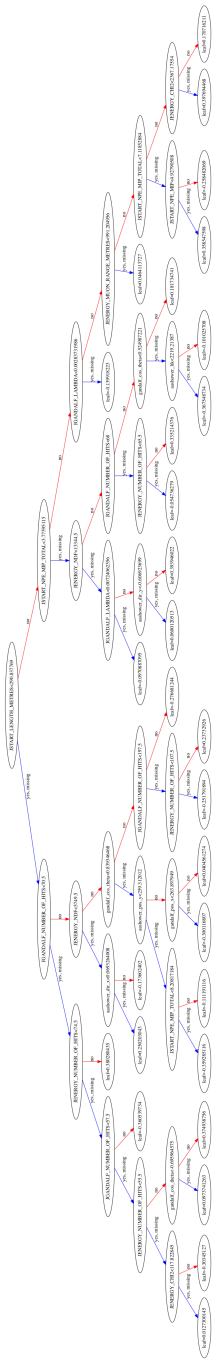

Figure B.3: Example of a decision tree.

References

[1] Véronique Van Elewyck et al. "Probing the earth's interior with neutrinos". In: *Europhysics News* 52.1 (Feb. 2021), pp. 19–21. DOI: 10.1051/epn/2021103.

[2] L. Maderer et al. *Unveiling the outer core composition with neutrino oscillation tomography*. 2022. DOI: 10.48550/ARXIV.2208.00532.

[3] A.L. Pedrajas and L. Maderer. "Poster: Parameter-based particle identification using machine learning techniques in KM3NeT-ORCA6". In: *Neutrino 2022*. 2022.

[4] W. Pauli. *Letter to the Group of "Radioactives*. 1930.

[5] C. L. Cowan et al. "Detection of the Free Neutrino: a Confirmation". In: *Science* 124.3212 (1956), pp. 103–104. DOI: 10.1126/science.124.3212.103.

[6] In: *Physics Reports* 427.5-6 (May 2006), pp. 257–454. ISSN: 0370-1573. DOI: 10.1016/j.physrep.2005.12.006.

[7] M. Aker et al. "Improved Upper Limit on the Neutrino Mass from a Direct Kinematic Method by KATRIN". In: *Physical Review Letters* 123.22 (Nov. 2019). ISSN: 1079-7114. DOI: 10.1103/physrevlett.123.221802.

[8] "Direct neutrino-mass measurement with sub-electronvolt sensitivity". In: *Nature Physics* 18.2 (Feb. 2022), pp. 160–166. ISSN: 1745-2481. DOI: 10.1038/s41567-021-01463-1.

[9] K.N. Abazajian et al. "Cosmological and astrophysical neutrino mass measurements". In: *Astroparticle Physics* 35.4 (2011), pp. 177–184. ISSN: 0927-6505. DOI: https://doi.org/10.1016/j.astropartphys.2011.07.002.

[10] Francesco Capozzi et al. "Addendum to "Global constraints on absolute neutrino masses and their ordering"". In: *Phys. Rev. D* 101 (11 June 2020), p. 116013. DOI: 10.1103/PhysRevD.101.116013.

[11] S. Bilenky. *Introduction to the Physics of Massive and Mixed Neutrinos*. Undetermined. Lecture Notes in Physics. ISBN: 978-3-642-14042-6. DOI: 10.1007/978-3-642-14043-3.

[12] S. Bilenky. "Neutrinos: Majorana or Dirac?" In: *Universe* 6.9 (2020). ISSN: 2218-1997. DOI: 10.3390/universe6090134.

[13] M. Agostini et al. "Final Results of GERDA on the Search for Neutrinoless Double-β Decay". In: *Phys. Rev. Lett.* 125 (25 Dec. 2020), p. 252502. DOI: 10.1103/PhysRevLett.125.252502.

[14] J. B. Albert, G. Anton, et al. "Search for Neutrinoless Double-Beta Decay with the Upgraded EXO-200 Detector". In: *Phys. Rev. Lett.* 120 (7 Feb. 2018), p. 072701. DOI: 10.1103/PhysRevLett.120.072701.

[15] Edoardo Vitagliano, Irene Tamborra, and Georg Raffelt. "Grand unified neutrino spectrum at Earth: Sources and spectral components". In: *Rev. Mod. Phys.* 92 (4 Dec. 2020), p. 045006. DOI: 10.1103/RevModPhys.92.045006.

[16] Gary Steigman. "Neutrinos and Big Bang Nucleosynthesis". In: *Advances in High Energy Physics* 2012 (Dec. 2012). Ed. by Arthur B. McDonald. Publisher: Hindawi Publishing Corporation, p. 268321. ISSN: 1687-7357. DOI: 10.1155/2012/268321.

[17] Raymond Davis. "A review of the homestake solar neutrino experiment". In: *Progress in Particle and Nuclear Physics* 32 (1994), pp. 13–32. ISSN: 0146-6410. DOI: https://doi.org/10.1016/0146-6410(94)90004-3.

[18] DB Guenther et al. "Standard solar model". In: *The Astrophysical Journal* 387 (1992), pp. 372–393.

[19] S. Fukuda, Y. Fukuda, T. Hayakawa, et al. "The Super-Kamiokande detector". In: *Nuclear Instruments and Methods in Physics Research Section A: Accelerators, Spectrometers, Detectors and Associated Equipment* 501.2 (2003), pp. 418–462. ISSN: 0168-9002. DOI: https://doi.org/10.1016/S0168-9002(03)00425-X.

[20] Hasan Yüksel and John F. Beacom. "Neutrino spectrum from SN 1987A and from cosmic supernovae". In: *Physical Review D* 76.8 (Oct. 2007). ISSN: 1550-2368. DOI: 10.1103/physrevd.76.083007.

[21] T. Araki et al. "Experimental investigation of geologically produced antineutrinos with KamLAND". In: *Nature* 436.7050 (July 2005), pp. 499–503. ISSN: 1476-4687. DOI: 10.1038/nature03980.

[22] G. Bellini, J. Benziger, et al. "Observation of geo-neutrinos". In: *Physics Letters B* 687.4 (2010), pp. 299–304. ISSN: 0370-2693. DOI: https://doi.org/10.1016/j.physletb.2010.03.051.

[23] S. Andringa et al. "Current Status and Future Prospects of the SNO+ Experiment". In: *Advances in High Energy Physics* 2016 (2016), pp. 1–21. ISSN: 1687-7357, 1687-7365. DOI: 10.1155/2016/6194250.

[24] Fengpeng An et al. "Neutrino physics with JUNO". In: *Journal of Physics G: Nuclear and Particle Physics* 43.3 (Feb. 2016), p. 030401. DOI: 10.1088/0954-3899/43/3/030401.

[25] O. Smirnov. "Experimental aspects of geoneutrino detection: Status and perspectives". In: *Progress in Particle and Nuclear Physics* 109 (Nov. 2019), p. 103712. ISSN: 0146-6410. DOI: 10.1016/j.ppnp.2019.103712.

[26] P Padovani et al. "Dissecting the region around IceCube-170922A: the blazar TXS 0506+056 as the first cosmic neutrino source". In: *Monthly Notices of the Royal Astronomical Society* 480.1 (Oct. 2018), pp. 192–203. ISSN: 0035-8711, 1365-2966. DOI: 10.1093/mnras/sty1852.

[27] Todor Stanev. "GZK cutoff and associated neutrinos". In: *Nuclear Physics B - Proceedings Supplements* 136 (2004). CRIS 2004 Proceedings of the Cosmic Ray International Seminars: GZK and Surroundings, pp. 103–110. ISSN: 0920-5632. DOI: https://doi.org/10.1016/j.nuclphysbps.2004.10.025.

[28] Thomas K. Gaisser. *Atmospheric Neutrinos*. 2019. arXiv: 1910.08851 [astro-ph.HE].

[29] Rhorry Gauld et al. "The prompt atmospheric neutrino flux in the light of LHCb". In: *Journal of High Energy Physics* 2016.2 (Feb. 2016). ISSN: 1029-8479. DOI: 10.1007/jhep02(2016)130.

[30] U.F. Katz and Ch. Spiering. "High-energy neutrino astrophysics: Status and perspectives". In: *Progress in Particle and Nuclear Physics* 67.3 (2012), pp. 651–704. ISSN: 0146-6410. DOI: https://doi.org/10.1016/j.ppnp.2011.12.001.

[31] Paolo Lipari, Todor Stanev, and T. K. Gaisser. "Geomagnetic effects on atmospheric neutrinos". In: *Physical Review D* 58.7 (Aug. 1998). ISSN: 1089-4918. DOI: 10.1103/physrevd.58.073003.

[32] Patrick Heix et al. *Seasonal Variation of Atmospheric Neutrinos in IceCube*. 2019. arXiv: 1909.02036 [astro-ph.HE].

[33] S. Adrián-Martínez et al. "Measurement of the atmospheric ν_μ energy spectrum from 100 GeV to 200 TeV with the ANTARES telescope". In: *The European Physical Journal C* 73.10 (Oct. 2013), p. 2606. ISSN: 1434-6052. DOI: 10.1140/epjc/s10052-013-2606-4.

[34] R. Abbasi et al. "Determination of the atmospheric neutrino flux and searches for new physics with AMANDA-II". In: *Phys. Rev. D* 79 (10 May 2009), p. 102005. DOI: 10.1103/PhysRevD.79.102005.

[35] R. Abbasi et al. "Measurement of the atmospheric neutrino energy spectrum from 100 GeV to 400 TeV with IceCube". In: *Phys. Rev. D* 83 (1 Jan. 2011), p. 012001. DOI: 10.1103/PhysRevD.83.012001.

[36] K. Daum et al. "Determination of the atmospheric neutrino spectra with the Fréjus detector". In: *Zeitschrift für Physik C Particles and Fields* 66.3 (Sept. 1995), pp. 417–428. ISSN: 1431-5858. DOI: 10.1007/BF01556368.

[37] M. Honda et al. "Atmospheric neutrino flux calculation using the NRLMSISE-00 atmospheric model". In: *Physical Review D* 92.2 (July 2015). ISSN: 1550-2368. DOI: 10.1103/physrevd.92.023004.

[38] M. Honda et al. *HKKM 2014 flux tables*. https://www.icrr.u-tokyo.ac.jp/~mhonda/nflx2014/index.html. Accessed: 2022-02-27.

[39] E. Richard et al. "Measurements of the atmospheric neutrino flux by Super-Kamiokande: Energy spectra, geomagnetic effects, and solar modulation". In: *Phys. Rev. D* 94 (5 Sept. 2016), p. 052001. DOI: 10.1103/PhysRevD.94.052001.

[40] Rikard Enberg, Mary Hall Reno, and Ina Sarcevic. "Prompt neutrino fluxes from atmospheric charm". In: *Physical Review D* 78.4 (Aug. 2008). arXiv: 0806.0418, p. 043005. ISSN: 1550-7998, 1550-2368. DOI: 10.1103/PhysRevD.78.043005.

[41] M. G. Aartsen et al. "Search for a diffuse flux of astrophysical muon neutrinos with the IceCube 59-string configuration". In: *Physical Review D* 89.6 (Mar. 2014). ISSN: 1550-2368. DOI: 10.1103/physrevd.89.062007.

[42] Yu Seon Jeong et al. *Prompt atmospheric neutrino flux*. 2016. arXiv: 1611.05120 [hep-ph].

[43] S Adrián-Martínez, M Ageron, et al. "Letter of intent for KM3NeT 2.0". In: 43.8 (June 2016), p. 084001. DOI: 10.1088/0954-3899/43/8/084001.

[44] B. Pontecorvo. "Neutrino Experiments and the Problem of Conservation of Leptonic Charge". In: *Zh. Eksp. Teor. Fiz.* 53 (1967), pp. 1717–1725.

[45] Ziro Maki, Masami Nakagawa, and Shoichi Sakata. "Remarks on the Unified Model of Elementary Particles". In: *Progress of Theoretical Physics* 28.5 (Nov. 1962), pp. 870–880. ISSN: 0033-068X. DOI: 10.1143/PTP.28.870.

[46] "Leptogenesis, CP violation and neutrino data: what can we learn?" In: *Nuclear Physics B* 640.1 (2002), pp. 202–232. ISSN: 0550-3213. DOI: https://doi.org/10.1016/S0550-3213(02)00478-9.

[47] Y. Fukuda et al. "Evidence for Oscillation of Atmospheric Neutrinos". In: *Physical Review Letters* 81.8 (Aug. 1998), pp. 1562–1567. DOI: 10.1103/physrevlett.81.1562.

[48] Q. R. Ahmad et al. "Direct Evidence for Neutrino Flavor Transformation from Neutral-Current Interactions in the Sudbury Neutrino Observatory". In: *Phys. Rev. Lett.* 89 (1 June 2002), p. 011301. DOI: 10.1103/PhysRevLett.89.011301.

[49] K. Eguchi et al. "First Results from KamLAND: Evidence for Reactor Antineutrino Disappearance". In: *Physical Review Letters* 90.2 (Jan. 2003). DOI: 10.1103/physrevlett.90.021802.

[50] G.L. Fogli et al. "Global analysis of three-flavor neutrino masses and mixings". In: *Progress in Particle and Nuclear Physics* 57.2 (Oct. 2006), pp. 742–795. DOI: 10.1016/j.ppnp.2005.08.002.

[51] Laura Lee Kormos and. "Towards seeking θ_{13}: Status and initial data from T2K". In: *Journal of Physics: Conference Series* 287 (Apr. 2011), p. 012033. DOI: 10.1088/1742-6596/287/1/012033.

[52] P. Adamson, D. J. Auty, et al. "Improved Search for Muon-Neutrino to Electron-Neutrino Oscillations in MINOS". In: *Phys. Rev. Lett.* 107 (18 Oct. 2011), p. 181802. DOI: 10.1103/PhysRevLett.107.181802.

[53] P. A. N. Machado et al. "Combining accelerator and reactor measurements of θ_{13}: the first result". In: *Journal of High Energy Physics* 2012.5 (May 2012), p. 23. ISSN: 1029-8479. DOI: 10.1007/JHEP05(2012)023.

[54] M. C. Gonzalez-Garcia and Carlos Peña-Garay. "Three-neutrino mixing after the first results from K2K and KamLAND". In: *Phys. Rev. D* 68 (9 Nov. 2003), p. 093003. DOI: 10.1103/PhysRevD.68.093003.

[55] Ivan Esteban et al. “The fate of hints: updated global analysis of three-flavor neutrino oscillations”. In: *Journal of High Energy Physics* 2020.9 (Sept. 2020). DOI: 10.1007/jhep09(2020)178.

[56] Jessica Elevant and Thomas Schwetz. “On the determination of the leptonic CP phase”. In: *Journal of High Energy Physics* 2015.9 (Sept. 2015), p. 16. ISSN: 1029-8479. DOI: 10.1007/JHEP09(2015)016.

[57] P. Dunne. ““Latest Neutrino Oscillation Results from T2K.”” In: (online conference). Talk given at the *XXIX International Conference on Neutrino Physics and Astrophysics*, Chicago, USA, June 2020.

[58] A. Himmel. ““New Oscillation Results from the NOvA Experiment.”” In: (online conference). Talk given at the *XXIX International Conference on Neutrino Physics and Astrophysics*, Chicago, USA, June 2020.

[59] Maria Concepcion Gonzalez-Garcia, Michele Maltoni, and Thomas Schwetz. “NuFIT: Three-Flavour Global Analyses of Neutrino Oscillation Experiments”. In: *Universe* 12 (Jan. 2021), p. 459. DOI: 10.3390/universe7120459.

[60] L. Wolfenstein. “Neutrino oscillations in matter”. In: *Phys. Rev. D* 17 (9 May 1978), pp. 2369–2374. DOI: 10.1103/PhysRevD.17.2369.

[61] S. P. Mikheyev and A. Yu. Smirnov. “Resonance Amplification of Oscillations in Matter and Spectroscopy of Solar Neutrinos”. In: *Sov. J. Nucl. Phys.* 42 (1985), pp. 913–917.

[62] Martin Freund. “Analytic approximations for three neutrino oscillation parameters and probabilities in matter”. In: *Physical Review D* 64.5 (July 2001). DOI: 10.1103/physrevd.64.053003.

[63] P.I. Krastev and A.Yu. Smirnov. “Parametric effects in neutrino oscillations”. In: *Physics Letters B* 226.3 (1989), pp. 341–346. ISSN: 0370-2693. DOI: https://doi.org/10.1016/0370-2693(89)91206-9.

[64] E. Kh. Akhmedov. “Parametric resonance in neutrino oscillations in matter”. In: (1999). DOI: 10.48550/ARXIV.HEP-PH/9907435.

[65] J. A. Formaggio and G. P. Zeller. “From eV to EeV: Neutrino cross sections across energy scales”. In: *Rev. Mod. Phys.* 84 (3 Sept. 2012), pp. 1307–1341. DOI: 10.1103/RevModPhys.84.1307.

[66] J. G. H. Groot, T. Hansl, et al. “Inclusive interactions of high-energy neutrinos and antineutrinos in iron”. In: *Zeitschrift für Physik C Particles and Fields* 1.2 (June 1979), pp. 143–162. ISSN: 0170-9739, 1434-6052. DOI: 10.1007/BF01445406.

[67] Andre Rubbia. *Lectures on Neutrino Physics at ETH Zürich*. 2014.

[68] P.A. Zyla et al. In: *Prog. Theor. Exp. Phys. 2020* 083C01 (2020).

[69] N. J. Baker et al. “Total Cross-sections for Muon-neutrino N and Muon-neutrino P Charged Current Interactions in the 7-ft Bubble Chamber”. In: *Phys. Rev. D* 25 (1982), pp. 617–623. DOI: 10.1103/PhysRevD.25.617.

[70] S. Ciampolillo et al. “Total Cross-section for Neutrino Charged Current Interactions at 3-GeV and 9-GeV”. In: *Phys. Lett. B* 84 (1979), pp. 281–284. DOI: 10.1016/0370-2693(79)90303-4.

[71] Y. Nakajima et al. “Measurement of inclusive charged current interactions on carbon in a few-GeV neutrino beam”. In: *Phys. Rev. D* 83 (1 Jan. 2011), p. 012005. DOI: 10.1103/PhysRevD.83.012005.

[72] D.C. Colley, G.T. Jones, S. O’Neale, et al. “Cross sections for charged current ν and $\bar{\nu}$ interactions in the energy range 10 to 50 GeV.” In: *Z. Phys. C - Particles and Fields* 2 (1979), pp. 187–190. DOI: https://doi.org/10.1007/BF01474659.

[73] C. H. Llewellyn Smith. “On the Determination of sin**2-Theta-w in Semileptonic Neutrino Interactions”. In: *Nucl. Phys. B* 228 (1983), pp. 205–215. DOI: 10.1016/0550-3213(83)90320-6.

[74] C. Andreopoulos et al. “The GENIE neutrino Monte Carlo generator”. In: *Nuclear Instruments and Methods in Physics Research Section A: Accelerators, Spectrometers, Detectors and Associated Equipment* 614.1 (Feb. 2010), pp. 87–104. ISSN: 0168-9002. DOI: 10.1016/j.nima.2009.12.009.

[75] Amanda Cooper-Sarkar, Philipp Mertsch, and Subir Sarkar. “The high energy neutrino cross-section in the Standard Model and its uncertainty”. In: *Journal of High Energy Physics* 2011.8 (Aug. 2011). ISSN: 1029-8479. DOI: 10.1007/jhep08(2011)042.

[76] Raj Gandhi et al. “Ultrahigh-energy neutrino interactions”. In: *Astroparticle Physics* 5.2 (1996), pp. 81–110. ISSN: 0927-6505. DOI: https://doi.org/10.1016/0927-6505(96)00008-4.

[77] Sheldon L. Glashow. “Resonant Scattering of Antineutrinos”. In: *Phys. Rev.* 118 (1 Apr. 1960), pp. 316–317. DOI: 10.1103/PhysRev.118.316.

[78] P. A. Cherenkov. “Visible luminescence of pure liquids under the influence of γ-radiation”. In: *Dokl. Akad. Nauk SSSR* 2.8 (1934), pp. 451–454. DOI: 10.3367/UFNr.0093.196710n.0385.

[79] P. A. Čerenkov. “Visible Radiation Produced by Electrons Moving in a Medium with Velocities Exceeding that of Light”. In: *Phys. Rev.* 52 (4 Aug. 1937), pp. 378–379. DOI: 10.1103/PhysRev.52.378.

[80] Travis M. Shaffer, Edwin C. Pratt, and Jan Grimm. “Utilizing the power of Cerenkov light with nanotechnology”. In: *Nature Nanotechnology* 12.2 (Feb. 2017). ISSN: 1748-3395. DOI: 10.1038/nnano.2016.301.

[81] I. M. Frank and I. E. Tamm. “Coherent visible radiation of fast electrons passing through matter”. In: *Compt. Rend. Acad. Sci. URSS* 14.3 (1937), pp. 109–114. DOI: 10.3367/UFNr.0093.196710o.0388.

[82] Pilar Coloma et al. “Double-Cascade Events from New Physics in Icecube”. In: *Phys. Rev. Lett.* 119 (20 Nov. 2017), p. 201804. DOI: 10.1103/PhysRevLett.119.201804.

[83] Steffen Hallmann. "Sensitivity to atmospheric tau-neutrino appearance and all-flavour search for neutrinos from the Fermi Bubbles with the deep-sea telescopes KM3NeT/ORCA and ANTARES". PhD thesis. Friedrich-Alexander-Universität Erlangen-Nürnberg (FAU), 2021.

[84] "The IceCube Neutrino Observatory: instrumentation and online systems". In: *Journal of Instrumentation* 12.03 (Mar. 2017), P03012–P03012. ISSN: 1748-0221. DOI: 10.1088/1748-0221/12/03/p03012.

[85] "The design and performance of IceCube DeepCore". In: *Astroparticle Physics* 35.10 (2012), pp. 615–624. ISSN: 0927-6505. DOI: https://doi.org/10.1016/j.astropartphys.2012.01.004.

[86] M. G. Aartsen et al. "Evidence for High-Energy Extraterrestrial Neutrinos at the IceCube Detector". In: *Science* 342.6161 (2013), p. 1242856. DOI: 10.1126/science.1242856.

[87] Markus Ackermann et al. *High-Energy and Ultra-High-Energy Neutrinos*. 2022. DOI: 10.48550/ARXIV.2203.08096.

[88] Francis Halzen and Ali Kheirandish. *IceCube and High-Energy Cosmic Neutrinos*. 2022. DOI: 10.48550/ARXIV.2202.00694.

[89] M. G. Aartsen et al. "Measurement of Atmospheric Neutrino Oscillations at 6–56 GeV with IceCube DeepCore". In: *Physical Review Letters* 120.7 (Feb. 2018). DOI: 10.1103/physrevlett.120.071801.

[90] M. G. Aartsen et al. "PINGU: A Vision for Neutrino and Particle Physics at the South Pole". In: *J. Phys.* G44.5 (2017), p. 054006. DOI: 10.1088/1361-6471/44/5/054006. arXiv: 1607.02671 [hep-ex].

[91] I. Sokalski. *The ANTARES experiment: past, present and future*. 2005. arXiv: hep-ex/0501003 [hep-ex].

[92] S. Aiello E. et al. *Determining the Neutrino Mass Ordering and Oscillation Parameters with KM3NeT/ORCA*. 2021. arXiv: 2103.09885 [hep-ex].

[93] Jarosław Stasielak et al. "High-Energy Neutrino Astronomy—Baikal-GVD Neutrino Telescope in Lake Baikal". In: *Symmetry* 13.3 (2021). ISSN: 2073-8994. DOI: 10.3390/sym13030377.

[94] Hyper-Kamiokande Proto-Collaboration et al. *Hyper-Kamiokande Design Report*. 2018. arXiv: 1805.04163 [physics.ins-det].

[95] M. Ackermann et al. "Optical properties of deep glacial ice at the South Pole". In: *Journal of Geophysical Research: Atmospheres* 111.D13 (2006). DOI: https://doi.org/10.1029/2005JD006687.

[96] P. Bagley et al. "Conceptual design report". In: (2008).

[97] V. Balkanov et al. "Simultaneous measurements of water optical properties by AC9 transmissometer and ASP-15 inherent optical properties meter in Lake Baikal". In: *Nuclear Instruments and Methods in Physics Research Section A: Accelerators, Spectrometers, Detectors and Associated Equipment* 498.1 (2003), pp. 231–239. ISSN: 0168-9002. DOI: https://doi.org/10.1016/S0168-9002(02)01789-8.

[98] A. Abed Abud et al. "Deep Underground Neutrino Experiment (DUNE) Near Detector Conceptual Design Report". In: (2021). arXiv: 2103.13910 [physics.ins-det].

[99] B. Abi et al. "Volume I. Introduction to DUNE". In: *Journal of Instrumentation* 15 (Aug. 2020), T08008–T08008. DOI: 10.1088/1748-0221/15/08/T08008.

[100] Nick Grant. "Neutrino energy reconstruction in the DUNE far detector". In: ().

[101] B. Abi et al. "Neutrino interaction classification with a convolutional neural network in the DUNE far detector". In: *Phys. Rev. D* 102 (9 Nov. 2020), p. 092003. DOI: 10.1103/PhysRevD.102.092003.

[102] R. Acciarri et al. "First Observation of Low Energy Electron Neutrinos in a Liquid Argon Time Projection Chamber". In: *Phys. Rev. D* 95.7 (2017), p. 072005. DOI: 10.1103/PhysRevD.95.072005. arXiv: 1610.04102 [hep-ex].

[103] Adams Douglas. *The Hitchhiker's Guide to the Galaxy*. 1979.

[104] Peter M. Shearer. *Introduction to Seismology: The wave equation and body waves*. June 2010.

[105] Thorne Lay and T. Wallace. "Modern Global Seimology". In: vol. 58. Jan. 1995.

[106] Dapeng Zhao. "Importance of later phases in seismic tomography". In: *Physics of The Earth and Planetary Interiors* 296 (Sept. 2019), p. 106314. DOI: 10.1016/j.pepi.2019.106314.

[107] K. E. Bullen. "Optimum and standard Earth models". In: *The Earth's Density*. Dordrecht: Springer Netherlands, 1975, pp. 352–366. ISBN: 978-94-009-5700-8. DOI: 10.1007/978-94-009-5700-8_16.

[108] A. M. Dziewonski and M. L. Anderson. "Preliminary reference Earth model". In: *Phys. Earth Planet. Int.* 25 (4) (1981), pp. 297–356.

[109] Brian Luzum et al. "The IAU 2009 system of astronomical constants: the report of the IAU working group on numerical standards for Fundamental Astronomy". In: *Celestial Mechanics and Dynamical Astronomy* 110.4 (July 2011), p. 293. ISSN: 1572-9478. DOI: 10.1007/s10569-011-9352-4.

[110] Wei Chen et al. "Consistent estimates of the dynamic figure parameters of the earth". In: *Journal of Geodesy* 89.2 (Feb. 2015), pp. 179–188. ISSN: 1432-1394. DOI: 10.1007/s00190-014-0768-y.

[111] B. L. N. Kennett, E. R. Engdahl, and R. Buland. "Constraints on seismic velocities in the Earth from traveltimes". In: *Geophysical Journal International* 122.1 (July 1995), pp. 108–124. ISSN: 0956-540X. DOI: 10.1111/j.1365-246X.1995.tb03540.x.

[112] F. Birch. "Composition of the Earth's Mantle". In: *Geophysical Journal International* 4.Supplement_1 (1961), pp. 295–311.

[113] Jean-Paul Poirier. "Light elements in the Earth's outer core: A critical review". In: *Physics of the Earth and Planetary Interiors* 85.3 (1994), pp. 319–337. ISSN: 0031-9201. DOI: https://doi.org/10.1016/0031-9201(94)90120-1.

[114] S. Hirose K. Labrosse and J. Hernlund. "Composition and State of the Core". In: *Annu. Rev. Earth Planet Sci.* 41 (2013), pp. 657–691.

[115] W. F. McDonough. "Compositional Model for the Earth's Core". In: *Treatise on Geochemistry*. Vol. 2. Elsevier, 2003, pp. 547–566.

[116] J. Badro et al. "Core formation and core composition from coupled geochemical and geophysical constraints". In: *PNAS* 112 (40) (2015), pp. 12310–12314.

[117] E. Kaminski and M. Javoy. "A two-stage scenario for the formation of the Earth's mantle and core". In: *Earth and Planetary Science Letters* 365 (2013), pp. 97–107.

[118] S. Tagawa et al. "Compression of Fe–Si–H alloys to core pressures". In: *Geophysical Research Letters* 43(8) (2016), pp. 3686–3692.

[119] T. Sakamaki et al. "Constraints on Earth's inner core composition inferred from measurements of the sound velocity of hcp-iron in extreme conditions". In: *Science Advances* 2.2 (2016), e1500802.

[120] Edward J. Garnero and Allen K. McNamara. "Structure and Dynamics of Earth's Lower Mantle". In: *Science* 320.5876 (2008), pp. 626–628. DOI: 10.1126/science.1148028.

[121] Allen K. McNamara. "A review of large low shear velocity provinces and ultra low velocity zones". In: *Tectonophysics* 760 (2019). Linking Plate Tectonics and Volcanism to Deep Earth Dynamics – a tribute to Trond H. Torsvik, pp. 199–220. ISSN: 0040-1951. DOI: https://doi.org/10.1016/j.tecto.2018.04.015.

[122] J. Ritsema et al. "S40RTS: a degree-40 shear-velocity model for the mantle from new Rayleigh wave dispersion, teleseismic traveltime and normal-mode splitting function measurements". In: *Geophysical Journal International* 184.3 (Mar. 2011), pp. 1223–1236. ISSN: 0956-540X. DOI: 10.1111/j.1365-246X.2010.04884.x.

[123] "Measurement of the multi-TeV neutrino interaction cross-section with IceCube using Earth absorption". In: *Nature* 551.7682 (Nov. 2017), pp. 596–600. ISSN: 1476-4687. DOI: 10.1038/nature24459.

[124] L.V. Volkova and G.T. Zatsepin. "On problem to neutrino passing through the Earth". In: *Izvestiya Akademii Nauk SSSR, Seriya Fizicheskaya* 38(5) (1974), pp. 1060–1063.

[125] Alfredo Placci and Emilio Zavattini. *On the possibility of using high-energy neutrinos to study the earth's interior*. Tech. rep. Geneva: CERN, Oct. 1973.

[126] Pankaj Jain, John P. Ralston, and George M. Frichter. "Neutrino absorption tomography of the Earth's interior using isotropic ultra-high energy flux". In: *Astroparticle Physics* 12.3 (Nov. 1999), pp. 193–198. ISSN: 0927-6505. DOI: 10.1016/S0927-6505(99)00088-2.

[127] Manfred Lindner et al. "Tomography of the Earth's core using supernova neutrinos". In: *Astroparticle Physics* 19.6 (2003), pp. 755–770. ISSN: 0927-6505. DOI: https://doi.org/10.1016/S0927-6505(03)00120-8.

[128] Walter Winter. "Atmospheric neutrino oscillations for Earth tomography". In: *Nuclear Physics B* 908 (2016). Neutrino Oscillations: Celebrating the Nobel Prize in Physics 2015, pp. 250–267. ISSN: 0550-3213. DOI: https://doi.org/10.1016/j.nuclphysb.2016.03.033.

[129] Kevin J. Kelly et al. "DUNE atmospheric neutrinos: Earth Tomography". In: *arXiv:2110.00003 [hep-ex, physics:hep-ph]* (Sept. 2021).

[130] Peter B. Denton and Rebekah Pestes. "Neutrino oscillations through the Earth's core". In: *Physical Review D* 104.11 (Dec. 2021). DOI: 10.1103/physrevd.104.113007.

[131] Simon Bourret, João A B Coelho, and Véronique Van Elewyck and. "Neutrino oscillation tomography of the Earth with KM3NeT-ORCA". In: *Journal of Physics: Conference Series* 888 (Sept. 2017), p. 012114. DOI: 10.1088/1742-6596/888/1/012114.

[132] F. Capozzi and S. T. Petcov. "Neutrino tomography of the Earth with ORCA detector". In: *The European Physical Journal C* 82.5 (May 2022), p. 461. ISSN: 1434-6052. DOI: 10.1140/epjc/s10052-022-10399-6.

[133] C. Rott, A. Taketa, and D. Bose. "Spectrometry of the Earth using Neutrino Oscillations". In: *Scientific Reports* 5.1 (Oct. 2015), p. 15225. ISSN: 2045-2322. DOI: 10.1038/srep15225.

[134] M. C. Gonzalez-Garcia et al. "Radiography of Earth's Core and Mantle with Atmospheric Neutrinos". In: *Physical Review Letters* 100.6 (Feb. 2008). ISSN: 1079-7114. DOI: 10.1103/physrevlett.100.061802.

[135] Anil Kumar and Sanjib Kumar Agarwalla. "Validating the Earth's core using atmospheric neutrinos with ICAL at INO". In: *Journal of High Energy Physics* 2021.8 (Aug. 2021). ISSN: 1029-8479. DOI: 10.1007/jhep08(2021)139.

[136] Andrea Donini, Sergio Palomares-Ruiz, and Jordi Salvado. "Neutrino tomography of Earth". In: *Nature Physics* 15.1 (Nov. 2018), pp. 37–40. ISSN: 1745-2481. DOI: 10.1038/s41567-018-0319-1.

[137] A. Sinopoulou et al. "Atmospheric neutrinos with the first detection units of KM3NeT/ARCA". en. In: *Journal of Instrumentation* 16.11 (Nov. 2021). Publisher: IOP Publishing. ISSN: 1748-0221. DOI: 10.1088/1748-0221/16/11/C11015.

[138] Lodewijk Nauta et al. "First neutrino oscillation measurement in KM3NeT/ORCA". In: *Proceedings of 37th International Cosmic Ray Conference — PoS(ICRC2021)*. Vol. 395. SISSA Medialab, July 2021, p. 1123. DOI: 10.22323/1.395.1123.

[139] Dorothea Samtleben et al. "The Calibration Units of KM3NeT". In: *PoS* ICRC2021 (2021), p. 1096. DOI: 10.22323/1.395.1096.

[140] S. Adrián-Martínez et al. "Long term monitoring of the optical background in the Capo Passero deep-sea site with the NEMO tower prototype". In: *The European Physical Journal C* 76.2 (Feb. 2016). ISSN: 1434-6052. DOI: 10.1140/epjc/s10052-016-3908-0.

[141] Christian Tamburini and ohters. “Deep-Sea Bioluminescence Blooms after Dense Water Formation at the Ocean Surface”. In: *PLOS ONE* 8.7 (July 2013), pp. 1–10. DOI: 10.1371/journal.pone.0067523.

[142] Distefano, Carla. “gSeaGen: A GENIE-based code for neutrino telescopes”. In: *EPJ Web of Conferences* 116 (2016), p. 08001. DOI: 10.1051/epjconf/201611608001.

[143] S. Jadach, J. H. Kühn, and Z. Was. “TAUOLA - a library of Monte Carlo programs to simulate decays of polarized τ leptons”. In: *Computer Physics Communications* 64.2 (1991), pp. 275–299. ISSN: 0010-4655. DOI: https://doi.org/10.1016/0010-4655(91)90038-M.

[144] G. Carminati et al. “Atmospheric MUons from PArametric formulas: a fast GEnerator for neutrino telescopes (MUPAGE)”. In: *Computer Physics Communications* 179.12 (Dec. 2008), pp. 915–923. DOI: 10.1016/j.cpc.2008.07.014.

[145] Y. Becherini et al. “A parameterisation of single and multiple muons in the deep water or ice”. In: *Astroparticle Physics* 25.1 (Feb. 2006), pp. 1–13. DOI: 10.1016/j.astropartphys.2005.10.005.

[146] A. G. Tsirigotis, A. Leisos, and S. E. Tzamarias. “HOU Reconstruction & Simulation (HOURS): A complete simulation and reconstruction package for very large volume underwater neutrino telescopes”. In: *Nucl. Instrum. Meth. A* 626-627 (2011). Ed. by E. G. Anassontzis, P. A. Rapidis, and L. K. Resvanis, S185–S187. DOI: 10.1016/j.nima.2010.06.258.

[147] Jannik Hofestädt. “Measuring the neutrino mass hierarchy with the future KM3NeT/ORCA detector”. PhD thesis. Friedrich-Alexander-Universität Erlangen-Nürnberg (FAU), 2017, p. 239.

[148] Liam Quinn. “Determining the Neutrino Mass Hierarchy with KM3NeT/ORCA”. PhD thesis. Aix-Marseille Université Centre de Physique des Particules de Marseille, 2018.

[149] Tianqi Chen and Carlos Guestrin. “XGBoost: A Scalable Tree Boosting System”. In: *Proceedings of the 22nd ACM SIGKDD International Conference on Knowledge Discovery and Data Mining*. KDD ’16. San Francisco, California, USA: ACM, 2016, pp. 785–794. ISBN: 978-1-4503-4232-2. DOI: 10.1145/2939672.2939785.

[150] Ping Li, Qiang Wu, and Christopher Burges. “McRank: Learning to Rank Using Multiple Classification and Gradient Boosting”. In: *Advances in Neural Information Processing Systems*. Ed. by J. Platt et al. Vol. 20. Curran Associates, Inc., 2008.

[151] Michael Moser. “Sensitivity studies on tau neutrino appearance with KM3NeT/ORCA using Deep Learning Techniques”. PhD thesis. Friedrich-Alexander-Universität Erlangen-Nürnberg (FAU), 2020.

[152] Fabian Pedregosa et al. “Scikit-learn: Machine learning in Python”. In: *Journal of machine learning research* 12.Oct (2011), pp. 2825–2830.

[153] S. Geißelsöder. “Classification of events for the ANTARES neutrino detector”. Master. Friedrich-Alexander-Universität Erlangen-Nürnberg (FAU), 2021.

[154] Maarten de Jong. *The probability density function of the arrival time of light*. https://common.pages.km3net.de/jpp/JPDF.PDF.

[155] R. Abbasi et al. "Improved Characterization of the Astrophysical Muon-Neutrino Flux with 9.5 Years of IceCube Data". In: (2021). DOI: 10.48550/ARXIV.2111.10299.

[156] Rene Brun and Fons Rademakers. *root-project/root: v6.18/02*. Version v6-18-02. Aug. 2019. DOI: 10.5281/zenodo.3895860.

[157] João B. Coelho. *OscProb*. https://github.com/joaoabcoelho/OscProb. 2021.

[158] Alfonso Garcia et al. "Complete predictions for high-energy neutrino propagation in matter". In: *Journal of Cosmology and Astroparticle Physics* 2020.09 (Sept. 2020), pp. 025–025. ISSN: 1475-7516. DOI: 10.1088/1475-7516/2020/09/025.

[159] Christopher Weaver and Jordi Salvade. *nuSQuIDS*. https://github.com/arguelles/nuSQuIDS. 2021.

[160] Carlos Alberto Arguelles Delgado, Jordi Salvado, and Christopher N. Weaver. *A Simple Quantum Integro-Differential Solver (SQuIDS)*. 2014. arXiv: 1412.3832 [hep-ph].

[161] M. C. Gonzalez-Garcia, Francis Halzen, and Michele Maltoni. "Physics reach of high-energy and high-statistics IceCube atmospheric neutrino data". In: *Physical Review D* 71.9 (May 2005). ISSN: 1550-2368. DOI: 10.1103/physrevd.71.093010.

[162] S. Bourret. "Neutrino oscillations and Earth tomography with KM3NeT-ORCA". PhD thesis. Université Sorbonne Paris Cité, 2018.

[163] Ronald Aylmer Fisher. "Dispersion on a sphere". In: *Proc. R. Soc. Lond.* 217 (1953), pp. 295–305. DOI: https://doi.org/10.1098/rspa.1953.0064.

[164] Joel Heinrich and Louis Lyons. "Systematic Errors". In: *Annual Review of Nuclear and Particle Science* 57.1 (Nov. 2007). Publisher: Annual Reviews, pp. 145–169. ISSN: 0163-8998. DOI: 10.1146/annurev.nucl.57.090506.123052.

[165] Roger Barlow and Christine Beeston. "Fitting using finite Monte Carlo samples". In: *Computer Physics Communications* 77.2 (1993), pp. 219–228. ISSN: 0010-4655. DOI: https://doi.org/10.1016/0010-4655(93)90005-W.

[166] M. Hatlo et al. "Developments of mathematical software libraries for the LHC experiments". In: *IEEE Trans. Nucl. Sci.* 52 (2005), pp. 2818–2822. DOI: 10.1109/TNS.2005.860152.

[167] F James and M Roos. "MINUIT: Function Minimization and Error Analysis". In: (Aug. 1998), p. 52.

[168] N. Chau et al. "Neutrino mass ordering determination through combined analysis with JUNO and KM3NeT/ORCA". In: *Journal of Instrumentation* 16.11 (Nov. 2021), p. C11007. DOI: 10.1088/1748-0221/16/11/c11007.

[169] Albert Tarantola. *Inverse Problem Theory and Methods for Model Parameter Estimation*. Society for Industrial and Applied Mathematics, Jan. 2005. DOI: 10.1137/1.9780898717921.

[170] R. van Tent et al. "An Analysis of Normal-Mode Based 3-D Mantle Density Models using Hamiltonian Monte Carlo Methods". In: *AGU Fall Meeting Abstracts*. Vol. 2020. Dec. 2020, pp. DI005–0003.

[171] Lukas Maderer et al. "KM3NeT performance on oscillation and absorption tomography of the Earth". In: *Proceedings of 37th International Cosmic Ray Conference — PoS(ICRC2021)*. Vol. 395. SISSA Medialab, Mar. 2021, p. 1172. DOI: 10.22323/1.395.1172.

[172] Tamas Gal. *KM3Pipe 9.0.0*. Version v9.0.0. Nov. 2020. DOI: 10.5281/zenodo.3813349.

[173] Maarten de Jong et al. *JPP*. https://common.pages.km3net.de/jpp/index.html.